Micromechanical Modeling of Soil-Water Interaction with Applications to Buried Structures

by

Ahmed Ibrahim

Department of Civil Engineering

McGill University, Montréal

July 2022

A thesis submitted to

McGill University

in partial fulfillment of the degree of

Doctor of Philosophy

Dedication

To my dear parents
Mohamed and *Salma*

To my beloved wife
Marwa

To my dear brothers
Sayed and *Alaa*

Abstract

The interaction between soil and water is a key factor that governs the behavior of various geotechnical systems. Examples for this include, but not limited to, stress-pore water pressure coupling, erosion, and piping. Depending on the scale and nature of the application, soil-water interaction may be accounted for differently. This may range from static and quasi-static conditions to fluid-body and fluid-particle interaction problems used in modeling debris flow problems. In these different cases, the level of physics and data acquisition varies significantly. For example, the conventional approach of accounting for water-soil interaction incorporates indirect macroscale relations that govern the state of stresses in soil as well as water flow. Darcy flow for seepage analysis, for instance, underlies the assumption of unchanging soil matrix over time, regardless of its heterogeneity. Such assumption is not valid in cases that involve inter-soil particle motion such as the case for suffusion and internal erosion. Similarly, in highly convective flow such as the flow of a soil-water mixture and debris flow, such macroscale constitutive relations are no longer sufficient to describe the dynamics of interest. As such, a more refined analysis needs to be used in these cases that can provide detailed information on both the flow field variables of water as well as the dynamics of the soil particles. That essentially calls for resolving the interactions at the microscale by solving the coupled momentum equations of the liquid phase (water) and the solid phase (soil). Notable to mention that incorporating microscale analysis does not necessarily mean that the targeted application itself is microscopic, instead, the data and level of interaction acquired from such analysis are resolved on the scale of individual particles. Such analysis, in addition to its inherent complexity, comes with a high computational cost that makes modeling practical systems computationally infeasible. As a result, despite its vast applications, only a limited number of studies exist in the field of civil and geotechnical engineering that utilize fully coupled soil-water interaction.

This thesis starts with a comprehensive review of the different numerical approaches and definitions involved with microscale modeling of soil-water systems. It also connects decades of model development in other disciplines such as chemical engineering to geotechnical engineering context. In chapter 3, the Two-Fluid Model (TFM) is explored in the context of internal erosion due to leaking from pressurized pipes. In this model, an equivalent continuum-based representation of the soil particles is made possible by incorporating the Kinetic Theory of Granular Flow (KTGF) to account for contact and shear forces between the soil particles. Such representation of the soil portion enables us to use mesh-based solvers such as finite element of finite volume methods to solve the governing equations of both water and soil. This technique typically requires significantly less

computational effort by avoiding the direct discrete representation of each soil particle. The model was first validated using a simple column seepage simulation and available experimental data. The results show good initial agreement of the model with the analytical solution as well the experimental results. Further insights into the erosion process are then presented highlighting the effect of soil polydispersity and the problem geometry.

Due to the numerical averaging process used in the TFM, it is fundamentally unable to capture some of the solid phase dynamics such as that of granular flow through orifice. A problem, for which, the granular flow rate is typically independent from the material height above the orifice due to the freefall arch effect. This directly applies to the sand erosion problem into defective sewer pipes discussed in chapter 4. A coupled Computational Fluid Dynamics-Discrete Element Method (CFD-DEM) is used to investigate the erosion process of sand into sewer pipes under the effect of groundwater. A parametric study was performed to examine the effect the defect geometry, groundwater table level, defect angle, and the sand layer height above the pipe. The results highlight the effect of groundwater in mobilizing the erosion process, both in extent and rate, while it suggests limited effect of the sand layer height above the pipe. It also sheds light on the role of groundwater on mobilizing erosions through cracks inclined from the pipe crown, which is a step towards better understanding accelerated soil erosion and appearance of sinkholes after heavy rainfall events. Finally, the model was used to explore the effect of geotextile clogging by fine soil particles driven by groundwater ingress into drained tunnels. A novel technique was developed to create and test the properties of non-woven geotextile. Coupled CFD-DEM simulations were conducted to examine the clogging effect on the hydraulic deterioration of the geotextile and the development of excessive water pressure in the drainage layer of the tunnel. A modified set of boundary conditions were developed to describe the flow of fine particles and water through cracks at which the geotextile is prone to clogging. The results show the model's ability to capture the behavior of the clogging as well as local piping through cracks located in high-hydraulic gradient zones. The analysis presents the distribution of excessive pressure in the drainage layer and the effect of different types of soils on the clogging process.

Résumé

L'interaction entre le sol et l'eau est un élément clef qui contrôle le comportement de nombreux problèmes en géotechnique tels que le couplage entre les contraintes et la pression interstitielle, l'érosion, et le phénomène de renard. Selon l'échelle et la fonction du problème géotechnique, l'interaction eau-sol peut être traitée de différentes façons, telles que les relations définissant les contraintes effectives dans le sol pour des conditions statiques ou quasi-statiques où l'eau est sous des conditions statiques ou encore les problèmes d'interaction fluide-structure décrivant les coulées de débris. Dans ces différents cas, le niveau de physique et de données acquises fluctue fortement. Par exemple, la méthode conventionnelle par laquelle l'interaction eau-sol est prise en compte contient des relations qui définissent indirectement les contraintes agissant dans le sol aussi bien que dans l'eau à l'échelle macroscopique. Notamment, le flux de Darcy qui exprime le débit d'un fluide au travers d'un milieu poreux présume que la matrice du sol ne change pas à travers le temps, peu importe son niveau d'hétérogénéité. Cette hypothèse n'est cependant pas valide pour les problèmes impliquant le mouvement des particules du sol tels que l'érosion interne et la suffusion. De même, les lois de comportement à l'échelle macroscopique ne sont pas suffisantes pour décrire les phénomènes dynamiques qui prennent place dans les flux convectifs comme le flux dans un mélange eau-sol ou une coulée de débris. Il est par conséquent primordial d'employer des méthodes d'analyses plus raffinées dans de tels cas afin de pouvoir décrire en bonne et due forme les variables du champ d'écoulement de l'eau et de la dynamique des particules. Cela se traduit par un besoin de solutionner les interactions à l'échelle microscopique en résolvant les équations couplées de la quantité de mouvement de la phase liquide (eau) et de la phase solide (sol). Il est important de stipuler que l'incorporation d'une analyse microscopique n'implique pas forcément que le problème en lui-même est microscopique mais plutôt que les données ainsi que le niveau d'interaction liés à l'analyse sont résolues à l'échelle individuelle des particules. Ce type d'analyse, au-delà de sa nature complexe, requiert d'amples ressources computationnelles ce qui rend la modélisation de systèmes pratiques impossible. En conséquence, malgré le vaste champ d'application de l'analyse couplée de l'interaction eau-sol, peu d'études ont été entreprises dans ce domaine en génie civil et en génie géotechnique.

Cette thèse débute par une revue complète des approches numériques et des définitions propres à la modélisation microscopique des systèmes eau-sol. En plus de fournir une revue de la littérature pertinente au sujet de cette thèse, le chapitre en question est motivé par le désir de résumer de façon claire et concise les innovations dans le domaine de la modélisation entreprises dans d'autres

disciplines telles que le génie chimique qui sont directement utilisables en génie géotechnique. Dans le troisième chapitre, le modèle à deux fluides est étudié dans le contexte de l'érosion interne causée par des fuites dans des tuyaux sous pression. Dans ce modèle, une représentation équivalente des particules du sol basée sur un milieu continu est réalisée grâce à l'incorporation de la théorie cinétique des flux granuleux qui prend en compte les forces de contact et de cisaillement entre les particules. Cette représentation du sol permet l'emploi de solveurs utilisant des maillages comme les solveurs pour la méthode des éléments finis pour résoudre les équations pour l'eau et le sol. Cette technique nécessite moins de ressources computationnelles en évitant la discrétisation directe de chaque particule du sol. Le modèle est premièrement validé en comparant des données expérimentales aux résultats d'une simulation d'écoulement en colonne. Les résultats coïncident aussi bien avec les données expérimentales qu'avec la solution analytique. De plus amples détails sur le processus d'érosion sont par ailleurs présentés, soulignant l'effet de la polydispersité du sol et de la géométrie du problème à l'étude.

En raison du processus effectuant la moyenne dans le modèle à deux fluides, ce dernier est incapable de prendre en compte certains aspects de la dynamique de la phase solide telle que la coulée de matière granuleuse par un orifice. Pour ce type de problème, le débit granuleux est généralement indépendant de la hauteur de matière granuleuse reposant au-dessus de l'orifice en raison de l'effet d'arc de chute libre. Ce phénomène est directement lié au problème de l'érosion du sable dans les tuyaux d'égouts défectueux qui est l'objet d'étude du chapitre 4. Une méthode couplant la mécanique des fluides numérique (MFN) et la méthode des éléments discrets (DEM) est utilisée pour étudier le processus de l'érosion du sable dans des tuyaux d'égouts sous l'effet de l'eau souterraine. Une étude paramétrique est réalisée afin d'analyser l'effet de la géométrie du défaut affectant le tuyau, le niveau de la nappe phréatique, l'angle du défaut, ainsi que la hauteur de la couche de sable reposant au-dessus du tuyau. Les résultats mettent en évidence le rôle que l'eau souterraine joue dans le processus d'érosion aussi bien dans son étendu que dans son débit et indiquent que l'influence de la hauteur de la couche de sable semble être minime. La simulation permet par ailleurs d'observer le rôle de la nappe phréatique dans le processus d'érosion par des fissures inclinées par rapport au sommet du tuyau, ce qui représente une avancée pour mieux comprendre le phénomène d'érosion accélérée et l'apparition de gouffre après de fortes précipitations. Enfin, le modèle est utilisé pour étudier l'obstruction d'un géotextile par un sol à grain fin entraînée par l'entrée d'eau souterraine dans des tunnels drainés. Une nouvelle technique est créée pour générer et tester les propriétés d'un géotextile non-tissé. Des simulations couplant la MFN et la DEM sont effectuées pour analyser l'influence du phénomène d'obstruction sur la détérioration hydraulique du géotextile et la formation de pression

interstitielle excessive dans la couche de drainage du tunnel. Un nouvel ensemble de conditions aux frontières sont générées afin de représenter le flux de particules fines et d'eau dans les fissures à cause desquelles le géotextile est susceptible de se faire obstruer. Les résultats montrent que le modèle est capable de capturer le phénomène d'obstruction ainsi que la formation locale de renard par des fissures situées dans des zones à forts gradients hydrauliques. L'analyse des résultats est une analyse quantitative de la distribution des pressions excessives dans la couche de drainage et de l'effet des différents types de sols sur le phénomène d'obstruction.

Acknowledgments

I would like to express my deepest gratitude to my PhD supervisor, Prof. Mohamed A. Meguid, for his continuous support, guidance, encouragement throughout this research. Professor Meguid always gave me the freedom to innovate and explore uncharted areas of research. I am grateful for his professional mentorship and kindness during my time in the Geo-group at McGill. I would also like to extend my thanks to the current and former Geo-group members: Mohamed Shokr, Romaric Desbrousses, Zainab Almheiri, Mohamed Alobaidi, Mohamed Imran Khan, Ge Gao and Luyu Wang for their support, kindness, and the amazing friendly environment they provided during my doctoral degree.

I would like to extend my gratitude to my parents, my parents in law, my brothers and friends in Canada, Japan, and Egypt for their unseizing encouragement through many hard times.

A special ‘Thank You’ to my dear wife for her unwavering belief in me and her enormous support especially through the hard lockdown times.

To all of you, I go on with a debt of gratitude for all the help and support I received, I am forever thankful.

List of Publications

The following publications have resulted from the research work completed towards the doctoral degree:

Refereed journal papers

[**J1**] Ibrahim, A., Meguid, M.A., 2020. Coupled Flow Modelling in Geotechnical and Ground Engineering: An Overview. *Int J Geosynth Ground Engineering* 6(3), 1-25.

[**J2**] Ibrahim, A., Meguid, M., 2021. Continuum-Based Approach to Model Particulate Soil-Water Interaction: Model Validation and Insight into Internal Erosion. *Processes* 9(5), 785.

[**J3**] Ibrahim, A., Meguid, M., 2022. CFD-DEM Simulation of Sand Erosion into Defective Gravity Pipes under Constant Groundwater table. *Tunneling and Underground Space Technology* (Under review).

[**J4**] Ibrahim, A., Meguid, M., 2022. CFD-DEM Modeling of the Geotextile Hydraulic Deterioration due to Fines Clogging in Tunnel Drainage Systems. *Geotextiles and Geomembranes Journal* (In press).

Conference proceedings papers:

[C1] Ibrahim, A., Meguid, M.A., 2020. On the development and challenges of particulate flow modeling in geotechnical engineering: A review. GeoVirtual 2020, Canadian Geotechnical Society, Calgary, Alberta, Canada.

[C2] Ibrahim, A., Meguid, M., 2021. The Applicability of the Two-Fluid Model to Simulate Soil Internal Fluidization Due to Pipe Leakage, Proceedings of the Canadian Society of Civil Engineering Annual Conference 2021. https://doi.org/10.1007/978-981-19-0968-9_34

[C3] Ibrahim, A., Meguid, M., 2022 Numerical Modeling of Groundwater-Driven Sand Infiltration into Defective Sewer Pipes using CFD-DEM, GeoCalgary 2022, Canadian Geotechnical Society, Calgary, Alberta, Canada.

Table of Contents

List of Tables

List of Figures

Chapter 1

Introduction

1.1 Background and research motivation

The interaction between water and soil body is one of the fundamental aspects that affects the overall behavior of soil. Such interaction involves a wide range of dynamics and underlying physics. On one end of the spectrum is static conditions where the effective stresses in soil is affected by the hydrostatic pressure of water. On the other end of the spectrum, we find more dynamic behavior such as the case in rainfall-driven landslides and debris flow. Conventionally, water existence in soil is accounted for via macroscale relations that governs the overall behavior of the soil-water body. Examples for this include Terzaghi's principle of effective stresses and Darcy flow equations where the soil matrix is assumed to in static or quasi-static conditions. In dynamic situations, where considerable soil deformation occurs accompanied by water flow, it is necessary to consider the fully coupled motion of both soil and water phases. This coupling enables us to access flow field information on fine spatial scale such as interparticle velocities and pressures as well as the positions and fate of soil particles. Such information is of utmost importance and relevance to several civil engineering applications such as internal erosion around buried utilities, earth dams and the extent of debris runout. In this thesis we make extensive use of continuum-based formulation of the coupled governing equations (e.g., Anderson and Jackson (1967a) and Gidaspow (1994)) and continuum-discrete formulations such as Computational Fluid Dynamics-Discrete Element Method (CFD-DEM) (Tsuji et al. (1993) to investigate internal erosion and tunnel drainage-related applications.

As coupled particulate analysis fundamentally underlies complex physics and often is computationally expensive beyond a tractable limit, it is quite challenging to implement this kind of analysis in civil and geotechnical engineering applications. This research is mainly motivated by presenting some practical solutions for relevant problems in the field. This includes work on two different fronts, the first is exploring and validating computationally feasible and scalable models such as the Two-Fluid Model (TFM). The second front is to carry out practical simulations in relatively small systems from which we can draw useful data regarding water-soil interaction in variety of applications.

1.2 Objectives and scope

The first objective of this thesis is to present a computationally feasible and scalable model for fully coupled soil-water flow that is the Two-Fluid Model. This model was utilized to investigate internal erosion of granular soil around leaking pressurized pipe. Towards this objective, the following sub-objectives are considered:

1- Formulating and compiling the codes for the TFM.
2- Validating the model using available analytical solutions and experimental data.
3- Examining the different model parameters on the produced results in the context of internal erosion problem.

The second objective is to provide some practical insights into computationally tractable geotechnical applications. This was achieved by incorporating CFD-DEM analysis to study two problems, (i) groundwater-driven sand erosion into defective sewer pipes, and (ii) the hydraulic deterioration of non-woven geotextile filters due to clogging by fine particles for adjacent soils in drained tunnels system. In these two studies, the sub-objectives are:

1- Formulate the problem and apply necessary boundary conditions needed to ensure the computational feasibility within the domain.
2- Model validation for the DEM and CFD components.
3- Carry out parametric analysis to investigate the effect of different factors.
4- Develop an approximate semi-analytical solution that describes the behavior or the model.

1.3 Original contribution

This thesis encloses original contribution on two fronts: (i) model development and (ii) application development. The following are the highlights of the original contribution provided in this work:

1- Providing model validation and practical simulation of densely packed granular assembly using the Two-Fluid Model.
2- Incorporating the effect of granular polydispersity in continuum modeling framework.
3- Carrying out detailed modeling of sand infiltration into sewer pipes under the effect of groundwater.
4- Demonstrating the role of groundwater and pipe cracks configuration on the erosion process.
5- Providing a framework to numerically create and test non-woven geotextiles.
6- Presenting a refined simulation of geotextile filter clogging in tunnel drainage system and

highlighting the role of different factor such as the nature of surrounding soil and the groundwater ingress into the tunnel.

1.4 Contributions of authors

The chapters of this thesis are the candidate's original work. Model formulation and development was conducted by the candidate with the guidance of Prof. Mohamed Meguid. Writing the manuscripts first draft and chapters of this thesis was carried out by the candidate. Rounds or revisions and edits were done by Prof. Mohamed Meguid.

1.5 Thesis organization

This thesis is a manuscript-based thesis, four out of six chapters included in this work are manuscripts for journal articles that are published or currently under review as indicated in the list of publications. Excluding this chapter, the organization of the thesis is as follows:

Chapter 2 presents a comprehensive literature and review for different approaches of particulate flow modeling. The review presented in this chapters first gives a general background on the coupled solid-fluid analysis that is then narrowed down to highlight aspects and provisions of using these models in civil and geotechnical engineering applications. This chapter revolves around relating a considerable body of literature from other disciplines such as chemical and mechanical engineering to a civil engineering perspective. In addition to the numerical model development, the chapter also includes a review of available modeling tools, upscaling techniques and outstanding challenges involved with this type of modeling. The author notes that this chapter was published as a review article in the International Journal of Geosynthetics and Ground Engineering in 2020. As such, relevant advances to the topic from the time of publication of this manuscript to the date of writing this thesis are systematically included in the introduction section of each paper.

Chapter 2 includes formulation and application of the continuum-based Two-Fluid Model to simulate internal erosion due to pressurized pipe leakage. Model validation was first conducted by comparing the model output to available analytical solutions and experimental data. The effect of pipe crack size and polydispersity of soil above the pipe are discussed later in the chapter.

Chapter 3 presents CFD-DEM analysis of sand erosion into defective gravity pipes under the effect of groundwater. Model validation and material calibration are first carried out. Afterward, a parametric study to examine the effect of defect size, groundwater level, defect angle, and

sand layer height above the pipe is carried out. Finally, an approximate relation for the cumulative eroded volume of sand is then proposed.

Chapter 4 introduces further CFD-DEM simulation of a more geometrically complex problem involving geotextile filters clogging by fine particles in adjacent soils that are driven by groundwater ingress into drained tunnels. The chapter includes a methodology for numerically producing and testing non-woven geotextiles for their permeating and retention properties. A set of new boundary conditions are then developed to handle the flow variable of both water and fine particles within a crack in the outermost shotcrete layer. The model is performance is validated by first running a series of simulations under previously known hydraulic gradient values. A parametric study is conducted to investigate the effect of the percentage of fine particles in the surrounding soil, groundwater ingress, and crack angle. Finally, a semi-analytical model is developed to describe the pressure increase in the drainage layer as a function in the fines content and crack inclination angle.

Chapter 6 of this thesis includes concluding remarks and recommendations for future work.

Preface to Chapter 2

Model development of particulate flow modeling underlies decades of work that is hereby reviewed. In this chapter, we attempt, in addition to the systematic review, to bring the advances in discrete and continuum particulate flow modeling to a geotechnical context. The motivation behind this is the overwhelming amount of relevant work that was originally developed to model fluidized beds, pneumatic conveyors and reactor systems in different industries. Since the attention in these studies is geared towards chemical engineering and industrial processes, it is necessary to highlight the relevant models suitable for geotechnical applications. In this chapter, we first review the different approaches of fluid-solid coupling and fluid-particle interaction forces. The relevant methods and constitutive relationships relevant to geotechnical engineering are then highlighted. Furthermore, we provide a review of the available modeling tools and outstanding challenges.

Chapter 2

Coupled Flow Modelling in Geotechnical and Ground Engineering: An Overview†

Abstract

Particulate flows of combined granular media and fluids are relevant to several natural phenomena as well as industrial applications. In geotechnical engineering, the existing modelling approaches mainly adopt a macroscopic-based continuum analysis which does not provide access to important information on the fluid flow interaction with granular media at the particle scale. Alternatively, particulate modelling can be a powerful tool in understanding the complex micro-mechanics of different phenomena such as landslide, debris flow and internal erosion. However, it is challenging to employ the existing particulate flow models on a scale that practically serves the design and risk assessment for earth structures. With rapid advances in computational power, particulate flow modelling can provide valuable insights on both the micro as well as the macro-scale levels. This paper reviews the different approaches of particulate flow modelling from a multidisciplinary perspective with emphasis on geotechnical applications. In addition, this study presents a summary of the available techniques for reducing the computational cost and highlights the outstanding challenges of particulate flow modelling in geotechnical engineering. This work should provide guidance to geotechnical engineers and researches to determine the appropriate modelling tool to approach particulate flow modelling and identify the major challenges associated with each approach.

Keywords: Flow modelling; Ground engineering; Multiscale modelling; Two-fluid model; Particulate flow; Computational fluid dynamics; Discrete element analysis

† A version of this manuscript has been published in the *International Journal of Geosynthetics and Ground Engineering* (2020).

2.1 Introduction

Flow of fluids in particulate media and flow of particle-fluid mixtures are interesting problems and relevant to several industries (e.g., pharmaceutical, chemical, civil, and mining). Understanding the mechanics of these phenomena is critical to solving important engineering problems (e.g., debris flow, soil erosion, liquefaction, and landslides) (Wachs, 2019). Aided by rapid advances in computational resources, coupled flow modelling, hereafter referred to as particulate flow, has significantly developed over the past few decades. The existing state-of-the-art models allow for capturing the detailed characteristics of the flow regime such as particle-particle and particle-fluid interactions. Despite the advances in computational power and algorithms, the simulation of industrial and phenomenological scale problems requires more computational resources than those available for most of engineers and researchers. Various particle upscaling techniques have been developed to overcome this obstacle and reduce computational cost (Sakai and Koshizuka, 2009; van der Hoef et al., 2006; Zhao, 2017). However, it is quite challenging to maintain the intricate level of detail from refined simulations upon the upscaling process. Zhu et al. (Zhu et al., 2007, 2008) attribute this issue to the absence of a general theory for particulate flow (e.g., accurate description of momentum transfer) that allows for proper upscaling. Such level of detail might be more important to some applications than others and proper use of different modelling tools and upscaling techniques could result in acceptable results. Therefore, it is essential to have a good understanding of the theoretical aspects, modelling tools, and upscaling techniques in particulate flow modelling.

The interest in fluid-granular media interaction is not new to geotechnical engineering. Examples include mechanical analysis of saturated and unsaturated soils, flow through water-retaining earth structures, and rain-driven landslides. Solid-fluid interaction is commonly estimated through macroscale-based constitutive models. These models utilize a simplified form of fluid flow in soils, e.g., Darcy flow, and constitutively link other parameters such as effective stresses and solid skeleton deformation to the flow variables (Schaufler et al., 2013; Vardoulakis et al., 1996; Yang et al., 2020). Such an approach can be appropriate when dealing with quasi-static applications where deformations in the solid skeleton can be neglected. However, when hydrodynamic forces are of significance to the analysis, more complex physics are required to fully resolve the interaction between soil and water and establish proper constitutive models. The major drawback with considering continuum-based analysis is that micromechanics of interest such as the development and evolution of piping or cavity evolution in earth embankments remains not fully understood. On the other hand, performing particulate

flow modelling by accounting for the micromechanics of both soil particles and fluid flow can provide a deeper understanding and help improve the existing constitutive models used to capture the response of such applications.

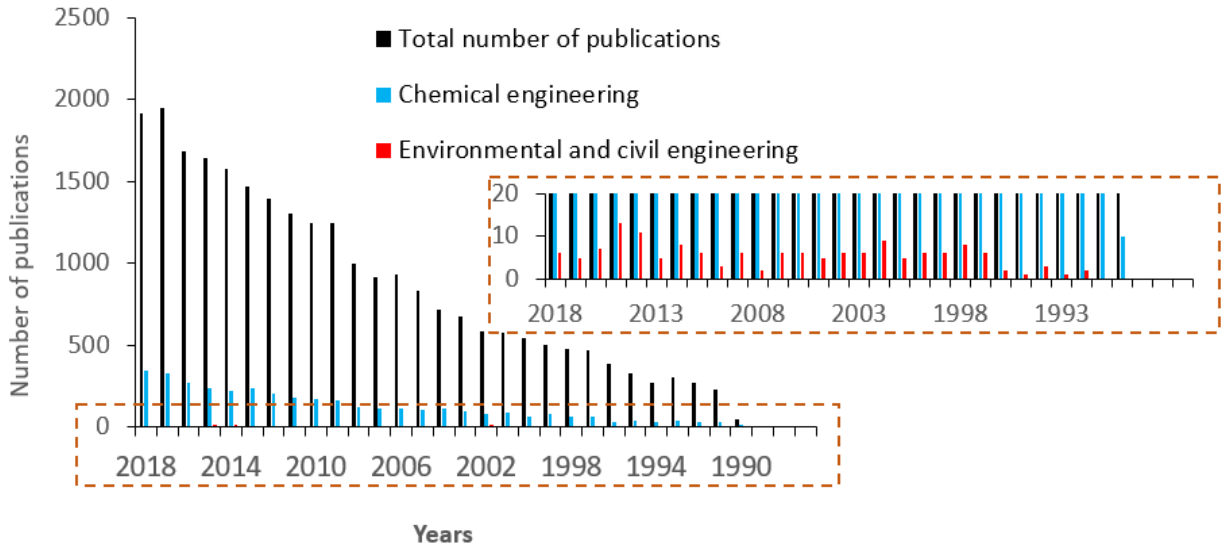

Figure 2.1. The total number of publications on the coupling of solid-fluid flow between 1990 and 2018. Source: web of science. Keywords: particulate flow, CFD-DEM, solid-fluid flow coupling.

It is notable that most of the major developments in particulate flow modelling were developed in the context of chemical engineering, with a special focus on fluidized beds and pneumatic conveying due to their vast applications. These developments were later incorporated in civil and geotechnical engineering to simulate a variety of phenomena such as liquefaction (Shamy and Zeghal, 2005; Zeghal and El Shamy, 2004), landslides (Shi et al., 2018; Zhao, 2017), erosion and cavity evolution (Guo and Yu, 2017), riverbed erosion and sediment transport (Harada et al., 2019; Harada et al., 2018), scour around pipelines (Hu et al., 2019), and debris flow (Jing et al., 2016; Shan and Zhao, 2014). However, the largest portion of the literature on particulate flow is found, and seemingly continues to be, in the context of chemical engineering (Figure 2.1). In contrast, civil and geotechnical engineering contribution to the subject is relatively limited. One reason for this limitation is the inherent large-scale nature of geotechnical applications such as earth dams and slope stability, which are computationally expensive to model. It could be argued that applications in chemical engineering are more relevant to particulate flow than geotechnical engineering, however, several geotechnical phenomena such as erosion, debris flow, and liquefaction are strongly

relevant to particulate flow modelling and still require in-depth understanding of the underlying dynamics. Indeed, such limited contribution on the side of geotechnical engineering limits the practitioners' accessibility to case studies and models catered to geotechnical engineering, which in turn hinders our understanding of particulate flow in geotechnical-related applications.

Several reviews of particulate flow modelling have been presented with emphasis on specific aspects of the models. For example, theoretical development and applications (Zhu et al., 2007, 2008), multiscale frameworks of multi-level constitutive relationships (Deen et al., 2007; van der Hoef et al., 2006), thermal exchange (Peters et al., 2019), momentum coupling methods (Zhou et al., 2010), reactive particulate flow systems (Zhong et al., 2016), and model development and modelling tools (Ariyaratne et al., 2018). Despite the rich knowledge provided in these reviews, they are mainly focused on fluidized beds and pneumatic conveyors, while applications in ground and geotechnical engineering are seldom discussed. Moreover, to our knowledge, a holistic summary of the methodology, available modelling tools, and upscaling methods focused on geotechnical engineering applications does not exist in the literature. In other words, a 'starter pack' for geotechnical engineering practitioners that aids the selection of appropriate modelling methodology, computationally feasible modelling tools, and proper upscaling technique is not yet available.

In this work, we aim to present a review of the available approaches for particulate flow modelling with a special focus to geotechnical applications, exploring the advantages and disadvantages of each approach with respect to the scale of the tackled problem. In addition, we review the available modelling tools (open source codes and commercial packages), highlighting the specific features of each package. Finally, we provide a detailed discussion on the current challenges related to multi-scale modelling, upscaling techniques and implementation of boundary conditions. In order to keep the article size manageable, aspects related to turbulent flow modelling is only briefly discussed for it is considered to be beyond the scope of this work.

2.2 The need for coupled flow modelling in ground and geotechnical engineering

Solid-fluid interaction in geotechnical engineering is a cornerstone in the mechanical analysis and design of earth structures. Existence of water within soils, for instance, fundamentally controls the state of stresses, deformation, and other soil properties. Accounting for such effect is essential for estimating the critical parameters and factors of safety needed for design. The existing conventional methods adopt a macroscopic approach for including such interaction.

This macroscopic view considers the properties of the bulk soil masses, either saturated or unsaturated, such as soil weight and shear strength parameters without direct reflection on the particulate nature of soils. Although conventional analysis is viable and can adequately serve the design purposes, it does not allow one to understand important aspects of these systems that can only be understood through the micromechanical analysis of coupled water-soil interaction.

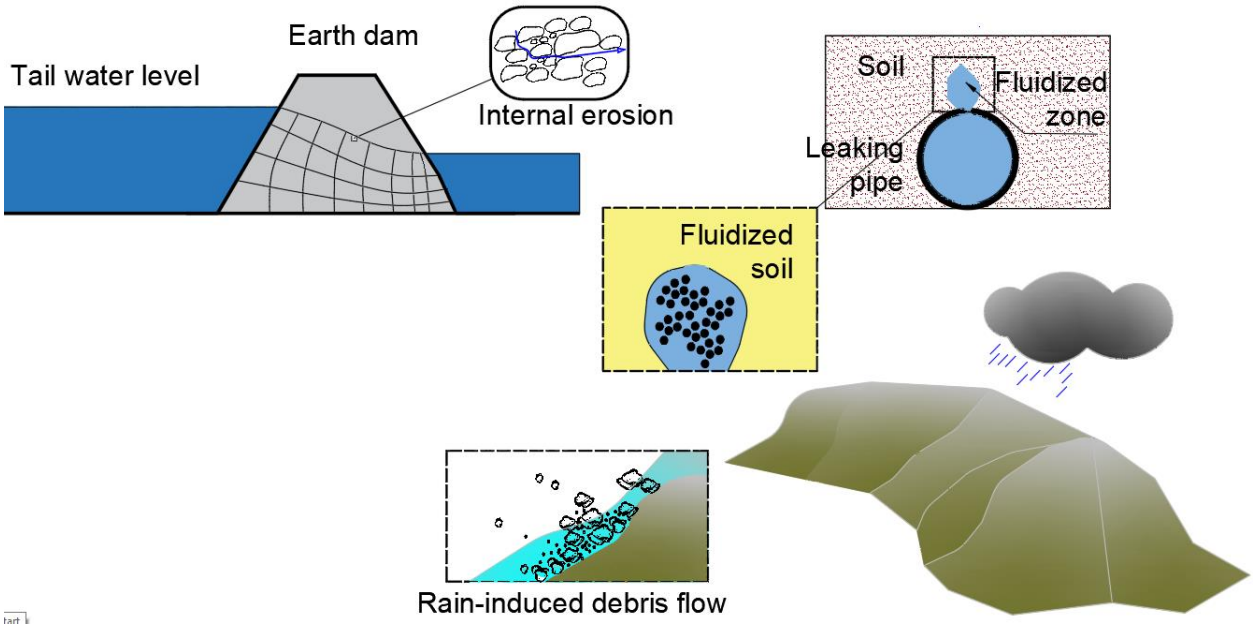

Figure 2.2. Examples for coupled water-soil interaction in geotechnical applications; internal erosion in earth dam, soil fluidization and sinkholes due to pipe leakage and rain-induced debris flow.

Considering an earth dam for example (2.2), the conventional analysis provides us with insights on the overall stability of the structure or the factors of safety against soil piping and highlights the need for special components such as drains and filters. However, it does not give us sufficient details on the process of internal erosion within the body of the dam where the interaction between soil particles and water needs to be resolved. In order to track the initiation and propagation of erosion, we need to incorporate coupled (particulate) flow that allows us to access the interparticle and particle-fluid interactions. Another example of the lack of information provided by macroscopic analysis is slope stability, for which rainfall and changes in groundwater levels are major drives. Despite the information we can obtain regarding the potential failure surfaces and factors of safety against failure, particle movement and relocation within the soil pores during water flow remains unknown.

In some situations, conducting particulate flow modelling becomes indispensable, for example, the case of determining the onset of fluidization around leaking pipes. As such leakage can wash soil particles away and can ultimately lead to the formation of cavities and sinkholes, it is important to understand the evolution of such a process at the particle level.

2.3 Particle-fluid interaction forces and momentum coupling

One of the most challenging aspects of particulate flow modelling is to accurately estimate the interaction forces and momentum transfer between fluid and solid phases. Such estimation depends on the material and flow characteristics of solids and fluids as well as the extent, to which, these interaction forces are considered significant. For instance, in particulate flows with little solid concentration, the solid phase is often dispersed and governed by the hydrodynamic forces with a negligible effect on the fluid motion, i.e., one-way coupling. For denser solid concentration, the motion of the solid particles can affect the fluid streamlines, which is referred to as two-way coupling. In most geotechnical applications, the concentration of solids is typically high and requires four-way coupling, that is, the iterative process of obtaining the mutual impact of solid and fluid phases on each other by accounting for the effect of the changed fluid motion back on particles as well as for particle-particle interactions. In two-way and four-way coupling, it is necessary to ensure that Newton's third law of motion is achieved, i.e., the impact of fluid on solids is equal in magnitude to the impact of solids on the fluid in opposite direction.

Although efforts have been made to resolve fluid-particle interactions, this aspect remains not fully understood and the models we have today are based on empirical or semi-empirical relations. This is because the underlying mechanics of such interaction are very complex and depend on many factors such as particle shape, material properties of solid and fluid phases, and the type of coupling considered in the problem. Nonetheless, the existing models have been proven to be robust and can adequately simulate particulate flow with good accuracy. In this section, we exhibit the existing forces considered in particle-fluid interaction, the theoretical basis and special considerations for each force and the range of application to different flow regimes.

2.3.1 Drag Force

Drag force is a result of fluid shearing on solid particles due to different velocity of each phase and acts in the direction of the relative velocity between fluid and solid particles (Figure 2.3) (Zhao, 2017). This force applies to the surface of the solid particle and is often assumed to be

effective at the centre of the particle, drag force can be generally expressed as:

$$\boldsymbol{F_d} = \beta(\boldsymbol{u_f} - \boldsymbol{u_p}) \tag{2.1}$$

where $\boldsymbol{F_d}$ is the drag force, $\boldsymbol{u_f}$ and $\boldsymbol{u_p}$ are the fluid and solid particle velocities, respectively, and β is the momentum transfer coefficient between fluid and solid particles. One of the early expression for β was presented by Ergun (1952):

$$\beta = \frac{3}{4}\frac{C_d n(1-\alpha)\rho_f}{D}\left|\boldsymbol{u_f} - \boldsymbol{u_p}\right| \tag{2.2}$$

where C_d is the drag force coefficient, ϵ is the porosity or fluid volume fraction, D is the diameter of the solid particle, and ρ_f is the fluid density. The drag coefficient given by Ergun is:

$$C_d = \frac{200(1-\alpha)}{nRe_p} + \frac{7}{3\epsilon} \tag{2.3}$$

where Re_p is the particle Reynolds number such that: $Re_p = \rho_f D\left|\boldsymbol{u_f} - \boldsymbol{u_p}\right|/\mu$, and μ is the dynamic viscosity of the fluid. The expression for C_d proposed by Ergun is mainly based on the experimental correlations obtained from the fluidization of dense granular beds, thus, it is not considered suitable for more dilute flows ($\epsilon \leq 0.8$) (Jackson, 2000). Therefore, another expression for C_d was proposed by Wen and Yu (1966) for flows with $\epsilon > 0.8$:

$$C_d = \begin{cases} \frac{24}{Re_p}\left(1 + 0.15(\mathrm{Re}_p)^{0.687}\right)\epsilon^{-2.65} & \mathrm{Re}_p < 1000 \\ 0.44\epsilon^{-2.65} & \mathrm{Re}_p \geq 1000 \end{cases} \tag{2.4}$$

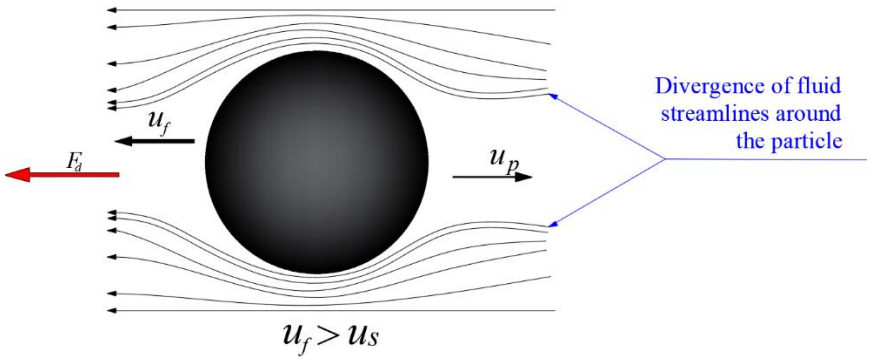

Figure 2.3.A schematic illustration of fluid drag force around a solid particle. The directions on the diagram are considered for a case where $\boldsymbol{u_f} > \boldsymbol{u_s}$ (as depicted by the line weight of velocity vectors).

Although combining Ergun's and Wen and Yu's models seems to be sufficient to cover the

entire spectrum of porosity that can be encountered, it was found to cause discontinuities in the solution when the porosity fluctuates around 0.8 (Kafui et al., 2002). Thus, a different correlation for drag force that accounts for porosity correction was introduced by Di Felice (1994):

$$\boldsymbol{F_d} = \frac{1}{2} C_d \rho_f \frac{\pi D^2}{4} \left|\boldsymbol{u_f} - \boldsymbol{u_p}\right| \left(\boldsymbol{u_f} - \boldsymbol{u_p}\right) \epsilon^{-\chi+1} \tag{2.5}$$

where the porosity correction function χ is given as:

$$\chi = 3.7 - 0.65 \exp\left[-\frac{\left(1.5 - \log_{10} \mathrm{Re}_p\right)^2}{2}\right] \tag{2.6}$$

The estimates for the drag force coefficient found in the literature can be traced back to the correlations of Stokes (1901). Different correlations are proposed by Schiller and Naumann (1935), DallaValle (1948), and Brown and Lawler (2003). A comparison between these correlations is conducted by Zhao (2017). Zhao concluded that the correlation of Brown and Lawler (2003) provides the best match with experimental data, especially for Reynolds number that ranges from 10^2 to 10^4.

Drag force is almost always accounted for in particulate flow modelling. The only exception is dilute flows with solid concentration of approximately less than 0.1%, in which the effect of particles on the relative velocity of other particles may be neglected and the velocity of the solid particles is nearly the same as the fluid velocity (Elghobashi, 1994). In geotechnical application, where solid concentration is typically larger than 0.1%, the drag force is always considered.

2.3.2 Pressure gradient force

The difference in pressure across a solid particle induces force that acts over the volume of the particle i.e., buoyancy. For a particle with volume (V_p) subjected to pressure gradient (∇p), the resulting force on the particle ($\boldsymbol{F}_{\nabla p}$) is:

$$\boldsymbol{F}_{\nabla p} = -V_p \nabla p \tag{2.7}$$

We note that the gradient term in Equation (2.7) is the total pressure acting on a particle that contains components of hydrostatic and hydrodynamic pressure. As pointed out by Crowe et al. (2012), the hydrostatic pressure component represents the buoyancy effect, thus Equation (2.7) can be decomposed as:

$$\boldsymbol{F}_{\nabla p} = \overbrace{-V_p \nabla p_{hydrostatic}}^{buoyancy\ force} - V_p \nabla p_{hydrodynamic} \tag{2.8}$$

As can be seen from the equations, the force is proportional to the volume of solid particles and the value of the pressure gradient. In geotechnical applications, this force can be significant, especially the buoyancy component, for submerged solid particles in quasi-static flows.

Table 2.1. Summary of particle-fluid interaction forces and their significance to geotechnical applications.

Force	Expression	Reference	Significance to geotechnical applications
Drag	$\boldsymbol{F_d} = \beta(\boldsymbol{u_f} - \boldsymbol{u_p})$ $\beta = \frac{3}{4}\frac{C_d n(1-\alpha)\rho_f}{D}\lvert\boldsymbol{u_f} - \boldsymbol{u_p}\rvert$ $C_d = \begin{cases} \frac{24}{Re_p}\left(1 + 0.15(\mathrm{Re}_p)^{0.687}\right)\alpha^{-2.65} & Re_p < 1000 \\ 0.44\alpha^{-2.65} & Re_p \geq 1000 \end{cases}$	Ergun (1952); Wen and Yu (1966)	Significant
Pressure gradient	$\boldsymbol{F_{\nabla p}} = -V_p \nabla p$	Anderson and Jackson (1967a)	Significant
Virtual mass	$\boldsymbol{F_{vm}} = \frac{\rho_f V_d}{2}\left(\frac{\mathrm{d}\boldsymbol{u_f}}{\mathrm{d}t} - \frac{\mathrm{d}\boldsymbol{u_s}}{\mathrm{d}t}\right)$	Auton et al. (1988)	Significant for highly unsteady flows
Basset force	$\boldsymbol{F_{Basset}} = \frac{3}{2}D^2\sqrt{\pi\rho_f\mu_f}\int_0^t \frac{1}{\sqrt{t-t'}}\frac{d}{dt}(\boldsymbol{u_f} - \boldsymbol{u_p})\ dt' + \frac{(\boldsymbol{u_f} - \boldsymbol{u_p})_0}{\sqrt{t}}$	Reeks and Mckee (1984)	Insignificant
Saffman force	$\boldsymbol{F_{saff}} = 1.61\rho_f\mu_f D^2\lvert\boldsymbol{\omega_f}\rvert^{-\frac{1}{2}}\ [\boldsymbol{u_f} - \boldsymbol{u_p}] \times \boldsymbol{\omega_f}$	Saffman (1965, 1968)	Significant for high shear flows
Magnus force	$\boldsymbol{F_{Mag}} = \frac{\pi}{8}D^2\rho_f\left[\left(\frac{1}{2}\nabla \times \boldsymbol{u_f} - \boldsymbol{\omega_p}\right) \times (\boldsymbol{u_f} - \boldsymbol{u_p})\right]$	Rubinow and Keller (1961)	Insignificant

2.3.3 Other particle-fluid interaction forces

Other particle-fluid interaction forces can be of significance to particulate flow modelling. These forces include the virtual mass force which accounts for the acceleration of particles within the fluid, Basset force which accounts for the time delay in the boundary layer development, and Saffman and Magnus forces which account for the rotational motion of solid particles. In Table 2.1 we include a summary of these forces and their significance in geotechnical applications.

In addition to particle-fluid interaction forces, turbulence effect can be significant to particulate flow modelling. Different closure models are adopted considering the nature of the modelled problem. For example, in seepage-type flows, where fluid velocity is typically small turbulence does not have a tangible effect on the flow. As flow might evolve into a more dynamic state (e.g., debris flow), turbulence closures are then needed to be employed in order to sufficiently capture the energy transport throughout the system. Examples for turbulence closures in particulate flow modelling include Large Eddy Simulation (LES) (Cheng et al., 2018; Harada et al., 2015), k-ε (Bakhtyar et al., 2009; Chauchat and Guillou, 2008; Hsu et al., 2003), and k-ω (Amoudry, 2014; Jha and Bombardelli, 2009, 2010).

2.4 Approaches for modelling particulate flows

The governing equations of particulate flows are challenging to solve analytically due to the various nonlinearities involved and complex boundary conditions encountered in real problems. Therefore, numerical analysis is conventionally used to solve the set of governing equations. From a numerical point of view, the nonlinear partial differential equations can be solved either using the Eulerian approach or the Lagrangian approach. In the Eulerian approach, the flow variables are viewed as a continuum on a spatially fixed or moving grid and the temporal changes in these variables are tracked locally within each computational cell. In the Lagrangian approach, the trajectory and other flow variables of the fluid or the solid particle are tracked over time for every single particle. Depending on the numerical treatment of both the fluid and the solid phase, particulate flow modelling can be classified into three main categories: (i) Eulerian-Eulerian, (ii) Eulerian-Lagrangian, and (iii) Lagrangian-Lagrangian (Figure 2.4). In the following section, we provide a thorough review of the different numerical approaches for particulate flow modelling and the underlying models presented under each approach.

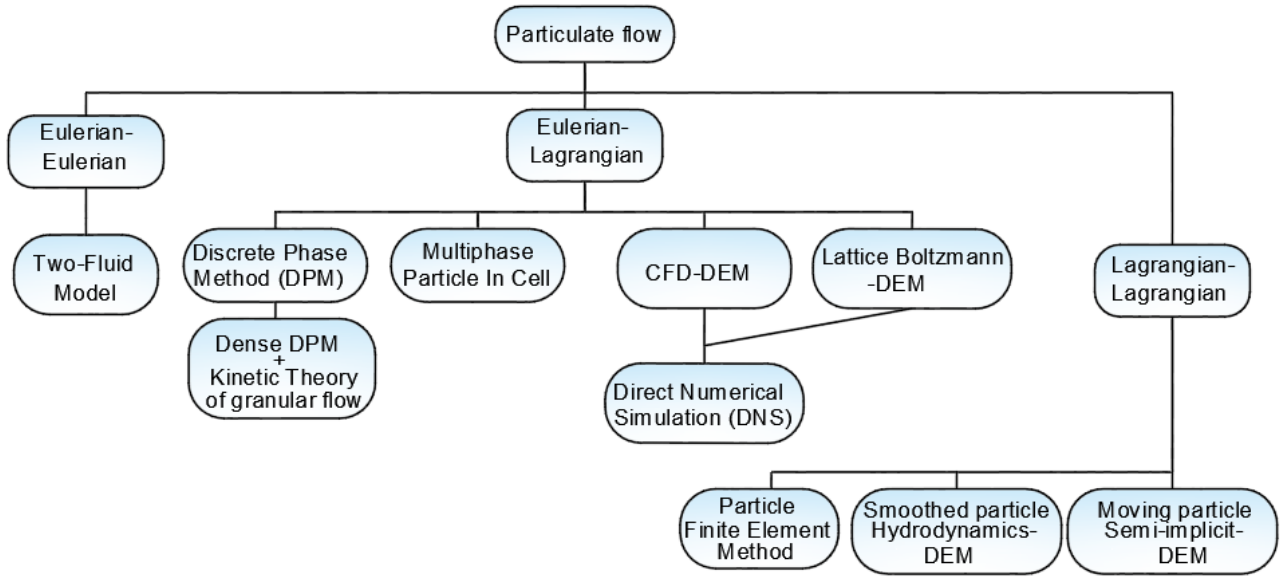

Figure 2.4**.** Different modelling approaches and their corresponding particulate flow methods.

2.4.1 Eulerian-Eulerian approach

The purely Eulerian approach (Eulerian-Eulerian) essentially depends on averaging the flow variables of solid particles and fluids. The most common type of averaging is volume averaging as the computations are often conducted within a computational cell of a finite volume (Crowe et al., 2012). One of the earliest attempts to average fluid flow with dispersed solids was presented by Van Deemter and Van der Laan (1961). The relationship they presented for fluid momentum is:

$$(1-\alpha_d)\rho_f \frac{D\boldsymbol{u}_i}{Dt} = (1-\alpha_d)\rho_f \boldsymbol{g}_i - \frac{\partial}{\partial x_j}\left(p\delta_{ij} - \boldsymbol{\tau}_{ij}\right) + \boldsymbol{f}_i \qquad (2.9)$$

where $\boldsymbol{u}_i$ is the velocity of the fluid, α_d is the volume fraction of the solid particles, ρ_f is the fluid density, $\boldsymbol{g}_i$ is the gravitational acceleration, p is the pressure acting on the fluid, δ_{ij} is the Kronecker delta, $\boldsymbol{\tau}_{ij}$ is the shear stress tensor, and $\boldsymbol{f}_i$ is the force per unit volume acting on the fluid from the solid phase. Two problematic terms in this equation are the fluid velocity, $\boldsymbol{u}_i$, and the force acting on the fluid, $\boldsymbol{f}_i$,because they vary significantly with the volume the fluid is averaged over. Moreover, the use of a single value for fluid velocity is not suitable to represent averaged fluid flow, especially in turbulent flows. Marble (1963) proposed a similar averaging procedure but ignored the effect of the solid phase on the fluid. This equation was derived for particulate flow with dilute dispersed solids. The equation presented by Marble is:

$$\rho_f \frac{\partial \boldsymbol{u}_i}{\partial t} + \rho_f \boldsymbol{u}_j \frac{\partial \boldsymbol{u}_i}{\partial x_j} = -\frac{\partial p}{\partial x_i} + \frac{\partial}{\partial x_j}\boldsymbol{\tau}_{ij} + \boldsymbol{f}_i \tag{2.10}$$

where the notation in Equation (2.10) denotes the same variables as those in Equation (2.9). The term $\boldsymbol{f}_i$ on the right-hand side of Equation (2.10), resembles the effect of the fluid motion on the dispersed solid particles. This essentially represents one-way coupling since the effect of the solid particles on the fluid is neglected. This equation is often referred to in the literature as the "dusty gas equation". Anderson and Jackson (Anderson and Jackson, 1967b) proposed an averaging technique to transform the point variables (discrete) to a locally averaged values (continuous) over a volume that is large enough to contain many particles, yet, small compared to the dimensions of the system. They presented the following form of the governing equations for mass and momentum conservation:

$$\frac{\partial \epsilon}{\partial t} + \frac{\partial \epsilon \boldsymbol{u}_{\mathbf{f}_i}}{\partial x_i} = 0 \tag{2.11}$$

$$\frac{\partial (1-\epsilon)}{\partial t} + \frac{\partial (1-\epsilon)\boldsymbol{u}_{\boldsymbol{s}_i}}{\partial x_i} = 0 \tag{2.12}$$

$$\rho_f \epsilon \left[\frac{\partial \boldsymbol{u}_{\boldsymbol{f}_i}}{\partial t} + \boldsymbol{u}_{\boldsymbol{f}_j}\frac{\partial \boldsymbol{u}_{\boldsymbol{f}_i}}{\partial x_j}\right] = \frac{\partial \boldsymbol{\varepsilon}_{ij}^f}{\partial x_j} + \epsilon \rho_f \boldsymbol{g}_i - \boldsymbol{f}_i \tag{2.13}$$

$$\rho_s (1-\epsilon) \left[\frac{\partial \boldsymbol{u}_{\boldsymbol{s}_i}}{\partial t} + \boldsymbol{u}_{\boldsymbol{s}_j}\frac{\partial \boldsymbol{u}_{\boldsymbol{s}_i}}{\partial x_j}\right] = \frac{\partial \boldsymbol{\varepsilon}_{ij}^s}{\partial x_j} + (1-\epsilon)\rho_s \boldsymbol{g}_i + \boldsymbol{f}_i \tag{2.14}$$

where ϵ is the porosity or volume fraction of the fluid in the averaged volume, $\boldsymbol{u}_{\boldsymbol{f}_i}$ and $\boldsymbol{u}_{\boldsymbol{s}_i}$ are the local mean velocity of the fluid and solid particles, respectively, ρ_f and ρ_s are the mass density of fluid and solids, respectively, and $\boldsymbol{f}_i$ is the average force exerted by the solid particles on the fluid estimated over the solid volume fraction. The first term on the right-hand side in equations (2.13) and (2.14) lumps the overall stresses acting on the fluid and the solid particles:

$$\boldsymbol{\varepsilon}_{ij}^f = -p_i^f \delta_{ij} + \epsilon \left(\lambda^f - \frac{2}{3}\mu^f\right)\delta_{ij}\frac{\partial \boldsymbol{u}_{\boldsymbol{f}_i}}{\partial x_i} + \epsilon \mu^f \left(\frac{\partial \boldsymbol{u}_{\boldsymbol{f}_i}}{\partial x_j} + \frac{\partial \boldsymbol{u}_{\boldsymbol{f}_j}}{\partial x_i}\right) \tag{2.15}$$

$$\boldsymbol{\varepsilon}_{ij}^{s} = -p_i^s \delta_{ij} + (1-\epsilon)\left(\lambda^s - \frac{2}{3}\mu^s\right)\delta_{ij}\frac{\partial \boldsymbol{u}_{s_i}}{\partial x_i} + (1-\epsilon)\mu^s\left(\frac{\partial \boldsymbol{u}_{s_i}}{\partial x_j} + \frac{\partial \boldsymbol{u}_{s_j}}{\partial x_i}\right) \tag{2.16}$$

where λ^f, μ^f and λ^s, μ^s are the effective bulk and shear viscosities for the fluid and solid phases, respectively, p_i^s is the pressure acting on solid particles due to particle contact (interparticle pressure), and p_i^f is the local average fluid pressure. As can be seen in equations (2.15) and (2.16), several closures are required to obtain the value of solid pressure and the shear stress tensor. These closures also need to be in the form of volume-averaged quantities to be consistent with the set of governing equations.

2.4.1.1 **The Two-Fluid Model (TFM)**

The Two-Fluid Model (TFM) emerged as a direct application of the volume averaging techniques. As noted by its name, the solid phase in the flow is treated as a fluid-like continuum with constitutive relationships used to describe the pressure and viscosity terms. In the TFM, both fluid and solid phases are considered as interpenetrating continua in the sense that both phases are expressed as a continuum over the same averaging volume. The concept of interpenetrating continua may be difficult to visualize because both phases are hypothesized to coexist in the same volume, yet, only partially occupying that volume. In Figure 2.5 we try to graphically illustrate this concept.

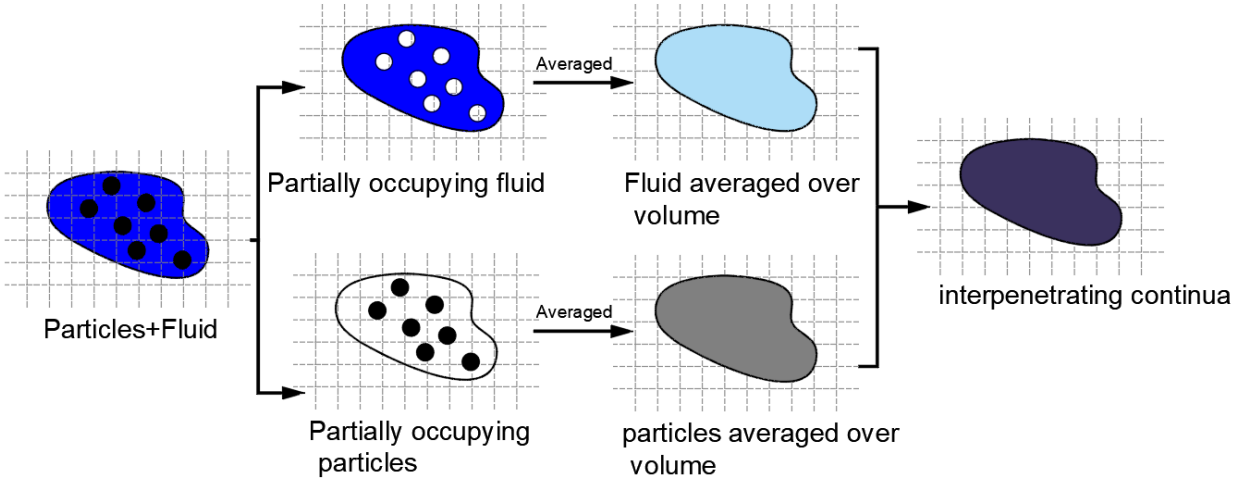

Figure 2.5 .A schematic illustration of the concept of local averaging and interpenetrating continua.

The core of the TFM is the constitutive relationships for the effective solid pressure p^s, and bulk and shear viscosities, λ^s and μ^s. The early closures for the viscous variables presented by Anderson and Jackson (1967b), Tsuo and Gidaspow (1990), and Kuipers et al. (1992) were fully empirical. Despite the simplicity of applying these closures, they did not account for the underlying characteristics of the solid phase rheology (van der Hoef et al., 2008). The Kinetic theory of Granular Flow (KTGF) (Ding and Cidaspow, 1990; Jenkins and Savage, 1983; Lun et al., 1984) is among the most popular methods for pressure and viscosity closures for the TFM. The solid flow variables expressed by KTGF are in terms of the solid volume fraction, $\varepsilon_s = (1 - \epsilon)$, the normal coefficient of restitution, e, and the granular temperature, θ. For example, the effective shear viscosity of the solid phase (μ^s) is expressed as (Gidaspow, 1994):

$$\mu^s = \frac{5\sqrt{\pi}}{12}\left(\frac{1}{(1+e)\gamma(\varepsilon_s)} + \frac{2}{5} + 0.193(1+e)\gamma(\varepsilon_s)\right)\rho_s d\sqrt{\theta} \qquad (2.17)$$

where, $\gamma(\varepsilon_s)$ is the excess compressibility of an elastic hard-sphere system, and d is the particle diameter. A more detailed discussion on the KTGF is found in Gidaspow (1994) and Crowe et al. (2012). Coupling the TFM with KTGF provides the advantage of conducting relatively large-scale simulations. Yet, the constitutive relationships are governed by the microscale characteristics of the flow (van der Hoef et al., 2008). This is in contrast to the previously presented empirical constants used for closure, which did not consider the underlying physics of the flow, and perhaps even argued to be unphysical (Zhu et al., 2007, 2008).

From the above discussion, it is obvious that the TFM, although being valid for the simulation of some particular problems, lacks the very basic description of particulate dynamics on the microscale. This is because all the interparticle and particle-fluid interactions are indirectly included through averaged values obtained from closures. Crowe et al. (2012) argue that the idea of the Two-Fluid Model is essentially flawed because the magnitude of averaging volume might significantly differ from the size of point volume, which does not give accurate representation of the fluctuations in point velocity (Figure 2.6). This averaging technique might be valid for gaseous flows where the mixture contains solid components of comparable size to the averaging volume, but cannot be generalized to the broad range of concentrations of dispersed solids in a fluid. For all these reasons, a model is needed to describes the flow characteristics at the particle scale level where no such averaging or heavy reliance on constitutive relationships is used.

2.4.2 Eulerian-Lagrangian approach

In the Eulerian-Lagrangian approach, the motion of the solid particles is tracked using the Newtonian laws of motion. The tracking of individual particles, with no dependence on a computational mesh, offers the advantage of accounting for the discrete nature of the solid phase. Moreover, the solid-fluid interaction forces (e.g., drag forces and pressure gradient forces) can be directly implemented instead of the previously used indirect averaging approach of the TFM. Indeed, the Lagrangian approach in simulating solid particles does not eliminate the complexity of the estimation of particle fluid-interaction forces because the complexity runs deeper than the issue of volume averaging. However, there is no doubt that the use of the Lagrangian approach for simulating the solid phase has refined the state of simulation and provided access to information on the microscale interactions that were impossible to obtain from the Eulerian-Eulerian approach.

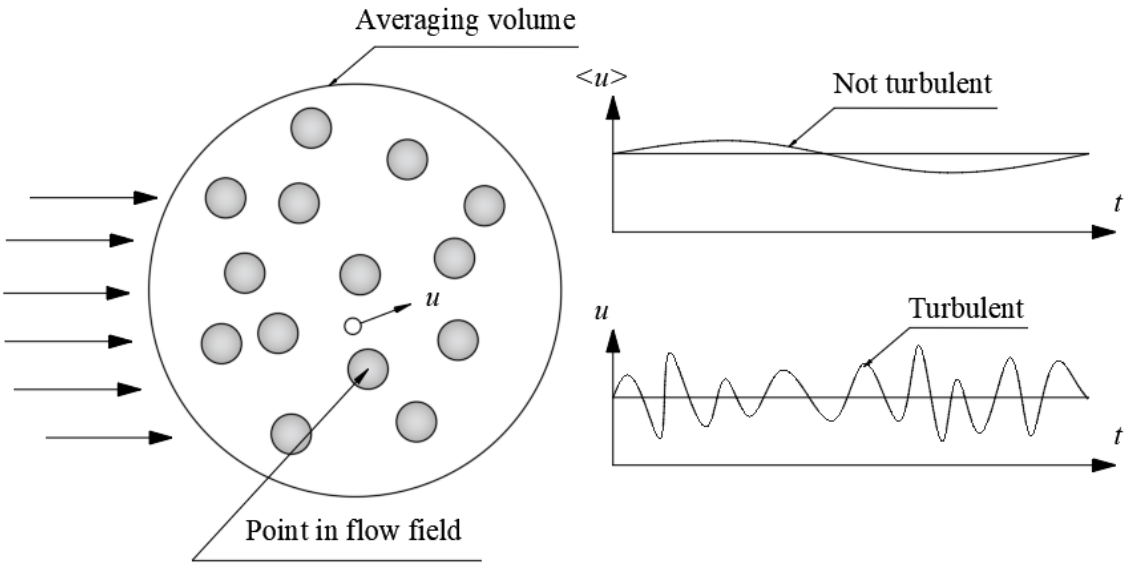

Figure 2.6. A comparison of velocity fluctuations between volume-averaged velocity $\langle \boldsymbol{u} \rangle$ and point velocity $\boldsymbol{u}$.

Several models have been presented for the simulation of both the Lagrangian and Eulerian numerical treatment in particulate multiphase flows. For the fluid phase (Eulerian), the locally averaged Navier-Stokes equations (Equation (2.13)) is the most commonly used. Alternatively, the Lattice Boltzmann method can be used to model the fluid phase, where the

fluid flow is modelled via streaming and collision processes on a two-dimensional or three-dimensional lattice. As for the Lagrangian treatment of solid particles, the most commonly used model is the Discrete Element Model (DEM). Other methods such as Discrete Phase Method (DPM) (Dickenson and Sansalone, 2009; Vakhrushev and Wu, 2013; Zahari et al., 2018), Dense Discrete Phase Method (DDPM) (Adamczyk et al., 2014; Cloete and Amini, 2017; Marchelli et al., 2017), and Multiphase Particle-In-Cell (MP-PIC) (Andrews and ORourke, 1996; Patankar and Joseph, 2001; Snider, 2001; Zeng et al., 2019) have also been used to simulate the motion of solid particles in a Lagrangian framework. In this section, we review the theoretical aspects, coupling strategies and the field of application of the Eulerian-Lagrangian-based models.

2.4.2.1 **Discrete Element Model**

The work of Cundall and Strack (1979) presented the first model for accurately simulating the motion of granular solids. The translational and rotational motion for a particle i with mass m_i and moment of inertia I_i are described by Newton's second law as:

$$m_i \frac{d\boldsymbol{v}_i}{dt} = \sum_j \boldsymbol{F}_{ij}^c + \sum_k \boldsymbol{F}_{ik}^{nc} + \boldsymbol{F}_i^f + \boldsymbol{F}_i^g \tag{2.18}$$

$$I_i \frac{d\boldsymbol{\omega}_i}{dt} = \sum_j \boldsymbol{M}_{ij} \tag{2.19}$$

where $\boldsymbol{v}_i$ and $\boldsymbol{\omega}_i$ are the translational and angular velocities of particle i, respectively, $\boldsymbol{F}_{ij}^c$ and $\boldsymbol{M}_{ij}$ are the contact force and moment acting on particle i by particle j or wall, $\boldsymbol{F}_{ik}^{nc}$ is the contactless forces (e.g., electrostatic or liquid bridge forces) acting on particle i by particle k, $\boldsymbol{F}_i^f$ is the particle-fluid interaction force on particle i, and $\boldsymbol{F}_i^g$ is the gravitational force acting on particle i. Figure 2.7 shows a schematic for the different contact and non-contact forces in a particle i by a particle in contact (j) and a particle not in contact (k).

Cundall and Strack (1979) proposed a linear spring-dashpot model to estimate the contact forces, where the spring part of the model is directly related to contact deformation (both normal and tangential); the dashpot part represents the viscous dissipation of the force.

The normal and tangential contact forces in the DEM model can be expressed as:

$$\boldsymbol{F}_{ij}^{cn} = -K_n \delta_{ij} \boldsymbol{n_c} - C_n (\boldsymbol{v_c} \cdot \boldsymbol{n_c}) \boldsymbol{n_c} \tag{2.20}$$

$$\boldsymbol{F}_{ij}^{t} = -K_t \boldsymbol{v_c^t} + C_t (\boldsymbol{v_c} \times \boldsymbol{n_c}) \times \boldsymbol{n_c} \tag{2.21}$$

where K_n and K_t are the normal and tangential spring stiffness, respectively, C_n and C_t are the viscous dissipation coefficients related to the dashpot, $\boldsymbol{v_c}$ is the relative velocity between particles in contact and $\boldsymbol{n_c}$ is the normal unit vector at the contact point. In addition to the contact forces between particles, models have been presented to estimate the non-contact forces such as electrostatic forces (Attard and Gillies, 2001), liquid bridge, and capillary forces (Gellespie and Settineri, 1968; Lian et al., 1993), and van der Waals forces (Hamaker, 1937; Israelachvili, 2011).

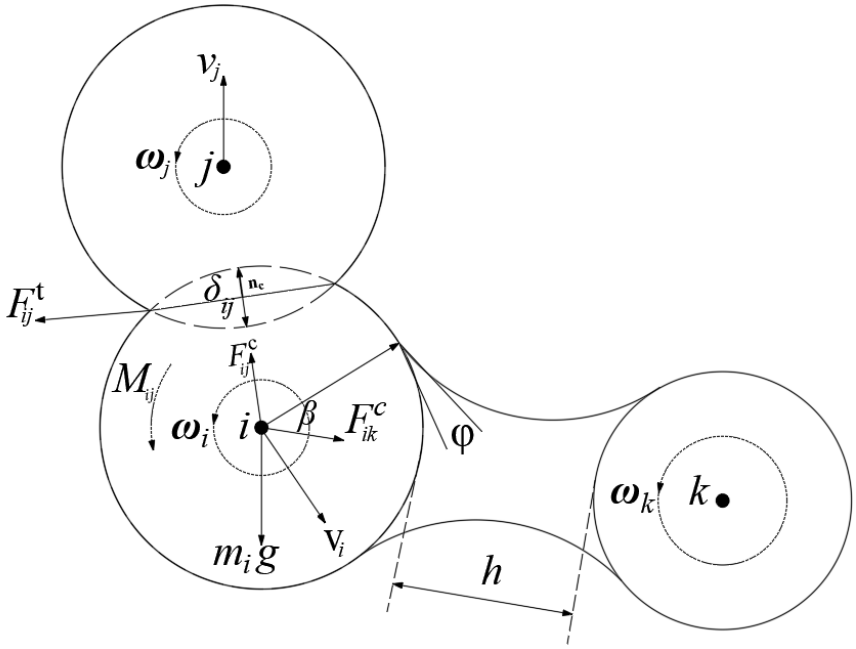

Figure 2.7. A schematic for the contact and non-contact forces affecting on particle *i* by (i) particle *j* in contact and (ii) particle *k* that is not in contact

2.4.2.2 **CFD-DEM model**

Coupling of DEM and Computational Fluid Dynamics (CFD) has been gaining more popularity since was first introduced by Tsuji et al. (1993). The use of DEM provided unprecedented advantages in simulating the motion of the solid phase of the flow, both translational and rotational, which was not achieved by any of the previous models. In addition, it facilitated the implementation of different particle shapes and interactions. Although nearly all the proposed models, except for Lattice Boltzmann methods, solve volume averaged Navier-Stokes

equations, the “CFD” term is exclusively used for the case of solving Navier-Stokes equations with DEM. The two-dimensional soft sphere (i.e., no collision) model presented by Tsuji et al. (1993) paved the way for many following developments. Examples for this include the model refinement by Xu and Yu (1997) where they presented a detailed coupling technique for the cell-averaged particle-fluid interaction forces. Hoomans et al. (1996) introduced a two-dimensional hard-sphere model that accounted for the collision of solid particles based on the conservation of linear and angular momentum of the colliding particles. Shortly after, Kawaguchi et al. (1998) successfully extended the model to 3D and obtained good agreement with experimental results.

The aforementioned developments were presented to mainly model solid-gas particulate flows in fluidized beds. However, the robustness and solid theoretical grounds of the approach makes it valid for many other applications. For example, it was extensively used in pneumatic conveying modelling (Zhang et al., 2007; Zhou et al., 2014; Zhou et al., 2016) and food processing (Azmir et al., 2019; Hilton et al., 2013). In geotechnical engineering, the CFD-DEM model was used to model soil liquefaction (Shamy and Zeghal, 2005; Zeghal and El Shamy, 2004), landslide (Shi et al., 2018; Zhao, 2017), erosion and cavity evolution (Guo and Yu, 2017; Suzuki et al., 2007; Zou et al., 2020).

The governing equations for the fluid phase are the same as those in the TFM (Equation (2.11) and Equation (2.13)) for volume-averaged continuity and Navier-Stokes equations, and the governing equations for the solid phase are the Newtonian equations of motion (Equation(2.18) and Equation (2.19)). The coupling between CFD and DEM is done as shown in (Figure 2.8). Firstly, solid particles are located within each fluid computational cell for porosity/volume fraction calculations. Afterward, the fluid flow is resolved using the averaged Navier-Stokes equations and the continuity equations to estimate the new fluid position and the fluid forces acting on the solid particles. Following the calculation of the forces on solid particles, the DEM simulation is conducted, typically, with a time step smaller than that required for the CFD simulation to ensure stability. Finally, the updated positions and initial conditions of the solid phase are sent back to the CFD solver to start a new time step until the simulation time is satisfied. This is referred to as “one-way coupling”, where only the effect of fluid forces on the solid phase is considered but the effect of the solid phase on the fluid motion is neglected. To conduct two-way coupling, the exported positions and forces from the DEM solver to the CFD solver is used to solve for fluid motion one last time before closing a single time step.

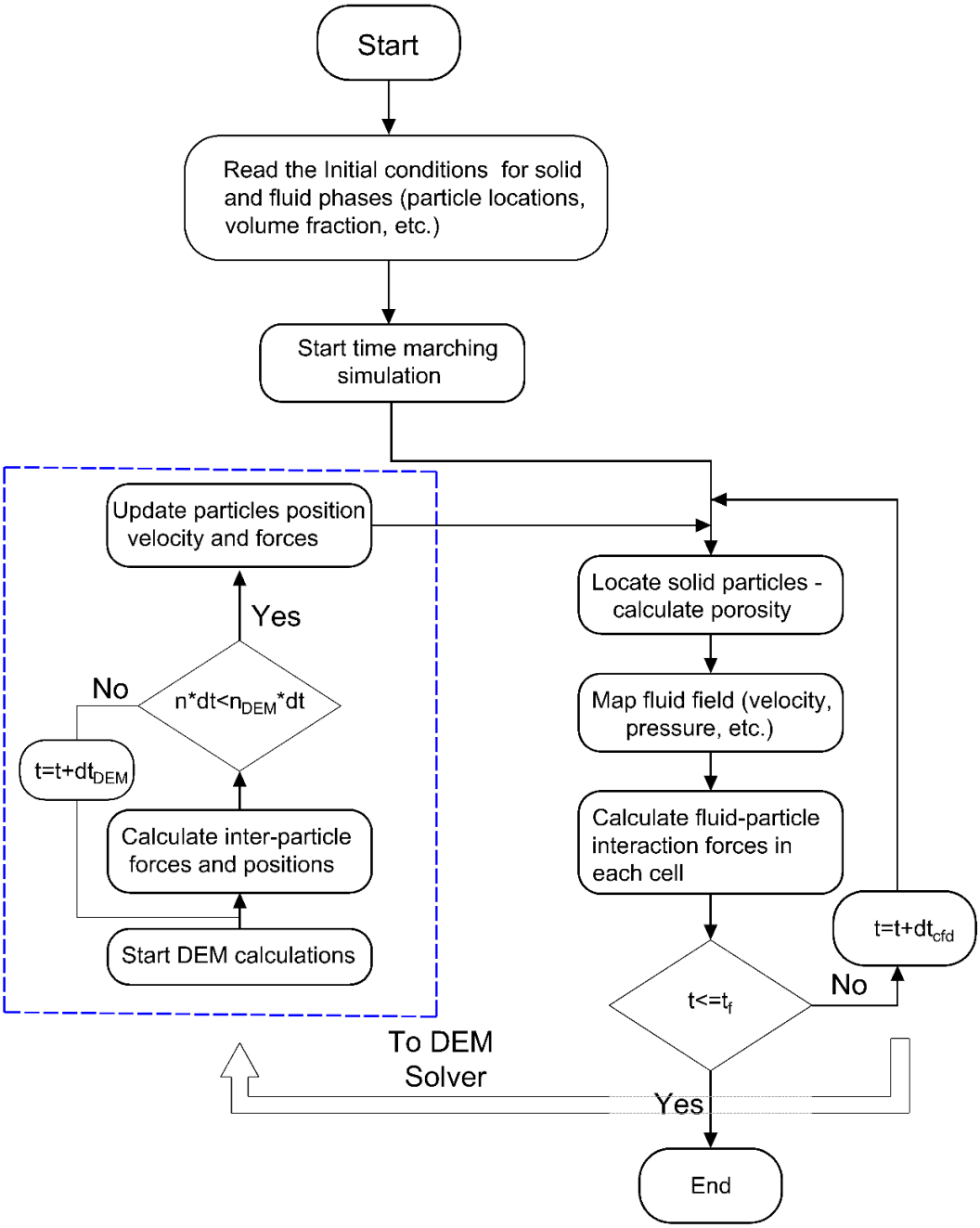

Figure 2.8. A flowchart illustrating the solution process of coupled CFD-DEM simulation

Since the time step required for DEM numerical stability is typically smaller than that used for CFD calculations (e.g., finite volume), the overall speed of simulation is governed by the DEM calculations. To have an insight into this issue, let us consider the DEM time step Δt as (Tsuji et al., 1992):

$$\Delta t \leq \lambda \sqrt{\frac{m}{K_n}} \tag{2.22}$$

where λ is a reduction factor to counteract the unphysical energy generation from the numerical approximation in the DEM solution, m is the mass of the particle and K_n is the normal stiffness of the solid particle. On the contrast, the stable time step for the CFD calculations can be determined using the Courant-Fredrich-Lewy (CFL) number (Courant et al., 1928; Zhao, 2017):

$$\Delta t \leq \frac{\Delta x}{\epsilon |u_f - u_p|} \tag{2.23}$$

where Δx is the size of the computational mesh cell for the CFD calculations. From Equations (2.22) and (2.23), the value of λ is essentially smaller than $1/\epsilon$. If we consider a typical analysis where the size of the computational cell is fairly larger than the particle size (e.g. 10 times larger), we approximately state that $\Delta x > 10D$, where D is the particle diameter. Where the particle mass is related to the particle diameter by:

$$D = \sqrt[3]{\frac{6m}{\pi \rho_s}} \tag{2.24}$$

$$\Delta x > 10 \sqrt[3]{\frac{6m}{\pi \rho_s}} \tag{2.25}$$

Now, for the sake of clarification, if we consider sand particles of 1 mm in diameter with a density of 2700 kg/m^3 and normal stiffness of 2×10^5 KN/m, one can tentatively conclude that the stable time step for the DEM is nearly two orders of magnitude higher than that for the CFD. This conclusion is confirmed by (Zhao, 2017) from a parametric analysis involving DEM time step such that no unphysical kinetic energy is generated in the system on 1250 randomly packed particles with elastic interparticle and wall-particle collision. The stable time step obtained for the DEM computations was found to be two orders of magnitude higher than that of the finite volume scheme used in CFD computations.

One of the drawbacks of the CFD-DEM model is the high computational cost associated with it. Despite its ability to capture the microscale interactions between fluid and solid phases, it takes extensive computational resources to perform such computations on a large scale. Hence, phenomenological scale simulations using CFD-DEM have not yet been successfully conducted. Reflecting on geotechnical applications, the previously mentioned contributions of the CFD-DEM model in geotechnical engineering have been successfully validated by

comparison either to experimental data or known analytical solutions. To get a perspective of this issue, modelling of internal erosion in earth dams might involve billions of DEM particles, the computational capacity needed to simulate is beyond the available resources. Moreover, if such extensive computational resources are available, carrying out such simulations will still not be feasible because it needs to be conductible within resources available for geotechnical engineers.

Another challenge with the application of the CFD-DEM model is the process of assigning and implementing fluid-particle interaction forces. This process can be troubling because both the position and size of the particles can cause disrupted force distribution. For example, as shown in Figure 2.9(a), a particle can exist partially within a cell, which means that duplication will occur if the force is assigned according to the number of the particles in a cell as the particle practically exists in two or more cells (Hirche et al., 2019). In addition, the ratio between particle size and cell size may cause false estimation of the porosity. As shown in Figure 2.9(b), if the particle size is large compared to the cell size, porosity can be overestimated. Similarly, it can be underestimated in some of the neighboring cells. This condition, where particles are smaller in size than computational cells, is often referred to in the literature as "unresolved simulation" (Kloss et al., 2012). For unresolved simulation, the misplacement of particles can lead to inevitable errors in summing the forces over CFD cells. As this assignment essentially depends on the porosity or the volume fraction of the solid particles, the size of a computational cell should be fairly larger than the size of the largest solid particle such that errors due to porosity fluctuations and force assignment are minimized (Goniva et al., 2012; Hirche et al., 2019). A proper ratio between the cell and particle sizes as suggested by Kloss et al. (2012) is 10.

It is important to note that the implemented fluid-particle interaction forces such as drag force are estimated for a single particle. Subsequently, for drag force as an example, the effect of surrounding particles on the drag is not considered (Zhu et al., 2007, 2008). Furthermore, to ensure that Newton's third law is not violated (i.e., the forces posed by the fluid on particles and vice versa are equal in magnitude), the forces are computed for each particle in the cell and then summed to obtain the interaction force at the cell scale. The sum of forces estimated for single particles with no account for the effect of other particles will not give an accurate representation for interaction forces. Besides, the previously pointed issues with estimating the volume fraction may give misleading results for the interaction force. The only available way, so far, to overcome these issues is to conduct the calculations using a relatively finer mesh for

the fluid and obtain the forces on solid particles by integrating the shear stress over the surface of the particle. This approach eliminates the need for volume averaging and constitutive relationships in the first place and referred to as “resolved” modelling (Figure 2.10).

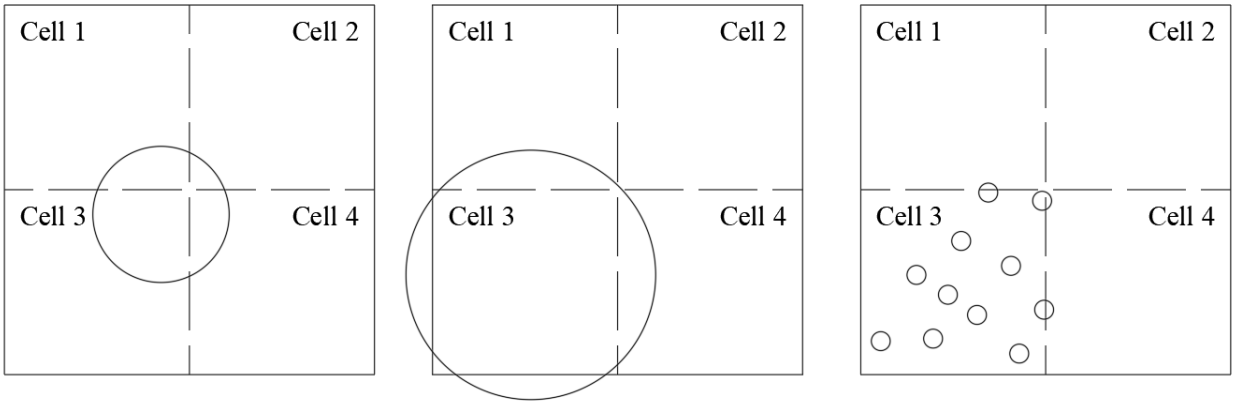

Figure 2.9. Different possible configurations of solid particles within a computational cell with respect to particle size and position (adapted from (Hirche et al., 2019))

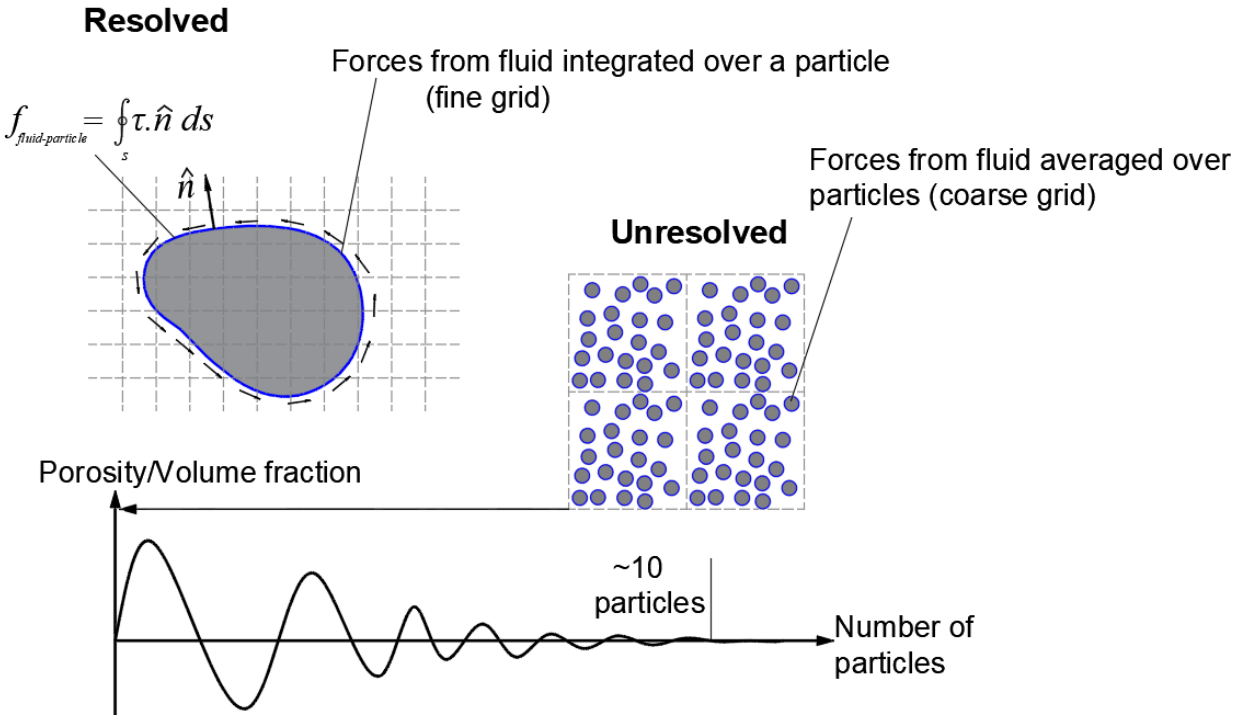

Figure 2.10. Illustration for resolved and unresolved numerical simulation for particulate flows and the porosity fluctuations in a control volume with respect to the number of particles.

In resolved modelling, the CFD mesh cells are sized to be small compared to interparticle spacing (Pan et al., 2002). By considering the solid particles as moving boundaries (Hu, 1996),

the fluid-particle interaction forces can be obtained by integrating the shear stresses over the particle's surface (Catalano et al., 2014). This approach can be practical when simulating relatively large bodies immersed in a fluid. However, for dense particulate systems involving a large number of particles with small interparticle spaces, the resolution of the simulation is most unlikely to be computationally feasible. Thus, the approach is seldom used for practical simulation and is rather used to refine the closure models for fluid-particle interaction forces (Wachs et al., 2018). This can also be seen in the multi-level hierarchy of multiscale simulations (Deen et al., 2007; van der Hoef et al., 2008; van der Hoef et al., 2006), where the very basic and most computationally expensive layer of the hierarchy is the direct numerical simulation used to obtain drag closures (Cook et al., 2004; Deen et al., 2007; Kruggel-Emden et al., 2016). In contrast to the case of unresolved modelling, where the overall efficiency of the simulation is dominated by DEM calculations, the efficiency of CFD computations becomes critical in resolved modelling. Thus, it is favourable in this case to use alternative and more efficient methods such as the Lattice Boltzmann Method (LBM) to simulate fluid flow.

2.4.2.3 **Lattice Boltzmann Method (LBM) - DEM**

The Lattice Boltzmann Method (LBM) is based on the discretization of the Boltzmann equation in space, time, and velocity field (Cui et al., 2014). The early development of the method is known as the Lattice Gas Automata (LGA) (Hardy et al., 1976). Although this method is originated from the kinetic theory of dilute gases, the continuity and Navier-Stokes equations could be successfully recovered from it up to the second-order in time and space (Chen and Doolen, 1998; Cook et al., 2004). In the LBM, the fluid is represented by packets of mass with properties characterized by a density distribution function PDF to avoid statistical noises encountered previously in the LGA method. These packets reside at the nodes of a lattice mesh, as shown in Figure 2.11, and are allowed to move with prescribed velocity in the specified direction for each node to the neighbouring node (streaming). After the streaming of the packets, the packets/particles colliding at a node change velocity according to certain rules that ensure the conservation of mass, momentum, and energy before and after the collision.

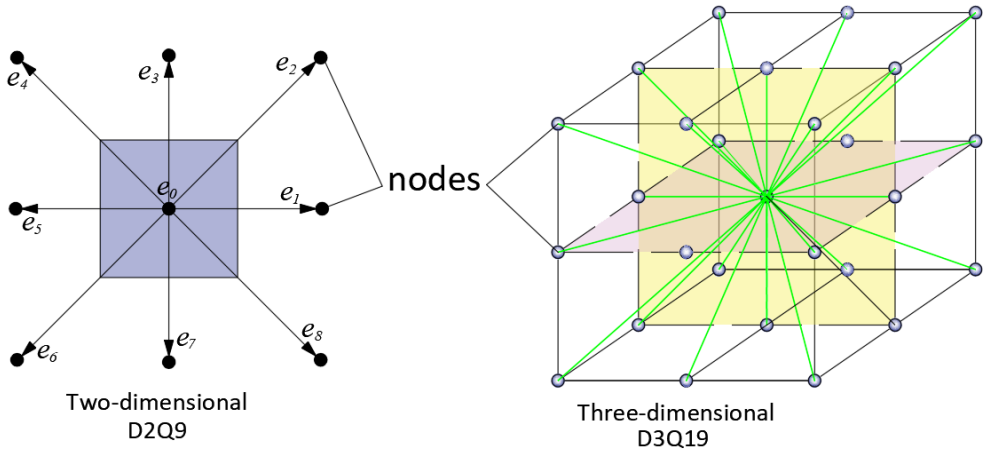

Figure 2.11. Two and three-dimensional computational lattice mesh and the principal directions of streaming and collision.

One of the most adopted methods for estimating and redistributing the particle velocities after collision is the Lattice Bhatnagar-Gross-Krook (BGK) single time relaxation model (Chen and Doolen, 1998), which is given as:

$$f_i(\boldsymbol{x} + \boldsymbol{e}_i\Delta t, t + \Delta t) = f_i(\boldsymbol{x}, t) - \frac{\Delta t}{\tau}\left(f_i(\boldsymbol{x}, t) - f_i^{eq}(\boldsymbol{x}, t)\right) \tag{2.26}$$

where $f_i(\boldsymbol{x}, t)$ is the probability density distribution of the fluid with velocity $\boldsymbol{e}_i$ located at distance $\boldsymbol{x}$ at time t, τ is the relaxation time, and $f_i^{eq}(\boldsymbol{x}, t)$ is the equilibrium density distribution of the fluid. In Equation (2.26), the second term on the right-hand side resembles the collision of fluid packets, and the left-hand side of the equation represents the streaming phase, where the term $(\boldsymbol{e}_i\Delta t)$ is the distance travelled by the particle in the direction of $\boldsymbol{e}_i$. For a two-dimensional simulation, also known as the D2Q9 lattice model, there are eight non-zero velocity distributions at nodes 1-8, and a rest distribution at node 0 (see Figure 2.11) (Qian et al., 1992). For particulate flows, LBM can be coupled with the DEM by introducing a term for fluid-particle interaction as:

$$\begin{aligned} &f_i(\boldsymbol{x} + \boldsymbol{e}_i\Delta t, t + \Delta t) \\ &\qquad = f_i(\boldsymbol{x}, t) - \frac{\Delta t}{\tau}(1 - B)\left(f_i(\boldsymbol{x}, t) - f_i^{eq}(\boldsymbol{x}, t)\right) + B\Omega_i^s \end{aligned} \tag{2.27}$$

where B is a weighting function to account for the volume fraction of the solid phase (ϵ) and characterized by the nodal area occupied by the solid particles and the dimensionless relaxation time τ^* as:

$$B(\epsilon, \tau^*) = \frac{\epsilon\left(\tau^* - \frac{1}{2}\right)}{(1-\epsilon) + \left(\tau^* - \frac{1}{2}\right)} \tag{2.28}$$

and Ω_i^s is known as the "bounce-back term" and is responsible for bouncing back the non-equilibrium part of the distribution, Ω_i^s is given as:

$$\Omega_i^s = f_{-i}(\boldsymbol{x}, t) - f_i(\boldsymbol{x}, t) + f_i^{eq}(\rho, \boldsymbol{v}_s) - f_{-i}^{eq}(\rho, \boldsymbol{v}) \tag{2.29}$$

A remarkable advantage of the LBM is that it eliminates the need to solve the full Navier-Stokes equations (volume-averaged for particulate flows), instead, it reduces to simpler local operations. This advantage makes LBM easier to program and therefore more efficient in conducting CFD calculations. As pointed by Satofuka and Nishioka (1999), the CPU time is reduced to half when LBM is used compared to the conventional CFD methods for the same grid size. However, it is important to keep in mind that in particulate flow simulations involving DEM, the majority of the computational load comes from the DEM part of the simulation. As shown in Figure 2.8, several DEM computations are conducted every time step for a single CFD computation because the stable time step of DEM is typically much smaller than this required for CFD (Zhao, 2017).

The LBM-DEM has been used successfully applied in various simulations such as fluidized beds (Third et al., 2015) sand production (Han and Cundall, 2017), internal fluidization and erosion of soil (Cui et al., 2014), and surface erosion in soils (Tang et al., 2017a; Tang et al., 2017b). However, the computational cost of this method for large-scale simulations is still questionable, because, as noted before, the DEM part of the computation remains critical in determining the overall computational cost of the model. This method is more efficient when very fine flow resolution is required as in the direct numerical simulations (Deen et al., 2007d; van der Hoef et al., 2008).

2.4.3 Lagrangian-Lagrangian approach

Throughout the previously discussed models, the fluid flow is always solved locally on a structured or unstructured grid. In contrast, the fully Lagrangian methods adopt trajectory tracking for both fluid and solid phases of particulate flows. One way to conduct such tracking is through a dynamically adaptive grid, where the gird follows the fluid particles/parcels throughout the calculation (e.g., Particle Finite Element Method (PFEM)). Alternatively, the fluid can be represented by a set of separate particles with no mesh structure (e.g., smoothed particle hydrodynamics (SPH) (Gingold and Monaghan, 1977; Lucy, 1977) and moving

particle semi-implicit (MPS) methods (Koshizuka and Oka, 1996)). The latter methods are often referred to as meshless/mesh-free or particle methods. Some other methods such as the Material Point Method (MPM) (Sulsky and Brackbill, 1991; Sulsky et al., 1995) involve the use of a computational grid for intermediate calculations, yet, it is overall considered as a particle method.

Lagrangian tracking provides the advantage of accurately modelling highly convective flows, fragmentation, and free surface flows. This is because the errors associated with the discretization of the convective terms in the Eulerian solvers such as finite volume and finite differences no longer exist. However, particle tracking on a large scale, semi-implicit solutions that require solving Poisson's equation for the pressure field, and dynamic mesh adaptations in the Lagrangian methods may results in higher computational cost as opposed to conventional mesh-based methods such as the Finite Volume Method (FVM). In the following section, we review the theoretical aspects, models, and applicability to geotechnical engineering of some of the major Lagrangian-Lagrangian models in the literature.

2.4.3.1 **Smoothed Particle Hydrodynamics (SPH)**

Smoothed Particle Hydrodynamics (SPH) has been first developed in the field of astrophysics by Lucy (1977) and Gingold and Monaghan (1977). Later on, the method was extensively used in hydrodynamic modelling and computational fluid dynamics. In SPH, the fluid continuum is expressed as a set of separate particles that carry information about the flow field such as velocity and pressure. The motion of these particles is governed by conservation laws such as mass, momentum, and energy. The flow properties at one particle are obtained by the super-positioning weighted properties of the surrounding particles within a smoothing length, h, via a smoothing function known as the smoothing kernel W (Figure 2.12). For instance, at a particle i, the value of a flow variable is the smoothed sum of the variable at a set of particles j that exist within the smoothing length κh, where κ is typically taken as 2 (Bui and Fukagawa, 2013).

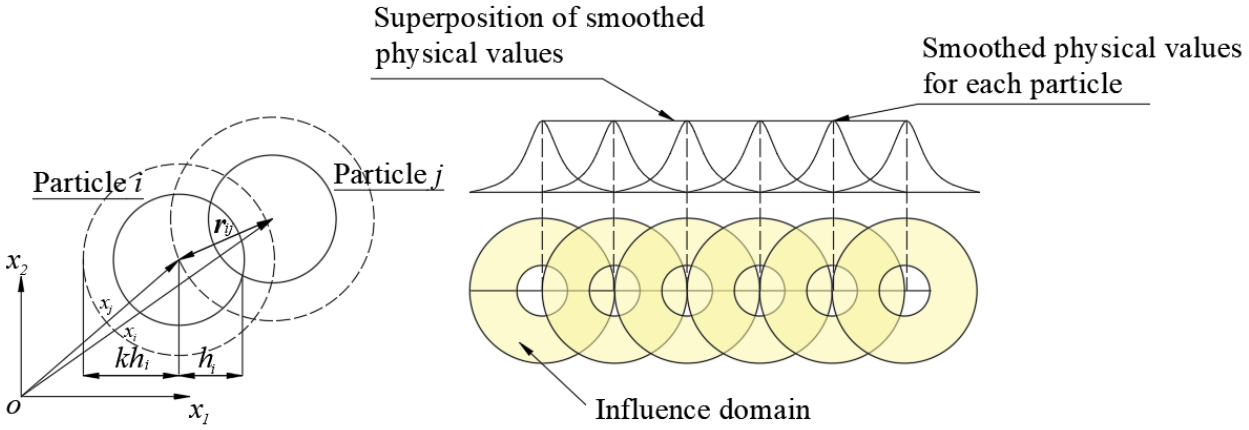

Figure 2.12. Illustration of particle representation as moving boundaries and the comparative cell size scale to interparticle spacing.

For a particle i, an averaged property $\langle f(x)\rangle_i$ is expressed as:

$$\langle f(x)\rangle_i = \sum_{j=1}^{N} m_j \frac{f(x)_j}{\rho_j} W\left(|\boldsymbol{r}_j - \boldsymbol{r}_i|, h\right) \tag{2.30}$$

where N is the count of particles that exist within the smoothing length, m_j is the mass of particle j, and $\boldsymbol{r}_i$ and $\boldsymbol{r}_j$ are the position vectors for particles i and j respectively. The gradient of $\langle f(x)\rangle_i$ can be estimated by applying Gauss's theorem to the integral of $\langle f(x)\rangle_i$ assuming full compact support (i.e., surrounding particles fully exist within a non-truncated sphere of radius κh) as:

$$\nabla\langle f(x)\rangle_i = \sum_{j=1}^{N} m_j \frac{f(x)_j}{\rho_j} \nabla W\left(|\boldsymbol{r}_j - \boldsymbol{r}_i|, h\right) \tag{2.31}$$

The continuity and Navier-Stokes equation in SPH framework is expressed as:

$$\left(\frac{D\rho}{dt}\right)_i = \sum_{j=1}^{N} m_j(\boldsymbol{u}_j - \boldsymbol{u}_i)\nabla W(|\boldsymbol{r}_i - \boldsymbol{r}_j|, h) \tag{2.32}$$

$$\left(\frac{D\boldsymbol{u}}{dt}\right)_i = -\sum_{j=1}^{N} m_j \left(\frac{p_j}{\rho_j^2} + \frac{p_i}{\rho_i^2}\right) \nabla W\left(|\boldsymbol{r}_i - \boldsymbol{r}_j|, h\right) + \sum_{j=1}^{N} \boldsymbol{\Pi}_{ij} + \boldsymbol{f}_{b_i} \tag{2.33}$$

where $\boldsymbol{\Pi}_{ij}$ is the artificial viscosity term included to ensure the stability of the calculations

and $\boldsymbol{f}_{b_i}$ is the body force acting on particle i. $\boldsymbol{\Pi}_{ij}$ is expressed as (Cleary and Monaghan, 1999):

$$\boldsymbol{\Pi}_{ij} = \frac{m_j(\mu_i + \mu_j)(\boldsymbol{r}_i - \boldsymbol{r}_j) \cdot \nabla_i W_{ij}}{\rho_i \rho_j (\boldsymbol{r}_i - \boldsymbol{r}_j)^2} (\boldsymbol{u}_i - \boldsymbol{u}_j) \tag{2.34}$$

where $\nabla_i W_{ij}$ is equivalent to $\nabla W(|\boldsymbol{r}_i - \boldsymbol{r}_j|, h)$. More detailed discussion on the derivation and implementation of SPH original formulations can be found in (Gotoh et al., 2013).

Over the past few decades, the SPH method has undergone several developments such as the projection-based velocity field decomposition (Shao and Lo, 2003), Higher-Order Laplacian formulation for pressure estimation (Khayyer and Gotoh, 2010), enforcing conservation of angular momentum (Khayyer and Gotoh, 2009), optimized particle shifting technology (Khayyer et al., 2017), higher order differential operators (Khayyer et al., 2009; Wang et al., 2019), enhanced hydroelastic coupled solver for fluid-structure interaction (FSI) (Khayyer et al., 2018a), and SPH with numerical diffusive terms δ-SPH (Marrone et al., 2011). The method was proven to be superior in accuracy compared to other mesh-based methods for free-surface and highly convective flows (e.g., wave breaking).

2.4.3.2 **SPH-DEM**

In particulate flow modelling, working within a fully Lagrangian framework can be more computationally convenient as the previously encountered problems due to the unresolved simulation approach in the CFD-DEM is no longer adopted. Potapov et al. (2001) presented one of the earliest models for coupling SPH and DEM. In their model, the fluid-solid coupling was achieved by introducing so-called "artificial SPH particles" that are small enough to occupy the interparticle space. The flow of these particles evolves in the same manner as the rest of SPH particles while at the boundaries of solid particles a no-slip condition is enforced to ensure that artificial particles have the same velocity as the solid particles. The fluid-particle interaction forces are then estimated in a resolved manner, similar to DNS, by summing the exerted fluid forces on solids in a direction opposite to the flow, which can be expressed as an additional term added to Equation (2.33).

Following the work of Potapov et al. (2001), Sakai and Maeda (2006) developed a three-phase SPH-DEM model to simulate seepage failure under sheet piles considering three-phase flow (air, water, and soil). A multi-layer analysis approach was used, where each phase is modelled separately and then connected phases through constitutive models. The soil phase

was assumed to be elastic-perfectly plastic, and combining fluid and solid phases was done using the mixture theory (Biot, 1941). A different approach was presented by Robinson et al. (2014) and Kwon and Cho (2016) to conduct a two-way coupling of SPH and DEM using the volume-averaged Navier-Stokes equations using discretized fluid-particle interaction forces in SPH framework. More recently, coupled SPH and DEM was used to simulate solid-fluid flows involving free surface and large deformations (He et al., 2018; Tang et al., 2018; Wu et al., 2016; Xu et al., 2019). In geotechnical and civil engineering applications, SPH-DEM has been used to model internal erosion and seepage flow (Gholami Korzani et al., 2017), transport of soil-water mixture and flow through porous media (Wang et al., 2016) and flow through porous media solely using SPH (Akbari and Pooyarad, 2020; Khayyer et al., 2018b), and soil liquefaction and lateral spread (Naili et al., 2005). In addition to coupling with DEM, SPH has also been used along with constitutive models for soils to model dynamic soil behaviour such as embankment failure (Bui and Fukagawa, 2013), seepage-induced dike failure (Zhang et al., 2016), and soil liquefaction (Huang et al., 2011). The summary in Table 2.2 includes a comparison between different modelling methods highlighting the numerical approach, computational cost, relevant work and applicability in geotechnical and ground engineering.

2.5 Modelling tools

In order to carry out particulate flow modelling, the previously governing equations need to be converted to computer code. It is common that researches construct their own in-house codes such that the applications are tailored for a special case of analysis. However, building and debugging codes can be a time-consuming process and more importantly, optimizing the code may require skillsets that are not available for most of the civil engineers. Thus, a good knowledge of the available computational packages, either open-source or commercial, is essential to facilitate the modelling process and save time and effort. There are specific calibres for selecting the proper modelling tool such as the numerical methods deployed in the package, the robustness of the solver, and the computational efficiency of the solver. While commercial packages are often preferred for use in industrial applications because of the robustness of the solver and the existence of a Graphical User Interface (GUI), they allow for a small room for development. On the other hand, open-source software, despite being less convenient in terms of use, allow for development and implementing different physics of choice.

Table 2.2 Summary of particulate flow models and their numerical treatment and computational cost.

Model	Treatment of solid phase	Treatment of Fluid phase	Reference	Applicability in geotechnical engineering	Computational cost
TFM	Eulerian	Eulerian	Anderson and Jackson (1967a)	Limited	Low
DPM	Lagrangian	Eulerian	Vakhrushev and Wu (2013)	Not applicable	Moderate
DDPM +KTGF	Lagrangian	Eulerian	Dickenson and Sansalone (2009)	Limited	Moderate
MP-PIC	Lagrangian	Eulerian	Andrews and ORourke (1996)	Limited applicability	Moderate
CFD-DEM	Lagrangian	Eulerian	Tsuji et al. (1993)	Applicable	High
LBM-DEM	Lagrangian	Eulerian	Cook et al. (2004)	Applicable	High
MPM	Lagrangian	Eulerian	Sulsky and Brackbill (1991)	Applicable	Moderate-High
SPH-DEM	Lagrangian	Lagrangian	Potapov et al. (2001)	Applicable	High
MPS-DEM	Lagrangian	Lagrangian	Sakai et al. (2012)	Applicable	High
PFEM	Lagrangian	Lagrangian	Idelsohn et al. (2004)	Applicable	Moderate

The modelling tools are seldom discussed in the major reviews on particulate flow modelling (e.g., Deen et al. (2007); van der Hoef et al. (2008); Zhu et al. (2007, 2008)). However, few summaries for the available modelling tools exist in literature within specific contexts such as pneumatic conveying (Ariyaratne et al., 2016, 2018), particulate flow in pipes (Zhou et al., 2019), and code parallelization (Norouzi et al., 2016). Although these reviews are not specifically catered to geotechnical engineering applications, most of the included tools have been successfully used to model geotechnical problems. For example, Guo and Yu (2017) used coupled COMSOL multi-physics and PFC3D software to evaluate different simulation methods, Shan and Zhao (2014) used LIGGGHTS and OpenFOAM to simulate the impact of granular material flow into a water reservoir, and Zou et al. (2020) coupled PFC3D with ANSYS Fluent to simulate the progression of internal erosion in gap-graded soils. In this section, we provide a summary of the available modelling tools for particulate flow modelling.

The tools are classified with respect to the numerical framework, as discussed in the previous section. Although the complete features of the computational packages are not reviewed here, the relevant literature in which these packages were used is provided for more information.

Table 2.3. Summary of computational packages for particulate flow modeling. The packages marked with (OS) refer to open-source packages and those marked with (CO) are the commercial packages.

method	Solid phase	Fluid phase	Description	Relevant publications
TFM	MFiX® (OS)		Multiphase (solid-fluid) solver based on the TFM model	Fullmer and Hrenya (2018)
	OpenFOAM® (OS) twoPhaseEulerFoam solver		Multiphase (fluid-fluid) solver with the option of KTGF for estimating the stresses in the solid phase	Passalacqua and Fox (2011)
CFD-DEM	PFC3D™ (CO)	OpenFOAM® (OS)	PFC3D code for DEM coupled with OpenFOAM and multi-physics COMSOL for fluid flow	Zhou et al. (2019)
		COMSOL® (CO)		Guo and Yu (2017)
	LIGGGHTS® (OS)	OpenFOAM® (OS)	LIGGGHTS (developed from LAAMPS) for DEM coupled with OpenFOAM	Shan and Zhao (2014)
	EDEM (CO)	ANSYS Fluent ® (CO)	EDEM software for DEM coupled with OpenFOAM and ANSYS Fluent for fluid flow	Sousani et al. (2019)
	MFiX-DEM® (OS)		Multi-phase MFiX code with DEM capability for the particulate solid phase	Bakshi et al. (2018)
	DPMFoam		OpenFOAM solver for multiphase Eulerian-Lagrangian flows	Fernandes et al. (2018)
	ESyS ® (OS)	OpenFOAM® (OS)	DEM solver (ESyS and YADE) combined with CFD solver OpenFOAM	Zhao et al. (2017)
	YADE ® (OS)	OpenFOAM® (OS)		Chen et al. (2011)
SPH	LOQUAT (OS)		Open-source software for SPH in geotechnical applications	Peng et al. (2019)

In particulate flow modelling, the common practice is to link two computational packages, one for simulating the fluid phase and the other for simulating the solid phase. The reason for this is mainly because modelling tools are well-established for simulating the relevant physics of each phase. This is most effective in Eulerian-Lagrangian methods such as the coupling of CFD packages (e.g., OpenFOAM® and ANSYS Fluent®) with DEM packages (PFC3D™, EDEM™, and LIGGGHTS®). Alternatively, a single computational package can be used for simulating both the fluid and solid phases such as MFiX® software. This is more common in the cases where the fluid phase and the solid phase receive the same numerical treatment (e.g., Eulerian-Eulerian or Lagrangian-Lagrangian). The summary provided in Table 2.3 includes the available packages with respect to the numerical method, the type of the software, whether open source or commercial, and the relevant literature to each package. As can be seen from the summary, the CFD-DEM approach has the largest number of available modelling tools compared to the Two-Fluid Eulerian model and SPH Lagrangian model. The reason for this is related to the rapid development taking place in the fields of discrete element modelling and computational fluid dynamics, while development is receding on the side of the Two-Fluid Model and the Lagrangian models are still relatively new to the development compared to the other two methods.

2.6 Working across scales

Among the obstacles in particulate flow modelling to geotechnical problems is the issue of scale. Some of the models such as the Two-Fluid Model are less computationally expensive. However, the particle-fluid interaction in this sort of simulation is not resolved. Therefore, there is always a compromise between the level of detail that computations can capture and the computational cost. For example, the CFD-DEM modelling provides an accurate description of the interparticle and fluid-particle interactions that can be valuable to understand the mechanics of geotechnical problems like internal erosion and cavity evolution. In literature, it is common that the computational codes are verified using a benchmark problem or well-established experimental results. Nonetheless, following the verification phase, the modelling is often applied to a problem at a laboratory bench scale or smaller. Indeed, in these studies, it is pointed out that the computational capacity does not allow for large scale computations. From the engineering perspective, this kind of simulations does not aid the design of new structures or assess the risk to existing ones.

A few attempts have been carried out to overcome the high computational cost through upscaled models or multi-level modelling framework (Sakai and Koshizuka, 2009; van der

Hoef et al., 2006; Zhao, 2017). The upscaling process typically involves using larger elements (e.g., discrete element particles) that are relatable to the original and smaller system through certain relations. This can dramatically help reduce the computational cost of simulating large systems such as embankments since the computational load is assigned to significantly a smaller number of particles. However, it is important to note that using larger elements, such as large parcels of discrete element particles, comes at the cost of losing access to information pertaining to fine particles in the system. This can be observed in some problems such as landslide, where the front propagation of the landslide is mostly governed by the small particles in the landslide. It is then up to the researcher or engineer to decide whether upscaling the system is feasible in terms of the lost information or not. Therefore, it is important for practitioners and researchers to have a good understanding of the upscaling techniques to facilitate making such a decision. In this section, we review three upscaling techniques (i) multi-level closure system, (ii) coarse-grain model (parcelling), and (iii) hybrid Eulerian-Lagrangian approach.

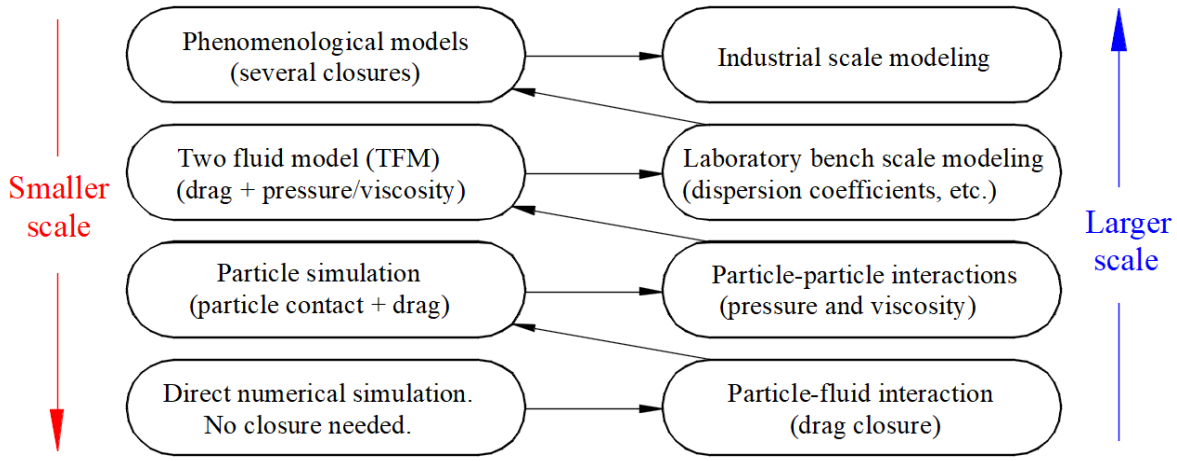

Figure 2.13. Multi-scale modelling strategy (after van der Hoef et al. (2006))

2.6.1 Multi-level modelling strategy

Using a multi-level modelling strategy was presented by van der Hoef et al. (2006), van der Hoef et al. (2008), and Deen et al. (2007). This strategy depends on obtaining closure models from smaller and more accurate models that can later be applied to larger and less

computationally expensive models. As can be seen in Figure 2.13, the base of the hierarchy is direct numerical simulation which is the most computationally expensive and accurate method. In fact, this technique is not novel to particulate flow modelling in general. For example, in CFD-DEM or LBM-DEM methods, the fluid-particle interaction forces are not resolved for each particle, rather averaged over the cell volume. Thus, drag closures from experimental or direct numerical simulations are often implemented to account for such forces in the simulations. Reflecting back on multi-scale modelling strategy, the same concept holds valid for larger scale problems.

This modelling strategy, to our knowledge, has not been applied to any geotechnical engineering applications. This is mainly because the model was proposed for fluidized beds, specifically gas-solid simulations. Nonetheless, this concept is quite common in civil and geotechnical engineering and can be seen in design charts and tables obtained from more intricate and more computationally expensive simulations. Thus, adopting some high-fidelity calculations to obtain closures or constitutive relations for problems at a larger scale may be useful to geotechnical problems. Indeed, to do that, extensive computational resources should be employed. However, conducting such highly expensive simulations can provide a better understanding of the mechanics behind many geotechnical problems and help create more robust constitutive relations.

2.6.2 Coarse-grained modelling

In discrete element modelling, it is common to make use of larger grains or parcels of particles to reduce the computational load. Such larger grains are often resembled by clumps of soils or larger elements that not only reduce the computational load but also help make the simulation results more realistic. In particulate flow modelling, however, the use of larger grains becomes more complex as the upscaling or parcelling should conserve the fluid-particle interaction forces in addition to the interparticle forces which is only considered in DEM. The behaviour of lumped particles can vary significantly from the original system of smaller particles due to the different effects of forces on smaller particles. The same scenario is to be expected when performing particulate flow modelling as the fluid forces are expected to mobilize fine particles easily compared to larger ones. This becomes critical when conducting certain simulations such as suffusion because the priority is to capture the motion of fine particles and their fate within larger pores. For more dynamic applications such as debris flow, it might be useful to adopt using larger particles.

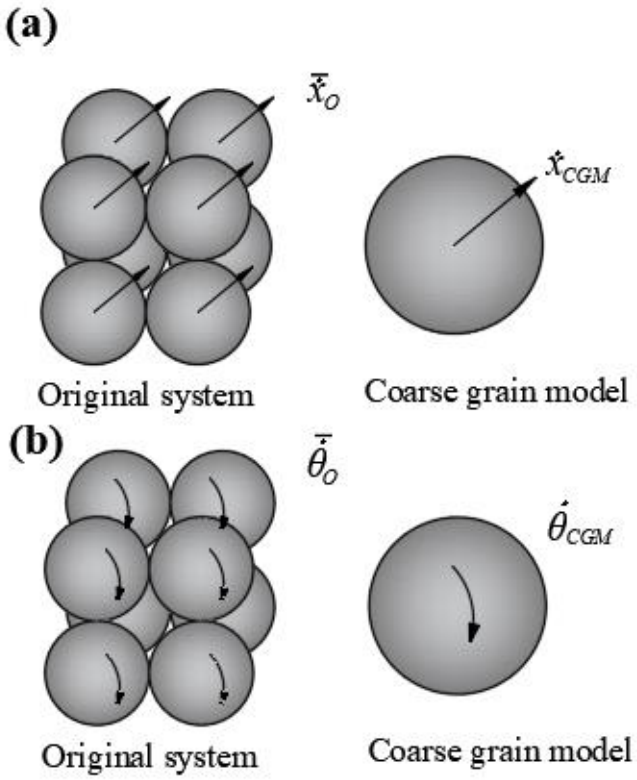

Figure 2.14.A schematic of the conservation of (a) translational and (b) rotational motion of the upscaled particles compared to the original set of particles.

Sakai and Koshizuka (2009) proposed a model for upscaled computations of coupled computational fluid dynamics and discrete element modelling. The criteria behind their model involve preserving the same response of the large (upscaled) particle compared to the original smaller ones to the interparticle forces and fluid-particle interaction forces. As shown Figure 2.14, the model is constructed such that the translational and rotational motion of the large particles are equivalent to those of the original set of smaller particles. The drivers of the motion can be interparticle forces, fluid-particle interaction forces, or any other external forces. For spherical particles, an upscaled particle of radius l larger than the original particles will have a volume that is l^3. Thus, to preserve the same response of translational and rotational motion the two systems are related as (Sakai and Koshizuka, 2009):

$$\frac{1}{2}m_{cg}\dot{\boldsymbol{x}}_{cg}^2 + \frac{1}{2}I_{cg}\,\dot{\theta}_{cg}^2 = l^3\left(\frac{1}{2}m_o\bar{\dot{\boldsymbol{x}}}_o^2 + \frac{1}{2}I_o\bar{\dot{\theta}}_o^2\right) \tag{2.35}$$

$$\ddot{\theta}_{cg} = \frac{T_{cg}}{I_{cg}} = \frac{\boldsymbol{r}_{cg} \times F_{cg}}{I_{cg}} = \frac{l\boldsymbol{r}_o \times l^3 F_o}{l^5 I_o} = \frac{1}{l}\ddot{\bar{\theta}}_o \tag{2.36}$$

where m, $\boldsymbol{x}$, I, θ, and l are the particle mass, position vector, moment of inertia, angular velocity, and the radius ratio between the coarse grain and the small grain, respectively. The subscripts cg and o refer to the coarse grain system and the original system, respectively. In a similar fashion, the relations between the normal and tangential contact forces as well as drag forces are derived based on the volume upscaling ratio l^3.

The results of the coarse grain model were compared to the experimental results of three-dimensional plug flow in a horizontal pipe of Konrad and Davidson (1984). The coarse grain model showed good agreement with the experimental results indicating the model's capability of reproducing the same particle behaviour of smaller particles. However, although that Sakai and Koshizuka (2009) point out that the model significantly reduces the computational cost, the speedup of the model was not explicitly stated. It is notable that this model was developed for gas-solid type flows. Nonetheless, it should be applicable to combined liquid-solid flows. From a geotechnical perspective, although particle parcelling for DEM calculations in particulate flows is quite common, this upscaling technique is yet to be applied in geotechnical applications.

2.6.3 Hybrid Eulerian-Lagrangian models

The pure continuum models, such as the TFM, are by far the most computationally feasible compared to discrete models. The downside of using such models is that they do not provide access to some interstitial information such as the resolved motion of solid particles or the fluid in the vicinity. However, in most cases, such accuracy is only needed locally. This can be seen in many geotechnical applications, for instance, in debris flow the front position and destructive energy are of more interest than other regions, same for piping in earth dams where the detailed flow characteristics around the eroded paths are more important to obtain than other regions. Thus, a smart numerical scheme that combines the accurate discrete element and computational fluid dynamics models along with continuum modelling can help reduce the computational cost of the model and direct the accuracy to certain subdomains of interest.

Hybrid Eulerian-Eulerian and Eulerian-Lagrangian models have been gaining attention recently because of their potential to allocate the computational load to specific subdomains. Such models typically utilize the TFM and DEM-CFD model interchangeably such that the overall execution time of the model is reduced. The model proposed by Hirche et al. (2019) is

an example of such computations. In this model, the authors introduce so-called pseudo Lagrangian particles that are included in the overall motion tracking but not in the DEM computations for collision and contact (Figure 2.15). Through the use of these particles, the domain can be tuned to use only a portion of the Lagrangian particles for the coupled DEM-CFD calculations while the rest of the pseudo particles are shifted into Eulerian-Eulerian computations.

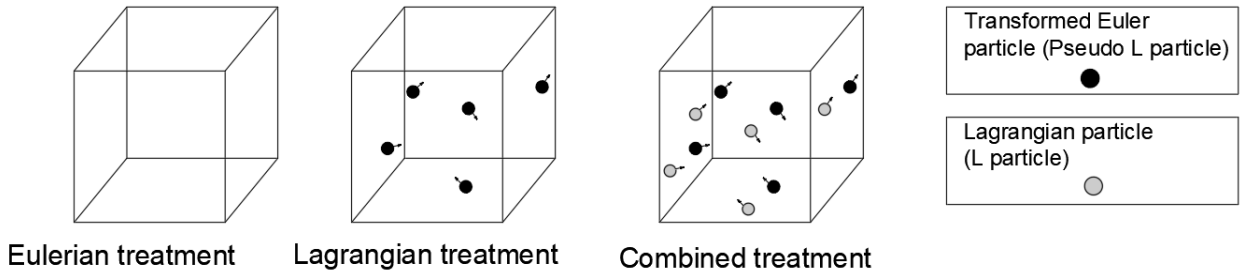

Figure 2.15. A schematic showing the computational framework of combined Eulerian-Eulerian and Eulerian-Lagrangian approaches.

This model was used to simulate gas-solid flow in fluidized beds and verified by comparison with experimental data from Link et al. (2008). The model speedup could be doubled using a pseudo particle ratio of 50%, compared to seven-fold speedup when using a purely Eulerian approach. Other active attempts are being carried out to develop a robust hybrid model such as the Hybrid MFiX solver (MFiX). Indeed, performing computations for real-scale systems requires more speedup than what is provided by this model. In addition, the development in hybrid models, to our knowledge, does not allow for a selective allocation of the computational load on a meaningful physical basis. In other words, a smarter model that can locally direct the precession and computational loads is yet to be developed.

2.7 Outstanding challenges of particulate flow modelling in geotechnical engineering

Particulate flow modelling can provide valuable data on several geotechnical applications that cannot be obtained through conventional methods or experiments. The main advantage lies in its ability to capture both microscale and macroscale mechanics of the system of the modelled systems. However, as pointed before, the computational cost of performing particulate flow computations on a scale that can serve the design and assessment processes is challenging. In addition to the computational cost, models that can describe complex systems and actual

boundary conditions still need to be developed. For example, most of the available literature on particulate modelling in geotechnical engineering use relatively small systems to test the developed models (e.g., Guo and Yu (2017); Shan and Zhao (2014); Zhao et al. (2017), and Cui et al. (2014)). These small models often contain a small number of particles that can be handled with the available computational resources; moreover, simple boundary conditions. The two most common boundary conditions are periodic boundary conditions and wall boundary conditions. In real-life applications, systems might have boundary conditions of loading, unloading, water draining, phase change, etc. This complexity is not often encountered in chemical engineering applications such as fluidized bed, for which most of the particulate flow models were developed. Thus, the geotechnical community needs to carry out its own development to tailor models that resemble tackled problems more accurately.

Another outstanding challenge is to develop a multi-resolution framework for particulate flow modelling, such that different spatial resolutions can be included without compromising the accuracy of the simulation. The previously presented hybrid Eulerian-Eulerian Eulerian-Lagrangian approach comes close to achieve this goal through tuning the pseudo Lagrangian particles. However, during the simulation process the resolution can only be globally set for the entire domain rather than incorporating multi-resolution for subdomains. In a recent study, Khayyer et al. (2019) proposed an adaptive multi-resolution MPS-based framework to simulate Fluid Structure Interaction (FSI) for elastic structures. The advantage of incorporating different spatial resolutions was found to help enhancing the efficiency of simulation while maintaining the intricacy of high-resolution simulations, as needed. As for particulate flow applications in geotechnical engineering, including robust multi-scale resolution can help enhance the simulation process for many systems that do not require refined spatial resolution for the entire domain, yet gives the advantage of accessing the information related to the micromechanics of the system. This can be particularly useful for modelling localized phenomena such as internal erosion.

More challenges involve dynamic processes related to soils and rocks. In contrast to other applications such as pneumatic conveying and spouted beds where solid particles are mainly mono-sized, soil particle sizes in natural soils can vary significantly, even in a small sample. Along with variable particle size distribution, the cohesion between particles, cementing, and fragmentation of a single soil clump can further complicate the dynamics of particulate flow to a great extent. To tackle these issues, constitutive models that account for water existence, whether static or dynamic, need to be developed.

2.8 Summary and conclusions

In this work, a comprehensive summary of the development and key challenges of particulate flow modelling were presented. The applicability and relevance of the existing particulate flow models to geotechnical applications were discussed. The key issues and challenges identified are:

1. Particulate flow modelling, despite its complexity, is needed to gain a better understanding of several geotechnical problems such as failure mechanics of earth structures subjected to high hydrodynamic forces and debris flow.
2. In the geotechnical field, such modelling is still underdeveloped and the existing literature mainly addresses small and elementary systems rather than actual structures (e.g., earth dams)
3. The high computational cost of conducting coupled solid-fluid modelling and the complexity of boundary conditions in real-life applications are the major obstacles to develop computationally feasible large-scale models and to develop constitutive models.
4. Robust upscaling techniques and multidisciplinary approaches are needed for closing the gap in this area of research and developing models directed for geotechnical engineers and researchers.

Preface to chapter 3

The overwhelming computational cost of performing coupled particulate flow modeling remains one of the most outstanding challenges with performing such analysis on proper scale. Such scale can be as small as a bench scale experiment, yet extensive computational resources are needed to generate useful data. As the main source of this computational cost is the discrete treatment of every solid particle, it would then be of great advantage if such simulation can be carried out in a continuum setting using conventional mesh-based methods. This does not only reduce the computational cost within a given space, but also opens a way for model scalability. In this chapter, we explore the potential of the Two-Fluid Model to simulate sand erosion around a pressurized leaking pipe. Initially, model validation is conducted by comparing the model to available analytical solutions and experimental data. Following model validation, a parametric study was conducted to examine the effect of crack configuration and sand polydispersity.

Chapter 3

Continuum-Based Approach to Model Particulate Soil-Water Interaction: Model Validation and Insights on Internal Erosion†

Abstract

Resolving the interaction between soil and water is critical to understanding a wide range of geotechnical applications. In cases when hydrodynamic forces are dominant and soil fluidization is expected, it is necessary to account for the microscale interactions between soil and water. Some of the existing models such as coupled Computational Fluid Dynamics-Discrete Element Method (CFD-DEM) can capture microscale interactions quite accurately. However, it is often computationally expensive and cannot be easily applied at a scale that would aid the design process. Contrastingly, continuum-based models such as the Two-Fluid Model (TFM) can be a computationally feasible and scalable alternative. In this study, we explore the potential of the TFM to simulate soil-water interactions in various flow conditions. The model was first validated by simulating an experiment involving upward water flow in a sand column and comparing the calculated results with analytical solution based on Darcy's equation as well as predict the hydraulic instability of the analyzed flow. The model was then used to simulate the internal erosion of soil around a leaking pipe. The numerical results show decent agreement with the experimental data in terms of excess pore water pressure, fluidization patterns, and physical deformations in violent flow regimes. Moreover, detailed soil characteristics such as particle size distribution could be implemented which was previously considered a shortcoming of the model. Overall, the model's performance indicates that TFM is a viable tool for the simulation of particulate soil-water mixtures.

Keywords: Pipe leakage, Two-fluid model; Soil fluidization; Internal erosion; Numerical analysis; Continuum modeling

† A version of this manuscript has been published in *Processes* journal (2021).

3.1 Introduction

The interaction between soil and water is fundamental to understanding the mechanical behavior of soils. The state of stresses in the soil depends, to a great extent, on the interaction between the soil particles and the water found within pores (e.g., seepage and consolidation). In civil and geotechnical engineering, the relationships governing water-soil interaction in static and quasi-static cases are well established. A key assumption adopted in the majority of these relations is that no significant deformations occur in the soil matrix such that Darcy flow is valid. However, in more dynamic cases when hydrodynamic forces become dominant (e.g., debris flow and internal fluidization) the soil integrity is most likely to be compromised and can no longer be characterized by conventional parameters such as hydraulic conductivity or permeability. In such cases, the need to carry out the analysis at the microscale level emerges, where accounting for the particulate nature of soil as well as the interaction forces between soil and water becomes necessary.

One of the examples of these dynamic interactions, which is the main focus of this study, is the internal fluidization and erosion in the soil around leaking water mains. Water leakage under pressure can lead to the erosion of the surrounding soil and decrease in effective stresses. This, in turn, can result in soil softening threatening the water main and the nearby structures (Ali and Choi, 2019). Characterizing and predicting internal fluidization of soils can be particularly challenging considering the complex underlying physics that govern fluidization (Cui et al., 2014). These physics involve the interaction mechanisms, momentum transfer, and force balance between soil particles and water, or other fluids (Zhu et al., 2007). Micromechanical analysis has been widely adopted in fluidized beds, where fluidization is induced by gas or liquid injection through an opening (Deen et al., 2007; Ostermeier et al., 2019; Tsuji et al., 1993). In ground engineering and earth structure, with a less controlled environment than that of fluidized beds, the analysis becomes more complex as the properties of soils such as cohesion and particle size variability come to play a major role (Suzuki et al., 2007; Zou et al., 2020). Furthermore, if cyclic pressure is to be considered (e.g., hydraulic transient), more complex interactions are to be expected such as soil infiltration into the pipe accompanied by wash-out of soil particles in the vicinity of leakage.

Analyzing internal fluidization requires access to information related to the micromechanics of the system and resolving the particle-fluid interaction. Several attempts have been made to investigate these interactions experimentally (Alsaydalani, 2010b; Alsaydalani and Clayton, 2014; van Zyl et al., 2013), numerically (Cui et al., 2014; Tang et al.,

2017b), and using simplified analytical models (Montella et al., 2016; Vardoulakis et al., 1996). Given the limited flexibility of experimental and analytical solutions in obtaining microscale information and dealing with a wide range of initial and boundary conditions, numerical analysis is mostly adopted. The two most common approaches are pure continuum analysis and coupled discrete-continuum analysis. In pure continuum analysis, the solid and fluid phases are treated as a single continuum with collective properties that account for the presence of both phases (i.e., a mixture). Alternatively, the two phases are interpreted as inter-penetrating continua each representing a single phase such as the case of the Two-Fluid Model (TFM) (Anderson and Jackson, 1967a; Gidaspow, 1994; Kuipers et al., 1992). On the other hand, in coupled discrete-continuum analysis the solid phase receives a discrete Lagrangian treatment while the fluid phase is considered as a continuum. Examples for this type of analysis involve the coupled Discrete Element Model-Computational Fluid Dynamics (DEM-CFD) (Tsuji et al., 1992) and Discrete Element Model-Lattice Boltzmann Model (DEM-LBM) (Cook et al., 2004).

Although utilizing discrete methods such as DEM-CFD allows for a relatively more accurate representation of the soil-water coupling compared to continuum-based approaches, it comes at a high computational cost (Ibrahim and Meguid, 2020). On the contrary, coupled continuum modeling such as the TFM is much more computationally feasible with a code execution time of approximately 7% of that of CFD-DEM (Hirche et al., 2019). Thus, it allows for analyzing larger and more realistic systems and producing results that can be incorporated into conventional analysis needed for design and risk assessment. The model's computational feasibility arises not only from its small execution time compared to discrete models but also from the flexibility in mesh refining that allows for directing the computational load to certain areas in the domain. This is particularly useful when dealing with large-scale systems where the mesh refinement might be required only locally. The application of the TFM, however, has so far been limited to a few cases in simulating sediment transport and riverbed morphology (Chauchat et al., 2017; Cheng et al., 2017). Rigorous testing for the model's potential to capture the basic characteristics of soil-water interactions is still needed.

In this study, we aim to explore the potential of the continuum-based two-fluid model to simulate soil-water interaction in a variety of flow and soil conditions. Model validation is first performed to build confidence in the model's performance by comparing the results with analytical solutions. Afterward, we investigate the model's ability to simulate internal erosion due to an upward water jet (i.e., leaking pressure pipe). Different aspects such as the evolution of excess pore water pressure, fluidized zones, and the implementation of particle size

distribution are then discussed.

3.2 Numerical Analysis

The soil-water mixture is represented as interpenetrating continua of fluid and solids, each characterized by volume fractions of ε_f and ε_s for fluid and solids, respectively. To account for variations in soil particle sizes and subsequent interactions with the fluid phase, the solid phase can be further divided into a number (n) of sub-phases such that:

$$\varepsilon_f + \sum_{i=1}^{n} \varepsilon_{si} = 1 \qquad 3.1)$$

The governing equations for this mixture consist of the volume-average continuity and momentum equations proposed by Anderson and Jackson (1967a). The volume-averaging of the governing equations for the solid phase results in a fluid-like resemblance of the solid phase, hence the model is also known as the Two-Fluid Model (TFM). With the assumption that there are no mass flux sources or sinks, the locally averaged continuity equations are expressed as:

$$\frac{\partial}{\partial t}\left(\varepsilon_f \rho_f\right) + \nabla \cdot \left(\varepsilon_f \rho_f \mathrm{v}_f\right) = 0 \qquad (3.2)$$

$$\frac{\partial}{\partial t}\left(\varepsilon_{si} \rho_{si}\right) + \nabla \cdot \left(\varepsilon_{si} \rho_{si} \mathrm{v}_{si}\right) = 0 \qquad (3.3)$$

where ε_f is the volume fraction of the fluid phase (e.g., porosity of saturated soil), ρ_f and ρ_{si} are the density of the fluid and i^{th} solid phases, respectively, ε_{si} is the volume fraction of the i^{th} solid phase, v_f and v_{si} are the velocities of the fluid phase and the i^{th} solid phase, respectively. For the fluid phase, the conservation of linear momentum appears in a similar form to that of a single-phase flow averaged by the fluid volume fraction. However, the outstanding difference is the inclusion of the particle-fluid interaction forces that accounts for the momentum transfer between the solid phase(s) and the fluid phase. The locally-averaged momentum equation for the fluid phase is given as:

$$\frac{\partial}{\partial t}\left(\varepsilon_f \rho_f \mathrm{v}_f\right) + \nabla \cdot \left(\varepsilon_f \rho_f \mathrm{v}_f \mathrm{v}_f\right) = -\nabla p_f + \nabla \cdot \tau_f + \varepsilon_f \rho_f \mathrm{g} - \sum_{i=1}^{n} f_{fs} \qquad (3.4)$$

where p_f is the fluid pressure, τ_f is the shear stress tensor of the fluid, g is the gravitational

acceleration, and f_{fs} is the particle-fluid interaction force. The interaction forces can include a wide range of different forces depending on the scope of simulation (Ibrahim and Meguid, 2020). For the interaction between soil and water in geotechnical engineering applications, buoyancy and drag forces are considered sufficient to describe the interaction forces. The particle-fluid interaction forces are expressed as:

$$f_{fs} = -\varepsilon_{si}\nabla p_f - F_d\left(\mathrm{v}_{si} - \mathrm{v}_f\right) \tag{3.5}$$

where F_d is the momentum transfer coefficient. The first term on the right-hand side of equation (3.5) denotes the buoyancy force, while the second term is the drag force. Different expressions have been reported for the momentum transfer coefficient (Ergun, 1952; Syamlal and Gidaspow, 1985). Here, we adopt the drag expression proposed by Syamlal and Obrien (1988):

$$F_d = \frac{3\varepsilon_{si}\varepsilon_f\rho_f}{4v_{rs}^2 d_{pi}} C_d\left(\frac{\mathrm{R}_{es}}{v_{rs}}\right)\left|\mathrm{v}_{si} - \mathrm{v}_f\right| \quad ; \tag{3.6}$$

where d_{pi} is the average particle diameter of the i^{th} solid phase, R_{es} is the particle Reynold's number of the i^{th} solid phase, v_{rs} is the terminal velocity of the i^{th} solid phase as given by Garside and Aldibouni (1977), and C_d is the drag coefficient (DallaValle, 1948):

$$C_d = \left(0.63 + \frac{4.8}{\sqrt{\mathrm{R}_{es}}}\right)^2 \tag{3.7}$$

The fluid shear stress tensor, under the assumption of a Newtonian fluid, is given as:

$$\tau_f = 2\varepsilon_f\mu_f\bar{\bar{D}}_f + \varepsilon_f\lambda_f\mathrm{tr}\left(\bar{\bar{D}}_f\right)\mathrm{I}\,; \tag{3.8}$$

where μ_f and λ_f are the fluid's shear and bulk viscosity, respectively, I is the identity matrix, and $\bar{\bar{D}}_f$ is the strain rate tensor such that:

$$\bar{\bar{D}}_f = \frac{1}{2}\left(\nabla\mathrm{v}_f + (\nabla\mathrm{v}_f)^{\mathrm{T}}\right) \tag{3.9}$$

Similar to the description of fluid motion, the momentum equation of the solid phase is given as:

$$\frac{\partial}{\partial t}\left(\varepsilon_s \rho_s \mathrm{v}_s\right)+\nabla\cdot\left(\varepsilon_s \rho_s \mathrm{v}_s \mathrm{v}_s\right)=-\nabla p_s+\nabla\cdot\tau_s+\varepsilon_s \rho_s \mathrm{g}+\sum_{i=1}^{n} f_{fs} \tag{3.10}$$

where p_s is the equivalent solid pressure resulting from particle contact and collision, and τ_s is the shear stress tensor of the solid phase. It is important to note that the last term on the right-hand side of equation (3.10) is essentially equal to that in equation (3.4) in magnitude and opposite in direction such that Newton's third law of motion is not violated.

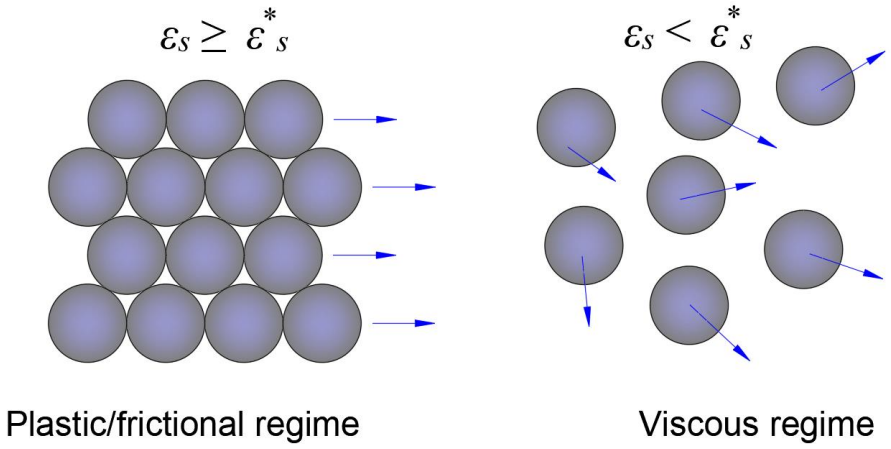

Figure 3.1.A schematic illustration of the plastic/frictional and viscous flow regimes in the solid phase.

The fluid-like representation of the solid phase in equation (3.10) requires equivalent values for the pressure field, shear viscosity, and bulk viscosity similar to those of the fluid phase. However, obtaining these equivalent values is not as straightforward considering the inherently discrete (particulate) nature of the solid phase. Therefore, closures are needed to express the behavior of the solid phase (e.g., contact pressure and collision) in terms of continuous pressure and viscosity. One of the most adopted approaches to achieve this is the Kinetic Theory of Granular Flow (KTGF) (Ding and Cidaspow, 1990; Gidaspow, 1994; Lun et al., 1984). Before incorporating the KTFG to obtain the needed closures, we first need to identify two main granular flow regimes (i) plastic or frictional flow and (ii) viscous flow (Figure 3.1). In the plastic flow regime, particle contact forces are dominant which is suitable for capturing the

behavior of static or quasi-static systems where no significant deformations take place. In the viscous flow regime solid particles are considered to be in a state of fluidization, that is, particles are no longer in contact, and their movement is only affected by collisions and interaction between the particles and the surrounding fluid.

In contrast to Discrete Element Modeling, the particle contact cannot be identified explicitly due to the averaging technique adopted in continuum modeling. Thus, there needs to be a porosity threshold that separates the frictional regime from the viscous regime. This threshold is set to be slightly less than the initial packing volume fraction, ε_s^*, at which the granular assembly is assumed to be in a static condition. For volume fractions greater than or equal to ε_s^*, the plastic regime is assumed to be in effect (marked with the superscript p), otherwise the viscous solid regime is valid (marked with the superscript v). Under these conditions, the shear stress tensor of the solid phase is given as:

$$\tau_{si}^{v} = 2\mu_{si}^{v}\bar{\bar{D}}_{si} + \lambda_{si}^{v}\mathrm{tr}\left(\bar{\bar{D}}_{si}\right)\mathrm{I} \tag{3.11}$$

$$\tau_{s1}^{p} = 2\mu_{s1}^{p}\bar{\bar{D}}_{s1} \tag{3.12}$$

where μ_{si}^{v} and λ_{si}^{v} are the shear and bulk viscosities of the i^{th} solid phase in a viscous flow regime, $\bar{\bar{D}}_{si} = 1/2\left[\nabla \mathrm{v}_{si} + (\nabla \mathrm{v}_{si})^{\mathrm{T}}\right]$ is the strain rate tensor of the i^{th} solid phase, and μ_{s1}^{p} is the shear viscosity of the first solid phase in plastic flow regime. A summary of the expressions for the pressure field, and shear and bulk viscosities is given in Table 3.2 following the formulation of Schaeffer (1987) and Jenike (1987). In Table 3.2 Θ denotes the granular temperature, $A = 10^{25}$, $n = 10$, ϕ is the angle of internal friction of the granular assembly, and $I_{2\left(\bar{\bar{D}}_s\right)}$ is the second invariant of the strain rate tensor. The evolution of the granular temperature is given as (Gidaspow, 1994):

$$\frac{3}{2}\frac{\partial}{\partial t}\sum_{i=1}^{n}\varepsilon_{si}\rho_{si}\Theta_i + \frac{3}{2}\nabla\cdot\sum_{i=1}^{n}\varepsilon_{si}\rho_{si}\Theta_i \mathrm{v}_{si} = \sum_{i=1}^{n}\left[\left(-p_s + \tau_s\right):\mathrm{v}_{si} - \nabla\cdot q_\Theta - \gamma_{\Theta i} + \phi_{fi} + \sum_{\substack{j=1 \\ j\neq i}}^{n}\phi_{ij}\right] \tag{3.13}$$

where $\gamma_{\Theta i}$ is the rate of granular energy dissipation due to particle collision, q_Θ granular

energy flux, ϕ_{fi} is the rate of energy transfer between the i^{th} solid phase and the fluid phase, and ϕ_{ij} is the rate of energy transfer between the i^{th} and j^{th} solid phases. In this research, the open-source code (MFiX) is used to carry out the numerical simulation incorporating the above governing equations. Additional details on the theoretical background and the numerical implementation can be found in Syamlal et al. (1993).

Table 3.1. The expressions for solid pressure, shear viscosity, and bulk viscosity of the solid phase after Jenike (1987) and Schaeffer (1987).

	Viscous regime	Plastic regime
p_s	$p_{si}^{v} = K_{1i}\varepsilon_{si}^{2}\Theta_i$	$p_{si}^{p} = A\varepsilon_{si}\left(\varepsilon_f^{*} - \varepsilon_f\right)^{n}$
μ_s	$\mu_{si}^{v} = K_{3i}\varepsilon_{si}\sqrt{\Theta_i}$	$\mu_{s1}^{p} = \dfrac{A\left(\varepsilon_f^{*} - \varepsilon_f\right)^{n}\sin(\phi)}{2\sqrt{I_{2(\bar{\bar{D}}_s)}}}$
λ_s	$\lambda_{si}^{v} = K_{2i}\varepsilon_{si}\sqrt{\Theta_i}$	-

3.3 Model validation

The utilization of continuum-based models to capture the micromechanics and hydrodynamic behavior of soil-water mixtures has been quite limited and rigorous validation of the model in the context of this study is, therefore, needed. Examples for the application of this approach include the work of Chauchat et al. (2017) and Cheng et al. (2018) on sediment transport and Tang et al. (2017b) on soil erosion due to upward injection. Despite the decent agreement reported by these studies with experimental observations, the model's ability to describe the basic soil-water interactions and transitions remains questionable. For instance, it is of great interest to test the model's ability to simulate simple seepage problems (e.g., Darcy flow) as well as the transition to hydraulic instability resulting from excessive pore water pressure.

The validation setup used in this study consists of a prismatic rectangular saturated sand column with a height of $H = 0.41$ m and width $b = 0.2$ m connected to a constant head tank that provides water at the bottom of the sample (Figure 3.2). The head difference between the water in the tank and the bottom of the sand column is h_w such that $h_w > H$. The pressure at

the top of the sand column is always set to atmospheric pressure to ensure that two-dimensional upward pressure is induced. A boundary condition of $v_s = 0$ is imposed in the direction normal to the base of the sand column to ensure that sand does not move out of the system (i.e., replicating the control screen at the bottom). The sand is assumed to consist of mono-dispersed spherical particles with a diameter of 1 mm. The simulation is carried out for different values of upstream pressure $p_u = \rho_w g h_w$ (applied pressure at the base of the sand column). A summary of the simulation parameters is provided in Table 3.2.

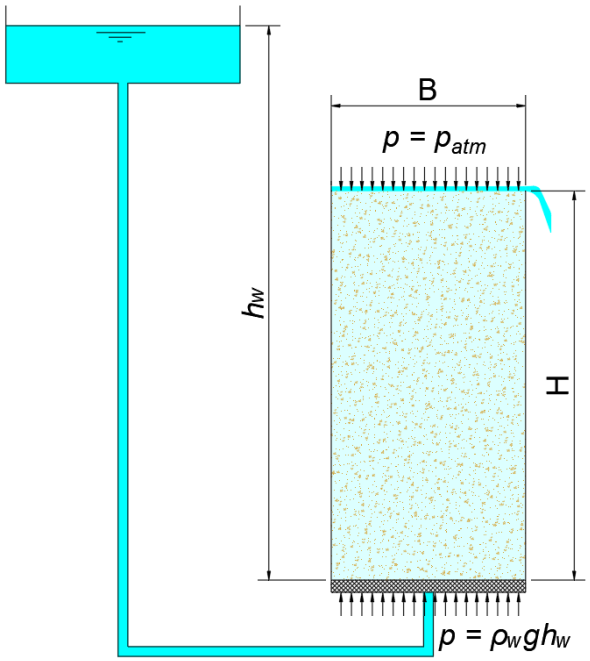

Figure 3.2. A schematic for the problem setup of Darcy flow simulation

Under low upstream pressure values (e.g., 5kPa), the soil matrix is expected to maintain its integrity and Darcy's law is assumed to be valid. The water steady-state velocity in the sand column velocity, v, is given as:

$$v = -\frac{k}{\mu_w}\nabla p_f \tag{3.14}$$

where k is the permeability of the sand and μ_w is the viscosity of water. As the water pressure gradient, ∇p_f, increases, the excess pore water pressure increases. At the point where the applied upstream pressure is equal to the total stress at the bottom (i.e., effective stress is zero), hydraulic instability will be initiated and the sand will start moving upward. The minimum

pressure to initiate fluidization, p_{inst}, can be expressed as:

$$p_{inst} = Hg\rho_w\left[\left(1-\varepsilon_f\right)G_s + \varepsilon_f\right] \tag{3.15}$$

where G_s is the specific gravity of the sand. For the parameters considered for the validation system, the minimum pressure to cause instability is approximately 8.2 kPa.

Table 3.2. Summary of simulation parameters for Darcy flow simulation

Column width (m)	Column height (m)	Fluid density (kg/m3)	Solids density (kg/m3)	Initial porosity [-]	Applied upstream pressure (kPa)
0.2	0.41	1000	2700	0.39	5, 5.5, 6, 6.5, 7 & 7.5

The results obtained for the case of steady-state water velocity for a range of upstream pressure values is shown in Figure 3.3. Water velocity is plotted along with values predicted from Darcy's equation using Hazen's and Kozeny-Carman's empirical formulas to calculate the permeability of sand. The velocity predictions from the two-fluid model show a good agreement with those from Darcy's equation. However, some slight deviation from Darcy's equation is noticed as the upstream approaches the limit of the fluidization pressure. The velocity values are further compared to the predictions from Ergun's equation (Ergun, 1952) to test if the cause of this deviation arises from nonlinearity in the relation between velocity and pressure. The comparison shows that the nonlinearity between velocity and pressure does not have a significant effect that the deviation can be attributed to. Nonetheless, the fact that the TFM-predicted velocities nearly fall on a straight line indicates that the model slightly overestimates the permeability of the sand. This is most likely to be a result of using mono-dispersed particles rather than including a realistic particle size distribution.

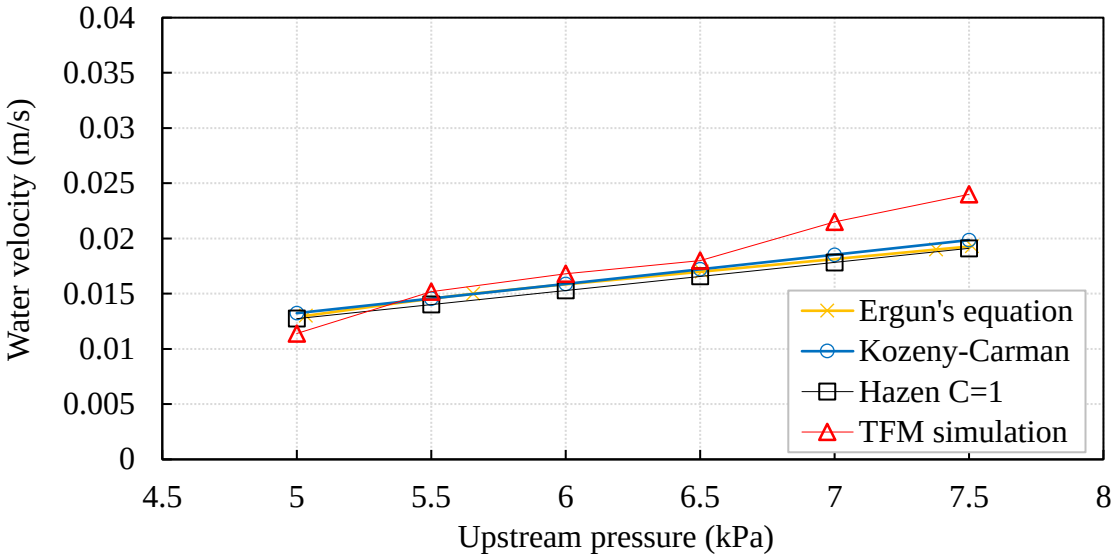

Figure 3.3. A comparison between the superficial velocity estimated by the TFM, Hazen's equation (C=1), and Kozeny-Carman equation.

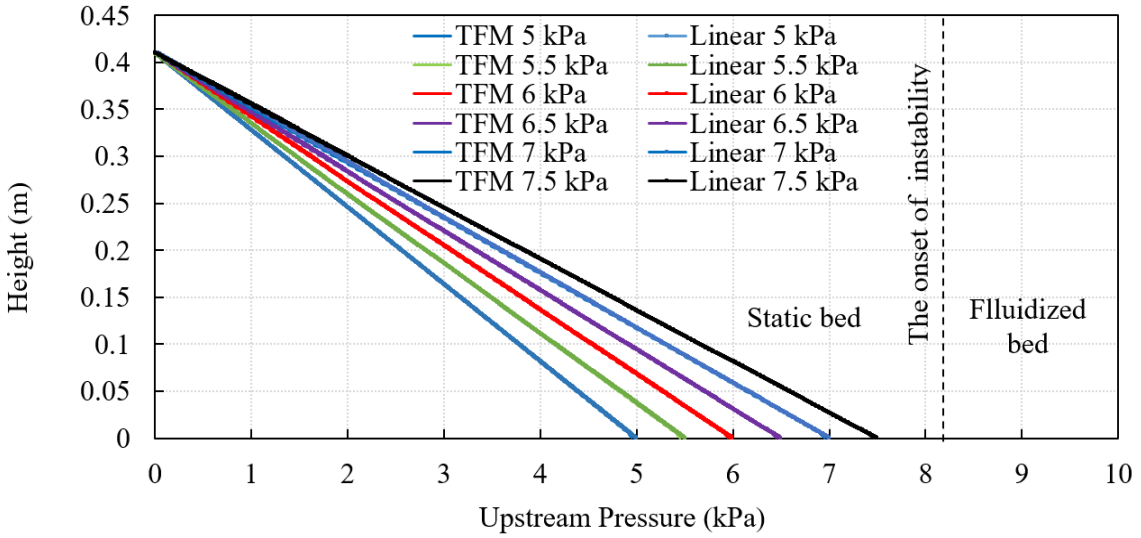

Figure 3.4. Pressure distribution along the centerline of the soil sample for upstream pressure values of 5, 5.5, 6, 6.5, 7 and 7.5 kPa.

At steady-state, the water pressure gradient should be constant, that is, the pressure distribution follows a straight line connecting the upstream pressure to zero at the top (atmospheric pressure). Figure 3.4 shows the pressure distribution from the simulation plotted along with linear pressure distribution. For all upstream pressure values, under the fluidization limit, the pressure distribution perfectly aligns with the linear pressure distribution. This can

be deduced from the momentum equation for the fluid phase (Equation (3.4)) by setting the temporal and spatial variations in velocity to zero and accounting only for the buoyancy in the interaction forces. Although the results shown in Figure 3.4 seem to be inherent to the model, it demonstrates the ability of the model to accurately calculate the interaction forces and detect the state of fluidization in terms of maintaining constant porosity.

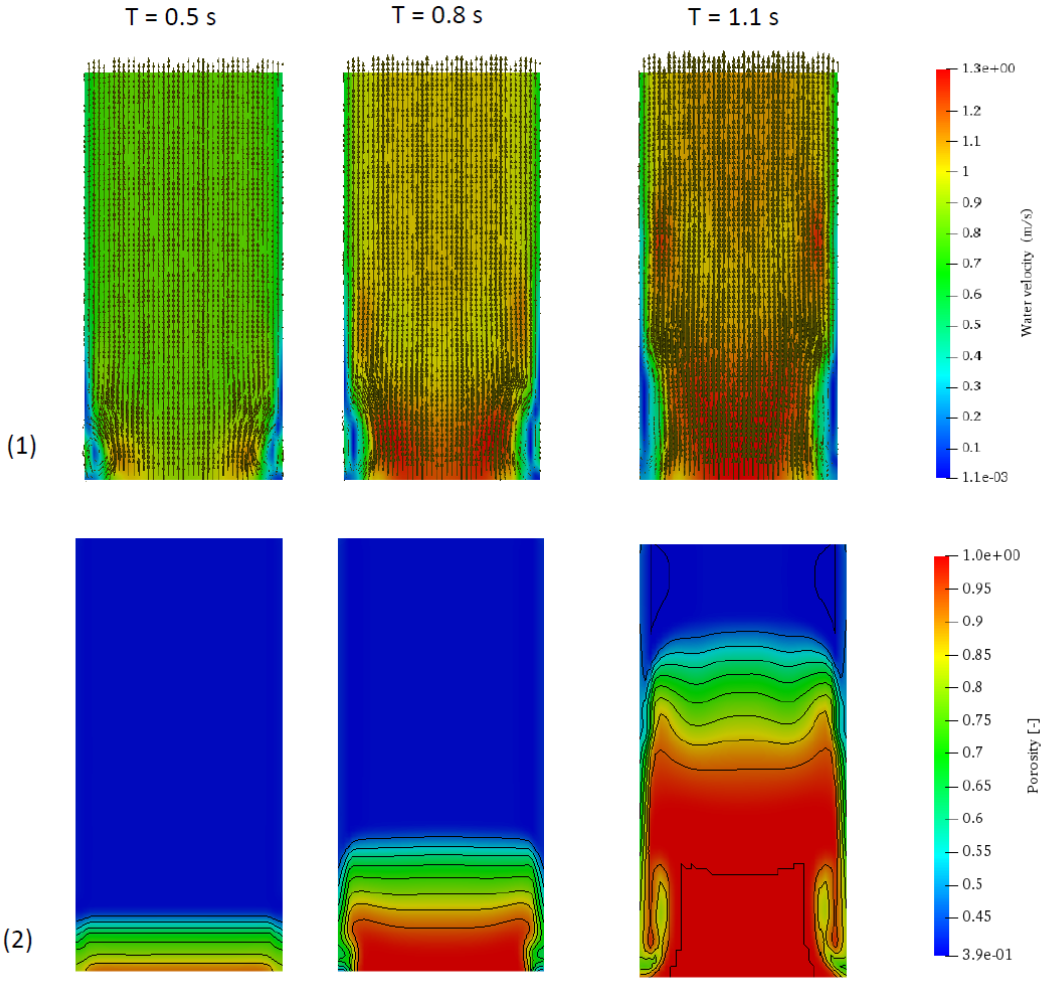

Figure 3.5. Evolution of (1) Water velocity and (2) porosity across the soil sample in the case of hydraulic instability (p_u = 8.2 kPa) at times 0.5, 0.8, and 1.1 seconds.

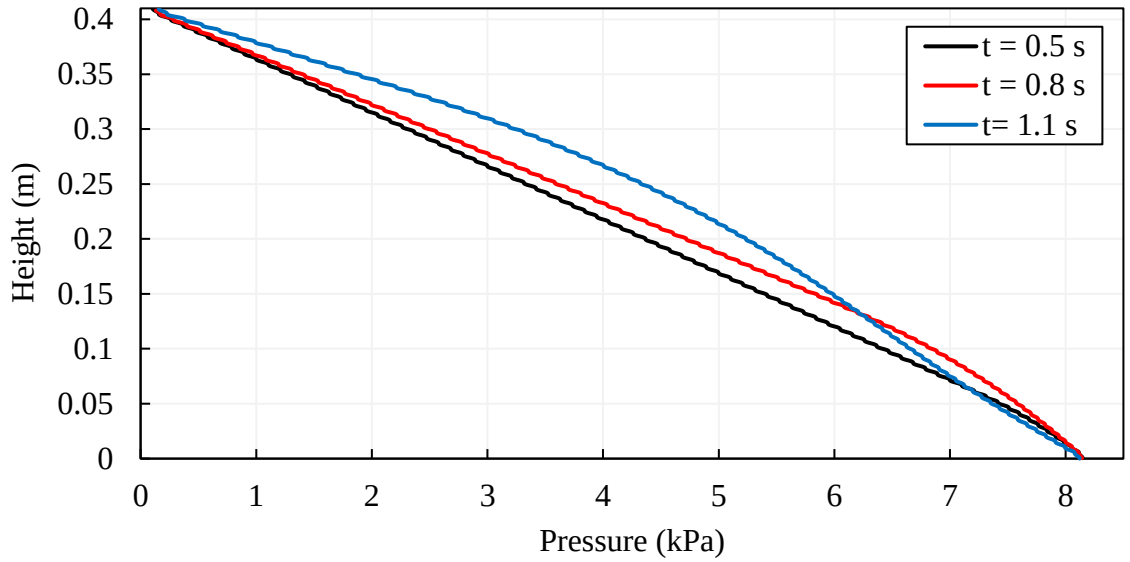

Figure 3.6. Pressure distribution along the centerline the soil sample in the case of hydraulic instability (p_u = 8.2 kPa) at times 0.5, 0.8 and 1.1 seconds.

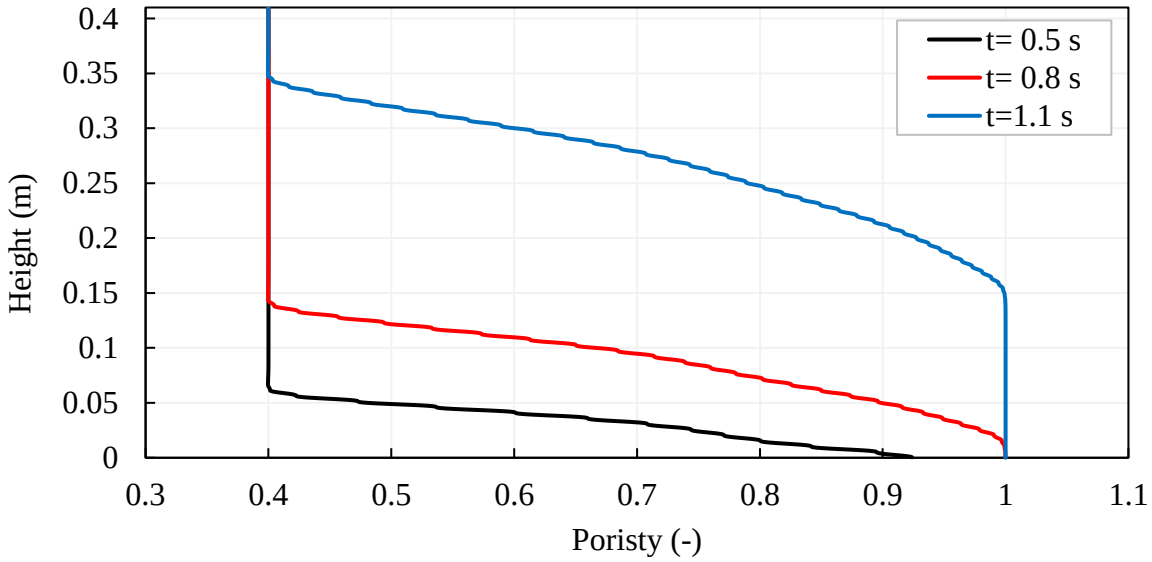

Figure 3.7. Porosity distribution along the centerline the soil sample in the case of hydraulic instability (p_u = 8.2 kPa) at times 0.5, 0.8 and 1.1 seconds.

When the upstream pressure is increased to 8.2 kPa, the water starts to push the sand upward as hydraulic instability is initiated. This could be seen through the simulation results in Figure 3.5 where a transient flow state is observed. The results show an initial uniform lifting

of the sand column base accompanied with an increase in water velocity, which is approximately constant in the purely water-filled region as the system approaches a pipe flow condition. As the water propagates, dead zones at the bottom right and left corners of the sand columns are observed, where water velocity is relatively low and traces of sand remain even after the water has moved to the top of the sand column. This is a result of the sharp inlet geometry as the streamlines of water will curve around the right and left edges creating local stagnation regions at both corners. The build-up of pressure and evolution of porosity are shown in Figure 3.6 and Figure 3.7. It can be observed that the pressure gradient increases significantly in the water-filled region compared to the regions where soil still exists. This aligns with the observations from the porosity plot (Figure 3.7), where the pressure distribution is linear where porosity equals 1, and transitions nonlinearly until the region where the soil porosity becomes the same as the initial porosity. Overall, the model demonstrates the ability to capture the fundamental flow characteristics of soil-water mixtures as well as flexibility in identifying and dealing with flow regime transition.

3.4 Simulation of internal soil erosion around leaking pipes

Internal soil fluidization and erosion can happen in the vicinity of leaking buried pipes due to local pressure increase and rapid water flow within the surrounding soil (Figure 3.8). When fluidized, the soil loses some or all of its shear strength (i.e., liquefied) due to the increase in pore water pressure. This can compromise the soil integrity, and strength and ultimately leads to softening, volume loss and the formation of sinkholes (Ali and Choi, 2019; Karoui et al., 2018). Approaching the problem of internal erosion around a leaking source is particularly challenging to detect since the compromised soil is not visible in contrast to backward erosion resulting from high exit gradients (Alsaydalani, 2010b). From a theoretical point of view, the problem poses further challenges to accurately determine the velocities and pressure in the vicinity of an orifice with exit blockage. Moreover, it is numerically and theoretically challenging to capture the transition between initial seepage flows and potential fluidization that may occur at high inlet pressure.

A few studies attempted to numerically tackle the problem of internal soil fluidization due to upward water jet using various methods such as the coupled Lattice Boltzmann Method-DEM (LBM-DEM) simulation (Cui et al., 2014; Tang et al., 2017a), continuum-based models (Tang et al., 2017b), or using simplified analytical techniques (Montella et al., 2016). A few issues, however, still need to be addressed to be able to practically incorporate these models in real-life problems. For example, in LBM-DEM simulations relatively small systems are often

adopted in order to avoid the high computational cost. For continuum-based modeling and semi-analytical models, the flexibility of the model to capture flow transitions with realistic boundary conditions as well as incorporating soil characteristics (e.g., particle size distribution) remains questionable.

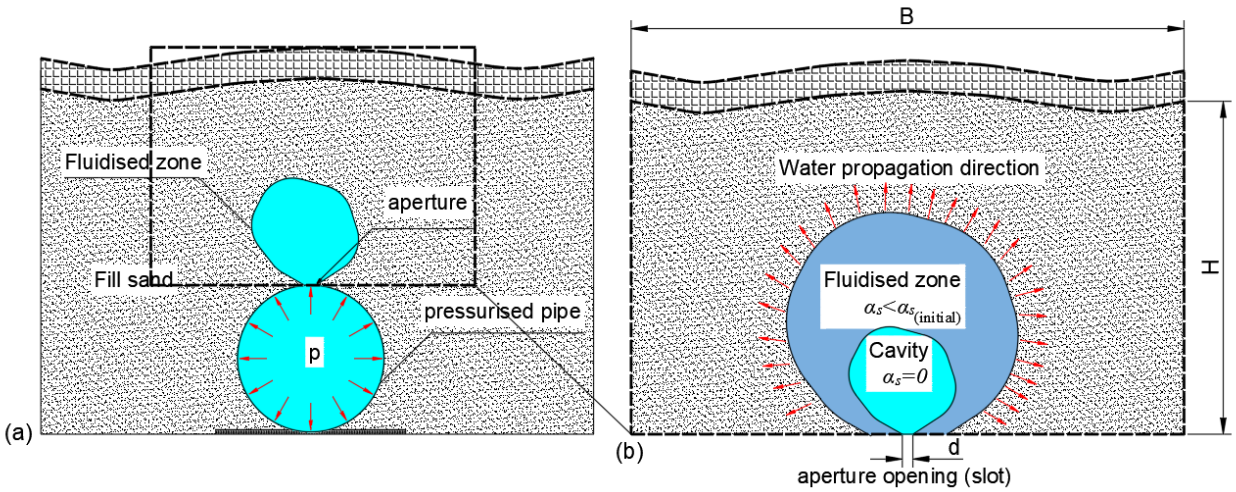

Figure 3.8. Schematic diagrams of soil fluidization in the vicinity of a leaking pressure pipe: (a) Illustration of the formation of internal fluidization; (b) A conceptual representation of the fluidization parameters around the aperture.

Alsaydalani and Clayton (2014) carried out an experimental investigation of the internal fluidization of sand due to water injection from a rectangular slot, which can be fairly represented by a two-dimensional simulation. A similar investigation was carried out by van Zyl et al. (2013) using a circular orifice opening at the inlet instead of a rectangular slot. In this study, we limit our numerical investigation to a two-dimensional case, however, a three-dimensional simulation should be doable using the same governing equations and numerical tools reported in this study.

The experimental setup proposed by Alsaydalani and Clayton (2014), which is adopted for simulation in this study, consists of a box filled with submerged silica sand (sand bed) subjected to water injection at the bottom similar to that shown in Figure 3.8. Water is injected at controlled pressures provided by a small pump through the rectangular slot opening, while flowrates are calculated from the water volume collected from the overflow at the top. Probes to measure the excess pore water pressure are placed along the centerline of the box and connected to sight-tubes to measure the development of excess pore water pressure throughout

the experiment. Snapshots of the deformation of the sand bed are taken throughout the experiment to monitor the surface heave, the extent of the fluidized zone, and the patterns of sand boiling at high flowrates. For the numerical simulation considered in this study, the height of sand inside the box is set to 0.3 m and width of 0.6 m. Sand is considered to be monodispersed with an average particle size of 0.9 mm and a slot opening of 0.62 mm. A summary of simulation parameters is provided in Table 3.3.

Table 3.3. Summary of the experimental parameters (Alsaydalani and Clayton, 2014)

Bed width (m)	Bed height (m)	Orifice size (mm)	Fluid density (kg/m^3)	Solids density (kg/m^3)	Initial porosity [-]	Applied upstream pressure (kPa)
0.6	0.3	0.62	1000	2680	0.35	10, 27, 60 &190

Initially, the system is set up with a fluid volume fraction of 0.38, which is higher than the desired porosity prescribed in the experiment $\varepsilon_f = 0.35$ to allow for interparticle forces to properly develop as solid packing occurs. Afterward, the solid particles are left to settle down to the prescribed volume fraction of 0.65 such that the total height of the silica sand submerged underwater is 0.3 m. After the particles have settled such that interparticle forces have properly developed and no initial motion is detected in the sand bed, water is injected at constant upstream pressure applied at the slot opening. Here, we chose to impose pressure boundary conditions instead of the velocity boundary condition adopted by Tang et al. (2017b). This is not to only align with the experimental procedure but also to provide a practical aspect to the simulation parameters. In the case of a local pressurized leakage, there would be many uncertainties related to estimating the leakage velocity, such as the size of the rupture and the soil conditions in the vicinity of the opening. On the other hand, the upstream pressure at the leakage condition could be easily determined from the pipe hydraulics. The boundary pressure values considered here are 10, 27, 60, and 190 kPa.

3.5 Results and discussion

The results of the numerical analysis, including excess pore pressure, flowrate, and the onset

of sand boiling, are summarized below.

3.5.1 Excess pore water pressure and fluidized zone

The excess pore water pressure, represented by the difference between the calculated dynamic pressure and the initial hydrostatic pressure, are shown in Figure 3.9. The results show a good agreement with the experimentally reported values in terms of the magnitudes and distribution pattern of excess pore water pressure. At low upstream pressure (e.g., 10 kPa), pressure build-up is observed in the vicinity of the location of injection. This build-up of pressure continues until it is large enough to mobilize the sand particles creating a small fluidized zone around the injection slot. Following fluidization, a drop in the pressure is observed in the fluidized zone which indicates pressure relief accompanied by a movement of the peak of excess pore water pressure to the top of the fluidized zone where the soil is still intact. This is consistent with the porosity distribution shown in Figure 3.11 as the porosity peaks to 0.9 near the location of injection. It is also observed that the peak porosity value is not located right after the inlet but rather shifted upwards before it declines again and drops sharply at the end of the fluidized zone. This can be interpreted as particles rearranging under gravity (i.e., soil self-healing) near the boundaries of the mobilized zone.

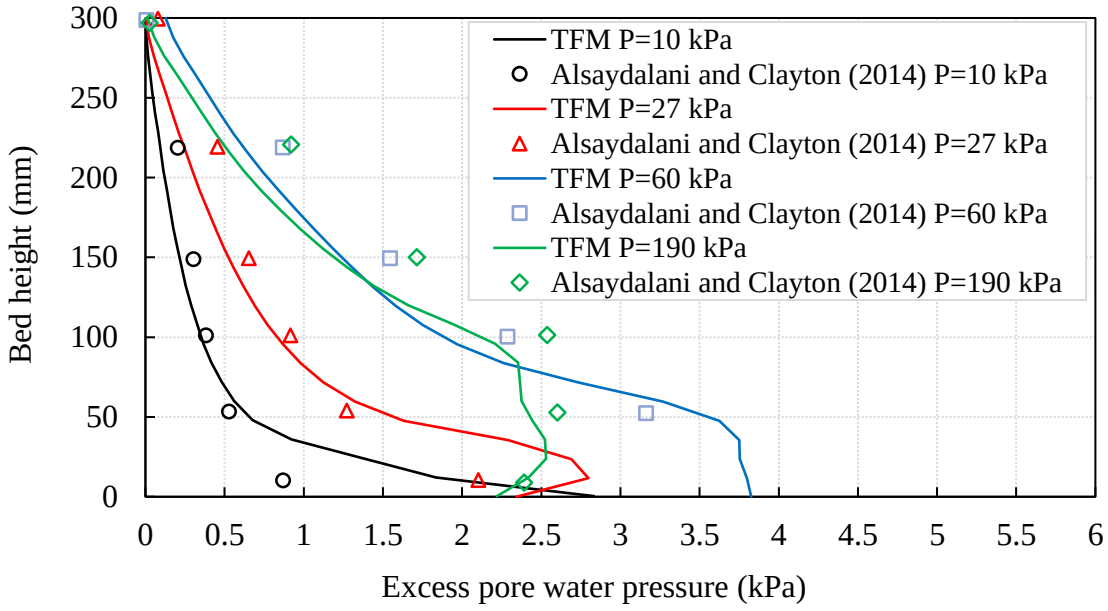

Figure 3.9. A comparison between the pressure distribution along the bed centerline from TFM simulation and the experimental results from Alsaydalani and Clayton (2014) for upstream pressures of 10, 27, 60 and 190 kPa and orifice opening of 0.62 mm.

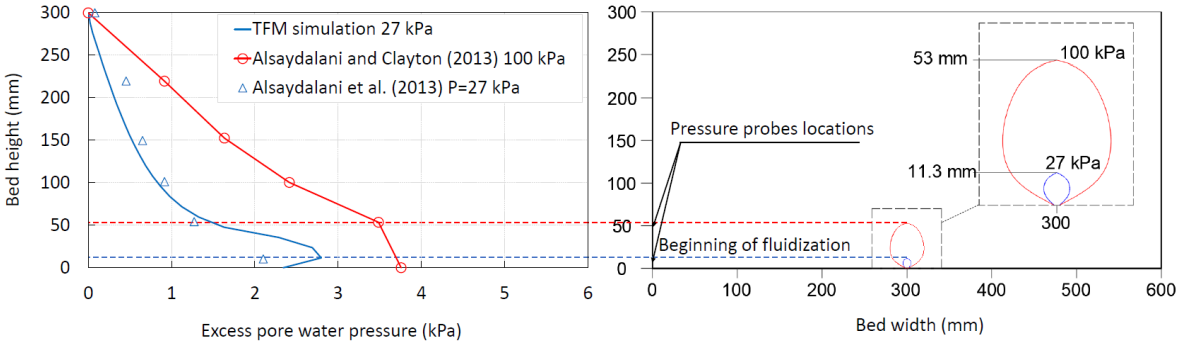

Figure 3.10. A comparison between the predicted initiation of fluidization and from the TFM simulation and the experimental data.

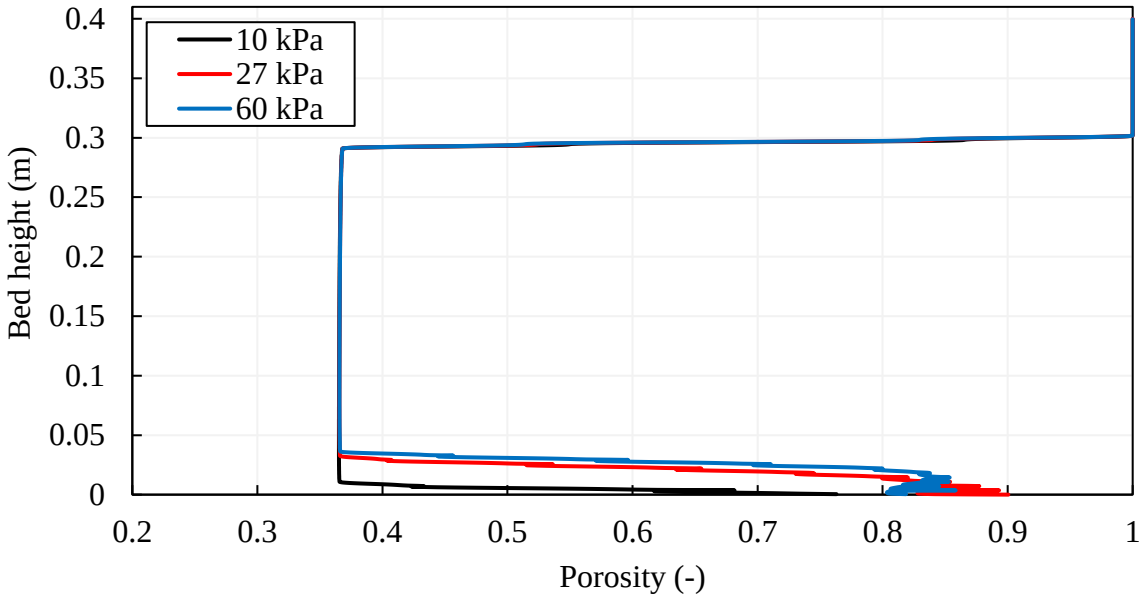

Figure 3.11. Porosity distribution along the bed centerline for upstream pressure values 10, 27 and 60 kPa.

The upstream pressure required to initiate fluidization reported by Alsaydalani and Clayton (2014) is approximately 100 kPa at a distance of 10 mm from the inlet and is characterized by the occurrence of a pressure drop at 53 mm from the inlet. In the current analysis, however, the occurrence of the first pressure drop is observed at upstream pressure of 27 kPa and a distance 11.3 mm from the inlet (Figure 3.10). Although this pressure seems to be much lower than that measured in the experiment, it is noted that the experimental excess pore water pressure data is measured using probes, of which, the lowest is placed at a height of

10 mm and 53 mm from the inlet. At the inlet location, however, pressure measurements are not available as placing a probe at the inlet will block the flow. Therefore, experimental detection of pressure drop initiation can only be obtained by comparing the first two probes, while pressure variations near the inlet are not accounted for. It is also observed that, above the location of the first probe, the simulation results seem to agree quite decently with the experimental data (Figure 3.10). This suggests that fluidization had already started at an upstream pressure of 27 kPa but was not captured due to limitations in pressure measuring tools, where the pressure drop is reported exactly at the same distance of the second measurement probe. This is confirmed by the good agreement observed between the simulation and the experiment at upstream pressure of 190 kPa at which the pressure drop occurs above 53 mm from the inlet location. A more important implication of the results is that the fluidization can happen within a limited domain around the location of the leakage. Although this is hardly observable at a relatively short distance from the leakage source, the increase in excess pore water pressure affects the entire sand bed, implying a significant reduction in effective stresses and shear strength of the soil.

3.5.2 Flowrate

Flowrate is calculated for each upstream pressure boundary value upon achieving a steady-state flow similar to that followed in the experiment. It is obtained by multiplying the inlet velocity by the width of the slot as for two-dimensional simulation. The results for flowrate compared to the experimental results are shown in Figure 3.12. The results show an overall good agreement with the experimental values at upstream pressure values of 10 kPa and 60 kPa. The maximum deviation in flowrate between the numerical and the numerical result is approximately 7%, and is observed at upstream pressure of 27 kPa. Interestingly, both the experimental data and numerical simulation indicate a relatively high increase in flowrate beyond 27 kPa which, again, suggests that fluidization had happened at a much lower pressure than experimentally reported.

3.5.3 Sand boiling at high inlet velocities

Another important aspect of the model's performance that is tested here is its ability to capture high deformations and fragmentations. An example of this is sand surface boiling as a water jet of high velocity penetrates through the sand bed. The experimental results reported by Alsaydalani (2010a) include a qualitative description of surface boiling in a shallow sand bed. The experimental setup and simulation parameters are the same as those used previously except

for the sand bed height and slot opening that are reduced to 150 mm and 0.33 mm, respectively.

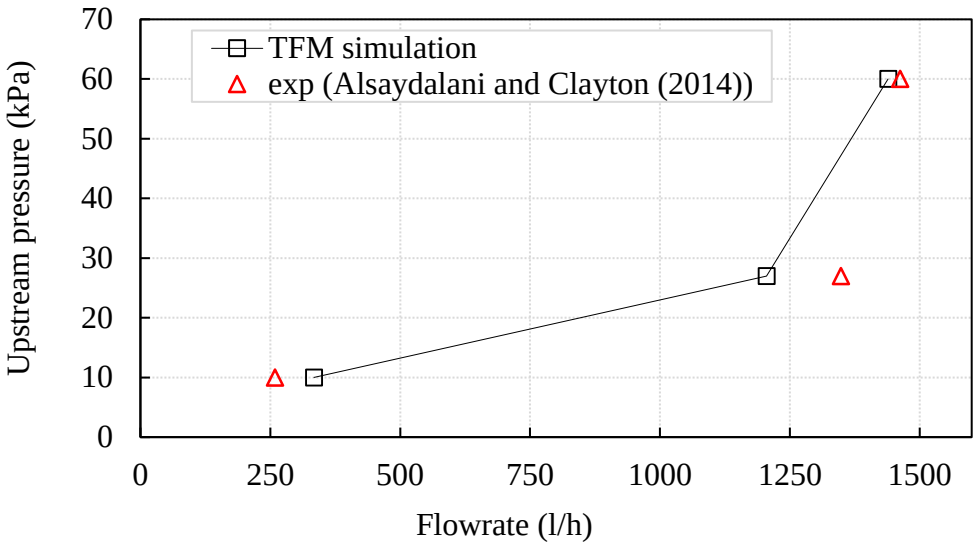

Figure 3.12. A comparison between the flowrates at steady-state flow from TFM simulation and the experimental results of Alsaydalani and Clayton (2014).

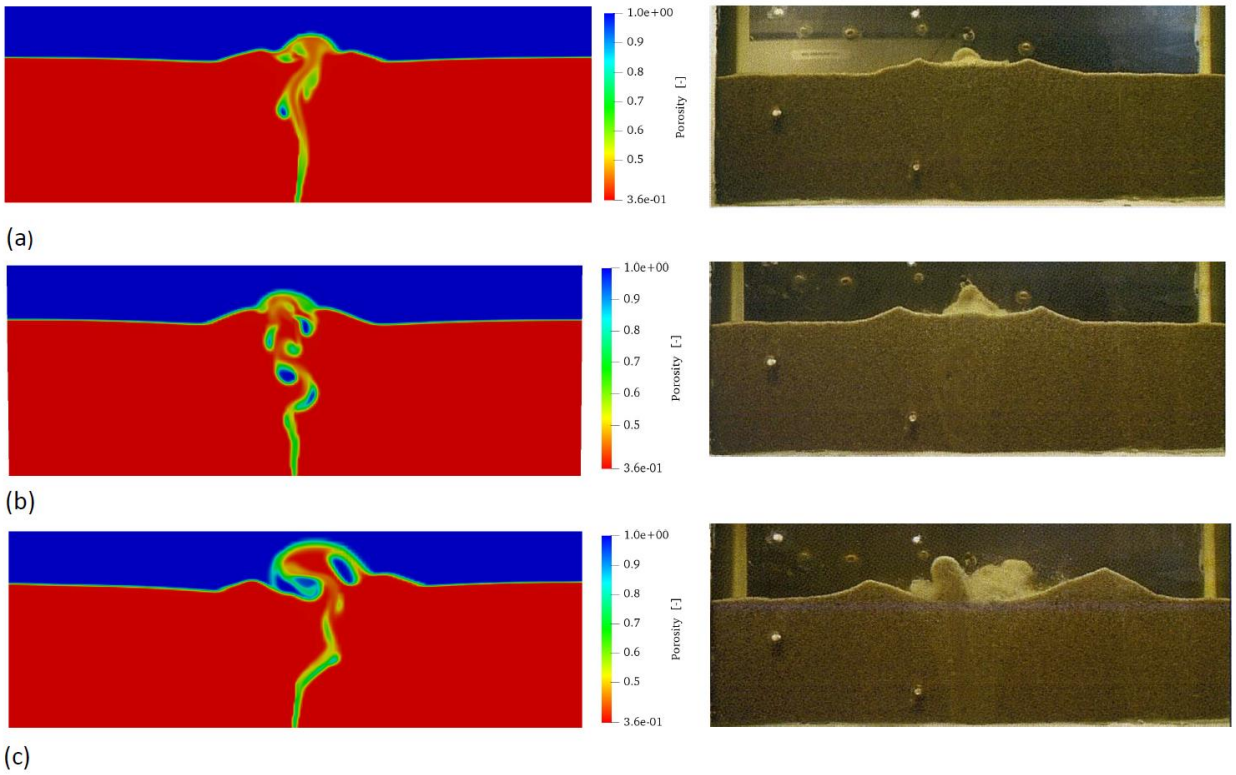

Figure 3.13. A comparison between the simulated sand boiling and the experimental photographs (Alsaydalani, 2010a) for flowrates (a) 700 l/h, (b) 900 l/h and (c) 1200 l/h for bed height150 mm and orifice opening 0.33 mm.

In this simulation case, a velocity boundary condition is imposed at the inlet to reproduce the flowrate boundary of 700 l/h, 900 l/h, and 1200 l/h. For each case, the simulation results are

displayed at the instant of water jet penetration out of the sand surface.

The results in Figure 3.13 show the physical deformation of the sand bed compared to the photographs taken for the corresponding inflow values in the experiment. It can be seen that the model could capture the basic characteristics of the bed deformation to a good extent. At inlet flowrates of 700 l/h and 900 l/h, the central plunging zone and the soil heave on both sides could be well-replicated by the model. The same behavior is also observed in the case of inflow of 1200 l/h; however, the model was not able to replicate the sand fragmentation around the central plunge. This shortcoming stems from the numerical diffusion involved with the discretization of the convective acceleration terms.

3.5.4 The effect of polydispersity

Polydispersity is an essential aspect that should be considered in conducting microscale analysis of granular soils. It is difficult to implement the variations in particle size distribution of soil when continuum-based approaches are adopted. This is mainly because of the volume averaging techniques that account for the effect of particle size implicitly as contributing factors to the interparticle and particle-fluid interaction forces. However, when the governing equations are written in terms of multiple solid phases as presented in this study, accounting for polydispersity becomes possible through assigning various particle sizes to the division of solid sub-phases. The sum of volume fractions of the fluid phase and the solid phases should sum up to 1 as per Equation 3.1).

The numerical results presented so far in this study only consider mono-dispersed granular soils. Although the effect of particle size variations has been reported both experimentally and numerically (Alsaydalani and Clayton, 2014; Tang et al., 2017b), uniform particle size was always used for each simulation case. This uniform particle size is characterized by an average value or more precisely the 50th percentile of particle sizes (D_{50}). The outstanding question is how representative this uniform value is of a granular assembly, especially with different assemblies that share the same D_{50}. To answer this question, three different particle size distributions (PSD1, PSD2, and PSD3) are synthesized such that they all have the same D_{50} (Figure 3.14). The particle size distributions are designed to represent three different soil types. The distribution PSD1 represents a well-graded soil with particle diameters ranging from 0.5 to 3 mm. The distribution PSD2 is also well-graded, however, a narrower range of particle sizes to mimic fine sand. The same particle size range of PSD1 is used for PSD3 but instead, it is characterized by two particle sizes of 0.5 and 3 mm to represent gap-graded soil. Three cases were conducted using the same system described earlier for the three

particle size distributions with a slot opening of 3 mm. At the inlet boundary, a water jet of a constant velocity of 3 m/s is set. The inlet velocity is set to be relatively high such that water jet penetration through the entire bed is achieved.

Table 3.4. The diameter and volume fraction allocated for particle size distributions PSD1, PSD2, and PSD3 for overall porosity of 0.4.

	PSD1		PSD2		PSD3	
	Diameter (mm)	Volume fraction	Diameter (mm)	Volume fraction	Diameter (mm)	Volume fraction
Solid 1	0.5	0.153	0.85	0.153	0.5	0.288
solid 2	0.9	0.147	0.9	0.147	0.9	0.012
solid 3	1.2	0.153	1	0.153	1.2	0.012
solid 4	3	0.147	1.5	0.147	3	0.288

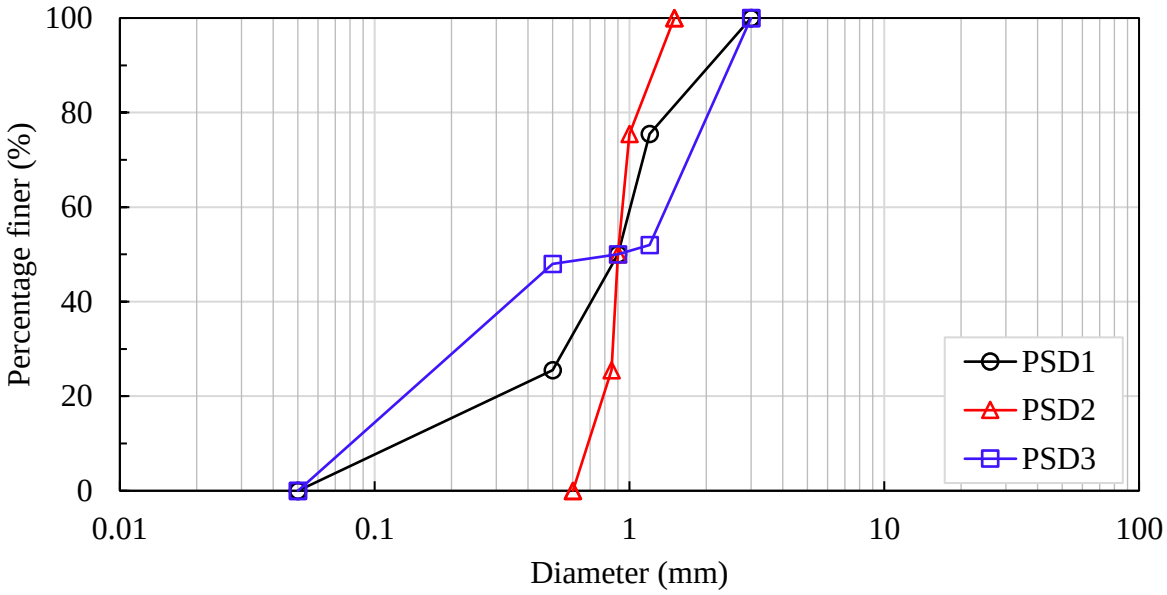

Figure 3.14. Synthesized particle size distribution curves with D_{50} = 0.9 mm to examine the effect of particle size distribution.

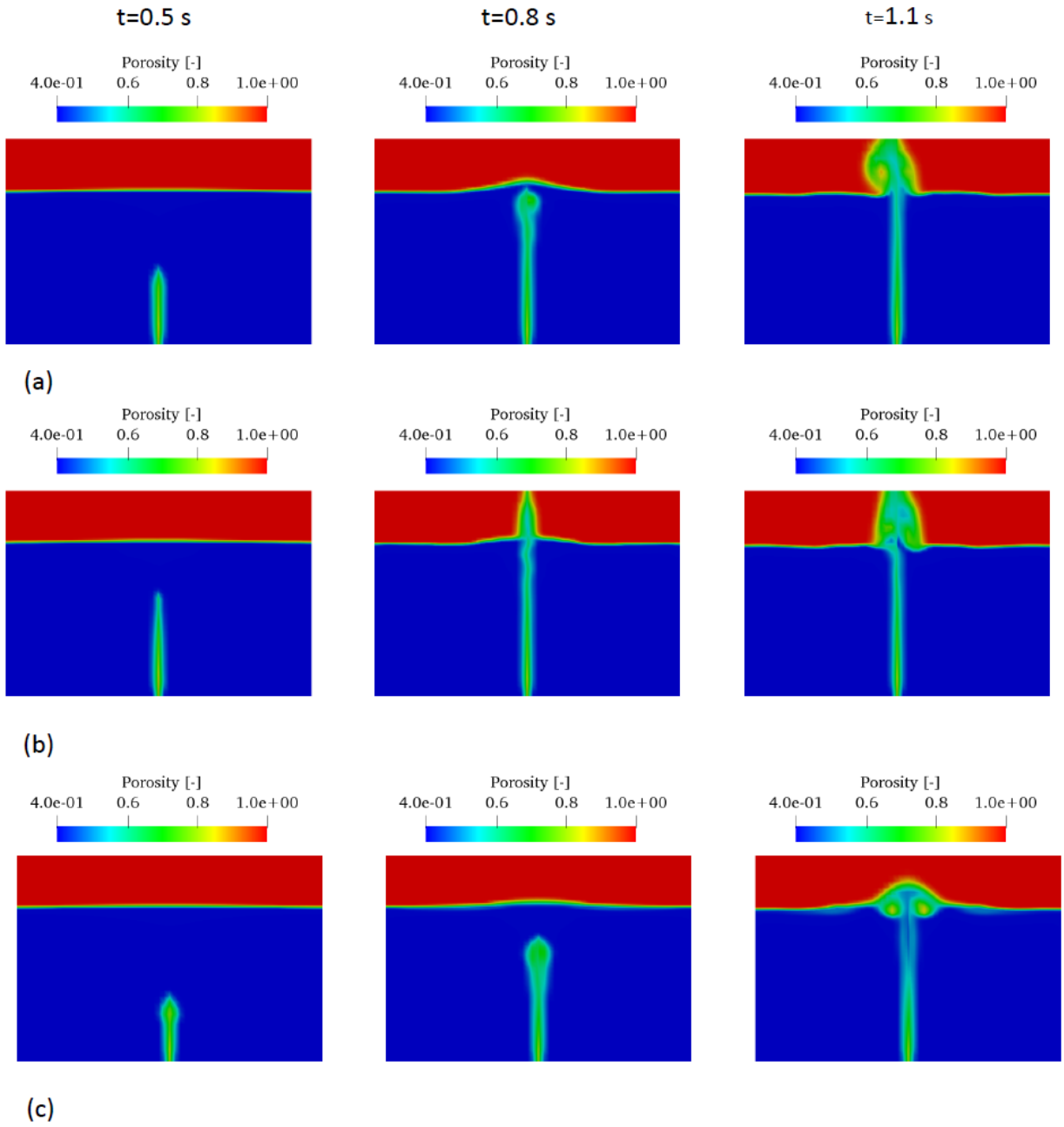

Figure 3.15. Porosity distribution over the sand bed at times 0.5, 0.8 and 1.1 seconds for particle distributions (a) PSD1, (b) PSD2 and (c) PSD3.

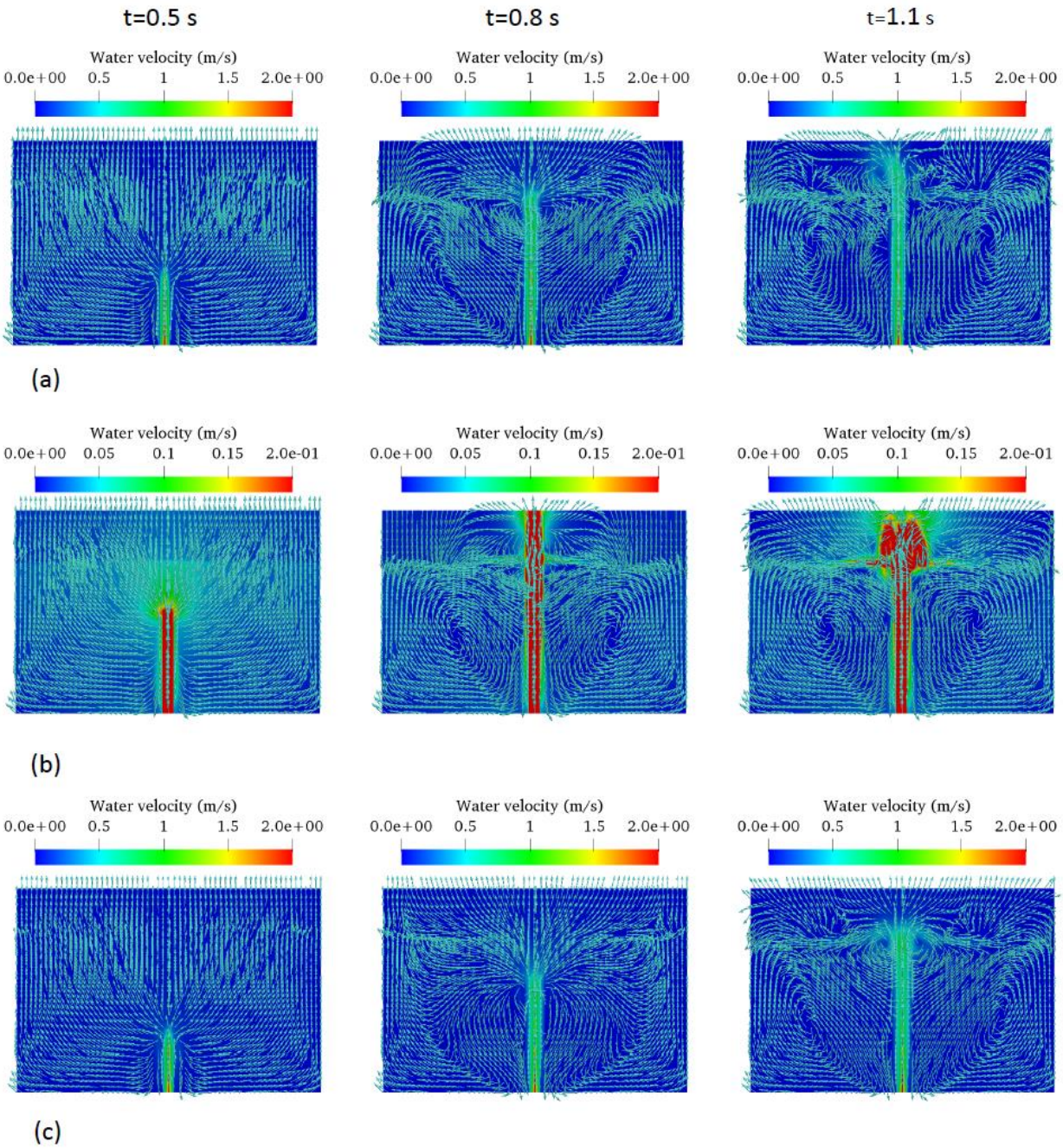

Figure 3.16. Water velocity distribution over the sand bed at times 0.5, 0.8 and 1.1 seconds for particle distributions (a) PSD1, (b) PSD2 and (c) PSD3

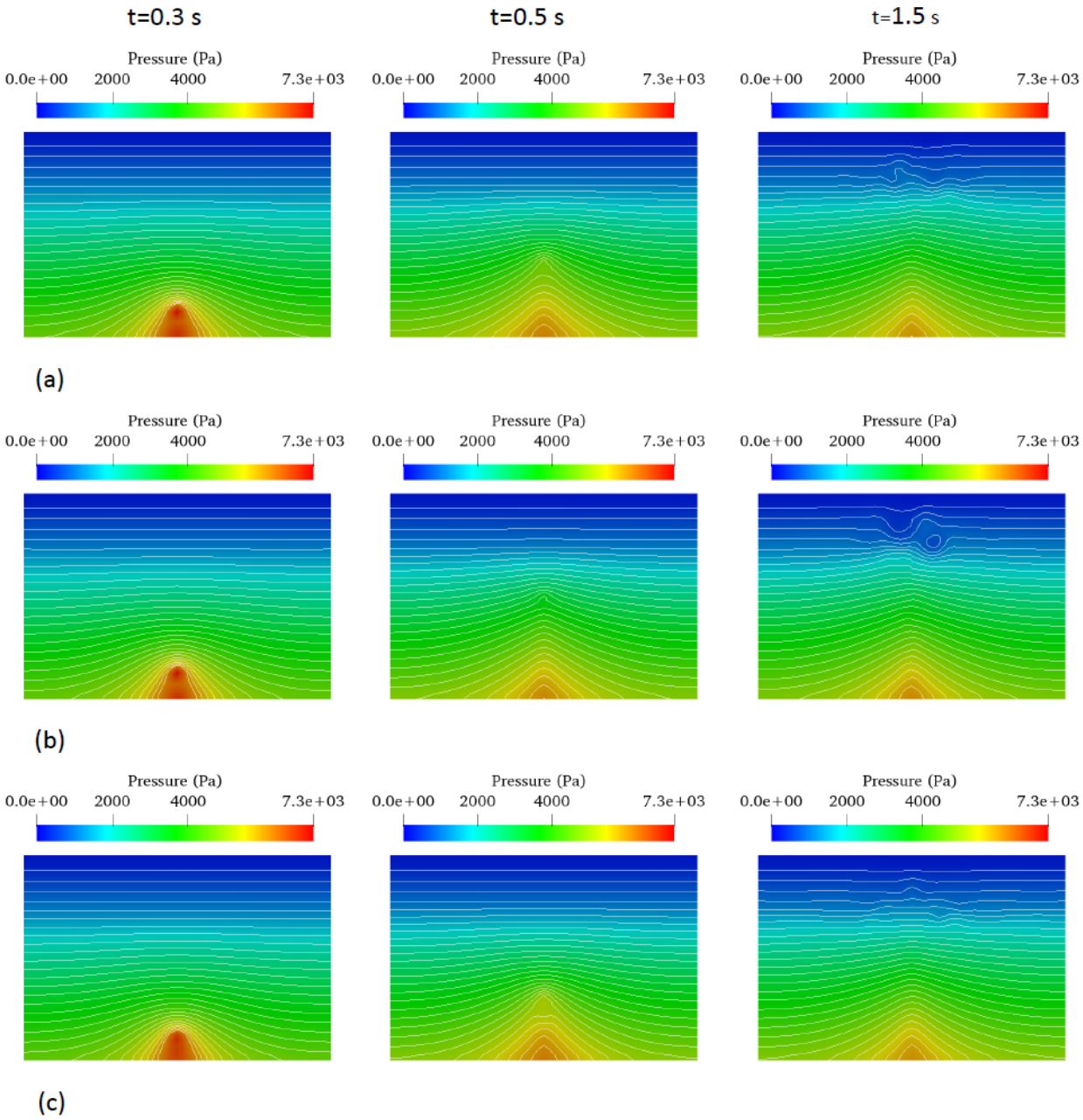

Figure 3.17. Water Pressure distribution over the sand bed at times 0.3, 0.5 and 1.5 seconds for particle distributions (a) PSD1, (b) PSD2 and (c) PSD3.

The evolution of porosity and velocity distributions across the sand bed is shown in Figure 3.15 and 16. Fundamental differences can be seen in the physical deformation of the bed and the velocity field. For PSD2, where well-graded fine particles exist, fast propagation of the water jet is observed with a narrow fluidization zone and minimal lateral spread. For PSD1 and PSD2, where larger particles appear to be more dominant, slower propagation of the water jet is observed with a wider lateral spread of fluidization. The width of the fluidized zone is maximum in PSD3, which represents gap-graded soils with the largest portions of both fine

and coarse particles of all three distributions. Although it is evident that the three distributions display different behavior, it is not clear what is exactly the underlying parameter. Tang et al. (2017b) attribute the slow jet propagation when large particles are dominant to an increase in soil permeability that helps to dissipate the excess pore water pressure. This might be valid for mono-dispersed systems, however, a quick look at the evolution of pressure field in Figure 3.17 shows no major differences between the three particle size distributions. One possible reason for the differences in behavior is the wash-out of finer particles as they are easier to mobilize. This aligns the lateral spread observations under nearly the same pressure distribution, especially that a full cavity was not developed, rather a region of higher porosity. Another interesting observation is seen in the velocity field that is the development of a trapezoidal-like wedge that characterizes the mobilized zone. This is consistent with the assumption of Cui et al. (2014) in their analysis for the critical inlet velocity. However, the breadth of the wedge is found to depend also on the particle size distribution, and therefore a modifier should be implemented to account for such variation if a single-values particle size is to be used.

3.6 Conclusions

Continuum-based modeling is seldom applied to coupled microscale simulation of coupled soil-water mixtures. In this study, we presented a model validation as well as a series of numerical simulations to test different aspects of the model's performance and limitations. The following conclusions can be identified:

1. The numerical results presented show the model's capability to capture the basic flow characteristics of soil-water mixtures as well as transitions in flow regime.
2. The model could successfully reproduce the evolution of internal soil fluidization due to local leakage.
3. More violent flows were also decently captured. However, a shortcoming is the model's inability to capture soil fragmentation accurately due to numerical diffusion.
4. Polydispersity could be successfully implemented and the simulation results suggest that using a mono-dispersed assembly is not sufficient to describe the soil-water properly.
5. Overall, the model shows good agreement with theoretical solutions and experimental data and can be a viable tool for investigating particulate soil-water flows in geotechnical applications.

Preface to chapter 4

The continuum representation adopted in the Two-Fluid Model is inherently unable to capture the dynamics of some flow regimes such as that of a freefall arch system. Although the TFM was able to capture the deformation and excessive water pressure, it cannot produce useful information when the flow regime is governed by rather local dynamics. This becomes clearer when we consider the problem of sand infiltration into the pipe, as opposed to the previous jet-like leakage. In this case, the flowrate of sand particles into the pipe is mainly governed by the formation and collapse of a temporary hemispherical arch directly above the crack. Therefore, in this chapter, we use coupled CFD-DEM method to investigate the groundwater-driven flow of sand-water mixture into defective gravity pipes. Following the model validation, we carry out a series of parametric analyses to examine the effect of fluctuations in groundwater table, the defect geometry and the height of sand over the pipe.

Chapter 4

CFD-DEM Simulation of Sand Erosion into Defective Gravity Pipes under Constant Groundwater table†

Abstract

As sewer pipes age, cracks and other forms of structural damage may develop leading to soil infiltration into the pipes that can cause sinkholes and damage the overlying roads and moving vehicles. The fluctuations in groundwater table following snow melt or heavy rainfall events can exacerbate soil erosion posing risk to the surrounding infrastructure. To understand and adequately characterize erosion in such cases, microscale analysis of both sand and water is needed to resolve the complex interactions around the pipe defects. In this study, a detailed numerical investigation is carried out using a series of coupled Computational Fluid Dynamics-Discrete Element method (CFD-DEM) simulations to evaluate the effects of groundwater table, crack size, defect angle, and the height of sand fill above the pipe on erosion. It is found that raising the groundwater table accelerates erosion only to a certain limit, above which, raising the groundwater level does not have tangible effect on erosion. This helps explain some of the misunderstandings reported in previous investigations regarding the effect of water level on the rate of erosion. With respect to the location of defects, it was found that, when groundwater is involved, the worst-case scenario for erosion develops for the case where the defect is located at the pipe crown. In addition, the thickness of the sand fill above the pipe was found to have little effect on the rate of erosion as a freefall arch regime was dominant in all simulations. Finally, simplified relationships were developed for estimating the total eroded mass for given sand properties, defect geometry, and location of groundwater table.

Keywords: Gravity pipes; structural defect; Internal erosion; CFD-DEM; Numerical analysis; Sand infiltration

† A version of this manuscript is currently under review in *Tunnelling and Underground Space Technology Journal*.

4.1 Introduction

As sewer pipes age, they become more prone to structural deterioration due to corrosion, cracking and ovalling of the pipe cross-section under the applied loads. This allows for the overlying and supporting soils to infiltrate into the pipe. Soil intrusion into defective sewer pipes can cause severe problems to the pipes, surrounding utilities, and the overlying superstructures. The loss of soil resulting from this intrusion can lead to voids forming around the pipes that might alter the state of stresses in the vicinity and compromise the structural integrity of the pipe and nearby structures (Balkaya et al., 2012; Meguid and Dang, 2009; Meguid and Kamel, 2014). Ultimately, a sinkhole might form when a sufficient amount of soil is lost such that overlying structures no longer have adequate support (Ali and Choi, 2019; Weil, 1995). The formation of voids and sinkholes due to internal erosion depends on several factors related to the characteristics of the defect, the supporting soil, and groundwater conditions. This involves the size and the angle of the defect, fluctuations in groundwater level, and the soil properties around the pipe (e.g. gradation, angle of internal friction and cohesion). Among these factors, the role of groundwater remains poorly understood and rather complicated to investigate both experimentally and numerically. Nonetheless, it has been frequently reported that the rise in groundwater level (e.g., after heavy rainfall) can mobilize and accelerate the erosion process causing sudden failures (Hilton et al., 2013; Indiketiya et al., 2019; Khudhair et al., 2021). This is particularly critical because the erosion mostly goes undetected until sudden failure occurs. Therefore, it is necessary to develop suitable modeling and testing tools to understand and quantify the impact of different factors affecting internal erosion in the presence of groundwater table.

Several studies attempted to characterize and assess the effect of different factors on internal erosion around cracked sewer pipes in the existence of groundwater (Guo et al., 2013a; Guo and Zhu, 2017; Guo and Yu, 2017; Tang et al., 2017c). The majority of these studies are experimental and present a set of parametric investigations on the effect of groundwater on the erosion process along with other factors such as crack size, angle, and soil grading. The focus is mainly geared towards granular soils such as sand, as cohesive soils are less likely to continuously erode compared to the looser cohesionless soils (Tang et al., 2017c). However, it is important to note that the formation of stable cavities in cohesive soils can sometimes be more threatening to the pipe's stability than granular soil, which is more likely to self-heal. Generally, the experimental setup in the majority of available studies consists of a submerged sand bed with an opening at the bottom that resembles the pipe defect. As erosion starts, the

water-sand mixture flows through the opening and the flowrates of both sand and water as well as the surface settlement and the final angle of repose are typically measured. It remains questionable, however, as to how far such system resembles the real conditions in the presence of groundwater. For instance, with such confined experiments of relatively small dimensions, the lowering of water level above the sand layer is usually rapid and may not represent the actual effect of the variations in groundwater levels. In addition, as far as groundwater effect is concerned, only cases involving varying water level is considered as opposed to comparison with dry soil cases. Indeed, the comparison with dry conditions (e.g., before rainfall) is essential to illustrate the role of groundwater in the initiation of soil erosion. Overall, the available experimental data does not provide sufficient insight into the mechanism of initiation and mobilization of erosion. As such, numerical modeling can be a viable tool as it allows for accessing information on multiple temporal and spatial scales that might not be readily available from the laboratory experiments.

A few studies presented numerical investigation and simplified analytical solution for the flow of soil-water mixtures around sewer pipes. Guo and Zhu (2017) presented a simplified formulation for the flow of sand and water based on the freefall arch theory (Beverloo et al., 1961). That is, the flow of sand particles into the vicinity is governed by a temporary arch or hemisphere, in which, the particles fall solely under the effect of gravity. In their work, the freefall arch theory was developed such that it accommodates the additional drag and buoyancy forces exerted by the fluid. More recently, Qian et al. (2021) presented a coupled Computational Fluid Dynamics-Discrete Element Method (CFD-DEM) simulation of the migration of fine particles through defects in segmented tunnels. In CFD-DEM simulation, the sand grains are generally represented as individual particles for which the movement and trajectory are determined by resolving the coupling of interparticle forces from DEM and particle-fluid interaction forces from CFD (Ibrahim and Meguid, 2020; Zhu et al., 2007). This is particularly challenging because it is computationally expensive to track such large number of particles and resolve the complex physics of soil-water interaction at the microscale level. Some simpler continuum-based models have been used in similar context such as simulating internal erosion around pressurized pipes (Ibrahim and Meguid, 2021; Salimi-Tarazouj et al., 2021; Tang et al., 2017b). Nonetheless, with the smoothing technique followed in these models, intricate interaction such as the formation of the freefall arch cannot be captured. Thus, residing to discrete particulate modeling as the case in CFD-DEM or Smoothed Particle Hydrodynamics (SPH-DEM) is necessary to understand the mechanism of erosion initiation and evolution as

well as its sensitivity to different parameters.

In this study, CFD-DEM analysis is utilized to numerically investigate the internal erosion of sandy soils around cracked sewer pipes. The CFD-DEM model is used to replicate the micromechanics of sand-water interaction and thus giving access to valuable data at the particle scale level. Initially, the DEM code is calibrated to ensure that the computational results adequately represent the actual behavior of sand (e.g., angle of repose). The erosion into a cracked pipe is then modeled for a dry case as a reference of comparison with the subsequent simulations where water is included. The dry erosion simulation is further validated by comparison with empirical relations available in literature. Finally, a series of simulations accounting for the presence of groundwater is conducted to examine the effects of groundwater table variation, crack size, crack angle, and the thickness of the sand layer on the erosion process.

4.2 Numerical Analysis

The CFD-DEM method was originally introduced by Tsuji et al. (1992) to simulate plug flow in a horizontal pipe and was later developed by Xu and Yu (1997) and Kawaguchi et al. (1998) into a more complete framework. In coupled CFD-DEM analysis, the fluid phase is numerically represented as a continuum for which mesh-based methods (e.g., finite volume) are used to resolve the flow. For the discrete solid phase, the motion of each solid particle is resolved within the Lagrangian framework of the DEM (Cundall and Strack, 1979). The interaction between the two phases is accounted for by considering the fluid-particle forces that represent the momentum transfer between the fluid and the solid particles.

4.2.1 The governing equations of the fluid phase

The governing equations for the fluid phase consist of the volume-averaged continuity and Navier-Stokes equations (Anderson and Jackson, 1967a; Kloss et al., 2012):

$$\frac{\partial \alpha_f}{\partial t} + \nabla \cdot \left(\alpha_f \mathbf{u}_f \right) = 0 \tag{4.1}$$

$$\frac{\partial \left(\alpha_f \mathbf{u}_f \right)}{\partial t} + \nabla \cdot \left(\alpha_f \mathbf{u}_f \mathbf{u}_f \right) = -\alpha_f \nabla \frac{p}{\rho_f} - \mathbf{R}_{pf} + \nabla \cdot \boldsymbol{\tau} \tag{4.2}$$

where α_f is the volume fraction of the fluid (e.g., water) within a computational cell, $\mathbf{u}_f$ is

the fluid velocity, p is the fluid pressure, $\boldsymbol{\tau}$ is the volume-average shear stress tensor of the fluid, ρ_f is the density of the fluid, and $\mathbf{R}_{pf}$ is a term for momentum transfer between the solid and fluid phases (i.e., particle-fluid interaction force). Various particle-fluid interaction forces such as drag force, Basset force, or virtual mass force can be considered to contribute momentum transfer and the selection of a proper subset of interaction forces depends mainly on the nature of the tackled problem. For sand-water interactions in geotechnical applications only buoyancy and drag forces are considered the most significant forces (Ibrahim and Meguid, 2020). We note that the formulation of the fluid pressure term in Eq. (4.2), which is commonly known in the literature as model A (Zhou et al., 2010; Zhu et al., 2007), implicitly accounts for the buoyancy force, and thus, drag forces exclusively contribute to the term $\mathbf{R}_{pf}$ such that:

$$\mathbf{R}_{pf} = \mathbf{K}_{pf}\left(\mathbf{u}_f - \left\langle \mathbf{u}_p \right\rangle\right) \tag{4.3}$$

where $\left\langle \mathbf{u}_p \right\rangle$ is the cell-based average velocity of a solid particle and $\mathbf{K}_{pf}$ is the momentum transfer coefficient. Different drag correlations are available in literature such as those proposed by Di Felice (1994) , Gidaspow (1994), Kafui et al. (2002), Koch and Hill (2001) and Tsuji et al. (2008).

In this study, a combination of the drag correlations of Wen and Yu (1966) Ergun (1952) are used. For $\alpha_f > 0.8$, that is relatively fluidized flow regime:

$$\mathbf{K}_{pf} = \frac{3}{4} C_d \frac{\alpha_f \left(1-\alpha_f\right)\left|\mathbf{u}_f - \mathbf{u}_p\right|}{d_p} \alpha_f^{-2.65} \tag{4.4}$$

where d_p is the mean particle diameter and C_d is the drag coefficient which is given as:

$$C_d = \frac{24}{\alpha_f \,\mathrm{Re}_p}\left[1 + 0.15\left(\alpha_f \,\mathrm{Re}_p\right)^{0.687}\right] \tag{4.5}$$

where Re_p is the particle Reynold's number: $\mathrm{Re}_p = \left|\mathbf{u}_f - \mathbf{u}_p\right| d_p / \nu_f$. For denser flows with

$\alpha_f \leq 0.8$, the momentum transfer coefficient is given by Ergun's equation:

$$\mathbf{K}_{pf} = 150\frac{\left(1-\alpha_f\right)^2 \nu_f}{\alpha_f d_p^2} + 1.75\frac{\left(1-\alpha_f\right)\left|\mathbf{u}_f - \mathbf{u}_p\right|}{d_p} \tag{4.6}$$

4.2.2 The governing equations of the solid phase

The equations of motion of the solid phase are given as (Kloss et al., 2012):

$$m_i \frac{d\mathbf{v}_i}{dt} = \sum_{j=1}^{k_c}(\mathbf{f}_{i,n} + \mathbf{f}_{i,t}) + \mathbf{f}_{i,b} + \mathbf{f}_{i,pf} \tag{4.7}$$

$$I_i \frac{d\boldsymbol{\omega}_i}{dt} = \sum_{j=1}^{k_c}\mathbf{r}_{ij} \times \mathbf{f}_{i,t} + \mathbf{M}_{i,r} \tag{4.8}$$

where m_i, I_i and $\mathbf{v}_i$ are the mass and moment of inertia particle *i*, respectively, $\mathbf{v}_i$ and $\boldsymbol{\omega}_i$ are its linear and angular velocities , respectively, $\mathbf{f}_{i,n}$ and $\mathbf{f}_{i,t}$ are the normal and tangential contact forces at contact points of particle *i* with neighboring particles, k_c is the number of neighboring particles, $\mathbf{f}_{i,b}$ is the weight and external body forces acting on particle *i*, $\mathbf{f}_{i,pf}$ is the interaction force exerted by the solid particle on the fluid, $\mathbf{r}_{ij}$ is the relative position vector between particle *i* and a neighboring particle *j*, and $\mathbf{M}_{i,r}$ is the additional moment exerted on the solid particle (e.g., rolling friction).

The particle-fluid interaction term, $\mathbf{f}_{i,pf}$, in Eq. (4.7) is analogous to the momentum transfer term, $\mathbf{K}_{pf}$, in Eq. (4.2). Although interaction forces exerted by each phase on the other should be equal in magnitude, the two terms are denoted differently to differentiate between the cell-based and particle-based numerical treatment. More details on the estimation of the interaction forces and how they are distributed from fluid cells to solid particles can be found

in (Kloss et al., 2012). For calculating the normal and tangential contact forces, Hertz-Mindlin model was used (Di Renzo and Di Maio, 2005):

$$\mathbf{f}_{i,n} = k_n \delta n_{ij} - c_n \mathbf{v}_{ij} n_{ij} \tag{4.9}$$

$$\mathbf{f}_{i,t} = \min\left\{\left|k_t \delta t_{ij} - c_t \mathbf{v}_{ij} t_{ij}\right|, \mu_s \mathbf{f}_{i,n}\right\} \tag{4.10}$$

where k_n and k_t, as shown in Figure 4.1, are the normal and tangential spring stiffnesses, respectively, c_n and c_t are the normal and tangential dashpot coefficients, respectively, δn_{ij} and δt_{ij} are the normal and tangential overlaps between particle *i* and particle *j*, respectively, μ_s is Coulomb friction coefficient, and $\mathbf{v}_{ij} t_{ij}$ is the relative velocity in the tangential directions. The nonlinear spring stiffness and dashpot coefficient are governed by the geometry and material properties and are given as:

$$k_n = \frac{4}{3} E^* \sqrt{R^* \delta_n} \tag{4.11}$$

$$c_n = -2\sqrt{\frac{5}{6}} \beta \sqrt{2E^* \sqrt{R^* \delta_n} m^*} \geq 0 \tag{4.12}$$

$$k_t = 8G^* \sqrt{R^* \delta_n} \tag{4.13}$$

$$c_t = -2\sqrt{\frac{5}{6}} \beta \sqrt{8G^* \sqrt{R^* \delta_n} m^*} \geq 0 \tag{4.14}$$

where m^*, R^*, E^*, and G^* are the equivalent mass, radius, elastic modulus, and shear modulus of two particles in contact, respectively, and β is constant such that: $\beta = \ln(e) / \sqrt{\ln^2(e) + \pi^2}$, where *e* is the coefficient of restitution. The only restraint applied to the normal contact is a divider or a no tension joint as shown in Figure 4.1. In the tangential (shear) direction, the particles are assumed to remain immobilized until the Coulomb friction threshold is reached. As spherical particles used in this study inherently lack geometrical

interlocking, it is necessary to introduce rolling friction moment to account for particle non-sphericity. In this study, we adopt the Elastic-Plastic Spring-Dashpot (EPSD2) (Ai et al., 2011), developed from the rolling friction model originally proposed by Iwashita and Oda (1998). Similar to normal and tangential forces, the rolling friction model consists of a rotational spring and damper such that:

$$\mathbf{M}_{i,r} = \min\left\{\left|-k_r \Delta\theta_r - C_r \dot{\theta}_r\right|, \mu_r R_r \mathbf{f}_{i,n}\right\} \tag{4.15}$$

where k_r is the stiffness of the rotational spring, $\Delta\theta_r$ is the angle of rotation during one timestep, C_r is the coefficient of rotational damper, $\dot{\theta}_r$ is the relative angle of rotation, μ_r is the coefficient of rolling friction, and R_r is the rolling radius. Similar to tangential forces, the mobilization of particles is governed by a threshold value that depends on the coefficient of rolling friction.

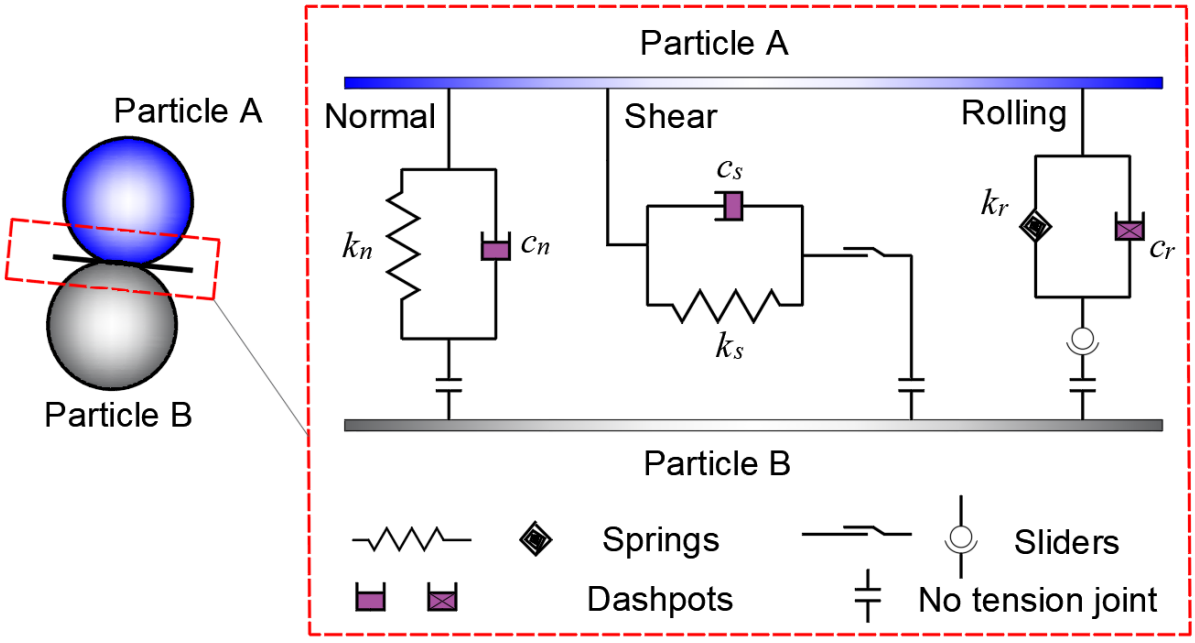

Figure 4.1.An illustration of the DEM contact model parameters of springs and dashpots for normal contact, shear contact and rolling friction.

4.2.3 CFD-DEM coupling

The coupling process relies mainly on continuously exchanging and updating the information of flow fields between the two separate solvers of CFD and DEM. As demonstrated in the

flowchart in Figure. 4.2, the contact forces of the granular assembly are first detected, then the equations of motion are solved to determine the new positions and velocities. As the stable time step for DEM is approximately two orders of magnitude greater than that for CFD, a loop is created in the DEM part to synchronize the data exchange. When the DEM loop iterations are satisfied, positions and velocities of the solid particles are projected onto the CFD grid to calculate the corresponding porosity and interaction forces. As such, the momentum exchange term is calculated for the CFD calculations and the fluid flow field is resolved. To close a single coupled iteration, the interaction forces are updated once more and exported back to the DEM solver. The governing equations and the coupling process are implemented using CFDEM® open-source platform (Goniva et al., 2012). The solver consists of LIGGGHTS® (Kloss et al., 2012) solver for DEM calculations and OpenFOAM® (Weller et al., 1998) solver for CFD calculations.

Although both the open-source codes for both DEM and CFD components are readily available, a substantial effort is made to properly perform the coupling and ensuring the overall numerical stability. In addition, the input files of creating geometry, specifying boundary conditions, and the different sorts of meshes involved in the simulation are to be independently prepared in advance using third-party tools. To illustrate, defining a wall element in DEM code basically involves incorporating STL meshes of the wall element itself, which while being 3D in nature, can sufficiently be represented by surface elements. On the other hand, a wall element in CFD computations is essentially a volumetric mesh that represents the entire simulation domain around the element. As such, a combination of supporting software such as AutoCAD, Gmsh, MeshLab were used for generating geometry and different sorts of meshes.

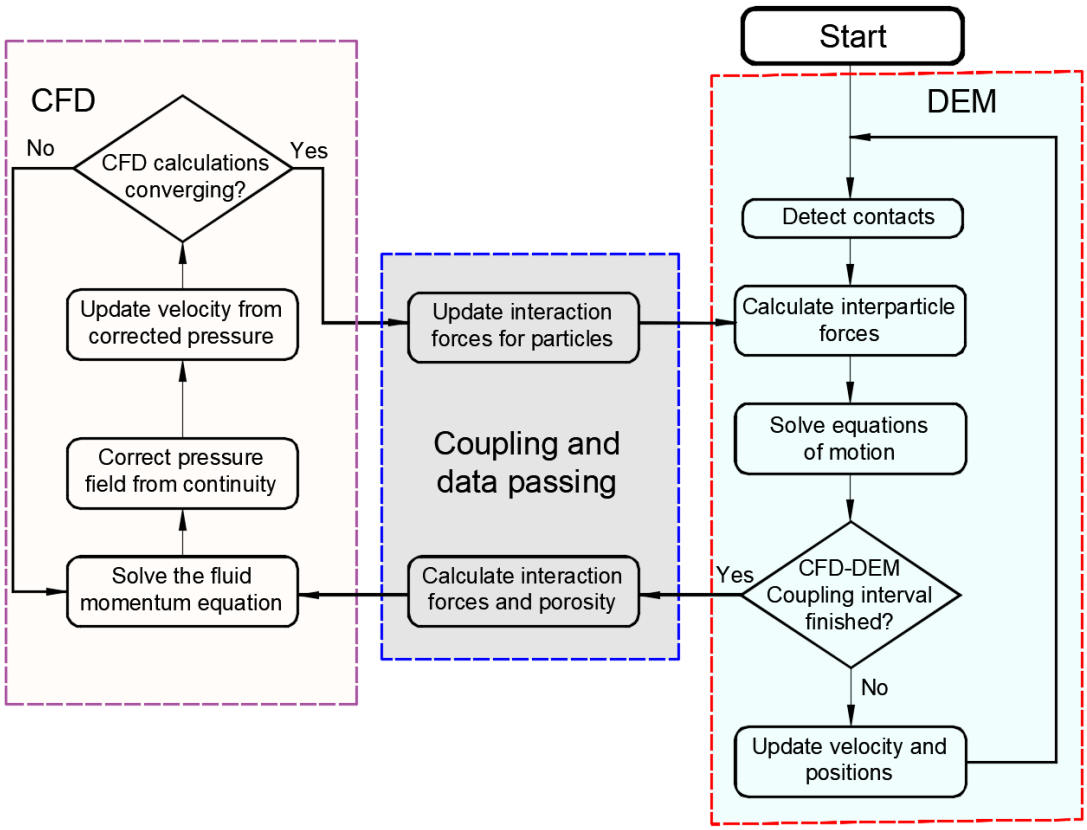

Figure. 4.2. A flowchart showing the sequence of the two-way coupling and information passing processes adopted in the CFD-DEM model.

4.3 Model validation

Before proceeding to the core simulations of this study, it is necessary to first validate the model's performance. Two validation cases were performed- the first involves the simulation of the terminal velocity of a single particle falling in water. While this problem allows for the calculation results to be compared with a well-established numerical solution, it lacks the complexity stemming from having a full granular assembly. The second validation case involves the re-production of the experimental results reported by Tang et al. (2017c), which covers important aspects related to soil erosion that can be further investigated using a parametric study.

4.3.1 Terminal velocity of a single particle falling in water

For a single particle falling in water, the balance of forces between gravitational forces on one hand and the drag and buoyance forces on the other hand leads to a constant terminal velocity. The velocity of the particle can then be expressed as (Zhao, 2017):

$$\frac{\partial U}{\partial t} = \left(1 - \frac{\rho_f}{\rho_s}\right) g - \frac{3\rho_f}{8 r \rho_s} C_d U^2 \tag{4.16}$$

where U is the relative velocity of the particle with respect to water, ρ_f and ρ_s are the densities of the fluid and the solid particle, respectively, r is the radius of the particle, and C_d is the drag coefficient. Since the drag coefficient also depends on relative velocity, //a direct solution of the differential equation is difficult to obtain and numerical solution will be most suitable. A forward finite difference in time scheme is used to discretize Eq. (4.16) such that:

$$U_{i+1} = \left\{ \left(1 - \frac{\rho_f}{\rho_s}\right) g - \frac{3\rho_f}{8 r \rho_s} C_d U_i^2 \right\} \Delta t \tag{4.17}$$

The simulation domain is a cube filled with water with side dimension of 0.1 m. The particle density ρ_s = 2680 kg/m^3 and water density ρ_f =1000 kg/m^3. The particle diameter is 1 mm and the motion of the particle starts from rest at the top surface of the cube. The propagation of the solid particle highlighting the velocity field in the vicinity is shown in Figure. 4.3. The comparison in Figure. 4.3-e shows a good agreement between the downward relative velocity of the solid particle obtained from the coupled CFD-DEM analysis and the numerical solution of Eq. (4.17). On a basic level, this indicates the ability of the model to capture the basic flow characteristics including the interaction forces between the solid and fluid phases.

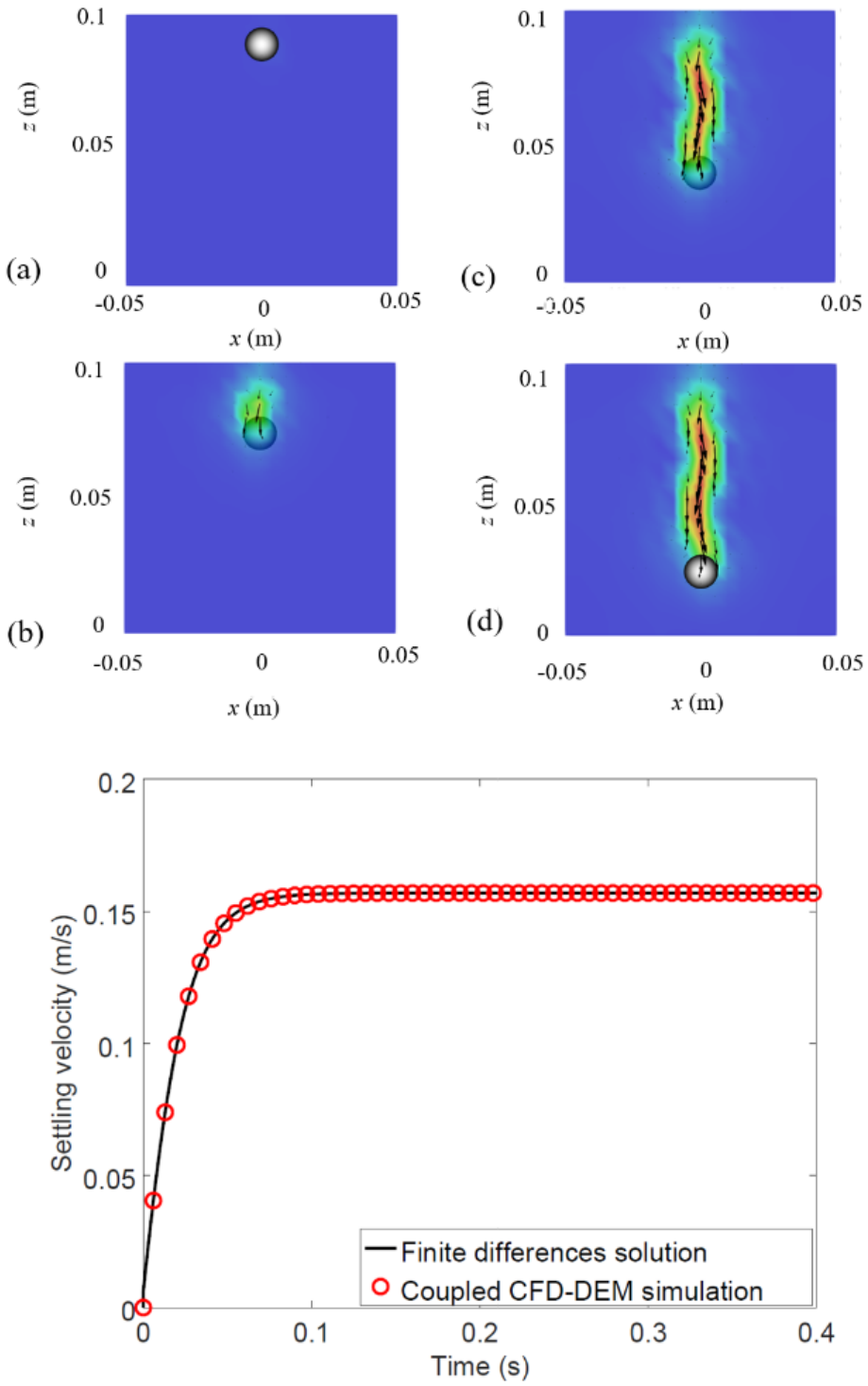

Figure. 4.3. Snapshots of a single particle falling in water at (a) t = 0 s, (b) t = 0.05 s, (c) t = 0.15 s, (d) t = 0.2 s, and (e) a comparison between the settling velocity obtained from coupled CFD-DEM simulation and forward finite difference solution of Equation (4.16).

4.3.2 Flow through a longitudinal crack at the pipe crown

The second case of validation carried out in this study is a reproduction of the experimental study of Tang et al. (2017c) shown in Figure. 4.4. The experimental setup consists of a box with a pipe attached at the bottom. The box is filled with sand up to a height of h_s that is submerged under a water height of h_w. For three inclination angles: $\theta = 90^o$, $\theta = 45^o$, and $\theta = 0^o$ measured from the horizontal, a rectangular slot/opening of width D is placed. As the experiment is initiated, the seal on the slot is removed and sand and water are allowed to flow through the opening. The discharge of sand and water is then directed through a ramp-like outlet that represents the slope of a sewer pipe as well as to prevent clogging within the interior of the pipe. Sand and water velocities within the sand bed are mapped throughout the experiment. In addition, the flowrates of water and sand through the outlet are recorded as well as the final deformation of the sand bed after all the water had moved out of the system. The output of the experiment is useful in validating the numerical model developed in this study as it provides important insights on the mobilization, rate and the final extent of erosion.

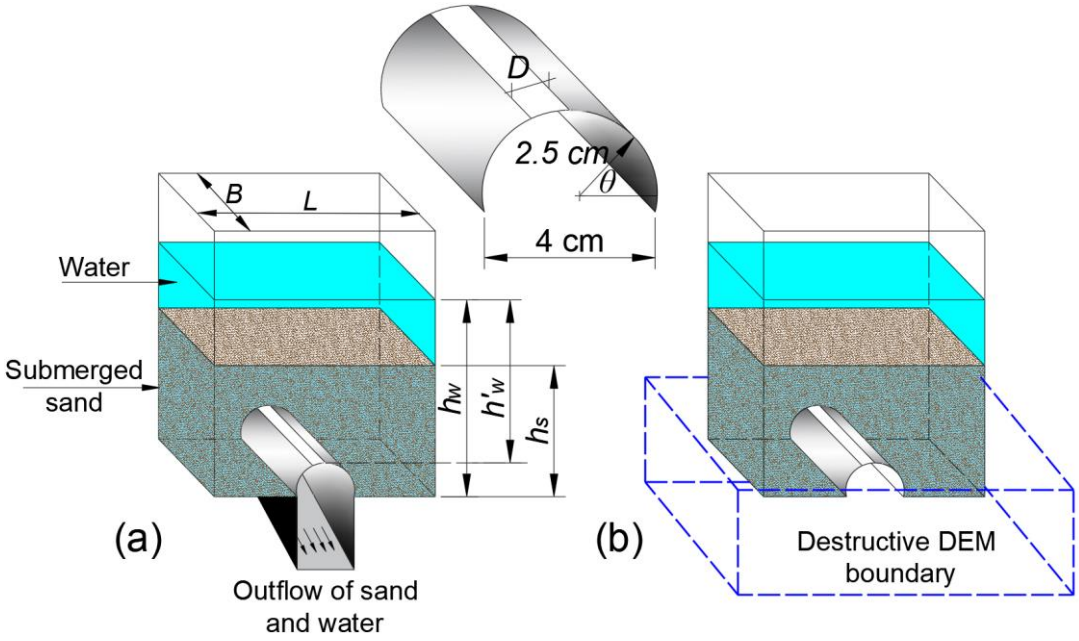

Figure. 4.4. A schematic illustration of (a) the experimental setup used in model validation after Tang et al. (2017c), and (b) the CFD-DEM adaptation of the outflow system in the experiment.

Another aspect of the study relates to the shape of the induced slot in the pipe structure as it resembles the shape of a longitudinal crack in a deteriorated gravity pipe, which is of interest to this study. Also, the shape of the opening results in a triangular prismatic (i.e., two-

dimensional) void, as opposed to a conical void that would develop if the opening was circular. This has the advantage of allowing for the downscaling of the model in the longitudinal direction. A fundamental difference, however, exists between the numerical model and the experiment when it comes to the variations in water level. While it is experimentally preferable to use a finite volume of water, it hardly represents the lateral extent of groundwater, which is generally much larger than the depth at which the pipe is buried. Thus, one should not expect the groundwater level to drop as quickly as it does in a finite small box, which makes considering a constant water level more realistic. On the other hand, numerically using a constant water level reduces the complexity of implementing interface-capturing calculations to account for the movement of the water surface. Subsequently, comparison between the coupled CFD-DEM and the experimental results will only be meaningful at early times where the water level is comparable to its initial value. Therefore, the comparison is limited to the first 10 seconds of the simulation to overcome discrepancies resulting from changes in water level and to keep the computational effort within an acceptable limit.

4.3.2.1 **Material calibration (angle of repose)**

Before starting the coupled simulation, it is necessary to make sure that properties of the sand matches that reported in the experiment. As there is no direct link between the micro-properties used in DEM simulation and macro-properties of the soil, this process is often iterative to tune the microscale properties. A set of DEM numerical tests is performed to determine the necessary parameters to achieve an angle of repose, $\varphi_r = 36^{\circ}$. The test consists of a cylindrical container with diameter and height of 10 cm. The container is filled with medium sand with particle size distribution (shown in Figure. 4.5) that is initially left to pack under its own weight until no movement in the system is detected. Afterward, the container is moved up with a relatively low velocity of 0.01 m/s allowing the sand particles to form a stable cone/heap. Reported values of the coefficient of friction, coefficient of restitution, modulus of elasticity, and Poisson's ratio are adopted (Qian et al. (2021) and Soltanbeigi et al. (2021)). The parameter left to tune here is the coefficient of rolling friction, μ_r, as the angle of repose is most sensitive to its value.

Figure. 4.6 shows snapshots of the formation of the sand cone as well as the final angle of repose of the sand. The corresponding micromechanical properties, that are later used as DEM input, used to achieve 36º angle of repose is shown in Table 4.1.

Table 4.1. DEM simulation parameters for the angle of repose test ($\varphi_r = 36^o$).

Parameter	Value
Solid density (ρ_s) [kg/m^3]	2600
Coefficient of particle-particle friction (μ_s)	0.3
Coefficient of particle-wall friction (μ_{sw})	0.25
Coefficient of restitution (e)	0.5
Poisson ratio	0.25
Young's modulus (E) [Pa]	2.5x10^8
Coefficient of rolling friction (μ_r)	0.4
DEM time step (Δt) [s]	2x10^{-7}

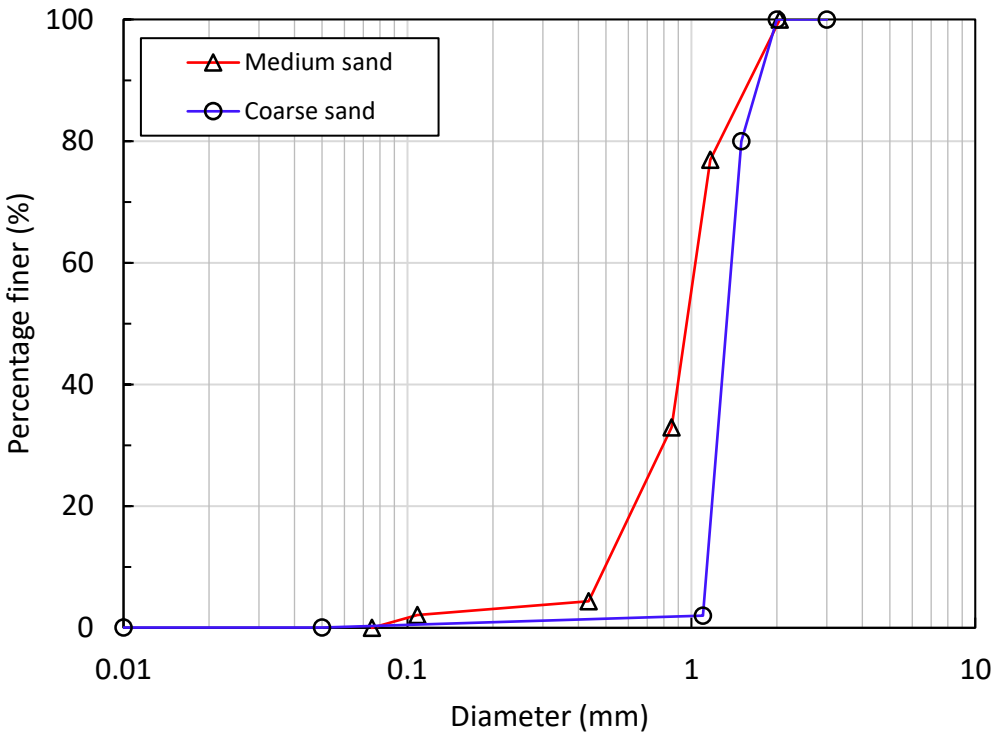

Figure. 4.5. The particle size distribution curves for the medium sand used in the model validation simulation and the coarse sand used in the parametric study.

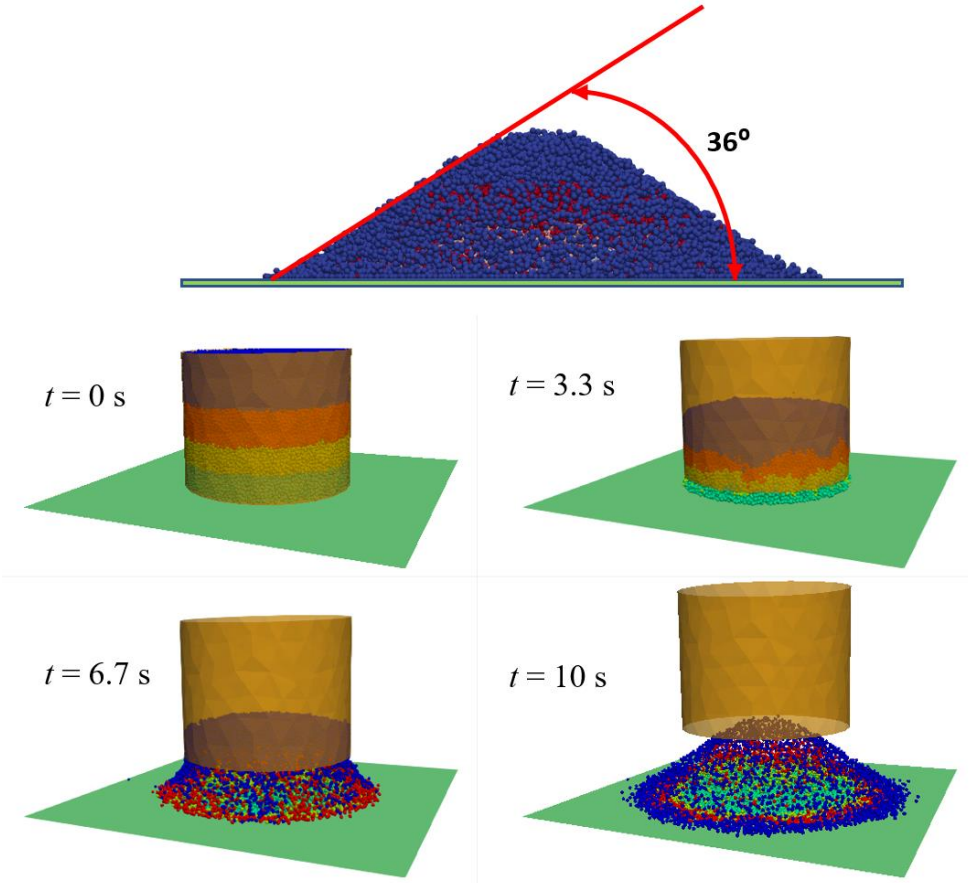

Figure. 4.6. The evolution of sand cone over time during DEM angle of repose test showing the final angle of repose.

4.3.2.2 **Numerical considerations and model validation**

In order to create the numerical model that maintains the balance between computational efficiency and reasonably replicating the experimental results, the following adjustments were considered. Firstly, the width, L, of the model was reduced from 0.5 m to 0.2 m in order to avoid unnecessarily adding DEM particles that will eventually end up in an undisturbed region at the end of the 10 seconds of simulation. Similarly, the thickness of the model, B, was reduced from 0.08 m to 0.01 m since the thickness of the model should not affect the shape of the eroded wedge, yet maintaining a thickness large enough (i.e., higher than$10D_{50}$ of 1.5 mm) to avoid arch formation in the transverse direction. The outlet configuration in the experiment is modelled by destructive DEM domain boundaries (Figure. 4.4) such that particles leaving the system are removed from the simulation. Notable to mention that CFD mesh requires some degree of coarseness to avoid sharp oscillations in porosity (volume fraction) calculations, yet

fine enough so that CFD calculations are not compromised. The recommended cell size should contain at least 5 to 10 solid particles (Ibrahim and Meguid, 2020; Zhao, 2017). Therefore, the meshing size was directly calculated using this criterion (approximately 5 mm). Nonetheless, as shown in Figure. 4.7, local mesh refining around the pipe geometry is inevitable to make sure that the geometric boundaries are well represented. A summary of the numerical parameters is provided in Table 4.2.

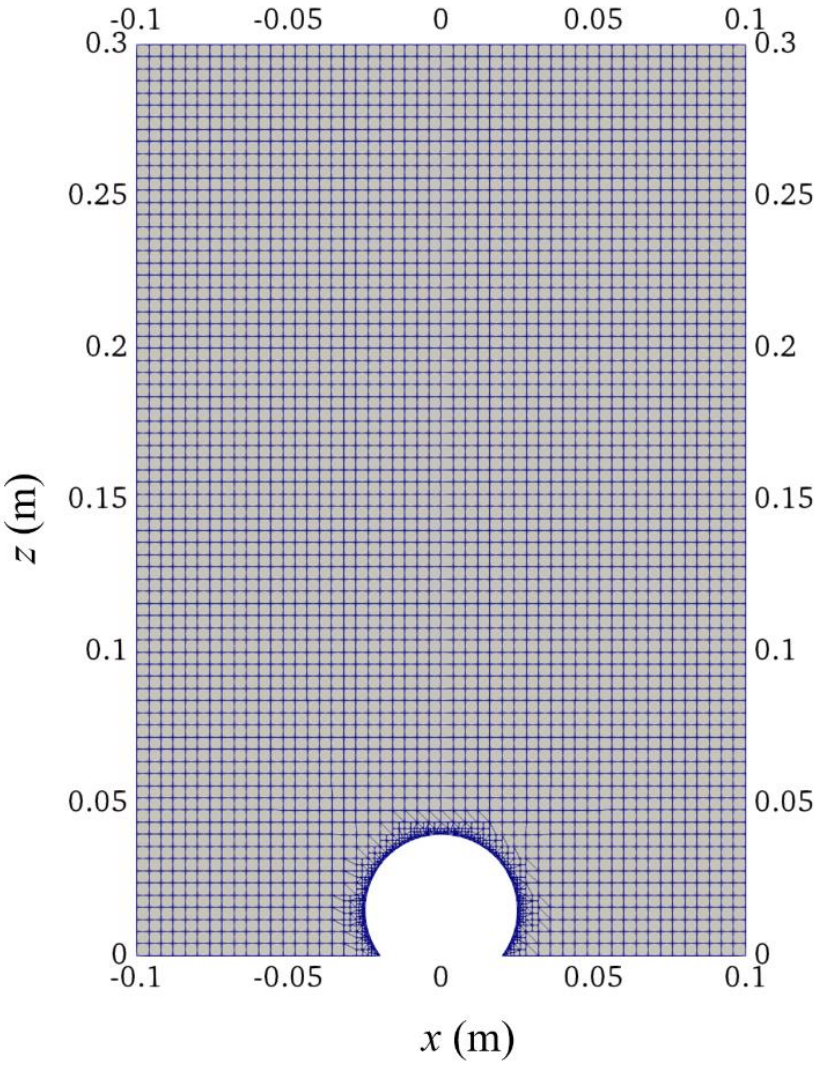

Figure. 4.7. The finite volume computational mesh for CFD calculations.

Table 4.2. Coupled CFD-DEM simulation parameters for model validation.

Parameter	Value
Water density (ρ_w) [kg/m^3]	1000
Water viscosity [m^2/s]	1x10^{-6}
Pipe diameter (D_0) [m]	0.05
Crack size (D) [m]	0.003
Model width (L) [m]	0.2
Model length (B) [m]	0.01
Sand layer thickness (h_s) [m]	0.2
Water level (h_w) [m]	0.3
DEM time step (Δt_{DEM}) [s]	1x10^{-7}
CFD time step (Δt_{CFD}) [s]	1x10^{-5}
CFD-DEM coupling interval [Δt_{DEM}]	100
Initial porosity of sand	0.4
CFD mesh size (Δx, Δy, and Δz) [m]	5x10^{-3}

The simulation results of the sand velocity field are presented in Figure. 4.8 and compared with snapshots from the experiment at three different time stamps, namely, 0.08, 5, and 10 seconds. It can be seen that the extent and velocity of the mobilized core of sand are comparable to those reported by Tang et al. (2017c) at the examined times. At 0.08 seconds, a relatively stagnant zone with lower velocity than the mobilized core is found in both the experimental and numerical results. This is a result of the flow dynamics considering that the sand does not flow continuously Instead, a submerged freefall arch develops which spontaneously creates cycles of obstruction and non-obstruction (flow) states. As such, lower sand velocity values can be observed near the outlet at the arch stabilization (obstruction) instances. Capturing this behavior is not guaranteed to match the experiment at all time steps for it is highly probabilistic and can simply be affected by the temporal resolution at which output is obtained. This can be observed at times 5, and 10 seconds as the sand velocity obtained from the numerical analysis appears to be slightly higher than the experimental values. Another reason for this could be the lower water head above the outlet compared to the numerical simulation, which incrementally decreases as time goes by. Further comparisons with other variables such as water and sand flowrates were not considered as the temporal resolution of the experimental data is 10 seconds in average. Nonetheless, the agreement between the overall extent of the mobilized core, velocity mapping, and the extent of the eroded

sand volume indicates that the model can capture the flow characteristics and deformations.

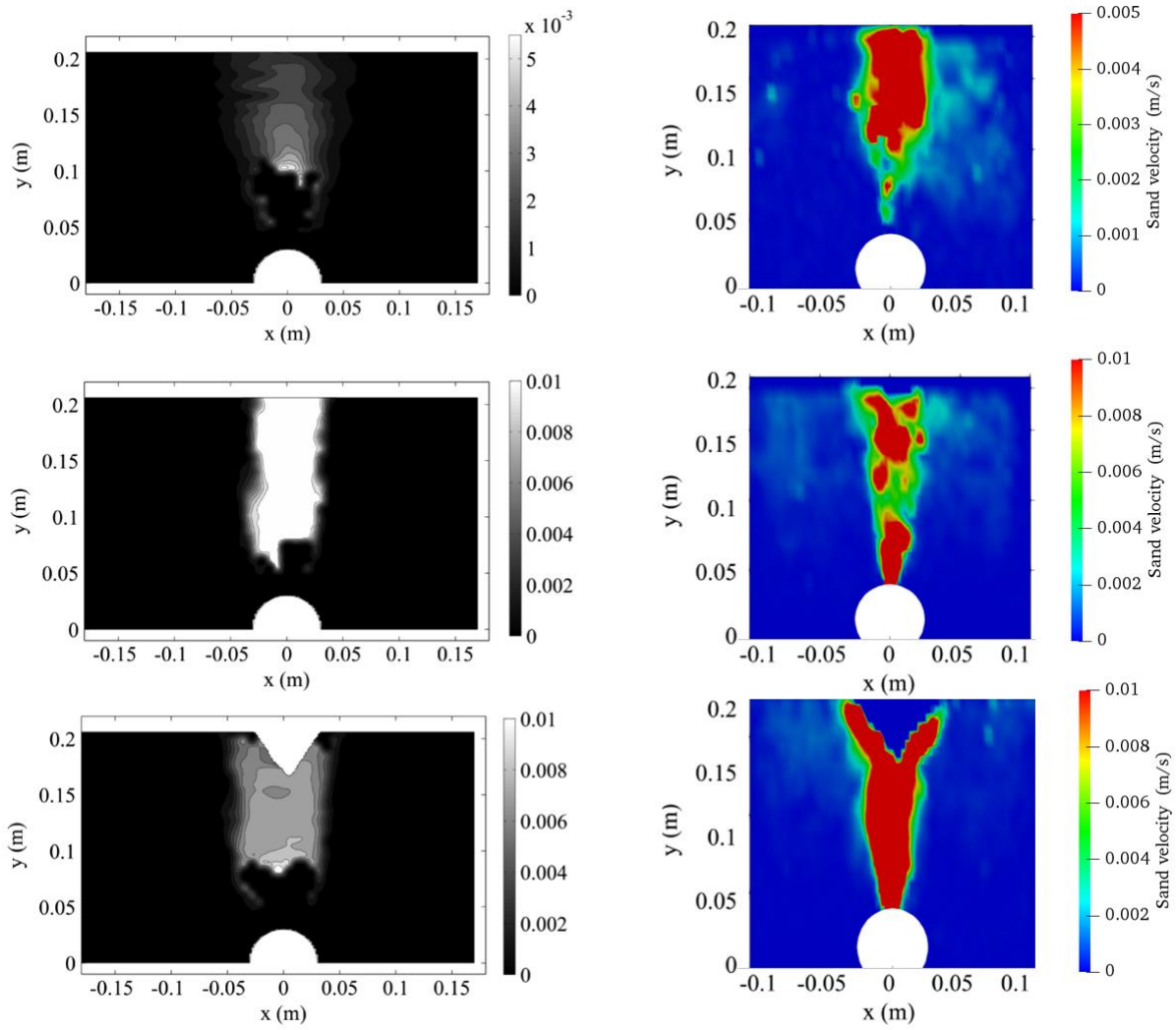

Figure. 4.8. A comparison between the sand velocity distribution obtained from the experiment (left) and the coupled CFD-DEM simulation (right) at times 0.08, 5 and 10 seconds.

4.4 Parametric analysis of sand erosion around sewer pipes

The parametric analysis is carried out in a similar numerical setting to that of the validation model shown in Figure. 4.4. The parameters considered for analysis are the water level (h_w), crack width (D), height of the sand layer (h_s), and the crack angle (θ) with respect to the horizontal. To further reduce the computational load, the height of the sand layer was kept to 0.15 m. Coarse sand with the particle size distribution shown in Figure. 4.5 is used, subsequently, the box width was taken as 0.02 m. The particle size distribution is nearly uniform with an average particle size of 1.5 mm. Thus, the effect of particle size distribution is

not discussed within the scope of this study, i.e., different mechanisms of erosion such as suffusion are not considered. Prior to the coupled CFD-DEM analysis, a series of only DEM simulations was performed to simulate the dry sand behavior. This is of utmost importance as it enables us to understand the fundamental difference between absence and presence of water. Furthermore, it provides an insight into the process of initiation of erosion driven by rise in water levels.

4.4.1 DEM simulation of dry sand

The flow of dry sand out of the crack was modeled with respect to three parameters: (i) crack width (D = 4 mm, 6 mm, 9 mm, and 12 mm), (ii) opening angle (θ = 90º, θ = 45º, and θ = 0º), and (iii) sand layer height (h_s = 0.1, 0.15, and 0.2 m). As for the latter, we also verify the existence of a freefall arch regime in the vicinity of the outlet. A freefall arch is a spontaneous spherical arch below which particles are allowed to fall freely under their own gravity as shown in Figure. 4.9 (Brown, 1961; Rubio-Largo et al., 2015). In the case of a rectangular opening, the arch is rather hemi-cylindrical as opposed to the hemispherical shape around a circular opening. The well-established Beverloo correlation (Beverloo et al., 1961) is used to describe the mass flowrate of granular materials in such regime as:

$$\frac{dM_s}{dt} = \frac{4\sqrt{C}}{\pi}\rho_s(1-n)\sqrt{g}\left(L-kd_p\right)\left(B-kd_p\right)^{1.5} \tag{4.18}$$

where M_s is the mass flowrate out of the crack, C is a constant that depends on the system; approximately equal to 0.58, n is the porosity of sand, L and B are the length and width of the crack, d_p is the mean particle diameter of sand grains, and k is another system constant ≈2.9.

The relationship in Eq. (4.18) implies that the mass flowrate of sand out of the system does not depend on the height of the sand layer above the outlet. Instead, it is controlled by the geometry of the crack and sand properties represented by the system constant. This is reflected in the simulation results in Figure. 4.10 showing the cumulative eroded mass for different sand layer heights. We note that although erosion results are better displayed in volume units, we hereafter show the results only in terms of eroded mass as it is the quantity measured directly from DEM simulations and so the accuracy of the results are not compromised. Nonetheless, one should be easily able to convert eroded mass to volume by dividing by $\rho_s(1-n)$. In Figure. 4.10, it can be seen that a constant rate of sand flow exists regardless of the initial height of the layer which is represented by a straight-line segment that agrees with Beverloo's correlation.

For h_s = 0.2 m and 0.15 m, the straight line segment continues till the end of the simulation time, indicating that the outlet was not exposed, i.e., the bottom of the eroded wedge remained above the outlet. For h_s = 0.1 m, a decline in the cumulative eroded mass is observed until it reaches a constant value when the flow completely stops.

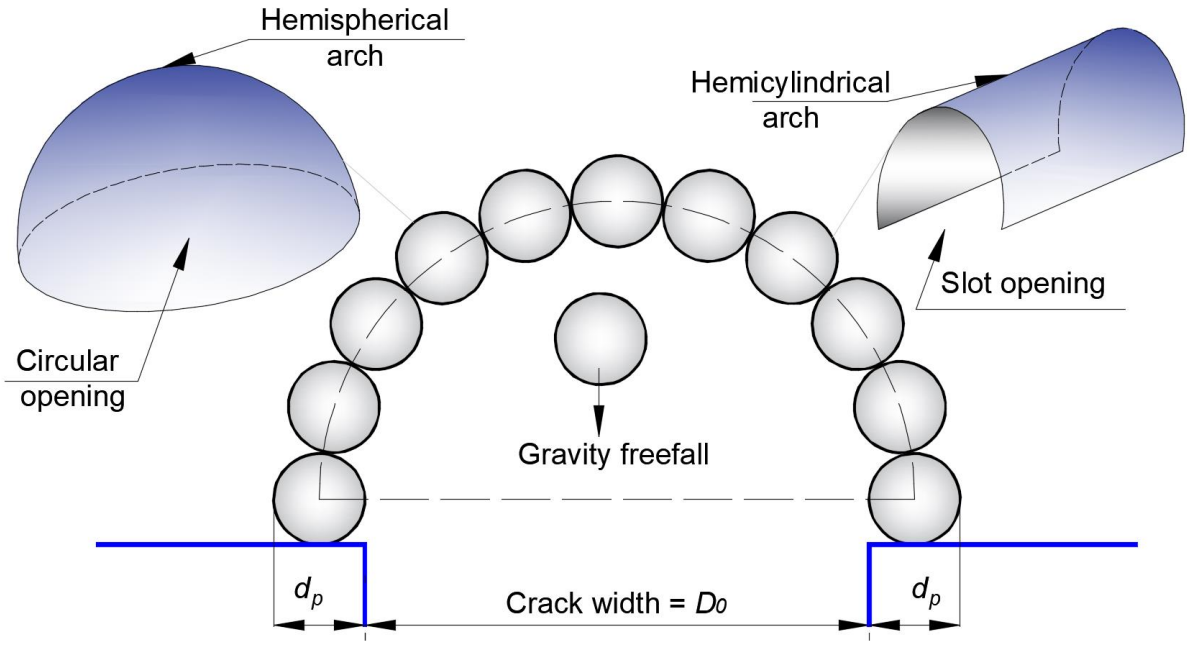

Figure. 4.9. A schematic for the spontaneous freefall arch around the pipe crack showing a three-dimensional depiction of the arch with respect to the shape of the crack.

The cycles of forming and collapsing the freefall arch can be interrupted by the formation of a so-called stable arch. In this case, the frictional forces developing between the particles are large enough to resist the avalanche energy, which dissipates gradually until the system comes to rest. This can be seen in the simulation cases for different opening angles shown in Fig. 4.11, where a stable arch was formed at angles 45º and 0º, while for vertical downward flow, θ = 90º, the flow of sand continued. Despite having the same opening size, D = 9 mm, for different inclination values, the maximum flow quantity and mobility is achieved when the flow direction aligns with gravity. This indicates that the recommended minimum opening width for having a continues flow of $D = 6d_p$ (Arevalo and Zuriguel, 2016; Rubio-Largo et al., 2015) is not valid for other opening inclinations as it is more likely to clog.

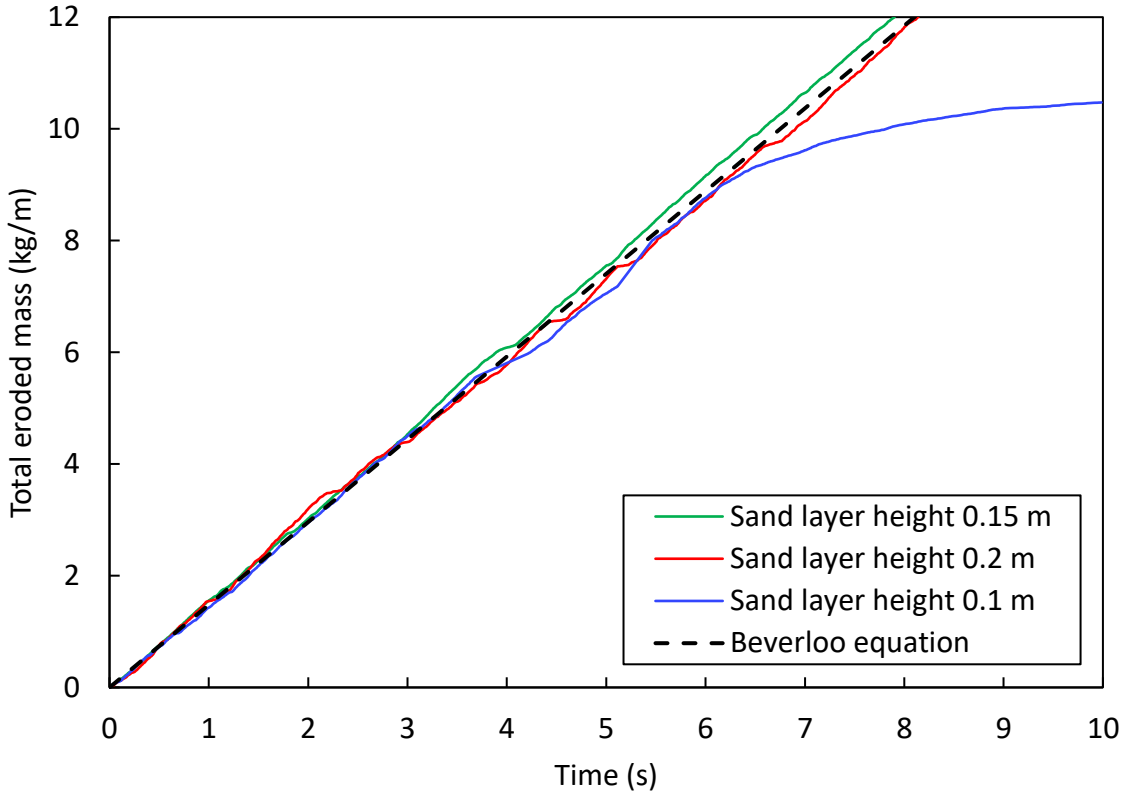

Figure. 4.10. The cumulative eroded mass during only DEM simulation for sand layer height 0.1, 0.15, and 0.2 meters in comparison with the cumulative mass from Beverloo correlation (Beverloo et al., 1961).

With respect to opening width, the formation of a stable arch seems to agree with the suggested minimum value of $6d_p$. For 6 mm and 4 mm opening size, it was observed that the flow was interrupted early on (Figure. 4.12) with approximately circular arch forming on top of the opening. The results for the cumulative eroded mass over time in Figure. 4.13 show that the formation of the stable arch happened almost immediately for the 4 mm opening case, while sand flow continued for approximately 2 seconds in the case of 6 mm opening. These observations are taken as a base for comparison between the behavior of dry and wet sand in terms of the erosion rate and the final eroded volume. Furthermore, the four specific scenarios where the outlet was clogged are of special interest as they provide an insight into the mobilization of particles and the initiation of internal erosion for previously stable situations.

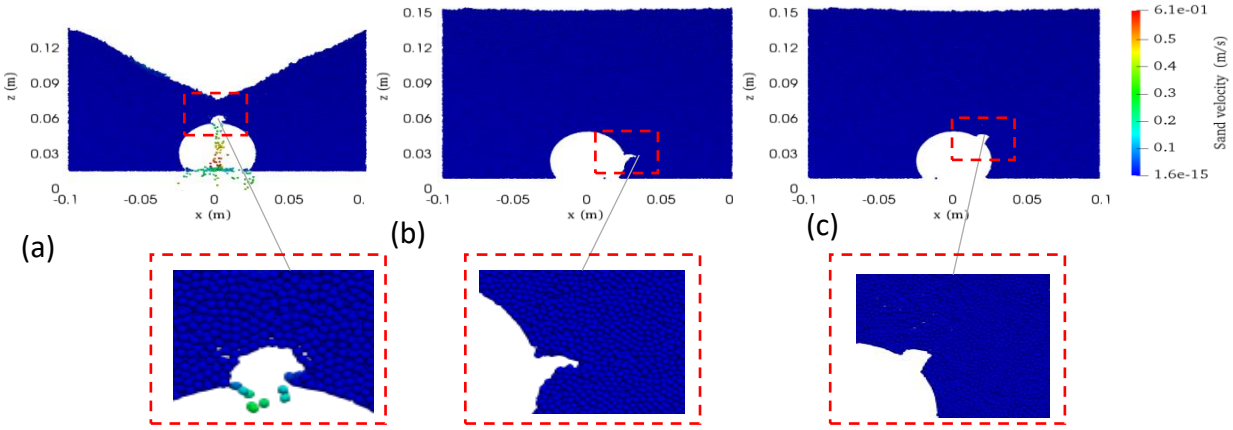

Fig. 4.11. DEM results at t = 10 s for the erosion of dry sand for opening angles (a) 90°, (b) 0°, and (c) 45°. It can be seen that erosion continues only for the 90° while a stable arch was formed in the other two cases.

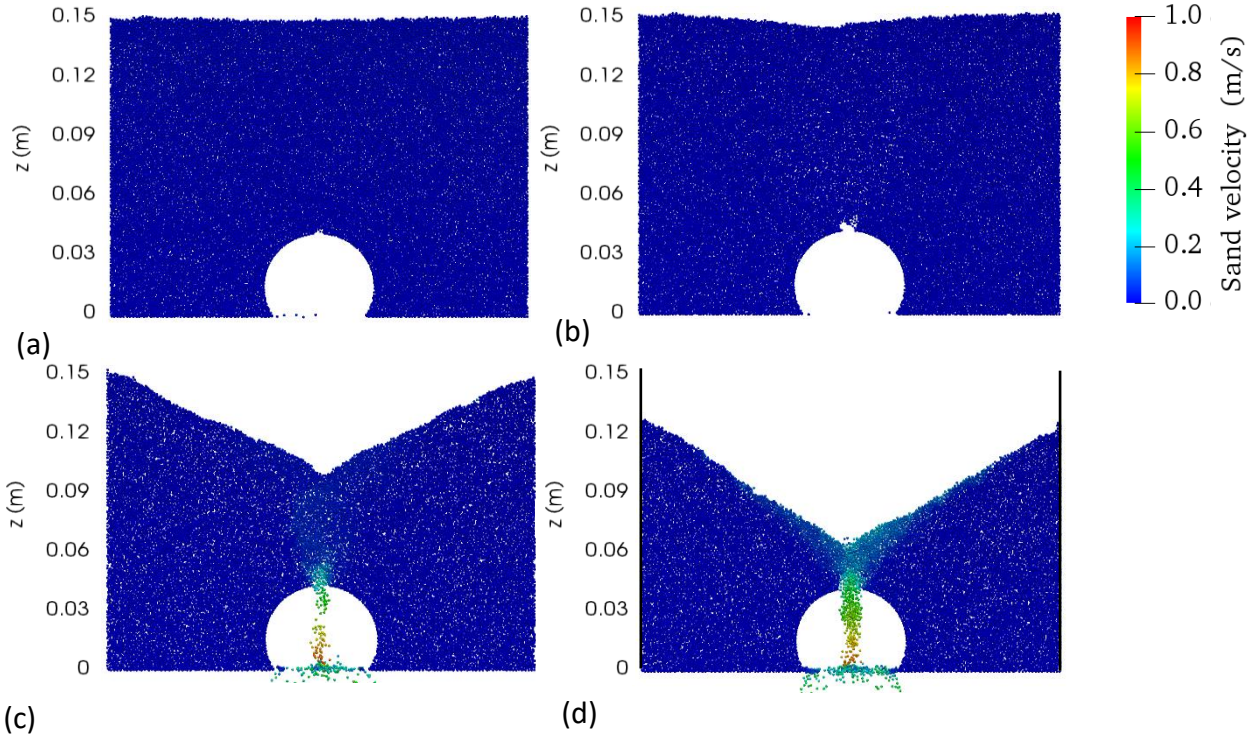

Figure. 4.12. DEM results at t = 5 s for the erosion of dry sand for different crack widths (a) 4 mm, (b) 6 mm, (c) 9 mm, and (d) 12 mm.

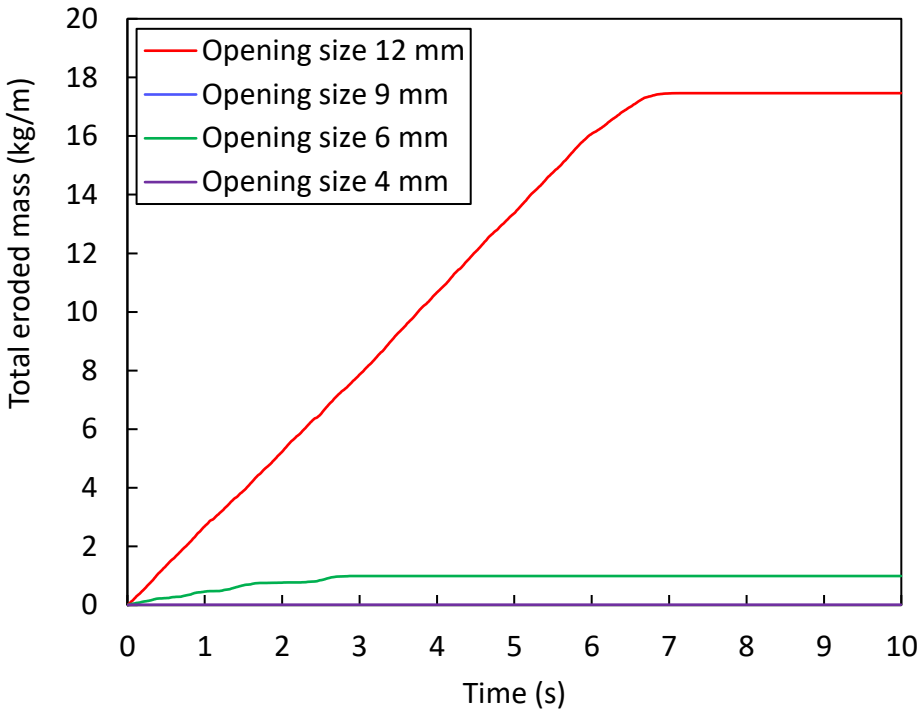

Figure. 4.13. DEM results for the cumulative eroded mass of dry sand over time for crack widths 4 mm, 6 mm, 9 mm and 12 mm.

4.4.2 The effect of variations in water level on erosion

The results for the cumulative eroded mass under different water levels in comparison with the dry sand case is shown in Figure. 4.14 for opening sizes of 9 mm and 12 mm. A basic observation is that the erosion mass rate and final eroded mass are always larger than that of dry sand. This is rather expected for the erosion rate because of the additional momentum provided by the water flow that drives the sand particles faster. Another important observation is that both the rate and total eroded mass are bound by an upper limit, referred to hereafter as the erosion plateau. Approaching this plateau value is represented in Figure. 4.14 by a decrease in the gap between the final eroded mass as water level increases. This implies that after reaching a certain water level both the rate and total eroded mass will not be affected by increasing the water level. This pattern appears in the 9 mm and 12 mm opening simulation cases, with a slight difference in the erosion plateau value. This could explain some of the experimental results reported in the literature such as Guo et al. (2013a). In their study, they report no significant variation in the erosion rate of sand with respect to groundwater level.

However, considering the relatively large water level used in the experiment compared to the defect size, the erosion rates have most likely been in the plateau region and therefore did not display significant changes. It is important to point out that this observation is not unconditionally valid for relatively high water levels (e.g., h_w > 5-6 h_s). This is because, when increasing the water level to such extent, different flow dynamics including powerful vorticity in the vicinity of the crack. Such violent vortices, when the thickness of the sand layer is relatively small, can lead to moving the sand particles upward and horizontally and expand the eroded area below the horizontal centerline of the pipe. Nonetheless, within the scope of this study, such extreme scenario is very unlikely as the ratio between groundwater level and the sand layer thickness is relatively small.

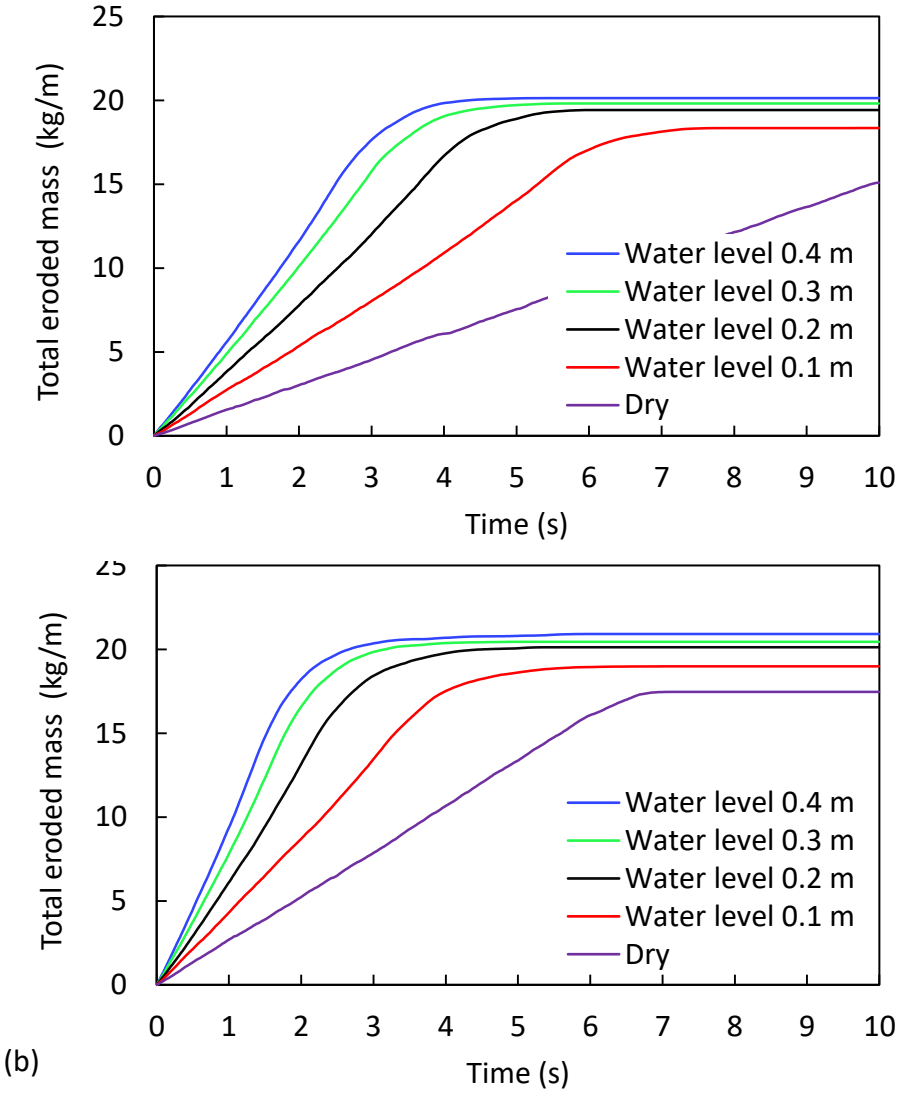

Figure. 4.14. Coupled CFD-DEM results for the cumulative eroded sand mass over time under

different water levels for (a) crack width 9 mm and (b) 12 mm.

Another variable of interest to quantify and characterize is the water flow in the vicinity of the crack into the pipe. This can be critical to estimate overflow into the pipe in case a relatively large defect exists or to characterize the transport of contaminants if they are to be washed away from the soil. Figure. 4.15 shows the volumetric flowrate of water through the outlet for different water level simulation cases. The evolution of water flowrate over time for all examined cases distinctly displays three different flow regimes. The first regime is seepage-like flow that is represented by the lower values on the left side of the graph. This regime corresponds to the freefall arch flow regime of sand where the flow of sand is relatively constant. At instances of arch collapse, the water flowrate is partially obstructed then relieved again in the instances of arch forming. This is evident in the non-monotonic pattern of water flowrate in the first regime as it shows slight fluctuations. The second flow regime manifests itself as a sharp increase in flowrate that also involves fluctuations similar to that of the first regime. This corresponds to the phase where the freefall arch flow system of sand is no longer valid and water no longer needs to percolate through sand out of the orifice. However, we note that during this phase the flow of sand has not yet come to a stop, hence the fluctuations of flowrate during this increase. The third and final flow regime is water flow solely out of the crack after the sand flow completely stops. This is represented by a horizontal flat line extending from the end of region 2 to the end of simulation time.

It is reasonable to approximately express the flow in the third region as orifice flow, where water flows under a constant head, $h_w^{'}$, through the outlet. The flowrate is then given as:

$$Q_w = C_d A\sqrt{2gh_w^{'}} \tag{4.19}$$

where C_d is the discharge coefficient, taken as 0.6, and A is the area of the orifice. The comparison in Figure. 4.16 shows a good match between the stead-state flowrate at the end of the simulation with the predicted values from orifice flow equation. As this further validates the accuracy of the results, the estimation of water flowrate during the freefall arch regime is not as straightforward. This is because considering seepage flow is only valid within the area outside the freefall arch. Within the arch region, the simultaneous flow of sand and water creates consecutive transient pressure waves as a result of throttling and relieving the flow (Fig.

4.17). These fluctuations in the pressure at the outlet is directly connected to the flowrate values and can be reduced to orifice flow such that: $Q_w = C_d A\sqrt{2\Delta p/\rho_w}$ as shown in Figure. 4.18. While the seepage flow approximated by a two-dimensional potential flow (Guo et al., 2013b) gives comparable results for flowrates, accounting for the effect of pressure transients might help explain the discrepancies between the numerical and experimental results.

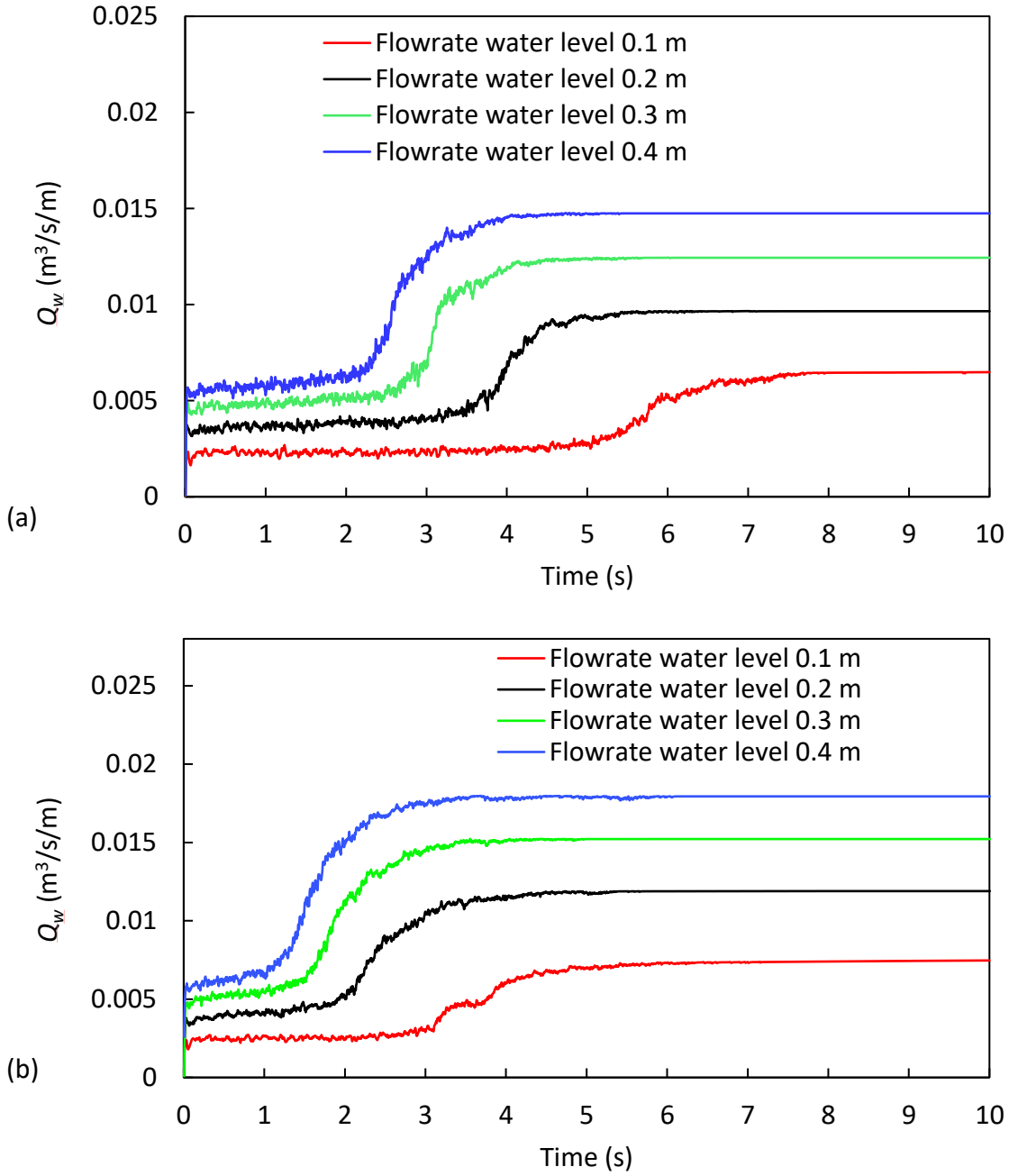

Figure. 4.15. Water flowrate through the crack under different water levels for opening size (a) 9 mm and (b) 12 mm.

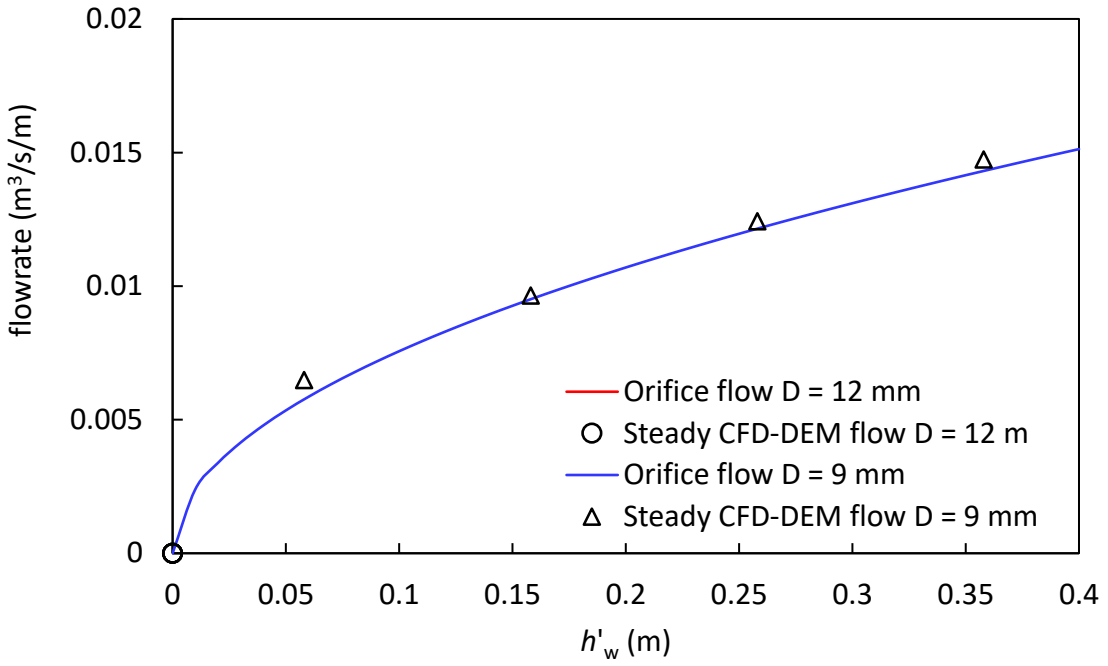

Figure. 4.16. A comparison between the flowrates obtained from CFD-DEM analysis and the corresponding orifice flowrate ($Q_w = C_d A\sqrt{2gh_w'}$) at steady state.

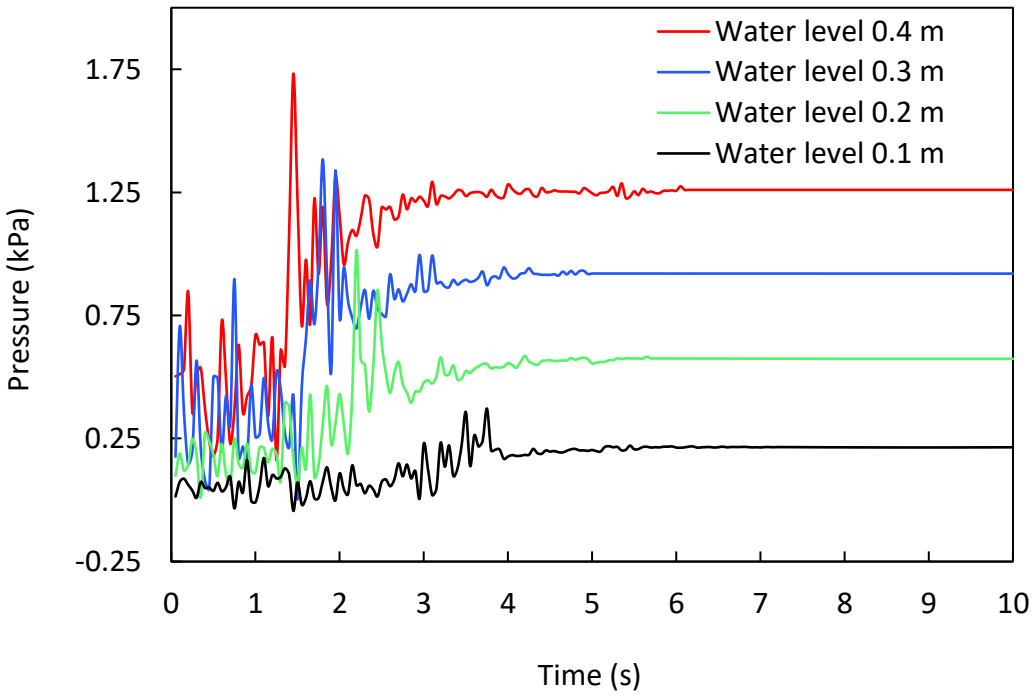

Fig. 4.17. The pressure time history at the pipe crack.

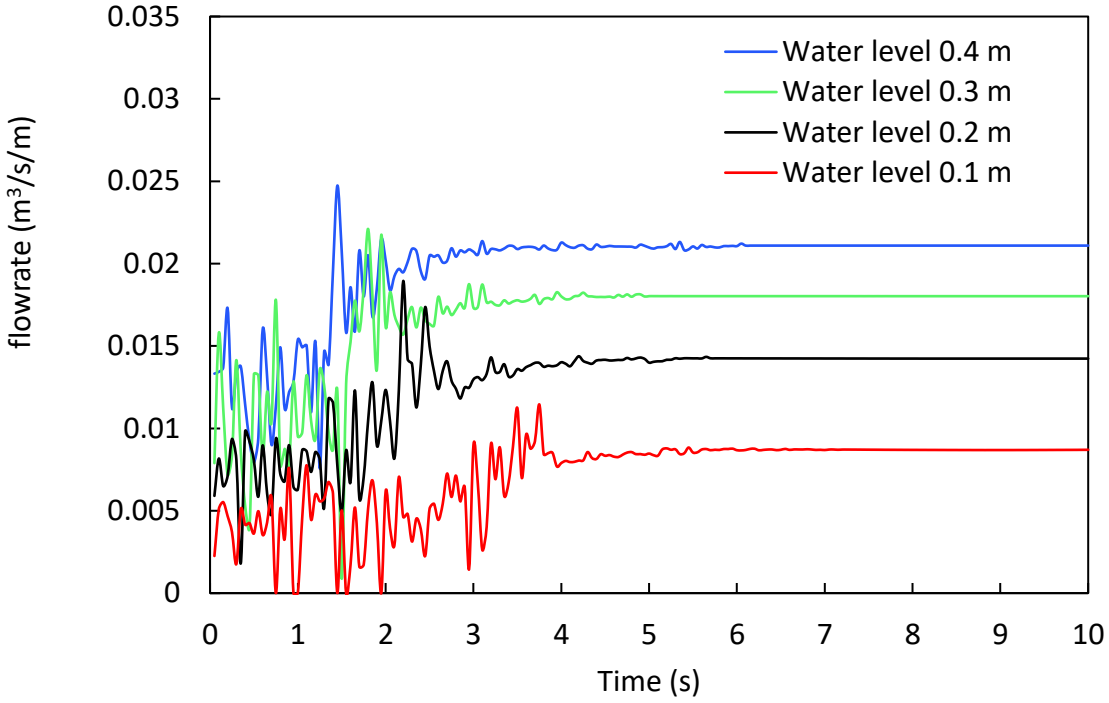

Figure. 4.18. The water flowrate values calculated from applying the orifice equation at the outlet following the pressure fluctuations at the outlet.

4.4.3 The effect of crack inclination angle

In the absence of water, the inclination of a crack, with respect to the vertical, provides a buffer against erosion as seen in the DEM simulation. With water involved, we can extend the investigation of the rate and extent of erosion to examine mobilizing erosion in situations that would otherwise be stagnant. The simulation results shown in Figure. 4.19 show the propagation of erosion for different crack inclination angles under a water level of 0.2 m. It can be seen that in addition to the increase in the rate of erosion experienced compared to the dry case for $\theta = 90^{o}$ (Figure. 4.14), the erosion continued for $\theta = 45^{o}$ and $\theta = 0^{o}$ as opposed to the dry case (Fig. 4.11). This is a direct result of the additional momentum contribution of water flow at the outlet which increases the kinetic energy of sand grains, and continuously disturbs the stability of the freefall arch. Furthermore, the fact that inclination angles smaller than 90^{o} pose larger water head at the outlet provides additional energy to the flow at the outlet. With that additional energy, however, the rate of erosion for $\theta = 45^{o}$ and $\theta = 0^{o}$ is observed to remain smaller than that of $\theta = 90^{o}$ where the flow of sand aligns with gravity (Figure. 4.20).

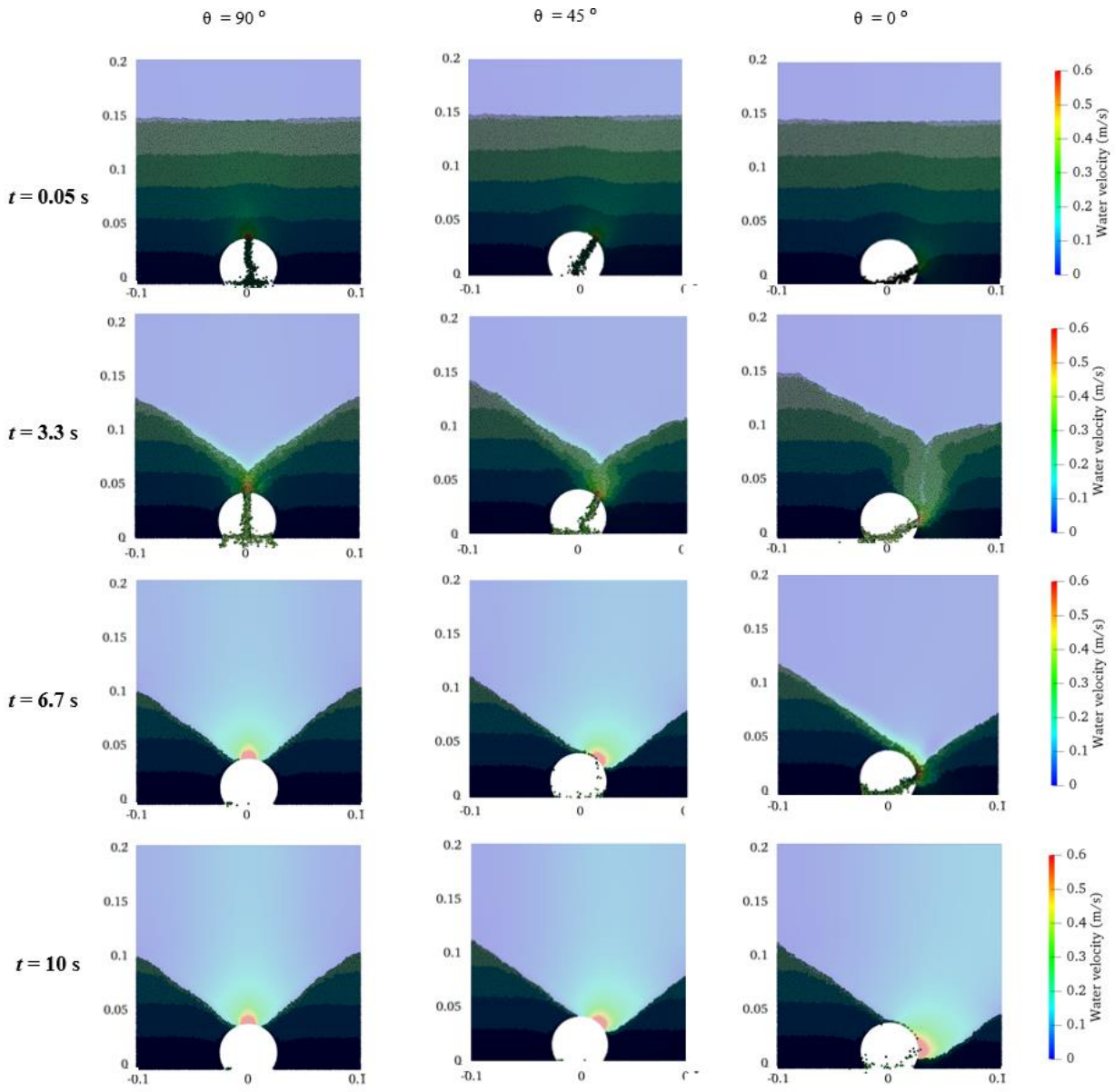

Figure. 4.19. Coupled CFD-DEM results for the erosion process $h_w = 0.2$ m for angles $\theta = 90°$, $\theta = 45°$ and $\theta = 0°$ a at $t = 0.05$, 3.3, 6.7 and 10 seconds.

Further investigation of the results of cumulative eroded mass shown in Figure. 4.20 shows that the total eroded mass, and the correspondingly eroded volume, became larger as the inclination angle decreased. The snapshots in Figure. 4.19 provide a better visual of this, where the point of intersection of the final resting slope and the pipe is slightly shifted from the edge of the crack. Thus, if we assume that the final deposition angle is comparable for different inclinations, the final eroded mass and volume are always larger for inclined cracks. This provides an interesting insight that allows one to define the critical condition for sand erosion

around a deteriorated pipe. That is, inclined cracks which are initially clogged in dry situations and would typically go undetected can become active and lead to large sinkholes or cavities. As one would not expect pipe cracks to always be at the pipe crown, we can fairly assume a number of clogged cracks that would only get activated upon a sudden rise in groundwater levels.

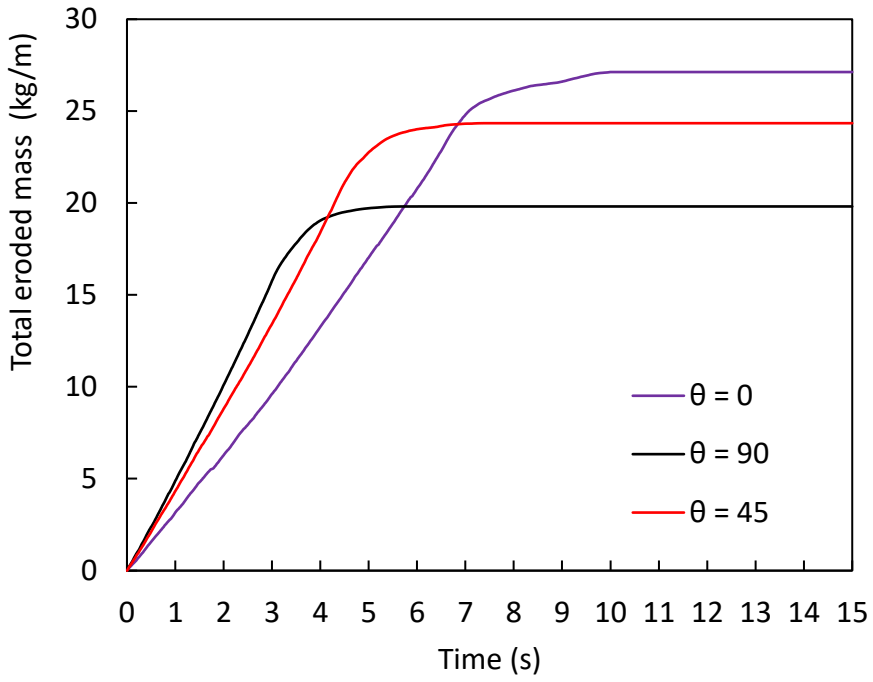

Figure. 4.20. The cumulative eroded mass of sand under water level 0.2 m for different angles.

4.4.4 The effect of crack size

The simulation results for different crack widths, D, under water level of 0.2 m are shown in Figure. 4.21. The results show the development of a stable arch for opening sizes of 4 mm and 6 mm similar to the flow behaviour in the dry condition. For a crack width of 6 mm, however, we observe continuation of the flow up to approximately 1 second before the flow stops. The total eroded mass is nearly 160% of that estimated in the dry case, which indicates some degree of mobilization that was yet not sufficient to continue driving the erosion. For crack width of 4 mm, the erosion almost stopped immediately at the beginning of the simulation with no noticeable differences from that of the dry case. In contrast to the mobilization of sand particles observed with crack inclination, narrowing the opening size below $6d_p$ seems to eventually stop

the sand erosion. One reason for this difference in mobilization could be because of the lateral force component exerted by water when the arch is inclined that work against its stability more than that if it were vertical.

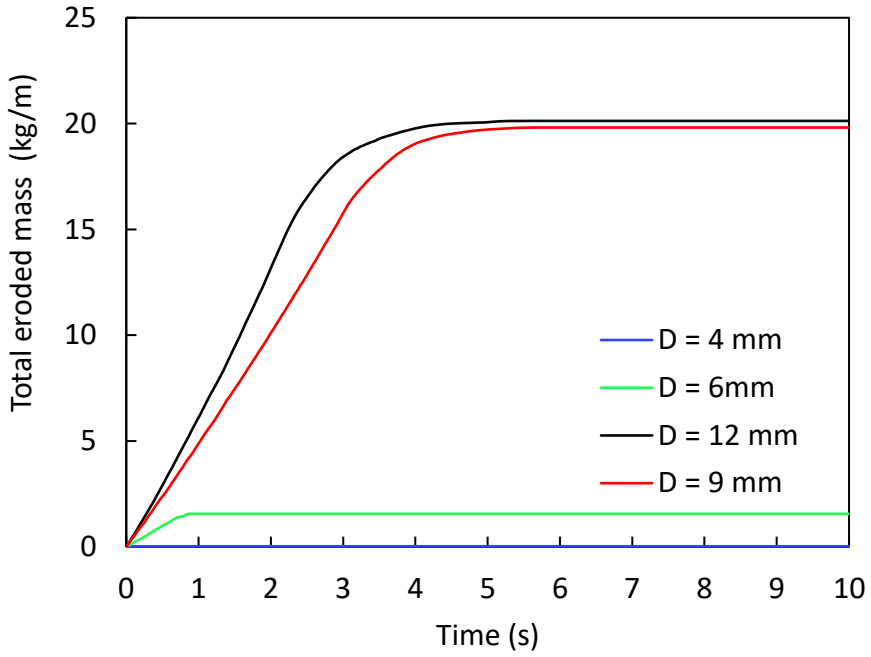

Figure. 4.21. The cumulative eroded mass of sand under water level 0.2 m for different crack sizes.

Another way to look at the issue of sand mobilization around the outlet is to examine the evolution of the kinetic energy of the system. As stated by Arevalo and Zuriguel (2016), the erosion process involves an initial avalanche that provides some kinetic energy required to help collapsing the arch formation at early times. Following that initial avalanche, if the kinetic energy of the particles in the vicinity of the outlet is sufficiently large, the erosion process will continue. Thus, a complete stoppage of erosion will be preceded by significant dissipation in the kinetic energy of the system. Here, we revisit the four "clogged" cases referred to earlier in the DEM simulation of dry sand. Figure. 4.22 shows the state of the sand bed in both dry and submerged cases as well as the evolution of kinetic energy over time in both cases. We observe that in the first two clogged cases of $\theta = 45^{o}$ and $\theta = 0^{o}$, the kinetic energy of the system continued to grow until a maximum value is reached near the end of the freefall arch regime before it starts decreasing as the sand deposition comes to a stable formation. In contrast, the

latter two clogged cases of D = 4 mm and D = 6 mm exhibit decline in the kinetic energy of the system until completely dissipated.

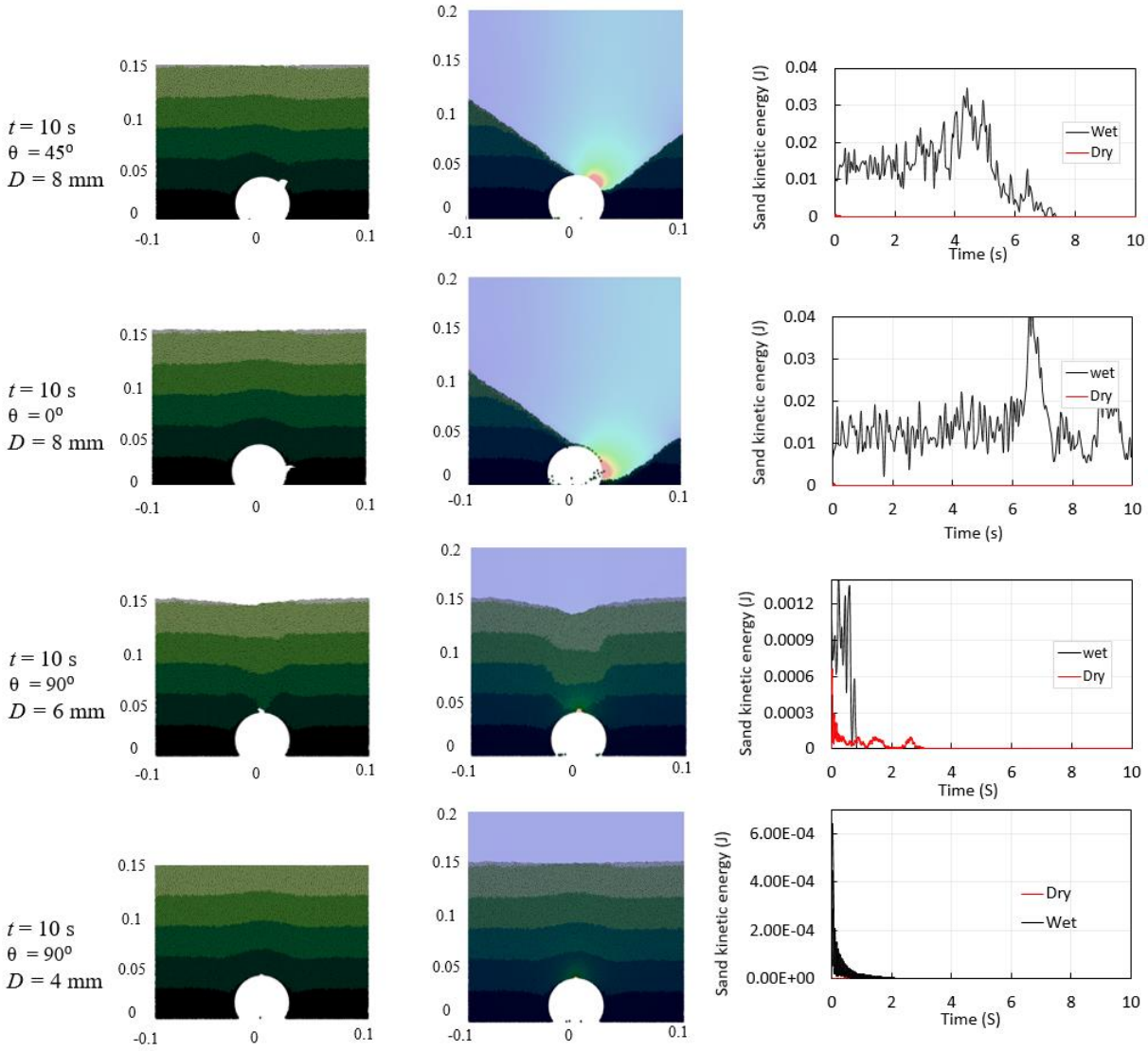

Figure. 4.22. A comparison between the dry and wet (h_w = 0.2 m) of the four cases where a stable arch was observed along with the corresponding evolution of the kinetic energy of sand in both cases.

4.4.5 The effect of sand layer thickness

With explanations of the erosion phenomenon made within the context of the freefall arch, we can expect a trend similar to that of Beverlee's correlation in the case of dry sand. That is, the thickness of the sand layer will not have a significant effect on the rate of erosion until the

outlet is exposed. Therefore, we conducted three different sets of simulation for three different

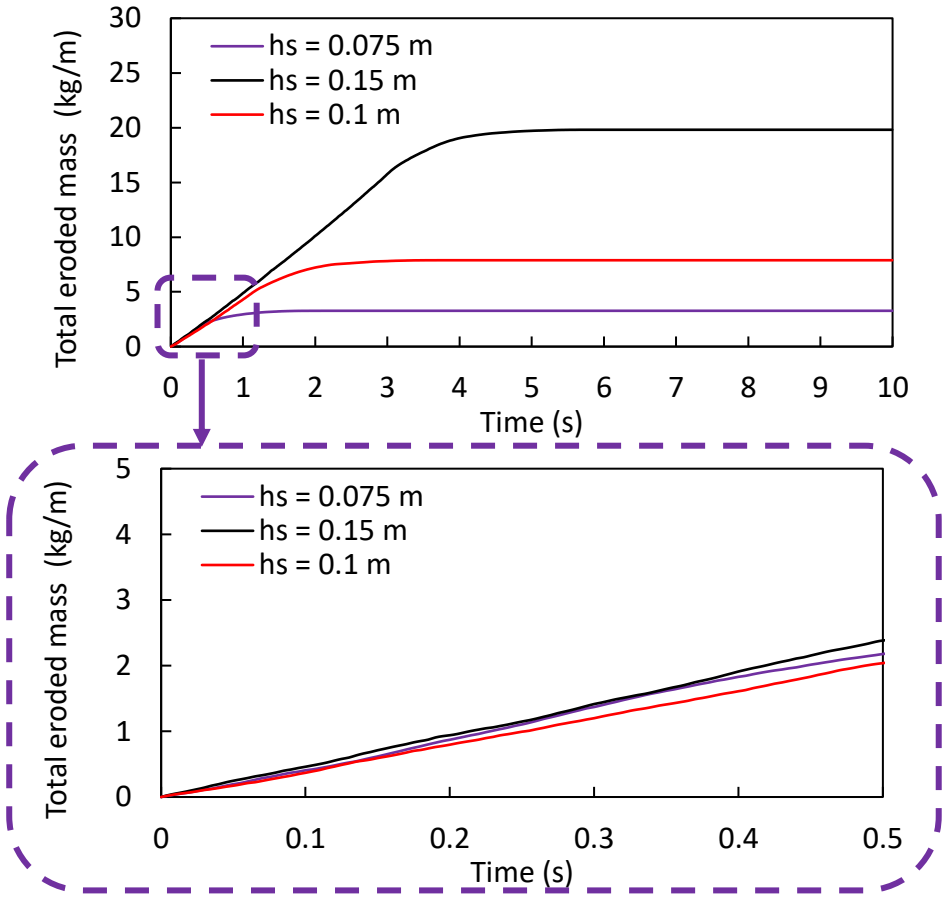

Figure. 4.23. The cumulative eroded mass of sand under water level 0.2 m for different sand layer height.

sand thickness, namely, h_s = 0.075 m, h_s = 0.1 m, and h_s = 0.15 m, under a water level of 0.2 m and opening size of 9 mm. It can be seen from the results in Figure. 4.23 that for the three different layer thicknesses the erosion rate calculated was nearly equal in the freefall arch region. This confirms our hypothesis on the erosion rate following a similar, yet larger, constant flowrate to that of Beverloo. Such increase in the sand flowrate can be attributed to a larger acceleration than that of g used in Beverloo's correlation caused by the contribution of drag forces. At the first glance, this observation seems to contradict the models proposed by Guo and Zhu (2017) and Tang et al. (2017c), in which, the thickness of the sand layer appears among the factors affecting the flowrate of sand. This can be explained in the light of the effect of the sand layer thickness on water flow, which is increased or decreased according to energy dissipated through sand. This in turn, affects the water seepage velocity which reflects on the contribution of drag force, and subsequently the sand flowrate. Considering the results obtained

in this study, the sand flowrate appears to be not sensitive to such indirect link between the sand layer thickness and the sand flowrate, neither during the decrease in sand layer height during erosion nor for different initial heights. Indeed, to validate this conclusion, further experimental and numerical investigations are needed to examine the sensitivity of the sand flowrate to variations in the thickness of the sand layer.

4.4.6 Approximate estimation of the total eroded mass

In this subsection we attempt to characterize and provide a simple approximation to estimate the extent of erosion, i.e., total eroded mass and volume. As observed from different simulations, the total eroded mass is always between a lower value that is the total erosion in the dry case and an upper value that is the erosion plateau. If we look at the relationship in Figure. 4.24 between the total eroded mass and the water level above the outlet, we can see that it follows an exponential plateau that can be expressed in the form:

$$M_e = M_0 + (M_t - M_0)\exp(-kh_w^{'}) \tag{4.20}$$

where M_e is the maximum eroded mass corresponding to differential water level $h_w^{'}$, M_0 is the maximum eroded mass for the dry condition, M_t is the value of the erosion plateau, and k is a system constant. By trial and error, it is found that the best value of k to fit the simulation data is $10/D$. In this case, Equation (4.20) is expressed as:

$$M_e = M_0 + (M_t - M_0)\exp(-h_w^{'}/10D) \tag{4.21}$$

With the value of M_0 and M_t drawn from the simulation data, we can construct the prediction shown in Figure. 4.24. Despite the good agreement obtained, it would be difficult to conventionally use such refined simulation to obtain the values of M_0 and M_t. Thus, by investigating the geometry of the final geometry of the sand bed after erosion we can draw some important relationships that reduce the estimation of M_0 and M_t to simpler geometric and material parameters. The first observation shown in Figure. 4.25 is that the final angle of repose is nearly equal in all simulations regardless of the water level above the crack. In our case the angle of repose of 36º remains constant under all different water levels. Notable to mention that this relationship is also valid for different inclinations of the crack. This observation enables us to construct the slope lines of the final sand formation given that we know where these lines intersect with the pipe in the vicinity of the crack. To determine this intersection, we first need to define the lateral scour region adjacent to the crack. As can be

seen in Figure. 4.25, the final slope intersects with the pipe at some distance (scour width), S_w, from the edge of the crack. This lateral shift does not exist in the dry case as the final slope intersects with the pipe right at the edge of the crack, while it becomes larger with increasing the water level. This is the main reason why the final eroded volume when water is involved is larger than that of dry sand despite ending at the same angle of repose.

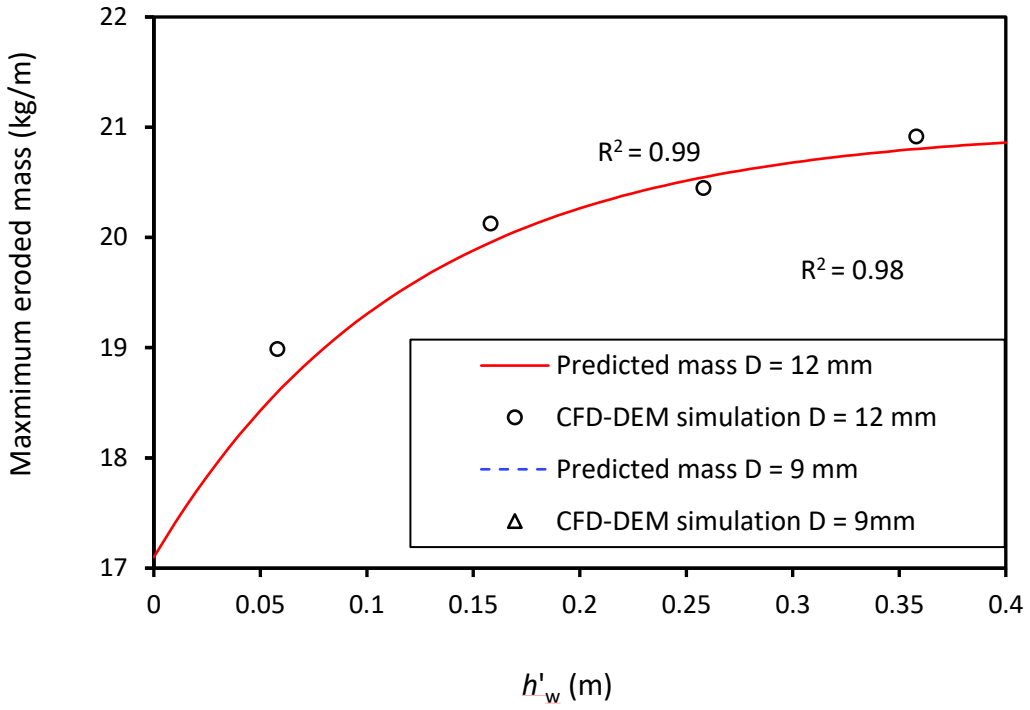

Figure. 4.24. The final eroded mass of sand under different water levels compared with the proposed exponential plateau correlation: $M_e = M_t - (M_t - M_0)\exp(-h_w'/10D)$.

The local scour regions around the crack are in fact generated after the outlet is completely exposed such that streamlines of water converge to reach steady-state. This can be seen in the slight curvature where the sand comes in contact with the pipe, which in fact represents the streamlines of water in that region. For simplicity, we neglect this curvature at the contact region and assume that final slope is a straight line. We also observe that the increment in the scour width decreases as the water level increases until it reaches a constant value, which indicates a more fundamental reason as to why the final eroded volume exhibits

the exponential plateau trend. In terms of quantifying the scour width, we find that the normalized scour width, S_w/D, and the water level above the crack is approximately the same for different crack sizes (Figure. 4.26). Indeed, this relationship needs further validation with a larger set of data, however, within the data availability here we can assume that this is a characteristic curve for the scour width. With the value of scour width obtained, we can fully characterize the final deposition of sand by only incorporating the angle of repose, water level, and the size of the crack. A simplified approximation is presented in Figure. 4.27 for the relationship between the water level and the normalized eroded mass, M_tD/S_w, which shows comparable results for different crack sizes. This final simplification reduces the calculation of the total eroded mass to only using the two curves provided in Figure. 4.26 and Figure. 4.27. Using these simplifications to recalculate the total eroded mass obtained from the numerical simulations results in deviation between 2.5%-5%, which is quite acceptable. Indeed, more validation remains necessary to build more confidence in these results both experimentally and numerically.

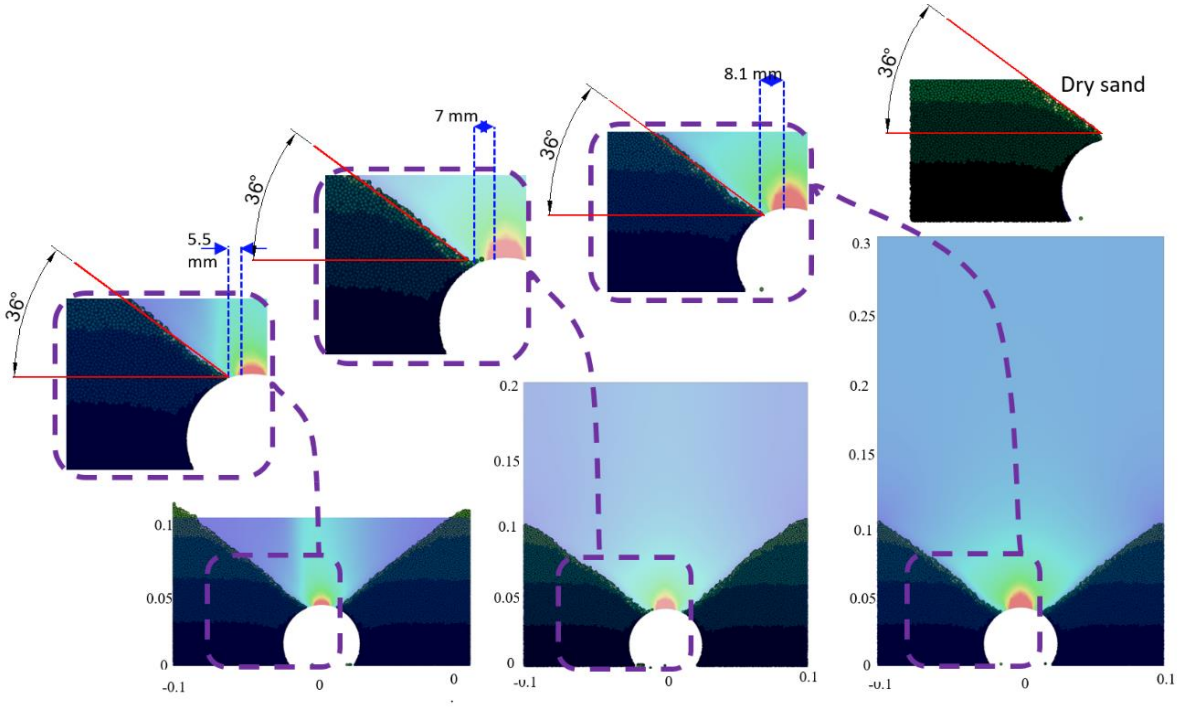

Figure. 4.25. The angle of repose and extent of the local scour region around the crack for different water levels and crack width of 9 mm.

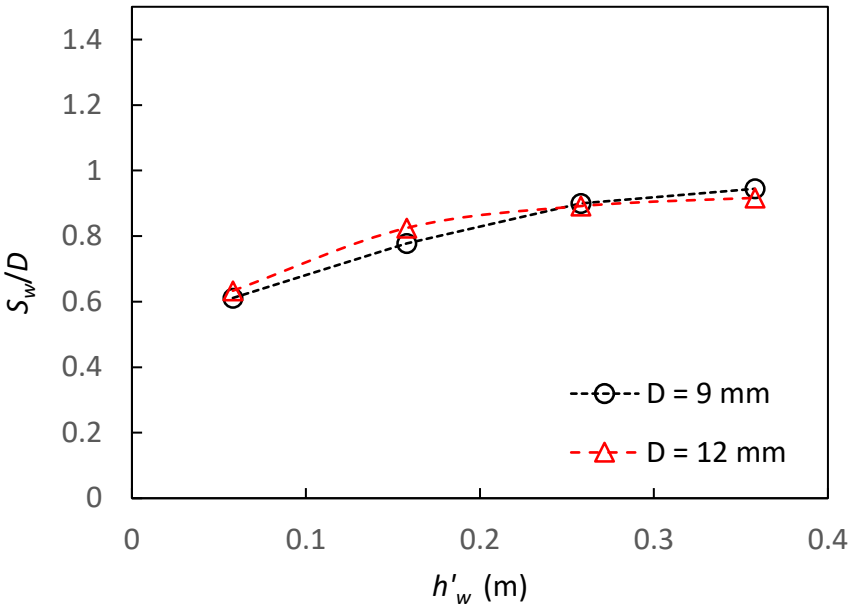

Figure. 4.26. The normalized width of local scour region S_w/D with respect to the differential water level h'_w (m).

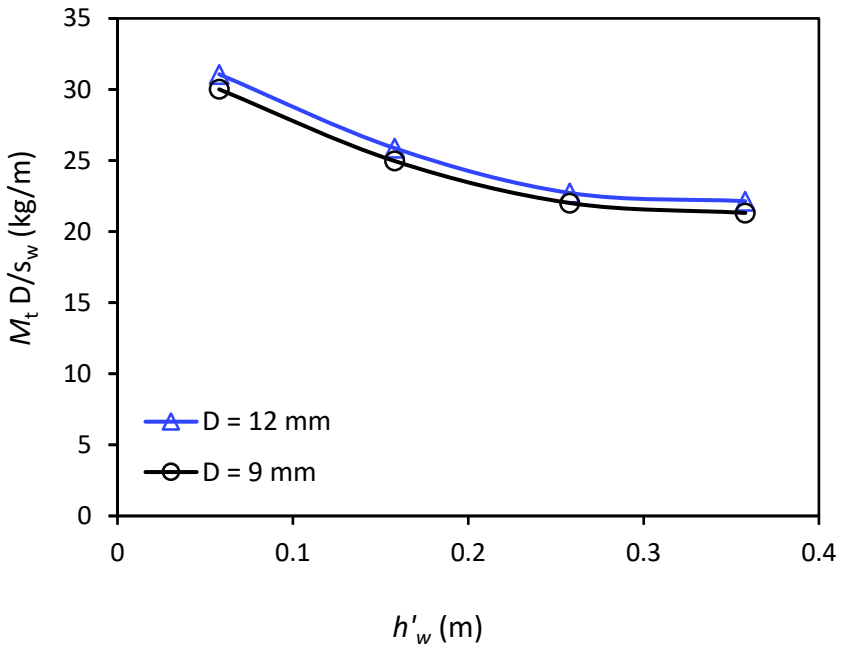

Figure. 4.27. The normalized total eroded mass, M_tD/S_w with respect to the differential water level h'_w (m).

4.5 Conclusions

In this study, a series of numerical investigations is performed to investigate sand erosion into defective gravity pipes in the presence of groundwater. Following the model validation, a parametric study was conducted to examine the effect of water level, the size and of defect, and the thickness of the sand layer above the pipe. In the light of these simulations, the following conclusions could be drawn:

1. The rate and the final extent of erosion increase with increasing the water level above the pipe.
2. The final eroded mass and volume are always bounded by a lower limit that occurs when the sand is dry, and an upper limit that occurs at a certain water level, above which, no increase in the eroded volume was observed.
3. The angle of repose in all examined cases was observed to be approximately equal to that of the dry sand and was not affected by changing the water level or the inclination angle of the defect.
4. A simplified relationship to obtain the final eroded volume with respect to different water levels is developed in terms of the angle of repose, crack width and the water level.
5. For defects inclined from the crown of the pipe, although less critical in dry cases, are likely to become active and cause larger eroded zones than defects located as the crown.
6. A freefall arch flow regime was present in both dry and submerged conditions where the erosion rate relies only on the geometry of the defect and the sand properties, where the thickness of the sand layer did not significantly affect the erosion rate in either case.

Preface to chapter 5

In chapter 5, we follow up on employing the coupled CFD-DEM model to practical geotechnical problem. Here, we investigate the clogging of geotextile filters by fine particles from adjacent soils in tunnel drainage systems. Initially, a framework for numerically representing and testing the non-woven geotextiles used in tunnel drainage. Afterwards, a set of boundary conditions on a scale of an idealized crack is developed. The properties of the geotextile drawn from the tests are then validated. Following validation, a parametric study is conducted to examine the effect of the content of fine particles in the surrounding soil, groundwater ingress, and the inclination angle of the crack. Finally, a semi-analytical model is developed to describe the pressure increase within the drainage layer due to clogging.

Chapter 5

CFD-DEM Modeling of the Geotextile Clogging in Tunnel Drainage Systems†

Abstract

In drained tunnels, it is crucial to maintain a properly functional drainage layer to avoid the build-up of water pressure. Reduction in the in-plane permeability of geotextiles used for drainage can lead to such excessive water pressure as the groundwater drainage capacity decreases. One of the reasons responsible for permeability reduction is the clogging of the geotextile filters by fine soil particles adjacent to the geotextile and mobilized by groundwater inflow or ground movement around the tunnel. In this study, we carry out a set of coupled Computational Fluid Dynamics-Discrete Element Method (CFD-DEM) simulations to numerically investigate the hydraulic deterioration of the geotextile layer on the spatial scale of a crack. Initially, a framework is developed to generate and test a numerical representation of non-woven geotextiles. A new set of boundary conditions are then derived to express the restraints on the water and fine particles movement within the crack. Parametric analysis is conducted to examine the effect of the content of fines, crack angle, and groundwater inflow. The results show that a general trend of pressure increase associated with increasing both the crack angle and the content of fines. This increase was observed to decay at larger crack angles in simulation cases involving high content of fines. The developed model was able to capture some interesting flow dynamics at high inflows such as local piping alongside the effect of clogging. Interestingly, increasing the groundwater inflow was found to have minimal effect on the final deposition of the clogging particles. Finally, an approximate semi-analytical model was developed to describe the pressure increase due to various cases of clogging. The model was able to decently provide a good match with the data obtained from the simulation.

Keywords:

Geosynthetics, tunnel drainage; CFD-DEM; hydraulic deterioration; geotextile clogging

† A version of this manuscript is currently available online in *Geotextiles and Geomembranes Journal*.

5.1 Introduction

Groundwater drainage is a critical component in tunnel systems that prevents undesired build-up of water pressure on tunnel linings. In some cases, such as that of sealed tunnels, the permanent lining is designed to withstand the hydrostatic water pressure. However, in drained tunnels, pressure accumulation on the permanent lining can be quite detrimental to the structural stability of the tunnel (Shin et al., 2005). Therefore, it is necessary that the drainage system performs properly over time so as to provide the needed pressure relief. In this study, an emphasis is placed on double-shell drainage system, which typically consists of a layer of impermeable geomembrane for sealing, overlain by a layer of non-woven geotextile (Kolymbas, 2005). The groundwater flow into the tunnel, radial flow in the case of circular tunnels, is collected within the geotextile drainage layer and guided circumferentially to the side drainage pipes (Figure 5.1). Above the geotextile layer, a layer of shotcrete exists as primary lining that is constructed early on during the excavation phase. Although the permeability of the shotcrete is significantly low (Wang et al., 2015), the groundwater flow into the tunnel passes through fissures/cracks and drainage pipes passing through the shotcrete layer. Within this system, the drainage functionality is mainly governed by the performance of the geotextile layer. Hydraulic deterioration of the geotextile (i.e., reduction in its in-plane permeability) leads to higher pressure gradients in the drainage layer and ultimately reduces the flow drainage capacity of the geotextile.

Hydraulic deterioration of geotextiles can happen for different reasons such as precipitation of carbonates or other compounds dissolved in groundwater (e.g., calcium) due to changes in pressure and temperature conditions (Kolymbas, 2005). Another reason for hydraulic deterioration is clogging by soil particles adjacent to the geotextile that are mobilized to infiltrate the geotextile under external pressure or suffusion through larger pores. The geotextile-water-soil interaction is not limited to clogging but includes a range of other phenomena such as blinding (external clogging) and piping (Lafleur, 1999). Several studies were conducted to investigate the hydromechanical impact of geotextile hydraulic deterioration on the structural element of tunnels (e.g., Jung et al. (2013); Shin (2008); Shin et al. (2014); Yoo (2016)). A significant body of literature on geotextile hydraulic performance is dedicated to filtration applications in landfills (e.g., Rowe et al. (2000) Palmeira et al. (2008); Rowe and Yu (2013); VanGulck and Rowe (2008)). In the context of tunnel drainage, Kim et al. (2020) recently presented an experimental and numerical investigation of deposition of different compounds such as iron oxides and calcium carbonate on the performance of geotextile

drainage layer in tunnels. A similar study was performed by Yoo (2016) to examine the hydromechanical interaction induced by pressure increase within the geotextile layer on the body of the tunnel. As far as these studies are concerned, some simplifying assumptions are always involved to reduce the complexity of the problem. This includes specifying mass inflow of a certain clogging component, starting off with predetermined pressure, or prescribing reduced geotextile permeability. Indeed, these assumptions are well-justified within the context of their respective studies. However, a more wholistic and general framework that explains the dynamics of hydraulic deterioration in terms of more fundamental factors such as the properties of the soil in the vicinity and groundwater conditions is yet to be developed. This, of course, is quite complicated and requires in-depth analysis of both the micro-mechanics and macro-mechanics of the system.

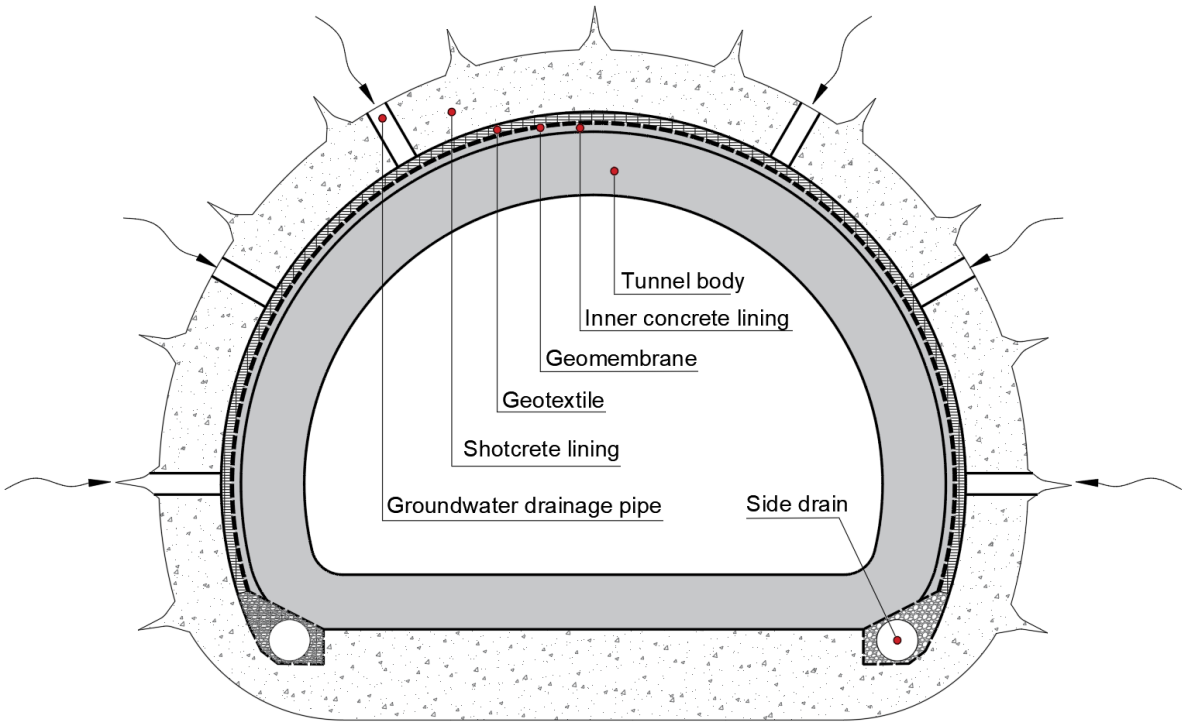

Figure 5.1. A schematic showing the configuration of the double-shell drainage system in a tunnel.

The outstanding challenge with developing this model is the overwhelming computational cost if we are to model a full-scale tunnel system. This is because the flow of both water and fine particles needs to be resolved at a scale smaller than that of the pore space of the geotextile. However, such refined analysis may turn feasible if performed on the spatial level of a crack/fissure such that upon assembling cracks at different locations it can help us map the

interactions over the tunnel perimeter. Coupled Computational Fluid Dynamics – Discrete Element Method (CFD-DEM) (Tsuji et al., 1993; Tsuji et al., 1992) is a suitable approach to perform the analysis of mixed water-fines flow within geotextiles. Although different frameworks for coupled analysis for solid-liquid mixtures are available, they are either relatively computationally expensive such as fully Lagrangian approaches (Naili et al., 2005) or involves local averaging that is not suitable for the nature of the problem such as continuum based methods (Ibrahim and Meguid, 2021). In CFD-DEM framework, the solid particles are tracked using the Newtonian equations of motion while the water flow is resolved using the volume-averaged Navier-Stokes equations (Anderson and Jackson, 1967). Some studies attempted to carry out coupled CFD-DEM analysis of soil-water mixture flow through geotextile filters (e.g., Puderbach et al. (2021); Rief et al. (2011)). In these studies, the geotextile filter is numerically represented as a wall element that prevents the flow of both water and solids. Such representation of the geotextile highlights a fundamental difference between these models and the problem considered in this study. That is, in filtration applications, woven geotextiles are generally used, which makes it possible to represent the geotextile numerically as perforated walls. The flow dynamics concerned in such case are basically the flow around the filter as well as passing/blocking of the particles. In tunnel drainage, however, nonwoven geotextiles are exclusively used, which adds magnitudes of complexity to the numerical analysis of the problem. In addition, the main flow dynamics of interest happen within the geotextile layer, and consequently, a significantly higher level of CFD mesh refinement is needed to resolve the flow within the textile filaments.

In this study, we numerically investigate the mechanism of non-woven geotextile clogging by fine particles coming from the adjacent soils in tunnel drainage systems. Firstly, a framework is developed for the numerical representation of non-woven geotextiles. The hydraulic and retention properties of the created geotextile are then tested to ensure that its properties align to a reasonable extent with values reported in the literature. After the validation of the geotextile properties, a new set of boundary conditions are developed to represent the flow restraints at a crack level. Initially, the developed configuration is tested considering unclogged conditions to further validate the properties of the geotextile and ensure that the modeled pressure gradients in the system match the theoretically expected values. For clogged conditions, the soil particles are allowed to infiltrate the geotextile under the effect of their own weight and radial flow. A parametric study is conducted to examine the effect of crack angle, percentage of fines in the soil and groundwater inflow into the tunnel. Finally, a simplified

mathematical model that describes the pressure changes in the geotextile layer due to clogging is developed based on the flow characteristics and the data obtained from the analysis.

5.2 Numerical analysis

5.2.1 Governing equations

In coupled CFD-DEM framework, the governing equations for the fluid phase consist of the volume-averaged continuity and Navier-Stokes equations (Anderson and Jackson, 1967a; Kloss et al., 2012):

$$\frac{\partial \alpha_f}{\partial t} + \nabla \cdot \left(\alpha_f \mathbf{u}_f \right) = 0 \tag{5.1}$$

$$\frac{\partial \left(\alpha_f \mathbf{u}_f \right)}{\partial t} + \nabla \cdot \left(\alpha_f \mathbf{u}_f \mathbf{u}_f \right) = -\alpha_f \nabla \frac{p}{\rho_f} - \mathbf{R}_{pf} + \nabla \cdot \boldsymbol{\tau} \tag{5.2}$$

where α_f is the volume fraction of the fluid, $\mathbf{u}_f$ is the fluid velocity, p is the fluid pressure, $\boldsymbol{\tau}$ is the volume-averaged shear stress tensor of the fluid, ρ_f is the density of the fluid, and $\mathbf{R}_{pf}$ is an equivalent tensor for the momentum transfer between the two phases representing interaction forces. Among different particle-fluid interaction forces, buoyance and drag forces are considered to be the most significant for water-fines interaction (Ibrahim and Meguid, 2020). With buoyance force implicitly accounted for in the pressure gradient term in Equation (4.2), the interaction tensor reads:

$$\mathbf{R}_{pf} = \mathbf{K}_{pf} \left(\mathbf{u}_f - \left\langle \mathbf{u}_p \right\rangle \right) \tag{5.3}$$

where $\left\langle \mathbf{u}_p \right\rangle$ is the cell-based average velocity of a solid particle and $\mathbf{K}_{pf}$ is the momentum transfer coefficient. Different drag correlations are available in literature such as those proposed by Di Felice (1994) , Gidaspow (1994), Kafui et al. (2002), Koch and Hill (2001) and Tsuji et al. (2008).

A combination of the drag correlations of Wen and Yu (1966) Ergun (1952) are used. For

$\alpha_f > 0.8$, that is relatively fluidized flow regime:

$$\mathbf{K}_{pf} = \frac{3}{4} C_d \frac{\alpha_f \left(1-\alpha_f\right)\left|\mathbf{u}_f - \mathbf{u}_p\right|}{d_p} \alpha_f^{-2.65} \tag{5.4}$$

where d_p is the mean particle diameter and C_d is the drag coefficient which is given as:

$$C_d = \frac{24}{\alpha_f \,\mathrm{Re}_p}\left[1+0.15\left(\alpha_f \,\mathrm{Re}_p\right)^{0.687}\right] \tag{5.5}$$

where Re_p is the particle Reynold's number: $\mathrm{Re}_p = \left|\mathbf{u}_f - \mathbf{u}_p\right| d_p / \nu_f$. For denser flows with $\alpha_f \le 0.8$, the momentum transfer coefficient is given by Ergun's equation:

$$\mathbf{K}_{pf} = 150 \frac{\left(1-\alpha_f\right)^2 \nu_f}{\alpha_f d_p^2} + 1.75 \frac{\left(1-\alpha_f\right)\left|\mathbf{u}_f - \mathbf{u}_p\right|}{d_p} \tag{5.6}$$

As for the solid phase, the equations of motion of the solid phase, considering the interaction forces with the surrounding fluid are given as (Kloss et al., 2012):

$$m_i \frac{d\mathbf{v}_i}{dt} = \sum_{j=1}^{k_c} (\mathbf{f}_{i,n} + \mathbf{f}_{i,t}) + \mathbf{f}_{i,b} + \mathbf{f}_{i,pf} \tag{5.7}$$

$$I_i \frac{d\boldsymbol{\omega}_i}{dt} = \sum_{j=1}^{k_c} \mathbf{r}_{ij} \times \mathbf{f}_{i,t} + \mathbf{M}_{i,r} \tag{5.8}$$

where m_i, I_i and $\mathbf{v}_i$ are the mass and moment of inertia particle *i*, respectively, $\mathbf{v}_i$ and $\boldsymbol{\omega}_i$ are its linear and angular velocities , respectively, $\mathbf{f}_{i,n}$ and $\mathbf{f}_{i,t}$ are the normal and tangential contact forces at contact points of particle *i* with neighboring particles, k_c is the number of neighboring particles, $\mathbf{f}_{i,b}$ is the weight and external body forces acting on particle *i*, $\mathbf{f}_{i,pf}$ is the interaction force exerted by the solid particle on the fluid, $\mathbf{r}_{ij}$ is the relative position vector

between particle *i* and a neighboring particle *j*, and $\mathbf{M}_{i,r}$ is the additional moment exerted on the solid particle (e.g., rolling friction).

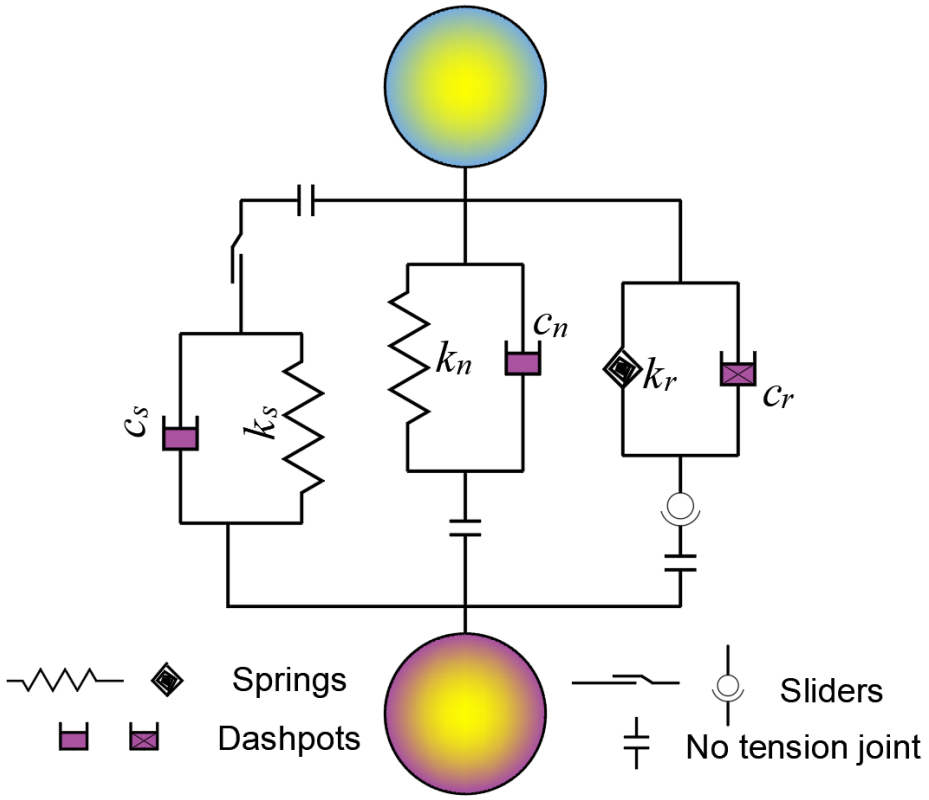

Figure 5.2. A schematic for the contact model for normal, tangential, and rotational inter-particle forces.

The particle-fluid interaction term, $\mathbf{f}_{i,pf}$, in Equation (5.7) is equivalent to the momentum transfer term $\mathbf{K}_{pf}$ in Eq. (4.2), however, denoted differently to differentiate between cell-based and particle-based numerical treatment. For calculating inter-particle contact forces, Hertz-Mindlin model was used (Di Renzo and Di Maio, 2005):

$$\mathbf{f}_{i,n} = k_n \delta n_{ij} - c_n \mathbf{v}_{ij} n_{ij} \tag{5.9}$$

$$\mathbf{f}_{i,t} = \min\left\{\left|k_t \delta t_{ij} - c_t \mathbf{v}_{ij} t_{ij}\right|, \mu_s \mathbf{f}_{i,n}\right\} \tag{5.10}$$

where k_n and k_t, as shown in Figure 5.2, are the normal and tangential spring stiffnesses,

respectively, c_n and c_t are the normal and tangential dashpot coefficients, respectively, δn_{ij} and δt_{ij} are the normal and tangential overlaps between particle *i* and particle *j*, respectively, μ_s is Coulomb friction coefficient, and $\mathbf{v}_{ij}t_{ij}$ is the relative velocity in the tangential directions. More details on the relationship between the spring stiffness and dashpot coefficient and the material properties can be found in Di Renzo and Di Maio (2005). The Elastic-Plastic Spring-Dashpot rolling friction model (Ai et al., 2011) was used to account for potential non-sphericity in the particle shapes such that:

$$\mathbf{M}_{i,r} = \min\left\{\left|-k_r\Delta\theta_r - C_r\dot{\theta}_r\right|, \mu_r R_r \mathbf{f}_{i,n}\right\} \tag{5.11}$$

where k_r is the stiffness of the rotational spring, $\Delta\theta_r$ is the angle of rotation during one timestep, C_r is the coefficient of rotational damper, $\dot{\theta}_r$ is the relative angle of rotation, μ_r is the coefficient of rolling friction, and R_r is the rolling radius.

5.2.2 CFD-DEM coupling

The coupling process is conducted by exchanging and updating the flow field data between CFD and DEM solvers. As shown in Figure 5.3, the contact forces between the solid particles are first calculated in the DEM code. Afterwards, the equations of motion are solved to determine the new positions and velocities of the solid particles. It may be necessary to iterate the DEM loop such that the data exchange between the solvers is synchronized, (i.e., adjusting coupling interval). The positions and other relevant solid information are then projected onto the CFD mesh to calculate the local porosity and interaction forces. The CFD solver then determines the corresponding pressure and velocity of the fluid flow field, which is exported back to the DEM code upon convergence. The governing equations and the coupling process are implemented using CFDEM® open-source platform (Goniva et al., 2012). The solver consists of LIGGGHTS® (Kloss et al., 2012) solver for DEM calculations and OpenFOAM® (Weller et al., 1998) solver for CFD calculations.

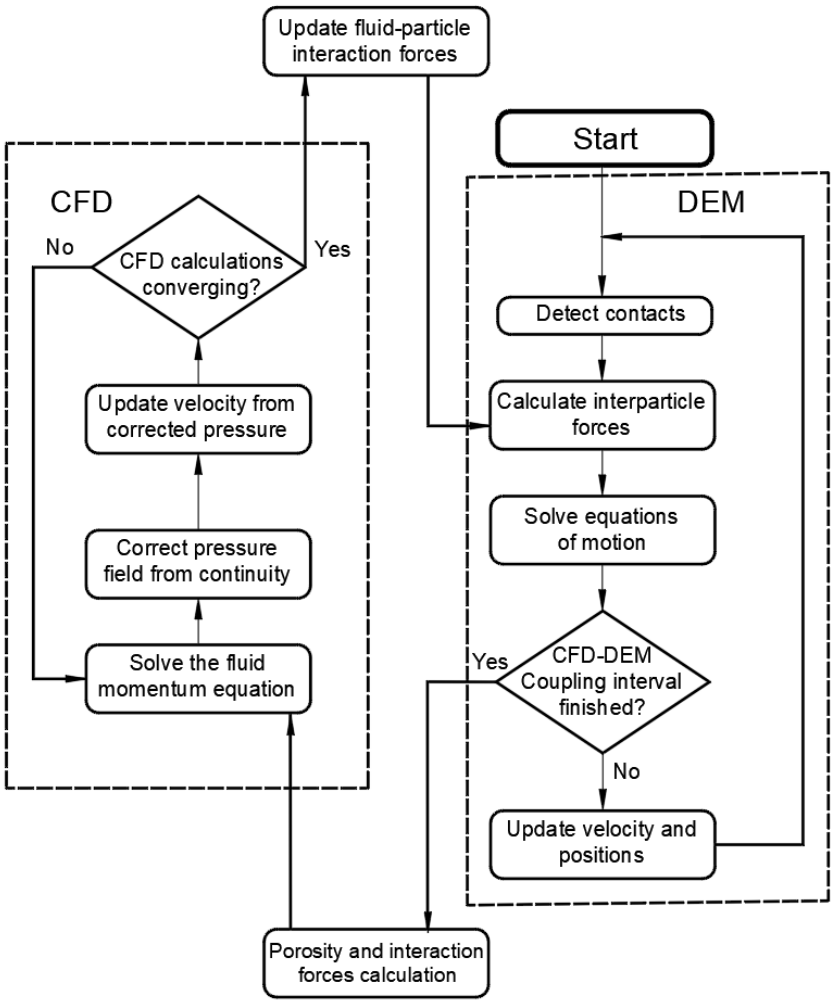

Figure 5.3. A flowchart illustrating the coupling procedure and data exchange between CFD and DEM solvers.

5.3 Numerical representation of a non-woven geotextile

As geotextiles used in tunnel drainage are exclusively non-woven, numerical representation of such textiles poses a few challenges. For instance, the geotextile geometry needs to be represented at filament-level instead of the thread-scale used to model woven geotextile in similar studies. Furthermore, it is necessary for the CFD mesh to be fine enough to capture the small pore spaces within the geotextile filaments, which results in fairly complex geometry and larger computational load. Another challenge is to provide a reasonable approach for generating the unstructured configuration of filaments that mimics the needle-punched geotextile. This is particularly important because adopting a structured configuration will ultimately lead to a binary behavior in particle clogging. That is, the fate of a single particle passing the geotextile is predetermined by the structured geometry and the size of the particle. Indeed, abandoning a

structured configuration prevents one from geometrically controlling some important properties of the geotextile such as the Apparent Opening Size (AOS) and Percentage Open Area (POA). Nonetheless, it is necessary to create a pore space that allows for capturing the basic dynamics of particle infiltration, clogging, and surface bridging.

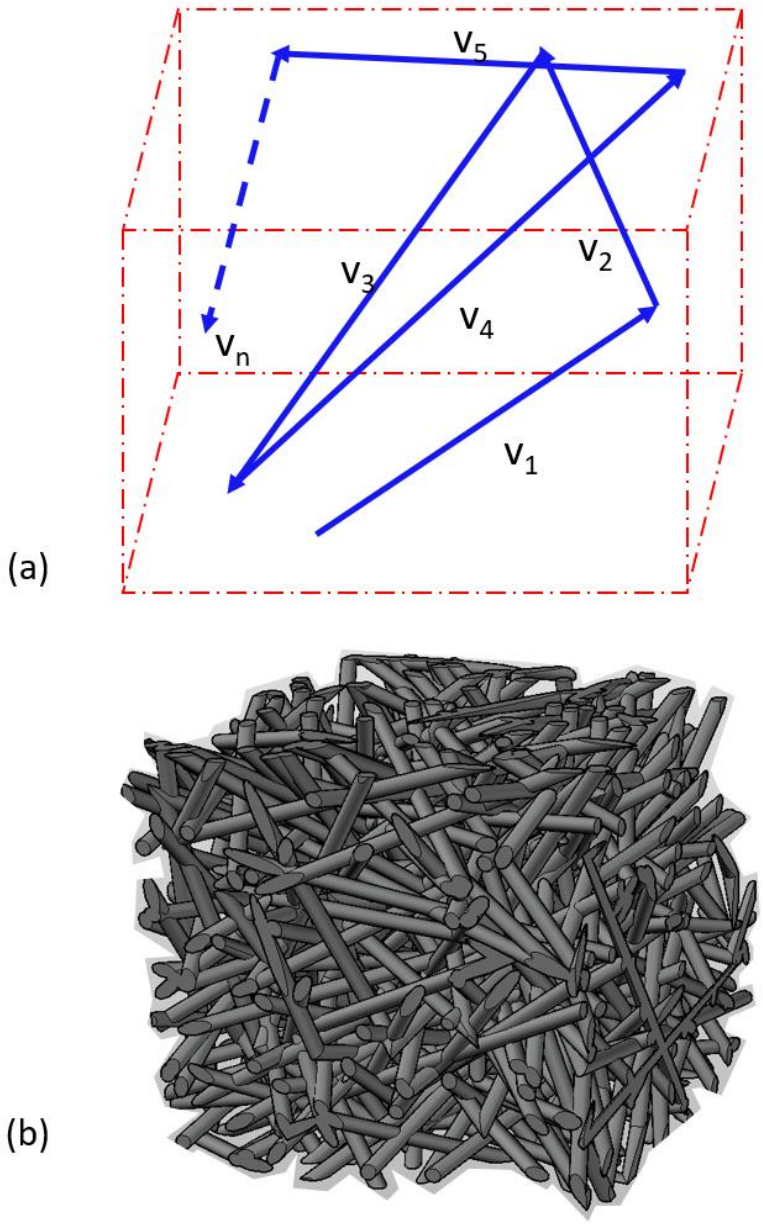

Figure 5.4. Illustration of the approach used to create the non-woven geotextile filaments: (a) conceptual 3D vectors as centerlines and (b) 3D representation of the filaments.

To create the filaments of a non-woven geotextile, we randomly generate a set of 3D vectors within a specified domain as show in Figure 5.4(a). The generated number of vectors (n),

represented by v_1, v_2, $v_3 \ldots v_n$, construct the filament centerlines. Filaments are created by converting the vectors to 3D elements of circular cross section with diameter, D_f = 75 μm (Figure 5.4(b)). Although this diameter is nearly 1.25 to 3 times larger than that of an actual geotextile reported in literature studies (e.g., Guo et al. (2020) and Kim et al. (2020)), it is necessary to keep the computational load within a tractable limit. As this simplification is adopted, it is important to note that we do not aim to create an exact replica of the geotextile fabric. Instead, what we target is creating an equivalent pore space and pore connectivity that produces comparable permeability and retention properties comparable to that of an actual geotextile of the same dimensions. The downside of using thicker filaments can be expected when geometrical changes to the fabric structures occur. This can happen when considering the compressibility of the geotextile under external pressure such that the evolution of porosity will be different from that of an actual geotextile. Therefore, we carry out additional testing of the effect of geotextile compressibility on the generated geotextile properties. Initial tests of the geotextile geometry generated from the 3D vectors show regions with relatively smaller filament density near the edges that becomes nearly uniform towards the center of the domain. Therefore, to ensure the uniformity of filament distribution, the domain is clipped by 20% of its original length from all sides. We note that the uniformity of distribution does not imply uniformity of pore space distribution, instead it enforces a consist density of filaments to avoid smaller filament density, and subsequent overestimation of permeability, near the sides. As filaments act as wall elements in both CFD and DEM analyses, the mechanical properties of the geotextile do not play a significant role in determining the water flow fields or the clogging mechanism. As such, preliminary testing of geotextile properties reduces to its permeability and retention properties. Certainly, the created numerical representation of the geotextile needs to undergo intensive testing to ensure the consistency of its properties compared to that of a typical geotextile.

With the filament cross sectional area kept constant, the only parameter we have control over is the number of filaments within a specific domain. This poses two major questions regarding the testing process, which the generated geotextile is considered a suitable representation based on their answer. The first question is: how consistent are the permeability and retention properties? To clarify, compared to average reported values in similar studies (e.g., Yoo (2016) and Guo et al. (2020)), a geotextile with AOS of 0.1 mm would typically have a coefficient of permeability in the range of 2×10^{-3} m/s to 5×10^{-3} m/s. Thus, the resulting values from numerically testing the generated geotextile need to be consistent with the ranges of expectation

for both retention and permeability without the need to adjust one over the other. The second question is: what is the effect of the randomized process of generating filaments on the resulting properties of the geotextile? That is, using the same number of filaments (i.e., vectors) will results in a different configuration each time the filaments are generated. Thus, it is necessary to examine the sensitivity of the geotextile properties to different configurations with the same number of filaments. Should the results vary significantly, this deems the approach inappropriate. To answer these questions, we carry out five different cases of simulation for different small samples of generated geotextile (3 mm x 3 mm x 3 mm). The first three samples, V1-300, V2-300, and V3-300, contain the same number of 300 filaments (**Figure** 5.5). The last two samples contain 400 filaments (V400) and 500 filaments (V500).

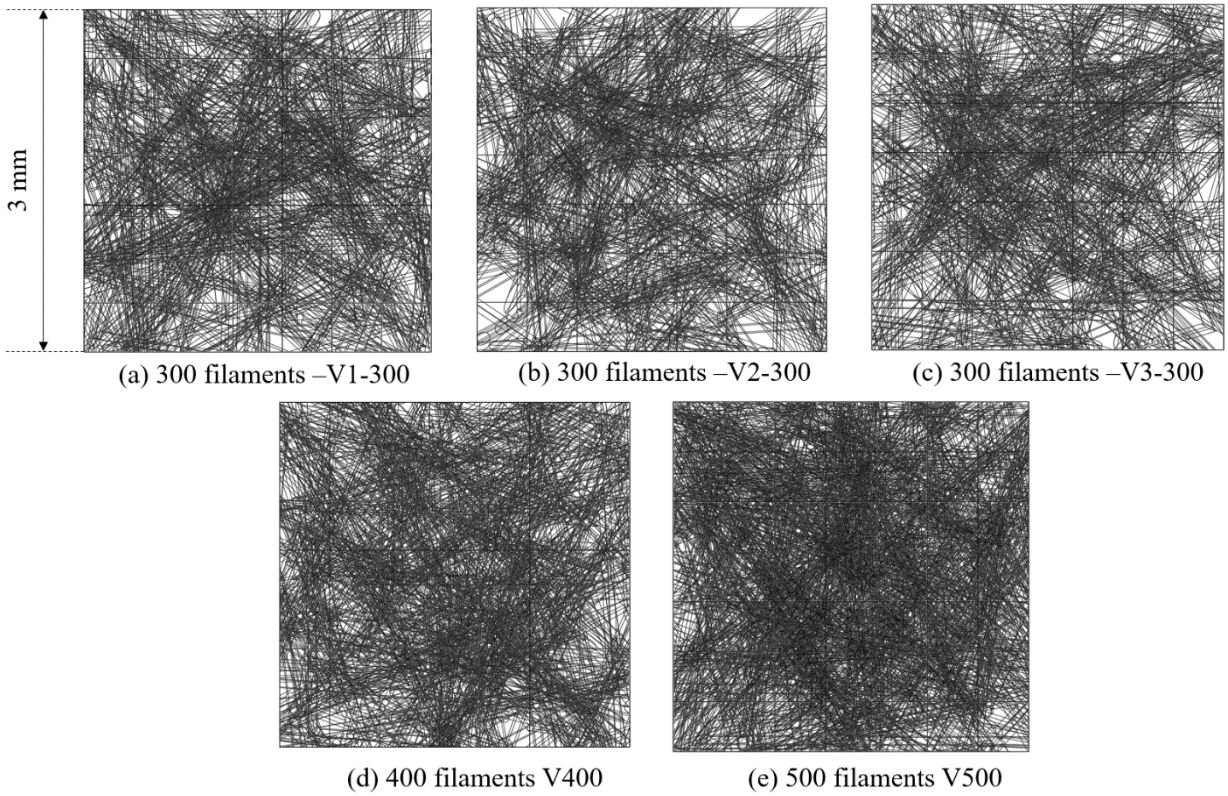

Figure 5.5. Plan view of the five geotextile samples used in the numerical tests.

5.3.1 Numerical permeability test

The permeability tests were conducted in a similar setting to that of ASTM D4716 (ASTM, 2013) and ASTM D4491 (ASTM, 2017). Water is allowed to flow unidirectionally in the in-plane direction under prescribed hydraulic gradients through two opposite. The hydraulic gradient is determined by the differential height of water and the thickness of the geotextile. In our simulation cases, the geotextile thickness is kept constant (3 mm) and the water level values

used are 10 mm, 40 mm, and 70 mm. A summary of the simulation parameters for the CFD permeability tests is provided in Table 5.1. The corresponding drainage (superficial) velocity in each case is calculated by measuring the outflow discharge of water at steady state flow and divide it by the area of the outflow face. This velocity averaging is important because the raw velocity values obtained from the CFD simulations are that of the seepage velocity (i.e., velocity of water between filaments) and is typically larger than the superficial velocity. The coefficient of permeability of the geotextile is then calculated using Darcy's equation by estimating the slope of the linear regression of the superficial velocity for each case plotted against the corresponding hydraulic gradient.

In the setting of CFD simulations, the geotextile filaments are treated as rigid walls that are assigned no-slip boundary conditions. Away from the filaments, the mesh needs to be fine enough such that the cell size is relatively small compared to the pore space. As the pore spaces near the intersection/overlapping of some filaments are significantly small, using a uniform CFD mesh all over the domain will be numerically infeasible. Therefore, local mesh refinement is done near the walls to allow for mesh optimization. It is important to note that such refinement comes at a cost regarding the numerical stability of the analysis as any slight increase in the velocity can generate high Courant numbers, which might ultimately lead to overall divergence of the simulation. To avoid this, a relatively small-time step was used (1×10^{-6} s). The analysis is run until a steady state flow is achieved, which is approximately 0.5 seconds from the beginning of the simulation.

Table 5.1. CFD simulation parameters for Permeability simulations

Parameter	Value
Water density (ρ_w) [kg/m^3]	1000
Water viscosity [m^2/s]	1×10^{-6}
Geotextile dimensions (L x B x W) [mm]	3
CFD time step (Δt_{CFD}) [s]	1×10^{-6}

The first set of results shown in Figure 5.6 correspond to simulation cases of geotextiles V1-300, V2-300, and V3-300. For a hydraulic gradient of 23.3, corresponding to 70 mm water head, the steady-state screenshots in Figure 5.6 (a) show quite comparable inter-filament velocity for the three cases of simulations. Although the non-uniform velocity field is unique for each case, we observe that the range of values and the distribution of high/low velocity is

nearly balanced in the three samples. A clearer comparison is presented in Figure 5.6 (b), which not only shows the nearly perfect linear relationship between the hydraulic gradient and seepage velocity, but also approximately equal value of line slope for the three cases. These results imply that the randomized generation of filaments does not have a tangible effect on the resulting coefficient of permeability of the geotextile. However, this should not be considered to be a global conclusion that is valid for any number of filaments. Instead, it should be rather considered that 300 filaments in a cubic domain of 3 mm side length is dense enough to the extent where the random generation process would produce, more or less, the same geotextile properties. The average coefficient of permeability from the simulations is 4.6×10^{-3} m/s, which falls within the range reported for non-woven geotextile of similar thickness (Yoo, 2016). The remaining numerical permeability tests are designed to test the effect of the number of filaments on the coefficient of permeability. The results shown in Figure 5.7(a) and Figure 5.7(b) show a noticeable reduction in the inter-filament velocity values for the V400 sample compared to the V2-300 sample. This reduction echoes in for the V500 sample, where the simulated coefficients of permeability for the V2-300, V400, and V500 are 4.6×10^{-3} m/s, 3.6×10^{-3} m/s, and 2.7×10^{-3} m/s, respectively (Figure 5.7(c)).

As geotextile becomes exposed to larger external load, either by accumulating water or earth pressures, its thickness decreases. A direct result of this decrease is a reduction in the in-plane drainage capacity of the geotextile. Therefore, we further examine the variations in the coefficient of permeability due to geotextile compressibility. Although this does not play a critical role in the model input covered in this study, it is necessary to gain more confidence in the behavior of the geotextile by examining its drainage related aspects. To do this, we consider four different geotextile samples of thickness 3.7 mm, 3.0 mm, 2.5 mm, and 2.0 mm that are identical to sample V2-300 in x and y (horizontal) directions but different in the z (vertical) scale. This resembles the change in the cross-sectional area due to compression where the x-y projection is not expected to vary significantly contrary to x-z and y-z projections. The permeability test is conducted with the same hydraulic gradient values as the previous samples and the resulting average coefficient of permeability for the three hydraulic gradients are compared to the permeability deterioration model of Giroud et al. (2000):

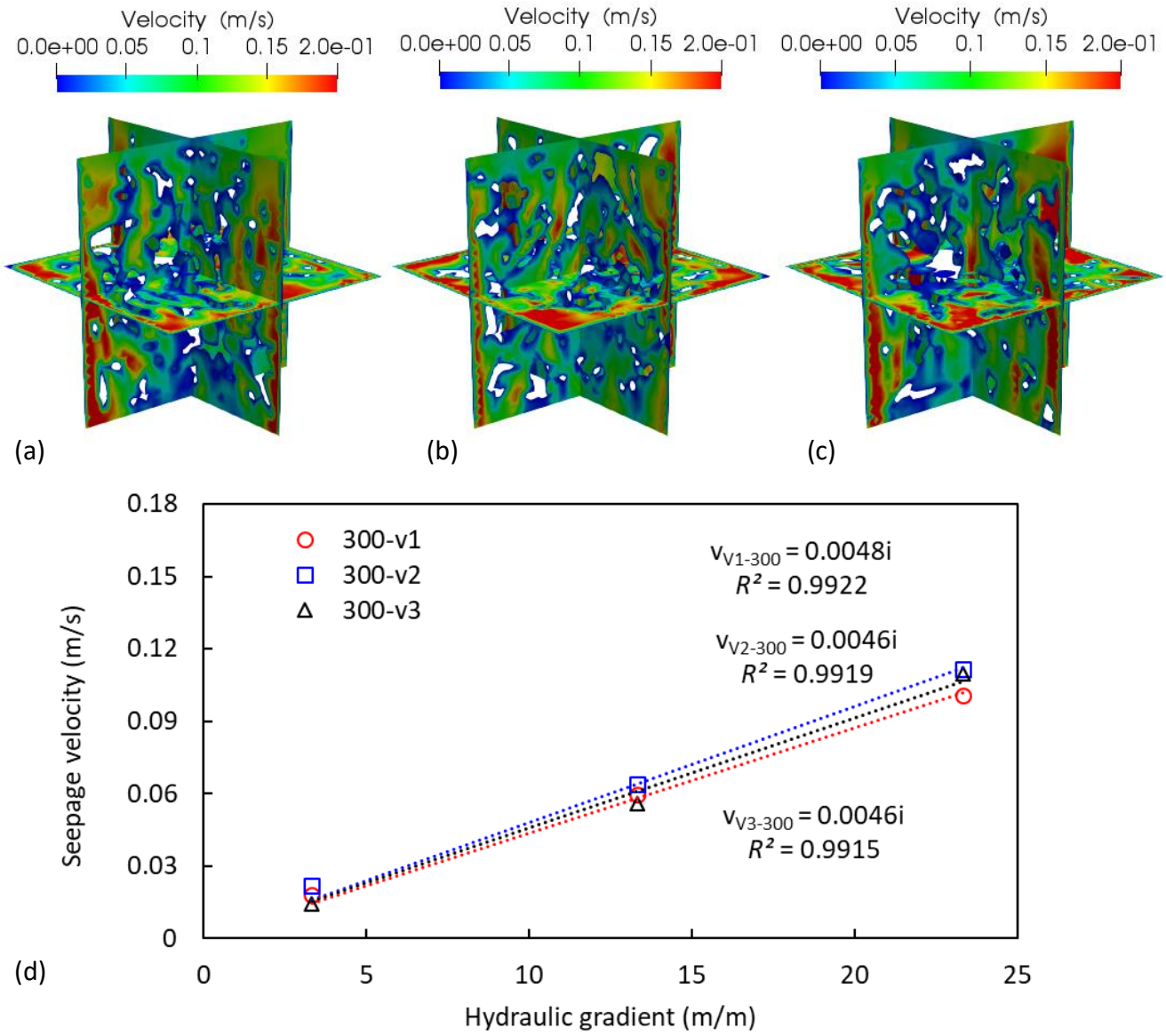

Figure 5.6. Results of numerical permeability tests: (a), (b), and (c) x, y, and z cross sections for 300 filament V1-300. V2-300, and V3-300 scenarios, respectively, (d) a plot of the seepage velocity and hydraulic gradient for V1-300. V2-300, and V3-300 scenarios.

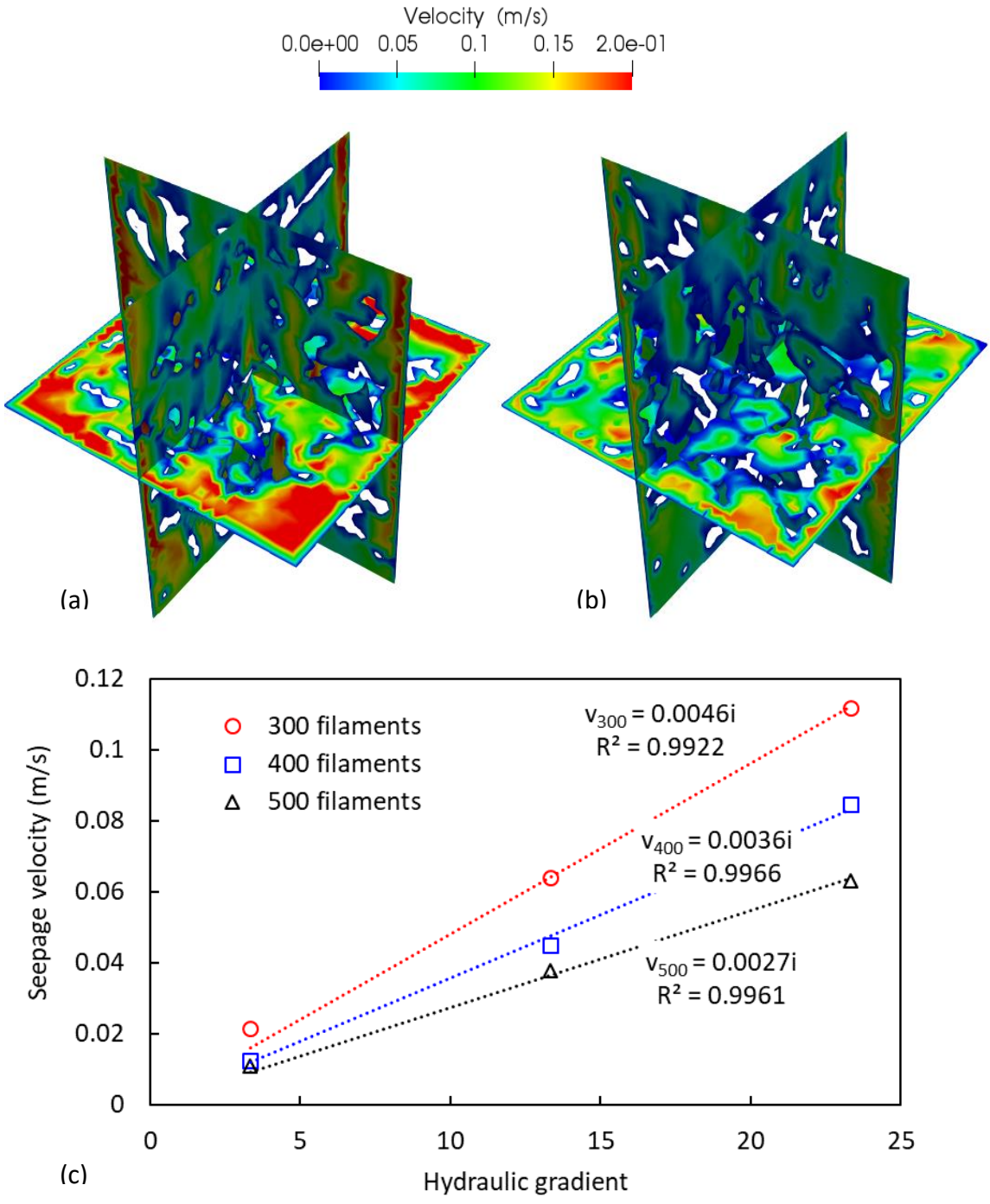

Figure 5.7. Results of numerical permeability tests: (a) x, y, and z cross sections for 300 filament V2-300 scenario, (b) x, y, and z cross sections for 400 filament V400 scenario and (c) a plot of the seepage velocity and hydraulic gradient for V2-300, V400, and V500 scenarios.

$$\frac{k_2}{k_1} = \left[1 - \frac{1-(t_2/t_1)^3}{n_1}\right]\frac{t_1}{t_2} \tag{5.12}$$

where k_1 and k_2 are the coefficients of permeability corresponding to geotextile thicknesses t_1 and t_2, respectively, and n_1 is the porosity of the geotextile with thickness t_1. Based on the preliminary numerical tests and analysis for the 3D geotextile sample, the values for t_1, k_1, and n_1 are taken 3.7 mm, 0.00682 m/s, and 0.84, respectively. The results shown in Figure 5.8 show the gradual decrease of the coefficient of permeability with thickness. Although the variation in the seepage velocity values cannot be clearly observed, the calculated outflow discharge reflected in the permeability calculation better shows the deterioration. The overall trend of deterioration aligns decently with that of Giroud et al. (2000) with a slight deviation observed near the 2.0 mm value. The reason for this deviation may be attributed to the difference of the rather thick filaments used in our 3D model, which is likely to produce lower porosity values as the compression continues. Nevertheless, the analysis shows that the constructed geotextile is able to a good extent to reproduce the behavior expected from an actual geotextile with comparable dimensions.

5.3.2 Numerical AOS test

An ideal test of the Apparent Opening Size (AOS) would be a close representation of ASTM D4751 (ASTM, 2016). Numerically, this would require involving moving mesh dynamics to represent the shaking recommended by the standard. As mesh moving utility is not available in LIGGGHTS®, the numerical test is conducted in static condition noting that the obtained AOS will be somewhat larger than that resulting from the dynamic case. The test setup consists of an initial assembly of particles generated in a cubic domain of 3 mm side length directly above the geotextile sample. As simulation starts, the particles fall freely under their own weight onto the geotextile. Generally, three distinct behaviors are to be expected in such simulation: (i) particles are retained at the surface either because the particle size is larger than the opening beneath or due to arching effect of a group of particles, (ii) particles going through the-

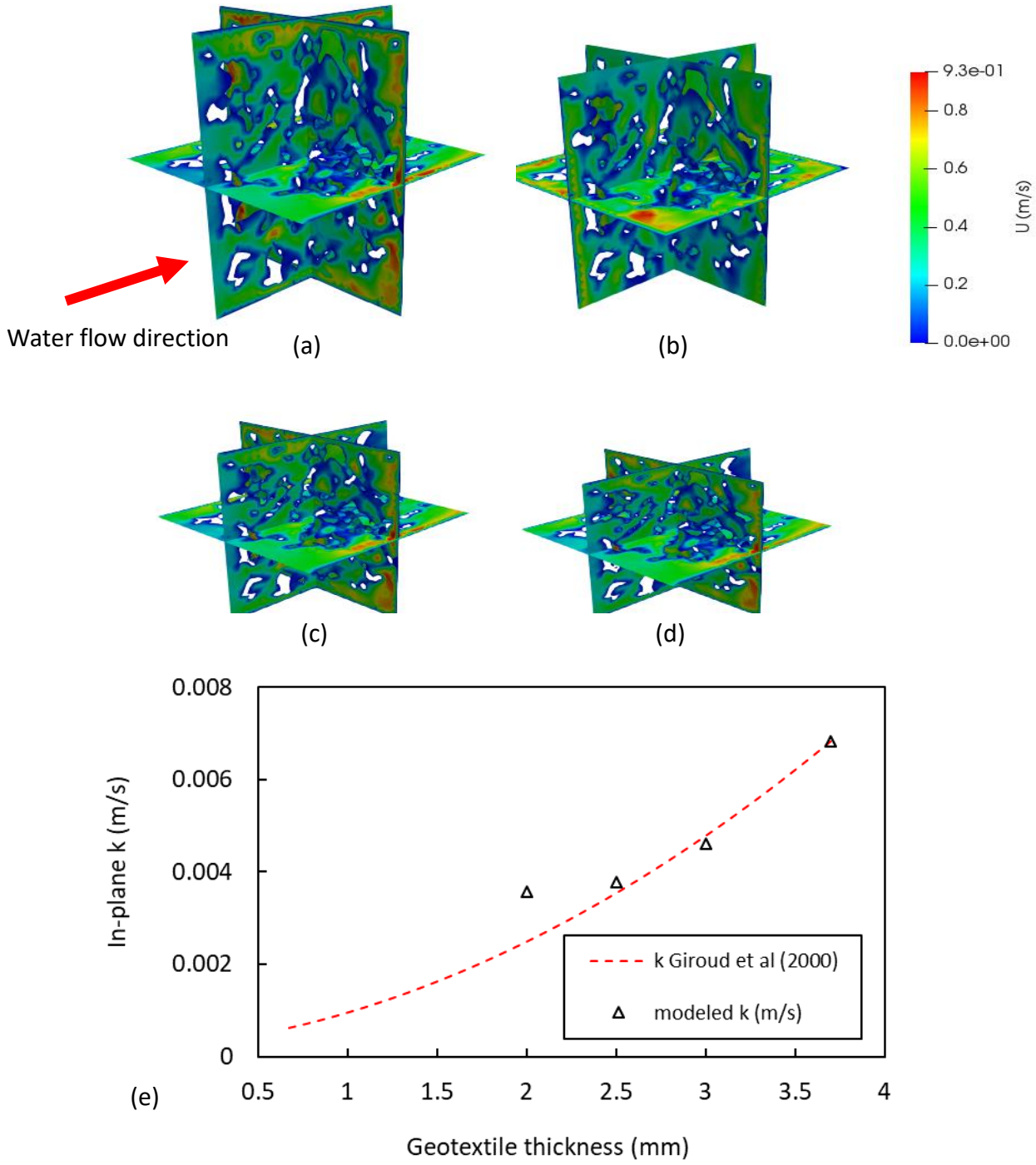

Figure 5.8. Results of numerical permeability tests: (a) t_g = 3.7 mm, (b) t_g = 3.0 mm, (c) t_g = 2.5 mm, (d) t_g = 2.0 mm, and (e) a comparison between the modelled values and the hydraulic deterioration model by Giroud et al. (2000)

geotextile ang get trapped within, and (iii) particles infiltrating the geotextile all the way through. The simulation is performed for the three geotextile samples V2-300, V400, and V500.

In each scenario, a separate run is conducted for a constant particle diameter of 0.03, 0.06, 0.1, 0.15, 0.2, and 0.25 mm. A summary of DEM simulation parameters is provided in Table 4.1. For each run, the mass of passing particles is compared to the initial mass of the total particles at the beginning of the simulations. The values of passing mass and particle diameters are then used to construct the pore size distribution curve for the geotextile, where the AOS corresponds to 5% passing mass (i.e., O_{95}).

Table 5.2. DEM simulation parameters for AOS simulations

Parameter	Value
Solid density (ρ_s) [kg/m^3]	2700
Coefficient of particle-particle friction (μ_s)	0.25
Coefficient of particle-wall friction (μ_{sw})	0.2
Coefficient of restitution (e)	0.6
Poisson ratio	0.25
Young's modulus (E) [Pa]	$3x10^8$
Coefficient of rolling friction (μ_r)	0.25
DEM time step (Δt) [s]	$5x10^{-8}$

A summary of the test results is provided in Table 5.3 and Figure 5.9 (c). The obtained AOS for the three samples V2-300, V400, and V500 are found to be approximately equal to 0.13 mm, 0.09 mm, and 0.08 mm, respectively. With these values, we can now assess the consistency of the geotextile's coefficient of permeability and AOS. For the 300-filament sample, a coefficient of permeability of 4.6 $x10^{-3}$ m/s and AOS of 0.13 compare decently to values of geotextiles of the similar thickness reported in literature (Yoo, 2016). The same conclusion can also be stated for the 400-filament and 500-filament geotextile samples. In a more realistic scenario, where the properties of an actual geotextile are readily made available by the manufacturer, the numerical tuning of the model to exactly match the geotextile properties is extremely challenging. Nonetheless, within the scope of this work we consider the V2-300 geotextile sample to fall within a proper properties range for a tunnel drainage layer.

Table 5.3. Summary of (%) mass passing through the three geotextile samples for diameters: 0.03, 0.06, 0.1, 0.15, 0.2, and 0.25 mm.

	Passing (%)					
Geotextile	D_0 = 0.03 mm	D_1 = 0.06 mm	D_2 = 0.1 mm	D_3 = 0.15 mm	D_3 = 0.2 mm	D_4 = 0.25 mm
V2-300	100	94.5	11.5	2.9	1.7	0.6
V400	100	90	1.6	0.06	0	0
V500	100	88	1.1	0.012	0	0

5.4 Boundary conditions

Considering the spatial scale of a crack adopted in this study, it is necessary to differentiate between two distinct boundary conditions. The first is global boundary conditions that describe the groundwater flow and the overall drainage capacity of the tunnel. The second is the truncated boundary conditions on the crack level that govern the small domain. As shown in **Figure** 5.10(a), the global boundary conditions for the tunnel are governed by the tunnel geometry, water level, and rock permeability. With some simplifying assumptions such as homogeneous and isotropic rock medium, and the hydraulic head boundary at the edge of the tunnel, some analytical solutions can be derived to describe the radial water flow into the tunnel (e.g., Kolymbas and Wagner (2007), El Tani (2003) and Goodman et al. (1965)). Considering the scope of our work, where the drainage layer can potentially be pressurized to accommodate pressure increase resulting from clogging, the model of Kolymbas and Wagner (2007) can be used:

$$Q_r = \frac{2\pi K_a (H - h_a)}{\ln \dfrac{r}{h_1 - \sqrt{h_1^2 - r^2}}} \tag{5.13}$$

where Q_r is the total groundwater ingress into the tunnel, K_a is the rock aquifer's coefficient of permeability, H is the water level above the ground surface, h_a is the piezometric head of the drainage layer measured from the ground surface, h_1 is the depth to the centre of the tunnel measured from the ground surface, and r is the tunnel radius. Such model, however, can only describe, or give a good approximation, for the groundwater flow into the tunnel. For instance, a key assumption in Kolymbas and Wagner's derivation is that the hydraulic head function is constant in the drainage layer (e.g., an equipotential line).

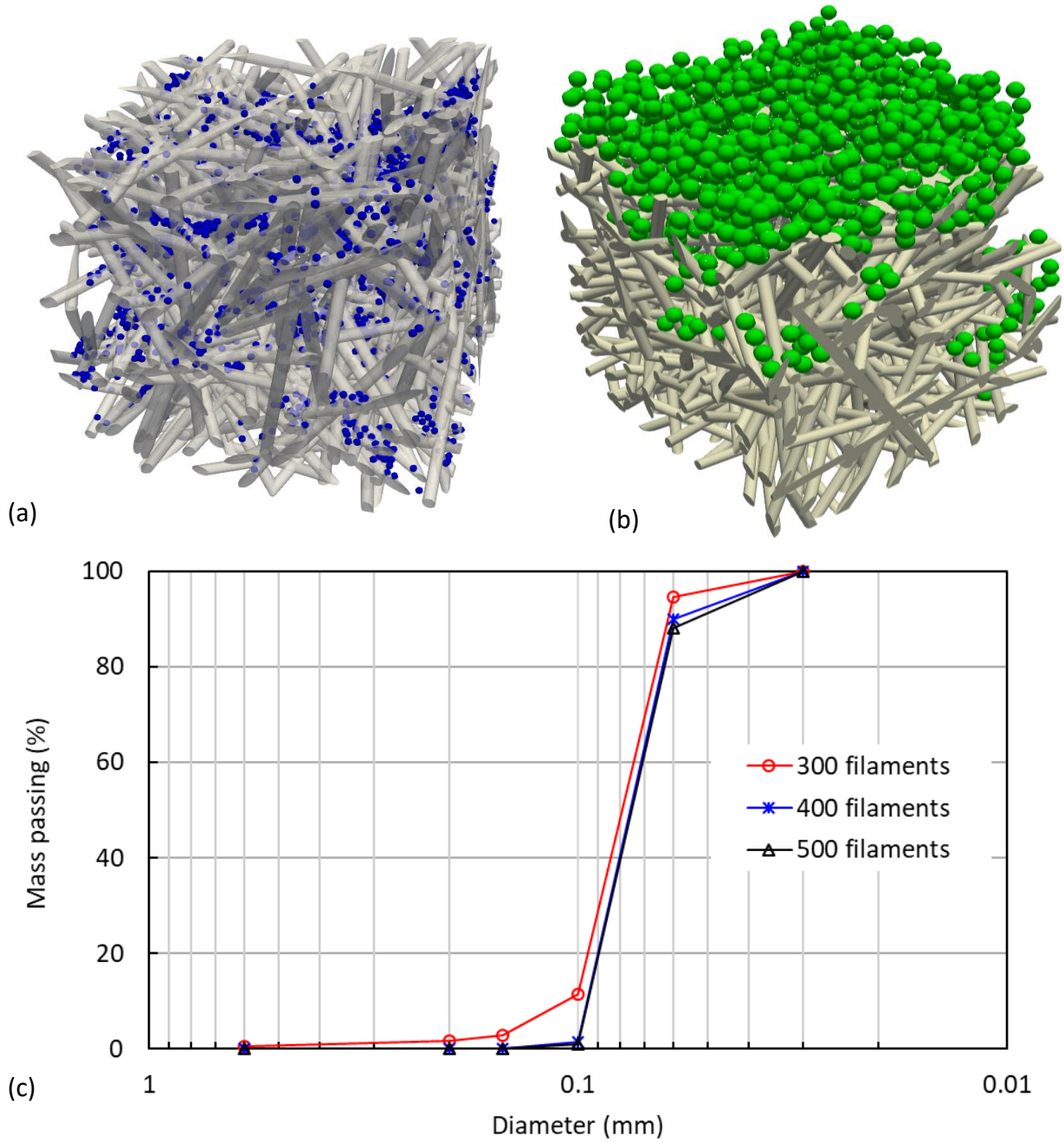

Figure 5.9. DEM results of solid particles infiltration through 300 filament sample (V2-300): (a) particle size 0.06 mm, (b) particle size 0.2 mm, and (c) pore size distribution for the 300, 400, and 500 filament samples.

As such, the water flow dynamics beyond the edges of the tunnel (i.e., flow in the drainage layer) cannot be dealt with using such models. Furthermore, as we consider the tunnel to be initially not pressurized, it is important to check the validity of using the expression in Equation

(5.13) at atmospheric pressure condition where $h_a = -h_1$. This is done by cross-checking the expression with the relationship presented by El Tani (2003) for unlined tunnels. We find that the resulting groundwater inflow is nearly identical from both expressions. Thus, we consider the expression in Equation (5.13) to be an acceptable approximation for the groundwater inflow at the edge of the tunnel. Inside the drainage layer, the water flow is assumed to be solely driven by the position head difference along the tunnel perimeter following Kim et al. (2020).

Moving to crack level (Figure 5.10(b)), we consider a crack spanning over a small angle, $d\theta$, with total in-plane width of, $rd\theta$, and out-of-plane width *w*. Within the crack, the geotextile is overlain by a layer of fine particles of drilling residual or blinding deposition. The outermost boundary condition is considered an inflow boundary where the total amount of water passing through is $wQ_r d\theta / 2\pi$, where Q_r is total ingress from Equation (5.13). This inflow value underlies the assumption that cracks are uniformly distributed throughout the perimeter and sufficiently extend out-of-plane so as to be considered two-dimensional. Here we consider the infiltration of the particles to be only driven by gravity and the momentum of the radial flow. Another inflow boundary is located on the left side representing the accumulated circumferential inflow from the crown of the tunnel up to the angle θ, at which the centerline of the crack is located. Above the geotextile on the left and right sides of the crack, the shotcrete boundaries are represented as wall boundary conditions. At the outlet boundary of the geotextile, a constant pressure boundary condition is imposed, $p = 0$, (i.e., datum). This particular selection of the outflow boundary condition governs the overall prediction framework of the model. This means, the pressure value calculated at the geotextile side inlet basically represent the differential pressure needed to drive the prescribed inflows through the geotextile within the crack.

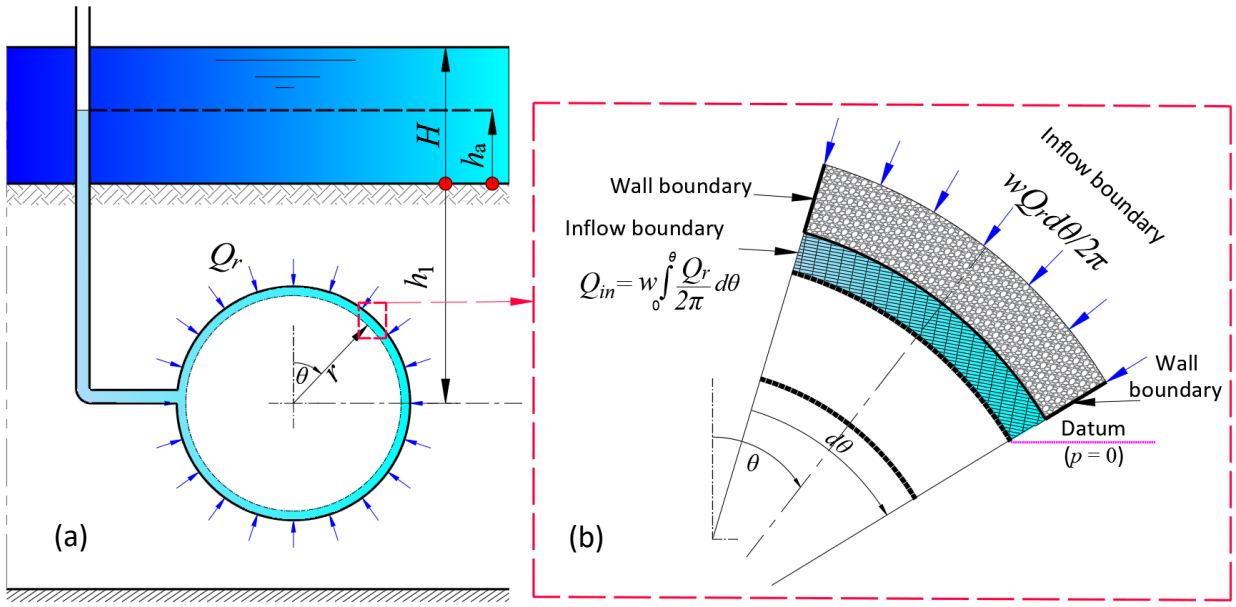

Figure 5.10. A schematic illustration of the global boundary conditions for groundwater ingress (left) and the truncated boundary conditions on a crack level expanding radially over $d\theta$ (right).

Such way of truncating the domain sums all the groundwater-rock-tunnel interactions beyond the drainage layer into inflow values. This eliminates case-uniqueness because a specific inflow value can result from infinite combinations of water level, geometry, rock permeability, and drainage point piezometric head. However, from mass conservation, the local path of water water from the surrounding rock through the geotextile is analogous to in-series flow. Therefore, the calculated head/pressure difference within a small element (i.e., the geotextile) should be correct for a specific inflow value regardless of the aquifer and groundwater conditions. The aquifer conditions step in to play a major role in the interactions subsequent to pressure or flow variations beyond the geotextile capacity. To clarify, since the water flow inside the geotextile is driven by the elevation difference, the hydraulic gradient is predetermined by the tunnel's geometry. As such, the geotextile drainage capacity depends only on the in-plane coefficient of permeability and thickness of the geotextile. Thus, following pressure increase in the drainage layer, the system needs to diffuse the extra pressure to maintain the same previous hydraulic gradient. This can be interpreted as an increase in the value of h_a in Equation (5.13), which then results a unique value of ingress reduction for a specific set of aquifer conditions.

Since pressure increase is a direct result of geotextile clogging, the reduction of groundwater flow into the tunnel can also be interpreted as deterioration of geotextile permeability. We note

that the CFD-DEM predictions of pressure increase due to clogging are neither restrained by the geotextile drainage capacity nor take into consideration the subsequent reduction in groundwater flow. For instance, if the geotextile becomes completely clogged such that the effective permeability approaches zero, the model will estimate an extremely large pressure gradient as to move water through. Therefore, as the scope of modeling in this study is concerned, the simulation is only a part of a chain that involves explicit adjustment of boundary conditions in order to capture the entire dynamics of the system. This involves the effect of the initial pressure increase on the groundwater inflow into the tunnel and the corresponding geotextile compression. Thus, we limit the scope of the model to predicting the preliminary pressure increase resulting from geotextile clogging. A schematic illustration of the system dynamics and the scope of simulation carried out in this study is highlighted in Figure 5.11.

Depending on the initial hydraulic gradient in the drainage layer and the inflow of groundwater, Kim et al. (2020) express the minimum in-plane coefficient of permeability, k_g, as:

$$k_g > \frac{Q_r}{2\pi\, t_g (1+\sin(\theta-\pi/2))} \frac{\theta^2}{} \tag{5.14}$$

where t_g is the geotextile thickness and θ is the angle of the outlet point measured from the crown of the tunnel. The expression in Equation (5.14) is more relevant to the design process to obtain the needed the geotextile properties. With known properties, such as the case with our simulation, it can be rearranged to determine the allowable groundwater inflow capacity, that is equivalent to the total groundwater ingress, Q_r. However, a major issue is associated with this particular approach, in Equation (5.14) the total outflow at angle θ is assumed to be driven by the elevation difference between the crown and the outlet. This can only be true if the considered flow is constant from the crown to the outlet. Instead, the flow in the geotextile layer increases gradually as more radial flow is collected on its way to the outlet. Therefore, at a small angle $d\theta$ located at the outlet, the collected flow $Q_r\theta/2\pi$ is driven with smaller gradient that is approximately $rd\theta\sin(\theta)/rd\theta = \sin(\theta)$. In such case, it is more appropriate to assume that the capacity of the geotextile is governed by the microscale outlet hydraulic gradient rather than an overall calculated hydraulic gradient. The maximum allowable inflow into the tunnel, based on the microscale outlet gradient, is $Q_r = 2\pi k_g t_g \sin(\theta)/\theta$. Comparing

this value of Q_r to that from Equation (5.14), we obtain a ratio of $(1+\sin(\theta-\pi/2))/\theta\sin(\theta)$, which is nearly constant in the interval $[-\pi/2:\pi/2]$ and yields a value of 0.5 to 0.6. This can be clearly seen in Figure 5.14 as the geotextile flow capacity based on the outlet hydraulic gradient is approximately twice that of Kim et al. (2020). This inflow value is hereafter adopted as the initial model input for radial inflow as it is consistent with the hydraulic gradient restraints. Larger inflow value essentially means we are to conduct the simulation with inflow beyond the capacity, which renders any pressure comparisons to the initial conditions useless.

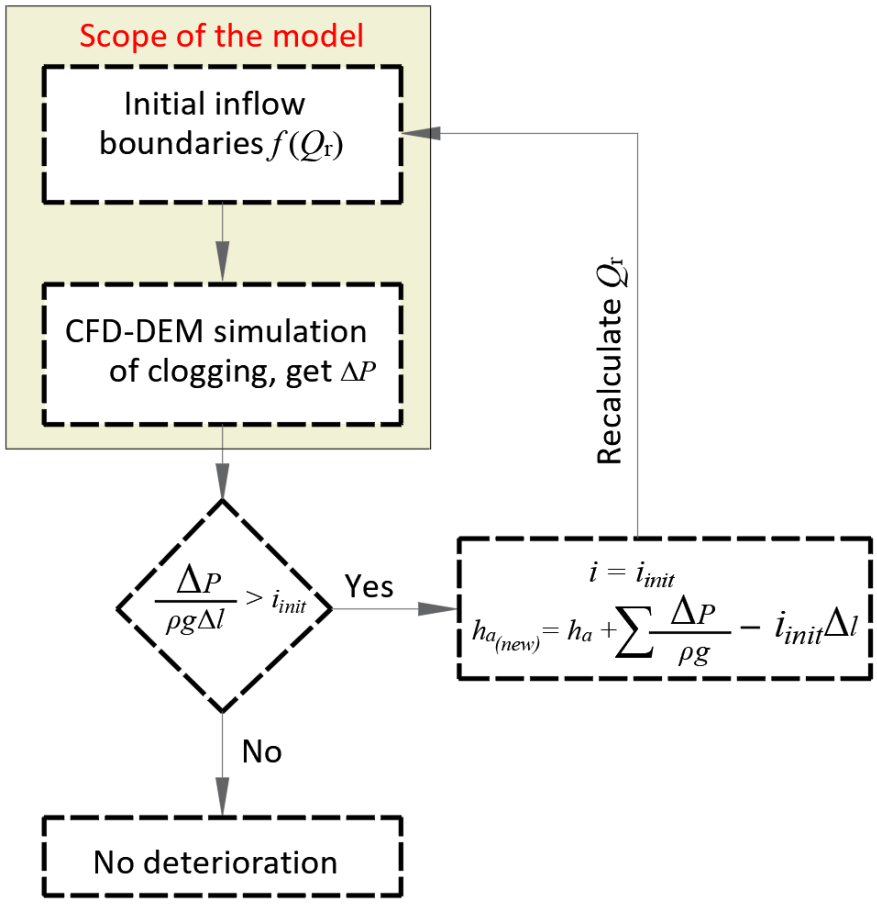

Figure 5.11. A schematic illustration of the dynamics of hydraulic deterioration and reduction of the groundwater flow into the tunnel highlighting the scope of the CFD-DEM modelling conducted in this study.

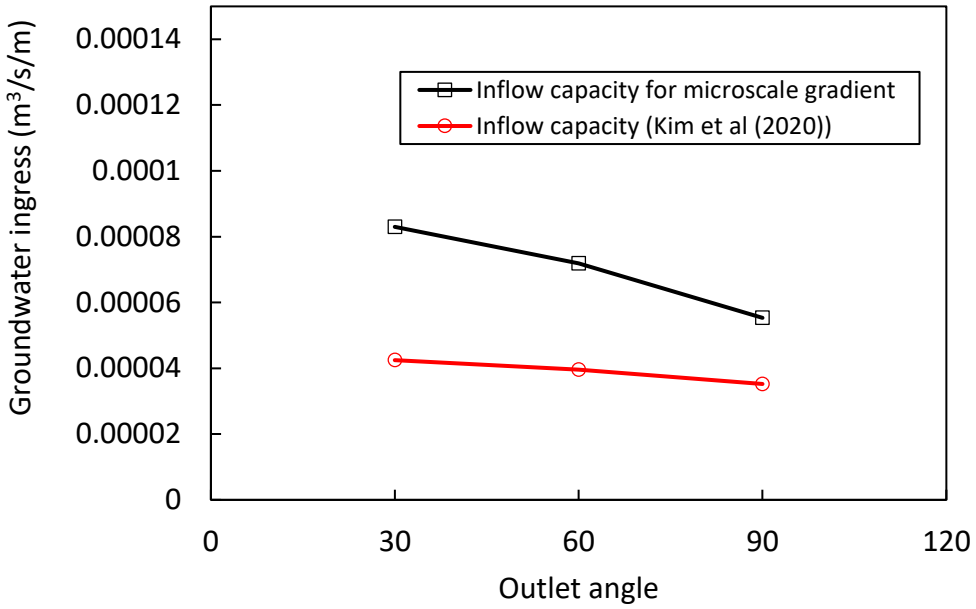

Figure 5.12. Variation of the maximum allowable Q_r based on overall all hydraulic gradient and local exit hydraulic gradient.

5.5 Numerical setup and parametric analysis

The simulation domain is similar to that shown in Figure 5.10(b). A geotextile layer identical to sample V2-300 of thickness of 3 mm, in-plane width of 1 cm, and out-of-plane width of 2.5 mm is used. Here, we consider a tunnel with a radius of 5 m, this corresponds to a crack that spans over an angle of 0.003°, with which the curvature of the tunnel is nearly negligible. The geotextile is overlain by 3 mm thick deposition of fine soil, with a wall boundary condition at the bottom edge representing the geomembrane sealing layer. The inflow boundary conditions are specified at the top of the soil deposition and the left side of the geotextile based on the value of Q_r calculated using the hydraulic gradient at outlet angle of 90°. In order to map the angular variation of pressure increase due to clogging, we consider four angles, θ = 0.003°, θ = 30°, θ = 60°, and θ = 90° along the tunnel perimeter. As for the effect of percentage of fines in the soil, three different samples, soil A, soil B, and Soil C, with fines content f_c = 10%, 20%, and 40%, respectively, are considered (Figure 5.13). These percentages are estimated based on the portion of particles with diameter smaller than the AOS of the geotextile such that it directly accounts the particles that can infiltrate through the geotextile. A typical case simulation

involves two stages of simulation. Initially, the particles are allowed to infiltrate to the maximum extent under the effect of radial flow and their own weight. After the kinetic energy of the particles is stabilized at a reasonably small value, 1 x10^{-13} J in our case, the side inflow is initiated. The rationale behind this is to achieve the maximum possible clogging that can happen since the side inflow may be orders of magnitude larger than the radial inflow which works against clogging. This is to avoid conducting numerically intractable time-dependent simulations. Instead, we target the worst-case clogging scenario that might occur. In reality, this can be considered as initial infiltration of fine particles before the installation of the geomembrane layer (i.e., temporary drainage). A summary of the simulation parameters of coupled CFD-DEM analysis is provided in Table 5.4. A summary of coupled CFD-DEM simulation parameters for crack-level analysis.

Table 5.4. A summary of coupled CFD-DEM simulation parameters for crack-level analysis.

Parameter	Value
Geotextile sample	V2-300
Geotextile thickness	0.003
Model in-plane width (L) [mm]	10
Model out-of-plane width (w) [mm]	2.5
CFD time step (Δt_{CFD}) [s]	1x10^{-6}
DEM time step (Δt_{DEM}) [s]	1x10^{-8}
CFD-DEM coupling interval [Δt_{DEM}]	100
Tunnel radius [m]	5
Geotextile coefficient of permeability [m/s]	4.6x10^{-3}
Geotextile AOS [mm]	0.13

An initial step of validation is first conducted before starting the parametric analysis simulations. In this step, a wall boundary is placed between the soil and the geotextile such that when the side inflow is released it only flows through the geotextile. The flow is released with values based on Q_r for different outlet angles calculated for the microscale gradient case in Figure 5.12, such that the total inflow value is $Q_r\theta / 2\pi$. The purpose of this simulation is to ensure that the model produces the correct pressure difference (i.e., differential head) expected at each angle. The resulting differential pressure can be then compared to the equivalent pressure of elevation head such that $\Delta p = \Delta l \sin(\theta)\rho g$, where Δl is the crack in-plane length (1 cm). In this case, the expected pressure generated at the inlet p' (kPa) $= 0.0981\sin(\theta)$. The

results shown in Figure 5.14 show the pressure field within the geotextile layer as well as the comparison between the modeled values and the predicted pressure drop across the crack. This validation, although relatively simple, is necessary to build confidence in later results. As for the effect of water level on the clogging process, it can be accounted for by increasing the value of Q_r. However, implementing larger Q_r values is merely transient as the system will soon revert back to flow capacity. In addition, since the circumferential flow increases in this case, more resistance to clogging is provided. This, in turn, does not give us any useful insights on the long-term deterioration of the drainage capacity of the geotextile. Therefore, variations in Q_r are applied only to the initial stage of the simulation, while maintaining final stage inflow at the capacity value, to examine the potential increase in fines infiltration into the geotextile.

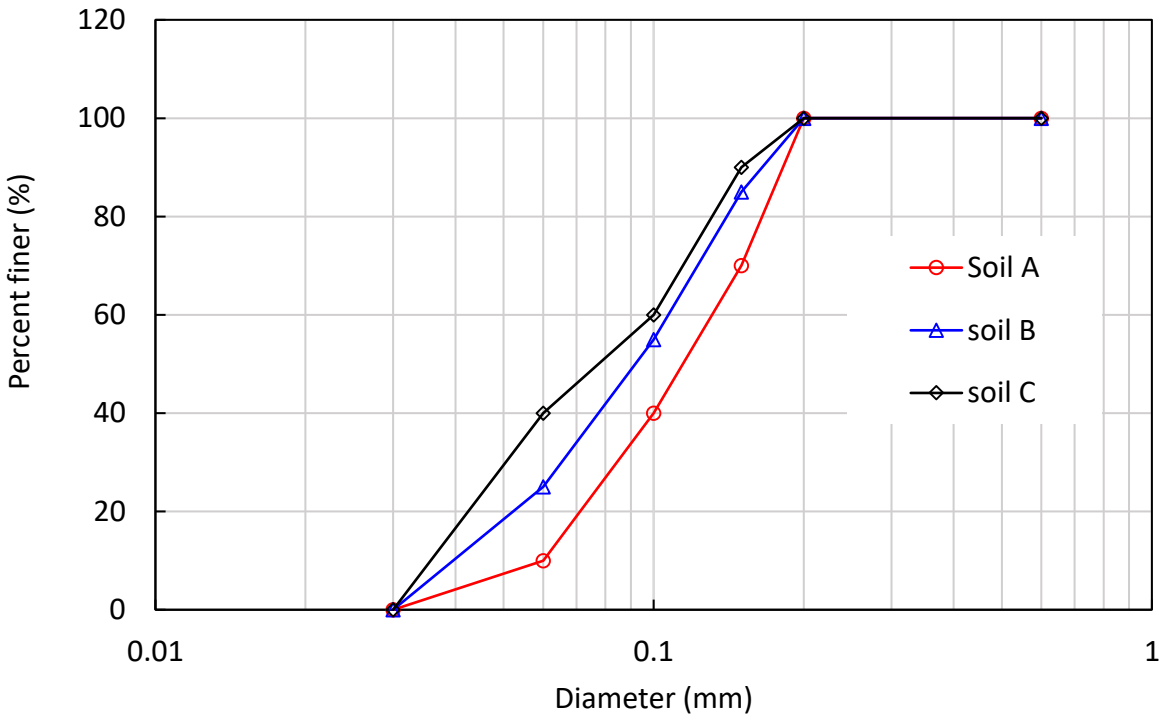

Figure 5.13. The particle size distribution of the three soil samples: soil A, soil B, and soil C.

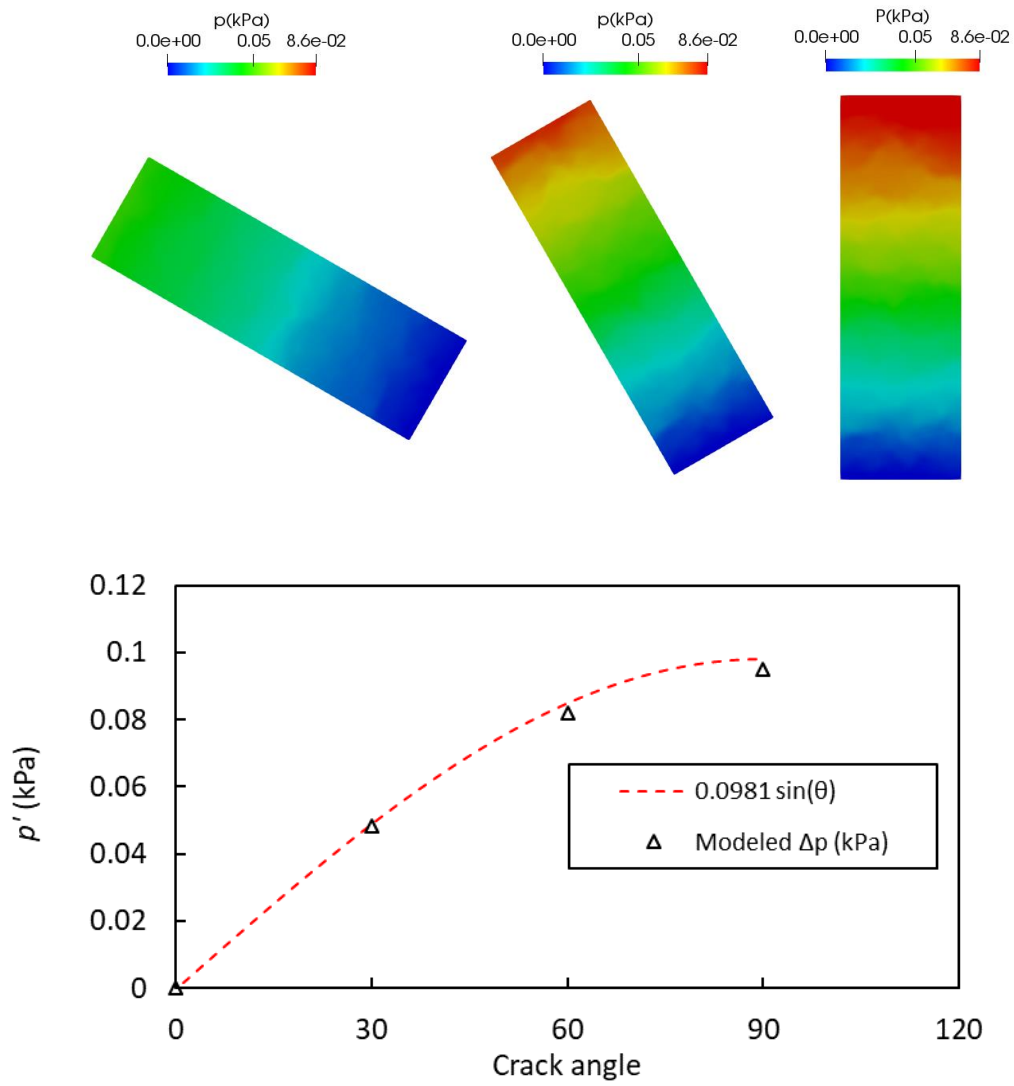

Figure 5.14. The generated inlet pressure considering three outlet angles 30°, 60°, and 90° compared to the values calculated from the prescribed hydraulic gradient and geotextile properties.

5.6 Results

The results for the parametric analysis of crack angle and soil type at steady-state flow are shown in Figure 5.15. Generally, the resulting pressure increase at the inlet is a compromise between fines infiltration and circumferential flow governed by the crack angle. On one hand, the driving force component for the fine particles infiltration decreases by increasing the crack angle, thus, the resulting clogging is maximized at the crown of the tunnel and reaches its minimum at $\theta = 90°$. On the other hand, the circumferential flow increases significantly as the crack angle increases, as a result, the slightest clogging magnifies the pressure increase. From the simulation results, we observe that in most cases the dominant side in this compromise to

be the circumferential flow value. This can be seen in Figure 5.15(a) and Figure 5.15(d) where the resulting pressure increase at , θ = 0.003° is approximately 1% of that at θ = 90°. A systematics pressure increase is seen with increasing the crack angle. Another systematic increase is noticed with increasing the content of fines. This is rather expected as the more fine particles exist the larger the clogged area becomes and subsequently the larger the calculated pressure is. However, at high circumferential flows, it is more likely that smaller particles get washed away, which in turn, reduces clogging. This echoes with the clogging patterns observed in all the simulation cases, were the majority of the stable clogging is caused by relatively larger particles in the top third of the geotextile. In regions below, the clogging particles are smaller, yet, significantly less than the top region. In addition, in some cases (e.g., Figure 5.15(c)-soil C and Figure 5.15(d)-soil C) we observe that a portion of the solid particles are washed away near the inlet where the water pressure is highest. For coarser solid particles, this behavior is not observed. This indicates that the model was not only able to capture the effect of clogging, but the local piping regime that happens near the inlet.

A closer look on the results shown in Figure 5.16 for the comparison between the modeled inlet pressure values, p', and the threshold pressure, p_{tr}, previously calculated (Figure 5.14) provides deeper insights into the clogging effect. For instance, at angles θ = 60° and θ = 90° the calculated inlet pressure values are quite comparable for soil B and soil C. Considering the pressure increase to be the difference between the modelled inlet pressure and the threshold pressure, we find that the pressure increase corresponding 60° is larger than that corresponding to 90°. This brings the aforementioned compromise back to the discussion, as contrary to the trend observed between the crown and the outlet, as the effect of the portion of infiltrated particles appears to have more weight to elevating the pressure than the flow increase. It is important to note that since the Q_r value is calculated based on the microscale gradient at outlet angle θ = 90°, the actual pressure increase should correspond to difference between the calculated pressure and control pressure values (p_c). These control values are based on the portion of flow at each crack angle computed from Q_r at the outlet, which is typically smaller than the threshold pressure values. The control-based increase, $p' - p_c$, shown in Figure 5.17, indicate that the maximum pressure increase for the three soil types occur at θ = 60°. However, the control-based comparison underlies a major flaw as the hydraulic gradient does not change. Since we do not consider the geotextile layer to be initially pressurized, the water should then be considered to partially fill the geotextile under the same hydraulic gradient. As the CFD calculations do not account for this, the control pressures calculated based on fully flowing

sections may not be accurate. Therefore, in the subsequent calculations for pressure increase we adhere to the difference between the calculated inlet pressure and the threshold pressure. In such case, the calculated pressure is considered excessive only if it exceeds the microscale hydraulic gradient equivalent pressure.

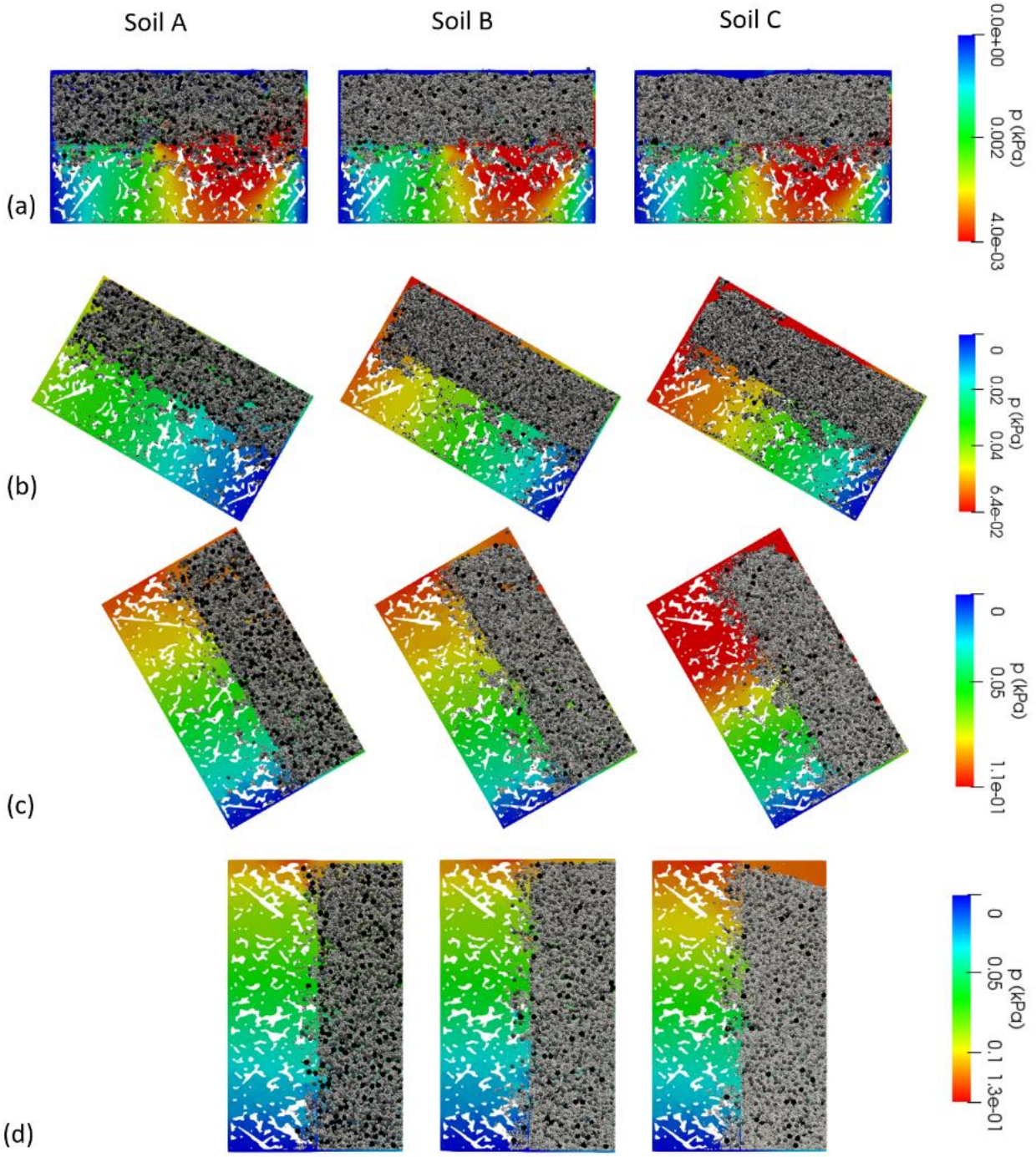

Figure 5.15. The results for pressure field highlighting the deposition patterns for soil A, soil B, and soil C for (a) $\theta = 0.003^{o}$, (b) $\theta = 30^{o}$, (c) $\theta = 60^{o}$, and (d) $\theta = 90^{o}$

As for the effect of initially increasing the radial flow on the final deposition of fine particles and the corresponding pressure increase, we carry out additional two tests for soil C under initial radial flow values of 1.5 Q_r and 2 Q_r. The reason we choose to conduct this analysis on soil C is that we wish to minimize the effect of clogging resulting from the geotextile pore spaces being of comparable size to the solid particles. In which case, the blocked particles are virtually immovable and may give misleading indication on the effect of increasing radial flow on clogging. At the end of the infiltration phase, we do not notice significant difference between the three cases. This may indicate that the dominant factor in driving the particles through the geotextile is their own weight. This may be an acceptable explanation considering the extremely small radial inflow value acting on a single crack for a tunnel radius of 5 m such that the additional momentum provided by water flow does not help further mobilizing the particles. In terms of calculated inlet pressures, we find the values for the three cases to be nearly identical (Figure 5.18).

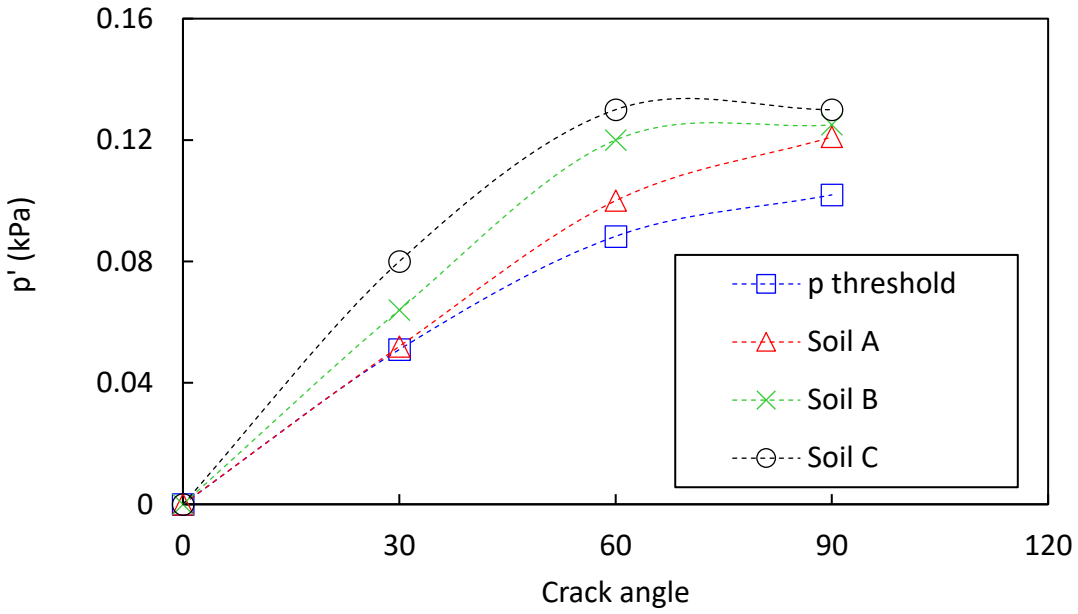

Figure 5.16. A comparison between the inlet pressure calculated from coupled CFD-DEM analysis and the threshold pressure corresponding to the critical hydraulic gradient in the drainage layer.

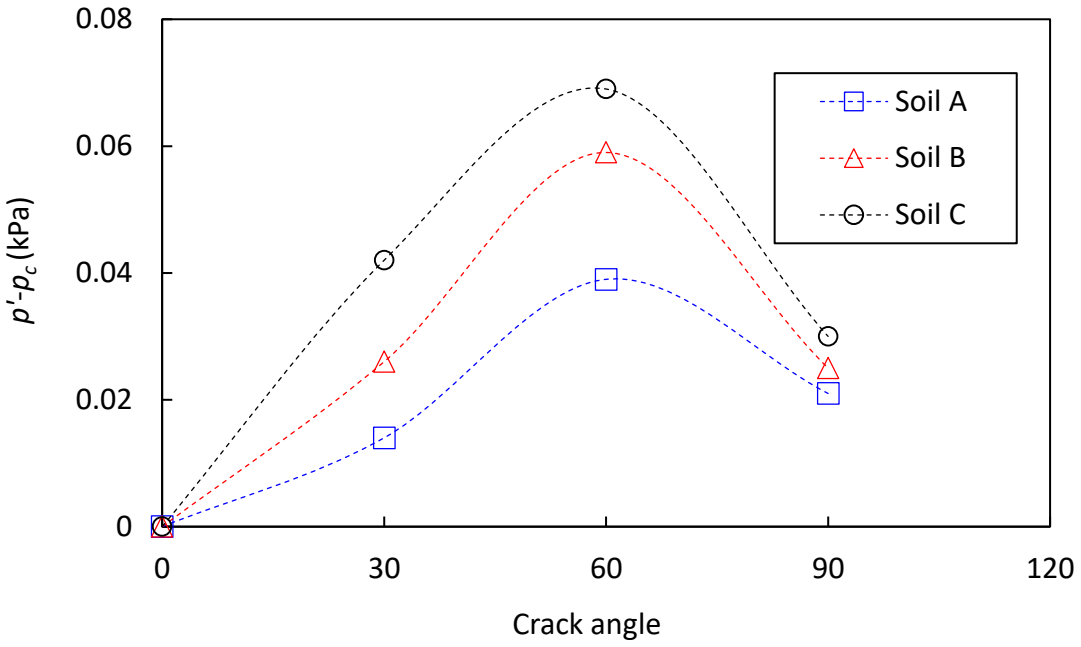

Figure 5.17. The relative pressure increase with respect to the control pressure values calculated based on capacity crack flow at $\theta = 90^{o}$.

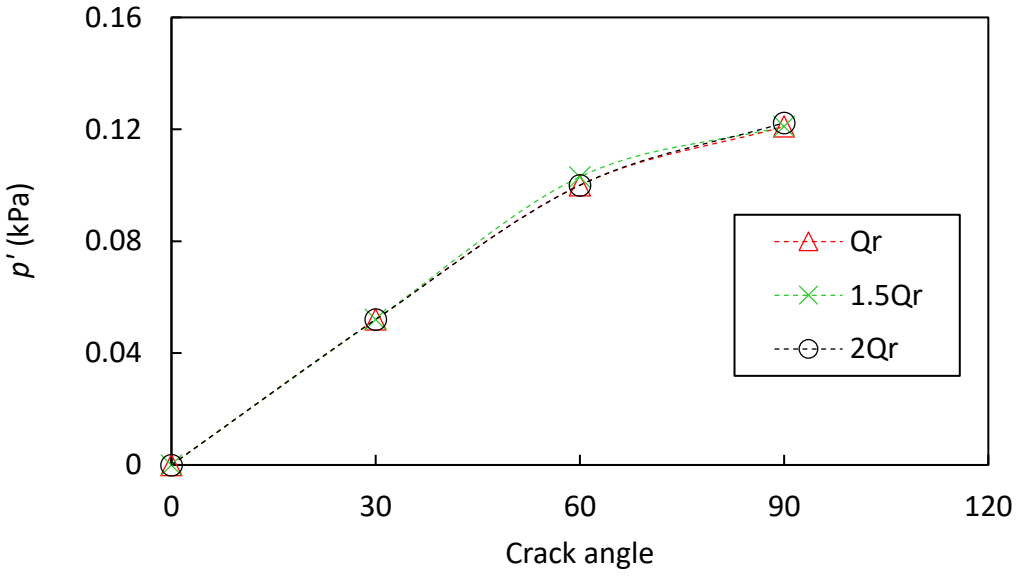

Figure 5.18. The resulting crack inlet pressure for initial radial inflow values of Q_r, $1.5Q_r$, and $2Q_r$

5.7 Approximate model for the pressure increase inside the crack

The general trend of the results shown in Figure 5.16 aligns with the sinusoidal distribution of

the threshold pressure values. This suggests the existence of some modifiers to the threshold pressure than may be able to express the calculated inlet pressure, p'. These modifiers are essentially a function in the percentage of fines, f_c, and the crack angle, θ. To obtain an expression for these modifiers we start off by looking at the flow conditions prior to clogging:

$$Q_{in} = k_g t_g i_{\text{int}} \tag{5.15}$$

where k_g is the in-plane coefficient of permeability of the geotextile, t_g is the geotextile thickness, and i_{int} is the initial hydraulic gradient derived from the crack geometry. Here we consider the contribution of the radial inflow to be negligible compared to the circumferential flow. After clogging, the effective thickness of the geotextile id reduces by some value, Δt_g, while the hydraulic gradient increases by i'. To maintain the same flow, Equation (5.15) can be expressed as:

$$Q_{in} = k_g (t_g - \Delta t_g)(i_{\text{int}} + i') \tag{5.16}$$

By expanding and rearranging the terms in Equation (5.16) we get:

$$k_g t_g i' = k_g \Delta t_g i_{\text{int}} + k_g \Delta t_g i' \tag{5.17}$$

Now, by establishing some fundamental relationships regarding the term Δt_g such that: $\Delta t_g \propto 1/\theta$ and $\Delta t_g \propto f_c$ we can state that: $\Delta t_g = A f_c t_g / \theta$, where A is a constant. Ideally, the constant A should be inflow or water level-dependent, however, we chose to role out the effect of inflow variations since they are do not significantly affect clogging in this case. Further expanding the hydraulic gradient terms such that: $i_{\text{int}} = p_{tr} / \rho g \Delta l$ and $i' = \Delta p' / \rho g \Delta l$, where Δl is the crack length, we can write:

$$\Delta p' = p_{tr} \frac{A f_c}{\theta\left(1 - \frac{A f_c}{\theta}\right)} \tag{5.18}$$

Equation (5.18) links provides the relationship between the pressure increase and the threshold pressure, where the predicted inlet pressure in this case is the sum of the pressure increase and

the threshold pressure. An issue is observed in Equation (5.18) regarding the value at the tunnel crown, $\theta = 0^{o}$ that leads to division by zero. However, since the crack has a finite length, the crack angle will always have a non-zero value. By comparing this expression to the calculated data, the best fit value for the constant A was found to be approximately 1.22. The results of the predicted values and the values calculated from the CFD-DEM analysis are shown in Figure 5.19. The results show an overall good match between the predicted and the modelled values. Some discrepancies are observed at high flowrate values at $\theta = 60^{o}$ and $\theta = 90^{o}$ for soil C and soil B. The reason for these discrepancies is likely to be caused by the local pressure relief in these particular cases due to the washout of some fine particles near the inlet. Such local changes in pressure are not accounted for in the derivation of the prediction model. Indeed, the predictive ability of the model depends greatly on the provided simulation data, which is rather limited in our case. Therefore, more investigation is still needed to confirm these calculations.

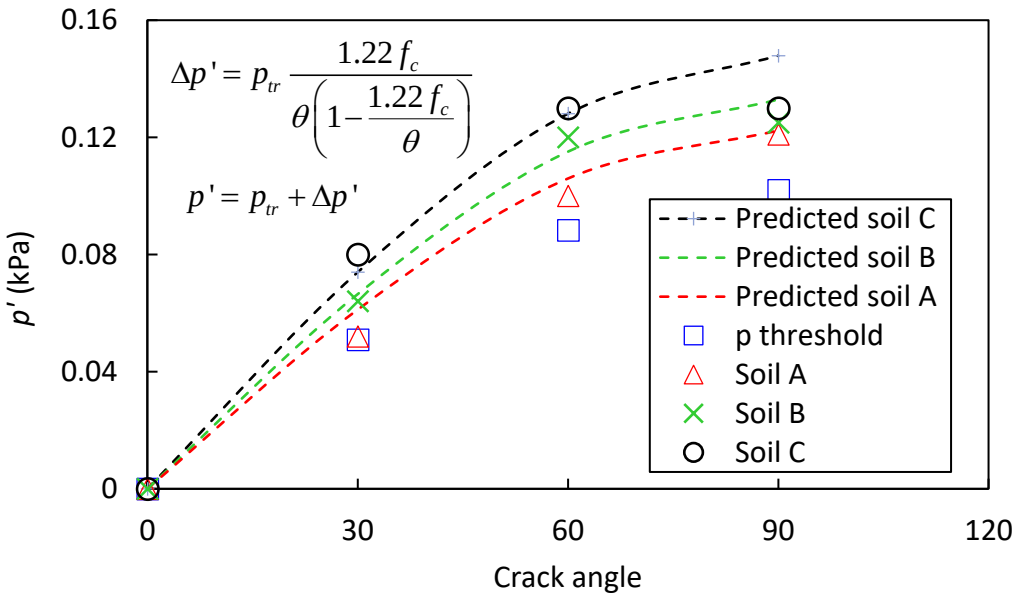

Figure 5.19. A comparison between the predicted inlet pressure values from the fitting model and the calculated values from the coupled CFD-DEM analysis.

5.8 Summary and conclusions

In this study we carry out numerical investigation of hydraulic deterioration of geotextiles used in double-shell tunnel drainage systems due to clogging by fine soil particles in the vicinity. A framework for generating and testing the non-woven geotextile is initially developed. A series of coupled CFD-DEM simulations are then conducted to validate and test the effect of the content of fines, crack angle, and inflow values on the clogging process. The following conclusions can be drawn:

1. The random 3D vector generation does not significantly affect the equivalent geotextile properties at high filament count.
2. The microscale-based estimation of the hydraulic gradient in the drainage layer provides more accurate estimation for the flow capacity of the geotextile than macroscale gradient.
3. Consistent pressure increase was observed with increasing the crack angle as well as the content of fines in the overlying soil
4. Increasing the radial inflow does not have a significant effect on the maximum clogging deposition of the solid particles.
5. At high inflow values, the model was about to capture local piping in addition to the clogging behavior in the geotextile.

Chapter 6

Conclusions and Recommendations for Future Work

6.1 General conclusions

In this thesis, a series of numerical simulations were presented including the Two-Fluid Model and coupled Computational Fluid Dynamics-Discrete Element analysis. The modeling was mainly conducted in the context of internal erosion of sandy soils around leaking pressurized and gravity pipes. In addition, a more complex simulation setting was presented in the last chapter of this thesis incorporating non-woven geotextiles used in tunnel drainage system. Within their respective studies, the models were validated using available analytical solutions or experimental data. Afterwards parametric analysis was conducted to investigate the effect of different factors on the results. The following general conclusions could be drawn from chapters 3 to 5:

In chapter 3, the Two-Fluid Model was found to provide a good representation of the interaction between water and sand in the context of water injection. This highlights the potential viability of this model in providing reasonable estimates of pressure changing and physical deformation of sand around leaking pipes. The effect of polydispersity was incorporated by dividing the solid phase into multiple solids which enabled us to investigate the behavior of different types of soil particle size distributions.

In chapter 4, the CFD-DEM simulations show a rather interesting conclusion regarding the effect of groundwater level on the erosion. Although the erosion rate is accelerated with increasing water level, it is only accelerated to a certain level, beyond which, the groundwater does not have a tangible effect on the erosion process. As for the sand layer height above the pipe, it was found to have a minor effect on the erosion rate and extent. The latter conclusion confirms the existence of a freefall arch regime even with the additional momentum provided by water flow. The investigation of the effect of crack angle shows that soil is often mobilized through inclined cracks under the effect of groundwater as opposed to mostly stable assembly existing in dry conditions. This indicates the role of sudden rise in groundwater around old and potentially cracked sewer pipes will most likely activate erosion through multiple inclined cracks, which can ultimately lead to the formation of a sinkhole.

In chapter 5, incorporating random 3D vectors to represent non-woven geotextiles could overall reproduce comparable results to that expected from an actual non-woven geotextile of the same thickness. In addition, the random process using the same seed for filament number was found to have little effect on the geotextile properties. This further supports the validity of the work flow to generate a numerical representation for non-woven geotextile. Further model validation using prescribed hydraulic gradients confirm the validity of the permeability values obtained from the CFD simulations. The model was able to capture the deposition pattern and the pressure rise for soils with different content of fines and different crack angles. It was observed that the model is able to capture localized dynamics within the crack such as piping near the inlet at high inlet flows. Increasing the radial inflow at the crack boundary was observed to have a minor effect on the final deposition of soil and the resulting pressure increase. This could be attributed to the multi-stage simulation strategy adopted in the simulation as well as the relatively small extent of the crack.

6.2 Recommendations for future work

The work presented in this thesis addresses only a limited portion of the potential applications for fully coupled microscale analysis of soil-water systems. Potential future work on this subject can be extended on both experimental and numerical fronts. The following are some recommendations for expanding the scope of this work:

- Extending the scope of the Two-Fluid Model to include the effect of cohesion in soil. This development would be quite valuable for predicting stable cavities in silts and clays.
- Carrying out an experimental study to confirm the effect of groundwater on the erosion of sand into gravity pipes.
- Expanding the scope of the sand infiltration model to include further variations of soil-water interactions such as regime change from pressurized to free-surface flows. This will help provide deeper insights into applications related to storm-surge flows and hydraulic transients in general.
- Expanding the CFD-DEM calculations to account for unsaturated mechanics, including the effect of capillary rise and humidity related effects.
- Exploring the modeling of woven geotextiles, which can provide viable insights into filtration and separation applications.

Bibliography

Adamczyk, W.P., Klimanek, A., Białecki, R.A., Węcel, G., Kozołub, P., Czakiert, T., 2014. Comparison of the standard Euler–Euler and hybrid Euler–Lagrange approaches for modeling particle transport in a pilot-scale circulating fluidized bed. Particuology 15, 129-137.

Ai, J., Chen, J.F., Rotter, J.M., Ooi, J.Y., 2011. Assessment of rolling resistance models in discrete element simulations. Powder Technology 206, 269-282.

Akbari, H., Pooyarad, A., 2020. Wave force on protected submarine pipelines over porous and impermeable beds using SPH numerical model. Appl Ocean Res 98.

Ali, H., Choi, J.H., 2019. A Review of Underground Pipeline Leakage and Sinkhole Monitoring Methods Based on Wireless Sensor Networking. Sustainability-Basel 11.

Alsaydalani, M.O.A., 2010a. Internal fluidisation of granular material. University of Southampton.

Alsaydalani, M.O.A., 2010b. Internal fluidisation of granular material. PhD thesis. University of Southampton.

Alsaydalani, M.O.A., Clayton, C.R.I., 2014. Internal Fluidization in Granular Soils. J Geotech Geoenviron 140.

Amoudry, L.O., 2014. Turbulence closure to two-phase sediment transport modelling: Application to oscillatory sheet flows. Adv Water Resour 72, 110-121.

Anderson, T.B., Jackson, R., 1967a. A fluid mechanical description of fluidized bed. Equations of motion. Industrial Engineering Industry Fundamentals 6, 527-539.

Anderson, T.B., Jackson, R., 1967b. A fluid mechanical description of fluidized bed. Equations of motion. . Industrial Engineering Industry Fundamentals 6, 527-539.

Andrews, M.J., ORourke, P.J., 1996. The multiphase particle-in-cell (MP-PIC) method for dense particulate flows. International Journal of Multiphase Flow 22, 379-402.

Arevalo, R., Zuriguel, I., 2016. Clogging of granular materials in silos: effect of gravity and outlet size. Soft Matter 12, 123-130.

Ariyaratne, W.K.H., Manjula, E.V.P.J., Ratnayake, C., Melaaen, M.C., 2016. CFD Approaches for Modeling Gas-Solids Multiphase Flows - A Review, Proceedings of The 9th EUROSIM Congress on Modelling and Simulation, EUROSIM 2016, The 57th SIMS Conference on Simulation and Modelling SIMS 2016, pp. 680-686.

Ariyaratne, W.K.H., Manjula, E.V.P.J., Ratnayake, C., Melaaen, M.C., 2018. CFD Approaches for Modeling Gas-Solids Multiphase Flows - A Review, Proceedings of The 9th EUROSIM Congress on Modelling and Simulation, EUROSIM 2016, The 57th SIMS Conference on Simulation and Modelling SIMS 2016, pp. 680-686.

ASTM, 2013. D4716 Standard test method for determining the (in-plane) flow rate per unit width and hydraulic transmissivity of a geosynthetic using a constant head. ASTM International West Conshohocken, PA, USA.

ASTM, 2016. D4751Standard Test Methods for Determining Apparent Opening Size of a Geotextile. ASTM International West Conshohocken, PA, USA.

ASTM, 2017. D4491, Test Methods for Water Permeability of Geotextiles by Permittivity, American Society for Testing and Materials.

Attard, P., Gillies, G., 2001. Deformation and adhesion of viscoelastic particles: Theory and experiment. Aust J Chem 54, 477-485.

Auton, T.R., Hunt, J.C.R., Prudhomme, M., 1988. The Force Exerted on a Body in Inviscid Unsteady Non-Uniform Rotational Flow. Journal of Fluid Mechanics 197, 241-257.

Azmir, J., Hou, Q., Yu, A., 2019. CFD-DEM simulation of drying of food grains with particle shrinkage. Powder Technology 343, 792-802.

Bakhtyar, R., Yeganeh-Bakhtiary, A., Barry, D.A., Ghaheri, A., 2009. Two-phase hydrodynamic and sediment transport modeling of wave-generated sheet flow. Adv Water Resour 32, 1267-1283.

Bakshi, A., Shahnam, M., Gel, A., Li, T., Altantzis, C., Rogers, W., Ghoniem, A.F., 2018. Comprehensive multivariate sensitivity analysis of CFD-DEM simulations: Critical model parameters and their impact on fluidization hydrodynamics. Powder Technology 338, 519-537.

Balkaya, M., Moore, I.D., Saglamer, A., 2012. Study of non-uniform bedding due to voids under jointed PVC water distribution pipes. Geotext Geomembranes 34, 39-50.

Beverloo, W.A., Leniger, H.A., Vandevelde, J., 1961. The Flow of Granular Solids through Orifices. Chemical Engineering Science 15, 260-&.

Biot, M.A., 1941. General theory of three-dimensional consolidation. J Appl Phys 12, 155-164.

Brown, P.P., Lawler, D.F., 2003. Sphere drag and settling velocity revisited. J Environ Eng-Asce 129, 222-231.

Brown, R.L., 1961. Minimum Energy Theorem for Flow of Dry Granules through Apertures. Nature 191, 458-&.

Bui, H.H., Fukagawa, R., 2013. An improved SPH method for saturated soils and its application to investigate the mechanisms of embankment failure: Case of hydrostatic pore-water pressure. International Journal for Numerical and Analytical Methods in Geomechanics 37, 31-50.

Catalano, E., Chareyre, B., Barthelemy, E., 2014. Pore-scale modeling of fluid-particles interaction and emerging poromechanical effects. International Journal for Numerical and Analytical Methods in Geomechanics 38, 51-71.

Chauchat, J., Cheng, Z., Nagel, T., Bonamy, C., Hsu, T.-J., 2017. SedFoam-2.0: a 3-D two-phase flow numerical model for sediment transport. Geoscientific Model Development 10, 4367-4392.

Chauchat, J., Guillou, S., 2008. On turbulence closures for two-phase sediment-laden flow models. Journal of Geophysical Research 113.

Chen, F., Drumm, E.C., Guiochon, G., 2011. Coupled discrete element and finite volume solution of two classical soil mechanics problems. Computers and Geotechnics 38, 638-647.

Chen, S., Doolen, G.D., 1998. Lattice Boltzmann method for fluid flows. Annual Review of Fluid Mechanics 30, 329-364.

Cheng, Z., Hsu, T.-J., Calantoni, J., 2017. SedFoam: A multi-dimensional Eulerian two-phase model for sediment transport and its application to momentary bed failure. Coastal Engineering 119, 32-50.

Cheng, Z., Hsu, T.-J., Chauchat, J., 2018. An Eulerian two-phase model for steady sheet flow using large-eddy simulation methodology. Adv Water Resour 111, 205-223.

Cleary, P.W., Monaghan, J.J., 1999. Conduction modelling using smoothed particle hydrodynamics. Journal of Computational Physics 148, 227-264.

Cloete, S., Amini, S., 2017. Implementing the Kinetic Theory of Granular Flows into the Lagrangian Dense Discrete Phase Model, 12th International Conference on CFD in Oil & Gas, Metallurgical and Process Industries, SINTEF, Trondheim, Norway.

Cook, B.K., Noble, D.R., Williams, J.R., 2004. A direct simulation method for particle-fluid systems. Engineering Computations 21, 151-168.

Courant, R., Friedrichs, K., Lewy, H., 1928

On the Partial Difference Equations of Mathematical

Physics. IBM Journal of Research and Development 11, 215-234.

Crowe, C.T., Schwarzkopf, J.D., Sommerfeld, M., Tsuji, Y., 2012. Multiphase flow with droplets and particles, 2nd ed. CRC Press.

Cui, X., Li, J., Chan, A., Chapman, D., 2014. Coupled DEM–LBM simulation of internal fluidisation induced by a leaking pipe. Powder Technology 254, 299-306.

Cundall, P.A., Strack, O.D.L., 1979. A discrete numerical model for granular assemblies. Geotechnique 29, 47-65.

DallaValle, J.M., 1948. Micromeritics : The Technology of Fine Particles, 2nd ed. Pitman Pub. Corp.

Deen, N.G., Van Sint Annaland, M., Van der Hoef, M.A., Kuipers, J.A.M., 2007. Review of discrete particle modeling of fluidized beds. Chemical Engineering Science 62, 28-44.

Di Felice, R., 1994. The Voidage Function for Fluid Particle Interaction Systems. International Journal of Multiphase Flow 20, 153-159.

Di Renzo, A., Di Maio, F.P., 2005. An improved integral non-linear model for the contact of particles in distinct element simulations. Chemical Engineering Science 60, 1303-1312.

Dickenson, J.A., Sansalone, J.J., 2009. Discrete Phase Model Representation of Particulate Matter (PM) for Simulating PM Separation by Hydrodynamic Unit Operations. Environ Sci Technol 43, 8220-8226.

Ding, J., Cidaspow, D., 1990. A Bubbling Fluidization Model Using Kinetic Theory of Granular Flow. AIChE Journal 36, 523-538.

El Tani, M., 2003. Circular tunnel in a semi-infinite aquifer. Tunn Undergr Sp Tech 18, 49-55.

Elghobashi, S., 1994. On Predicting Particle-Laden Turbulent Flows. Appl Sci Res 52, 309-329.

Ergun, S., 1952. Fluid Flow through Packed Columns. Chem Eng Prog 48, 89-94.

Fernandes, C., Semyonov, D., Ferrás, L.L., Nóbrega, J.M., 2018. Validation of the CFD-DPM solver DPMFoam in OpenFOAM® through analytical, numerical and experimental comparisons. Granular Matter 20.

Fullmer, W.D., Hrenya, C.M., 2018. Continuum prediction of scale-dependent, anisotropic fluctuating kinetic energy in gas-solid flows. Chemical Engineering Science 186, 84-87.

Garside, J., Aldibouni, M.R., 1977. Velocity-Voidage Relationships for Fluidization and Sedimentation in Solid-Liquid Systems. Ind Eng Chem Proc Dd 16, 206-214.

Gellespie, T., Settineri, W.J., 1968. The Effect of Capillary Liquid on the Force of Adhesion between Spherical Solid Particles. JOURNAL OF COLLOID AND INTERFACE SCIENCE 26, 199-202.

Gholami Korzani, M., Galindo-Torres, S.A., Scheuermann, A., Williams, D.J., 2017. SPH approach for simulating hydro-mechanical processes with large deformations and variable permeabilities. Acta Geotechnica.

Gidaspow, D., 1994. Multiphase Flow and Fluidization: Continuum and Kinetic Theory Descriptions. Boston: Academic.

Gingold, R.A., Monaghan, J.J., 1977. Smoothed Particle Hydrodynamics - Theory and Application to Non-Spherical Stars. Mon Not R Astron Soc 181, 375-389.

Giroud, J.P., Zhao, A., Richardson, G.N., 2000. Effect of thickness reduction on geosynthetic hydraulic transmissivity. Geosynth Int 7, 433-452.

Goniva, C., Kloss, C., Deen, N.G., Kuipers, J.A.M., Pirker, S., 2012. Influence of rolling friction on single spout fluidized bed simulation. Particuology 10, 582-591.

Goodman, R.E., Moye, D.G., Van Schalkwyk, A., Javandel, I., 1965. Ground water inflows during tunnel driving. Eng Geol 2, 39-56.

Gotoh, H., Okayasu, A., Watanabe, Y., 2013. Computational wave dynamics. World Scientific, Hackensack New Jersey.

Guo, C.Y., Wu, J.W., Zhu, Y., Lin, Z.B., He, S., Qian, Y.Z., Yang, H.Y., Li, H., Mao, W., 2020. Influence of clogging substances on pore characteristics and permeability of geotextile envelopes of subsurface drainage pipes in arid areas. Geotext Geomembranes 48, 735-746.

Guo, S., Shao, Y., Zhang, T.Q., Zhu, D.Z., Zhang, Y.P., 2013a. Physical Modeling on Sand Erosion around Defective Sewer Pipes under the Influence of Groundwater. Journal of Hydraulic Engineering 139, 1247-1257.

Guo, S., Zhang, T.Q., Zhang, Y.P., Zhu, D.Z., 2013b. An approximate solution for two-dimensional groundwater infiltration in sewer systems. Water Sci Technol 67, 347-352.

Guo, S., Zhu, D.Z., 2017. Soil and Groundwater Erosion Rates into a Sewer Pipe Crack. Journal of Hydraulic Engineering 143.

Guo, Y., Yu, X., 2017. Comparison of the implementation of three common types of coupled CFD-DEM model for simulating soil surface erosion. International Journal of Multiphase Flow 91, 89-100.

Hamaker, H.C., 1937. THE LONDON--VAN DER WAALS ATTRACTION BETWEEN SPHERICAL PARTICLESf. Physica 10, 1058-1072.

Han, Y., Cundall, P., 2017. Verification of two-dimensional LBM-DEM coupling approach and its application in modeling episodic sand production in borehole. Petroleum 3, 179-189.

Harada, E., Gotoh, H., Ikari, H., Khayyer, A., 2019. Numerical simulation for sediment transport using MPS-DEM coupling model. Adv Water Resour 129, 354-364.

Harada, E., Gotoh, H., Tsuruta, N., 2015. Vertical sorting process under oscillatory sheet flow condition by resolved discrete particle model. Journal of Hydraulic Research 53, 332-350.

Harada, E., Ikari, H., Shimizu, Y., Khayyer, A., Gotoh, H., 2018. Numerical Investigation of the Morphological Dynamics of a Step-and-Pool Riverbed Using DEM-MPS. Journal of Hydraulic Engineering 144.

Hardy, J., Depazzis, O., Pomeau, Y., 1976. Molecular-Dynamics of a Classical Lattice Gas - Transport Properties and Time Correlation-Functions. Phys Rev A 13, 1949-1961.

He, Y., Bayly, A.E., Hassanpour, A., Muller, F., Wu, K., Yang, D., 2018. A GPU-based coupled SPH-DEM method for particle-fluid flow with free surfaces. Powder Technology 338, 548-562.

Hilton, J.E., Ying, D.Y., Cleary, P.W., 2013. Modelling spray coating using a combined CFD–DEM and spherical harmonic formulation. Chemical Engineering Science 99, 141-160.

Hirche, D., Birkholz, F., Hinrichsen, O., 2019. A hybrid Eulerian-Eulerian-Lagrangian model for gas-solid simulations. Chemical Engineering Journal 377.

Hoomans, B.P.B., Kuipers, J.A.M., Briels, W.J., Swaaij, W.P.M., 1996. Discrete particle simulation of bubble and slug formation in a two-dimensional gas-fluidised bed: A hard-sphere approach. Chemical Engineering Science 51, 99-118.

Hsu, T.i.-J., Jenkins, J.T., Liu, P.L.-F., 2003. On two-phase sediment transport: sheet flow of massive particles. JOURNAL OF GEOPHYSICAL RESEARCH 108, 2223–2250.

Hu, D., Tang, W., Sun, L., Li, F., Ji, X., Duan, Z., 2019. Numerical simulation of local scour around two pipelines in tandem using CFD–DEM method. Appl Ocean Res 93.

Hu, H.H., 1996. Direct simulation of flows of solid-liquid mixtures. International journal of Multiphase Flow 22, 335-352.

Huang, Y., Zhang, W., Mao, W., Jin, C., 2011. Flow analysis of liquefied soils based on smoothed particle hydrodynamics. Natural Hazards 59, 1547-1560.

Ibrahim, A., Meguid, M., 2021. Continuum-Based Approach to Model Particulate Soil-Water Interaction: Model Validation and Insight into Internal Erosion. Processes 9.

Ibrahim, A., Meguid, M.A., 2020. Coupled Flow Modelling in Geotechnical and Ground Engineering: An Overview. Int J Geosynth Groun 6.

Idelsohn, S.R., Oñate, E., Pin, F.D., 2004. The particle finite element method: a powerful tool to solve incompressible flows with free-surfaces and breaking waves. International Journal for Numerical Methods in Engineering 61, 964-989.

Indiketiya, S., Jegatheesan, P., Rajeev, P., Kuwano, R., 2019. The influence of pipe embedment material on sinkhole formation due to erosion around defective sewers. Transp Geotech 19, 110-125.

Israelachvili, J.N., 2011. Intermolecular and Surface Forces, 3rd Edition. Intermolecular and Surface Forces, 3rd Edition, 1-674.

Iwashita, K., Oda, M., 1998. Rolling resistance at contacts in simulation of shear band development by DEM. J Eng Mech-Asce 124, 285-292.

Jackson, R., 2000. The dynamics of fluidized particles. Cambridge University Press, Cambridge ; New York.

Jenike, A.W., 1987. A Theory of Flow of Particulate Solids in Converging and Diverging Channels Based on a Conical Yield Function. Powder Technology 50, 229-236.

Jenkins, J.T., Savage, S.B., 1983. A theory for the rapid flow of identical, smooth, nearly elastic, spherical particles. Journal of Fluid Mechanics 130.

Jha, S.K., Bombardelli, F.A., 2009. Two-phase modeling of turbulence in dilute sediment-laden, open-channel flows. Environmental Fluid Mechanics 9, 237-266.

Jha, S.K., Bombardelli, F.A., 2010. Toward two-phase flow modeling of nondilute sediment transport in open channels. Journal of Geophysical Research 115.

Jing, L., Kwok, C.Y., Leung, Y.F., Sobral, Y.D., 2016. Extended CFD-DEM for free-surface flow with multi-size granules. International Journal for Numerical and Analytical Methods in Geomechanics 40, 62-79.

Jung, H.S., Han, Y.S., Chung, S.R., Chun, B.S., Lee, Y.J., 2013. Evaluation of advanced drainage treatment for old tunnel drainage system in Korea. Tunn Undergr Sp Tech 38, 476-486.

Kafui, K.D., Thornton, C., Adams, M.J., 2002. Discrete particle-continuum fluid modelling of gas-solid fluidised beds. Chemical Engineering Science 57, 2395-2410.

Karoui, T., Jeong, S.Y., Jeong, Y.H., Kim, D.S., 2018. Experimental Study of Ground Subsidence Mechanism Caused by Sewer Pipe Cracks. Appl Sci-Basel 8.

Kawaguchi, T., Tanaka, T., Tsuji, Y., 1998. Numerical simulation of two-dimensional fluidized beds using the discrete element method (comparison between the two- and three-dimensional models). Powder Technology 96, 129-138.

Khayyer, A., Gotoh, H., 2009. Wave Impact Pressure Calculations by Improved SPH Methods. Int J Offshore Polar 19, 300-307.

Khayyer, A., Gotoh, H., 2010. A higher order Laplacian model for enhancement and stabilization of pressure calculation by the MPS method. Appl Ocean Res 32, 124-131.

Khayyer, A., Gotoh, H., Falahaty, H., Shimizu, Y., 2018a. An enhanced ISPH–SPH coupled method for simulation of incompressible fluid–elastic structure interactions. Comput Phys Commun 232, 139-164.

Khayyer, A., Gotoh, H., Shao, S., 2009. Enhanced predictions of wave impact pressure by improved incompressible SPH methods. Appl Ocean Res 31, 111-131.

Khayyer, A., Gotoh, H., Shimizu, Y., 2017. Comparative study on accuracy and conservation properties of two particle regularization schemes and proposal of an optimized particle shifting scheme in ISPH context. Journal of Computational Physics 332, 236-256.

Khayyer, A., Gotoh, H., Shimizu, Y., Gotoh, K., Falahaty, H., Shao, S., 2018b. Development of a projection-based SPH method for numerical wave flume with porous media of variable porosity. Coastal Engineering 140, 1-22.

Khayyer, A., Tsuruta, N., Shimizu, Y., Gotoh, H., 2019. Multi-resolution MPS for incompressible fluid-elastic structure interactions in ocean engineering. Appl Ocean Res 82, 397-414.

Khudhair, H.H., Basim, K.N., Al-Baidhani, H., 2021. Experimental study of the effect on soil erosion of using tiny gravel as bedding for defective sewer pipes

4th International Conference on Engineering Sciences (ICES 2020). IOP Publishing.

Kim, K.H., Park, N.H., Kim, H.J., Shin, J.H., 2020. Modelling of hydraulic deterioration of geotextile filter in tunnel drainage system. Geotext Geomembranes 48, 210-219.

Kloss, C., Goniva, C., Hager, A., Amberger, S., Pirker, S., 2012. Models, algorithms and validation for opensource DEM and CFD-DEM. Progress in Computational Fluid Dynamics, An International Journal 12.

Koch, D.L., Hill, R.J., 2001. Inertial effects in suspension and porous-media flows. Annual Review of Fluid Mechanics 33, 619-647.

Kolymbas, D., 2005. Tunelling [sic] and tunnel mechanics : a rational approach to tunnelling, 1st ed. Springer, Berlin ; New York.

Kolymbas, D., Wagner, P., 2007. Groundwater ingress to tunnels - The exact analytical solution. Tunn Undergr Sp Tech 22, 23-27.

Konrad, K., Davidson, J.F., 1984. The Gas-Liquid Analogy in Horizontal Dense-Phase Pneumatic Conveying. Powder Technology 39, 191-198.

Koshizuka, S., Oka, Y., 1996. Moving-Particle Semi-Implicit Method for Fragmentation of Incompressible Fluid. Nuclear Science and Engineering 123, 421-434.

Kruggel-Emden, H., Kravets, B., Suryanarayana, M.K., Jasevicius, R., 2016. Direct numerical simulation of coupled fluid flow and heat transfer for single particles and particle packings by a LBM-approach. Powder Technology 294, 236-251.

Kuipers, J.A.M., Duin, K.J.V., Beckum, V., Swaaij, W.P.M.V., 1992. A numerical model of gas-fluidized beds. chemical Engineering Science 47, 1913-1924.

Kwon, J., Cho, H., 2016. Simulation of solid-liquid flows using a two-way coupled smoothed particle hydrodynamics-discrete element method model. Korean Journal of Chemical Engineering 33, 2830-2841.

Lafleur, J., 1999. Selection of geotextiles to filter broadly graded cohesionless soils. Geotext Geomembranes 17, 299-312.

Lian, G., Thornton, C., Adams, M.J., 1993. A theoretical Study of the Liquid Bridge Forces between Two Rigid Spherical Bodies. Journal of Colloid and Interface Science 161, 138-147.

Link, J.M., Deen, N.G., Kuipers, J.A.M., Fan, X., Ingram, A., Parker, D.J., Wood, J., Seville, J.P.K., 2008. PEPT and discrete particle simulation study of spout-fluid bed regimes. Aiche Journal 54, 1189-1202.

Lucy, L.B., 1977. Numerical Approach to Testing of Fission Hypothesis. Astron J 82, 1013-1024.

Lun, C.K.K., Savage, S.B., Jeffrey, D.J., Chepurniy, N., 1984. Kinetic theories for granular flow: inelastic particles in Couette flow and slightly inelastic particles in a general flowfield. Journal of Fluid Mechanics 140, 223-256.

Marble, F.E., 1963. Dynamics of a Gas containing small solid particles, 5th AGRAD symp., Braunschwig, GE, p. 175.

Marchelli, F., Bove, D., Moliner, C., Bosio, B., Arato, E., 2017. Discrete element method for the prediction of the onset velocity in a spouted bed. Powder Technology 321, 119-131.

Marrone, S., Antuono, M., Colagrossi, A., Colicchio, G., Le Touzé, D., Graziani, G., 2011. δ-SPH model for simulating violent impact flows. Computer Methods in Applied Mechanics and Engineering 200, 1526-1542.

Meguid, M.A., Dang, H.K., 2009. The effect of erosion voids on existing tunnel linings. Tunn Undergr Sp Tech 24, 278-286.

Meguid, M.A., Kamel, S., 2014. A three-dimensional analysis of the effects of erosion voids on rigid pipes. Tunn Undergr Sp Tech 43, 276-289.

MFiX, MFiX hybrid Eulerian-Lagrangian-Eulerian, available at: https://mfix.netl.doe.gov/doc/mfix/19.1.4/about.html.

Montella, E.P., Toraldo, M., Chareyre, B., Sibille, L., 2016. Localized fluidization in granular materials: Theoretical and numerical study. Phys Rev E 94.

Naili, M., Matsushima, T., Yamada, Y., 2005. A 2D Smoothed Particle Hydrodynamics method for liquefaction induced lateral spreading analysis. Journal of applied mechanics 8, 591-599.

Norouzi, H.R., Zarghami, R., Sotudeh-Gharebagh, R., Mostoufi, N., 2016. Coupled CFD-DEM Modeling: Formulation, Implementation, and Application to Multiphase Flows, First Edition ed. John Wiley & Sons, Ltd.

Ostermeier, P., DeYoung, S., Vandersickel, A., Gleis, S., Spliethoff, H., 2019. Comprehensive investigation and comparison of TFM, DenseDPM and CFD-DEM for dense fluidized beds. Chemical Engineering Science 196, 291-309.

Palmeira, E.M., Remigio, A.F.N., Ramos, M.L.G., Bernardes, R.S., 2008. A study on biological clogging of nonwoven geotextiles under leachate flow. Geotext Geomembranes 26, 205-219.

Pan, T.W., Joseph, D.D., Bai, R., Glowinski, R., Sarin, V., 2002. Fluidization of 1204 spheres: simulation and experiment. Journal of Fluid Mechanics 451, 169-191.

Passalacqua, A., Fox, R.O., 2011. Implementation of an iterative solution procedure for multi-fluid gas–particle flow models on unstructured grids. Powder Technology 213, 174-187.

Patankar, N.A., Joseph, D.D., 2001. Modeling and numerical simulation of particulate flows by the Eulerian-Lagrangian approach. International Journal of Multiphase Flow 27, 1659-1684.

Peng, C., Wang, S., Wu, W., Yu, H.-s., Wang, C., Chen, J.-y., 2019. LOQUAT: an open-source GPU-accelerated SPH solver for geotechnical modeling. Acta Geotechnica 14, 1269-1287.

Peters, B., Baniasadi, M., Baniasadi, M., Besseron, X., Donoso, A.E., Mohseni, M., Pozzetti, G., 2019. XDEM multi-physics and multi-scale simulation technology: Review of DEM–CFD coupling, methodology and engineering applications. Particuology 44, 176-193.

Potapov, A.V., Hunt, M.L., Campbell, C.S., 2001. Liquid–solid flows using smoothed particle hydrodynamics and the discrete element method. Powder Technology 116, 204–213.

Puderbach, V., Schmidt, K., Antonyuk, S., 2021. A Coupled CFD-DEM Model for Resolved Simulation of Filter Cake Formation during Solid-Liquid Separation. Processes 9.

Qian, J.G., Li, W.Y., Yin, Z.Y., Yang, Y., 2021. Influences of buried depth and grain size distribution on seepage erosion in granular soils around tunnel by coupled CFD-DEM approach. Transp Geotech 29.

Qian, Y.H., Dhumieres, D., Lallemand, P., 1992. Lattice Bgk Models for Navier-Stokes Equation. Europhys Lett 17, 479-484.

Reeks, M.W., Mckee, S., 1984. The Dispersive Effects of Basset History Forces on Particle Motion in a Turbulent-Flow. Phys Fluids 27, 1573-1582.

Rief, S., Glatt, E., Laourine, E., Aibibu, D., Cherif, C., Wiegmann, A., 2011. Modeling and Cfd-Simulation of Woven Textiles to Determine Permeability and Retention Properties. Autex Res J 11, 78-83.

Robinson, M., Ramaioli, M., Luding, S., 2014. Fluid–particle flow simulations using two-way-coupled mesoscale SPH–DEM and validation. International Journal of Multiphase Flow 59, 121-134.

Rowe, R.K., Armstrong, M.D., Cullimore, D.R., 2000. Particle size and clogging of granular media permeated with leachate. J Geotech Geoenviron 126, 775-786.

Rowe, R.K., Yu, Y., 2013. Modeling of Leachate Characteristics and Clogging of Gravel Drainage Mesocosms Permeated with Landfill Leachate. J Geotech Geoenviron 139, 1022-1034.

Rubinow, S.I., Keller, J.B., 1961. The Transverse Force on a Spinning Sphere Moving in a Viscous Fluid. Journal of Fluid Mechanics 11, 447-459.

Rubio-Largo, S.M., Janda, A., Maza, D., Zuriguel, I., Hidalgo, R.C., 2015. Disentangling the Free-Fall Arch Paradox in Silo Discharge. Phys Rev Lett 114.

Saffman, P.G., 1965. Lift on a Small Sphere in a Slow Shear Flow. Journal of Fluid Mechanics 22, 385-&.

Saffman, P.G., 1968. Correction. Journal of Fluid Mechanics 31, 624-&.

Sakai, H., Maeda, K., 2006. Seepage failure of granular ground accounting for soil-water-gas interaction. Proc Monogr Eng Wate, 273-279.

Sakai, M., Koshizuka, S., 2009. Large-scale discrete element modeling in pneumatic conveying. Chemical Engineering Science 64, 533-539.

Sakai, M., Shigeto, Y., Sun, X., Aoki, T., Saito, T., Xiong, J., Koshizuka, S., 2012. Lagrangian–Lagrangian modeling for a solid–liquid flow in a cylindrical tank. Chemical Engineering Journal 200-202, 663-672.

Salimi-Tarazouj, A., Hsu, T.J., Traykovski, P., Chauchat, J., 2021. Eulerian Two-Phase Model Reveals the Importance of Wave Period in Ripple Evolution and Equilibrium Geometry. J Geophys Res-Earth 126.

Satofuka, N., Nishioka, T., 1999. Parallelization of lattice Boltzmann method for incompressible flow computations. Comput Mech 23, 164-171.

Schaeffer, D.G., 1987. Instability in the Evolution-Equations Describing Incompressible Antigranulocytes Flow. J Differ Equations 66, 19-50.

Schaufler, A., Becker, C., Steeb, H., 2013. Infiltration processes in cohesionless soils. Zamm-Z Angew Math Me 93, 138-146.

Schiller, L., Naumann, A., 1935. A drag coefficient correlation. Zeitschrift des Vereins Deutscher Ingenieure 77, 318–320.

Shamy, U.E., Zeghal, M., 2005. Coupled Continuum-Discrete Model for Saturated Granular Soils. JOURNAL OF ENGINEERING MECHANICS 131, 413–426.

Shan, T., Zhao, J., 2014. A coupled CFD-DEM analysis of granular flow impacting on a water reservoir. Acta Mechanica 225, 2449-2470.

Shao, S.D., Lo, E.Y.M., 2003. Incompressible SPH method for simulating Newtonian and non-Newtonian flows with a free surface. Adv Water Resour 26, 787-800.

Shi, Z.-M., Zheng, H.-C., Yu, S.-B., Peng, M., Jiang, T., 2018. Application of CFD-DEM to investigate seepage characteristics of landslide dam materials. Computers and Geotechnics 101, 23-33.

Shin, J.H., 2008. Numerical modeling of coupled structural and hydraulic interactions in tunnel linings. Struct Eng Mech 29, 1-16.

Shin, J.H., Lee, I.K., Joo, E.J., 2014. Behavior of double lining due to long-term hydraulic deterioration of drainage system. Struct Eng Mech 52, 1257-1271.

Shin, J.H., Potts, D.M., Zdravkovic, L., 2005. The effect of pore-water pressure on NATM tunnel linings in decomposed granite soil. Canadian Geotechnical Journal 42, 1585-1599.

Snider, D.M., 2001. An Incompressible Three-Dimensional Multiphase Particle-in-Cell Model for Dense Particle Flows. Journal of Computational Physics 170, 523-549.

Soltanbeigi, B., Podlozhnyuk, A., Kloss, C., Pirker, S., Ooi, J.Y., Papanicolopulos, S.A., 2021. Influence of various DEM shape representation methods on packing and shearing of granular assemblies. Granular Matter 23.

Sousani, M., Hobbs, A.M., Anderson, A., Wood, R., 2019. Accelerated heat transfer simulations using coupled DEM and CFD. Powder Technology 357, 367-376.

Stokes, G.G., 1901. Mathematical and physical papers. (Cambridge University Press) 416.

Sulsky, D., Brackbill, J.U., 1991. A Numerical-Method for Suspension Flow. Journal of Computational Physics 96, 339-368.

Sulsky, D., Zhou, S.J., Schreyer, H.L., 1995. Application of a Particle-in-Cell Method to Solid Mechanics. Comput Phys Commun 87, 236-252.

Suzuki, K., Bardet, J.P., Oda, M., Iwashita, K., Tsuji, Y., Tanaka, T., Kawaguchi, T., 2007. Simulation of upward seepage flow in a single column of spheres using discrete-element method with fluid-particle interaction. J Geotech Geoenviron 133, 104-109.

Syamlal, M., Gidaspow, D., 1985. Hydrodynamics of Fluidization - Prediction of Wall to Bed Heat-Transfer Coefficients. Aiche Journal 31, 127-135.

Syamlal, M., Obrien, T.J., 1988. Simulation of Granular Layer Inversion in Liquid Fluidized-Beds. International Journal of Multiphase Flow 14, 473-481.

Syamlal, M., Rogers, W., O`Brien, T.J., 1993. MFIX documentation theory guide, United States: N. p.

Tang, Y., Chan, D.H., Zhu, D.Z., 2017a. A coupled discrete element model for the simulation of soil and water flow through an orifice. International Journal for Numerical and Analytical Methods in Geomechanics 41, 1477-1493.

Tang, Y., Chan, D.H., Zhu, D.Z., 2017b. Numerical Investigation of Sand-Bed Erosion by an Upward Water Jet. Journal of Engineering Mechanics 143.

Tang, Y., Jiang, Q., Zhou, C., 2018. A Lagrangian-based SPH-DEM model for fluid–solid interaction with free surface flow in two dimensions. Applied Mathematical Modelling 62, 436-460.

Tang, Y., Zhu, D.Z., Chan, D.H., 2017c. Experimental Study on Submerged Sand Erosion through a Slot on a Defective Pipe. Journal of Hydraulic Engineering 143.

Third, J.R., Chen, Y., Müller, C.R., 2015. Comparison between finite volume and lattice-Boltzmann method simulations of gas-fluidised beds: bed expansion and particle–fluid interaction force. Computational Particle Mechanics 3, 373-381.

Tsuji, T., Yabumoto, K., Tanaka, T., 2008. Spontaneous structures in three-dimensional bubbling gas-fluidized bed by parallel DEM-CFD coupling simulation. Powder Technology 184, 132-140.

Tsuji, Y., Kawaguchi, T., Tanaka, T., 1993. Discrete particle simulation of two-dimensional fluidized bed. Powder Technology 77, 79-87.

Tsuji, Y., Tanaka, T., Ishida, T., 1992. Lagrangian Numerical-Simulation of Plug Flow of Cohesionless Particles in a Horizontal Pipe. Powder Technology 71, 239-250.

Tsuo, Y.P., Gidaspow, D., 1990. Computation of Flow Patterns in Circulating Fluidized Beds. AIChE Journal 36, 885-896.

Vakhrushev, A., Wu, M., 2013. Verification of a Discrete Phase Model with Water-Particle Flow Experiments in a Tundish, The 5th International Conference STEELSIM, VŠB - Technical University of Ostrava,Czech Republic.

Van Deemter, J.J., Van der Laan, E.T., 1961. Momentum and Energy balances for dispersed two-phase flow. Appl. Sci. Res. 10, 102-108.

van der Hoef, M.A., van Sint Annaland, M., Deen, N.G., Kuipers, J.A.M., 2008. Numerical Simulation of Dense Gas-Solid Fluidized Beds: A Multiscale Modeling Strategy. Annual Review of Fluid Mechanics 40, 47-70.

van der Hoef, M.A., Ye, M., van Sint Annaland, M., Andrews, A.T., Sundaresan, S., Kuipers, J.A.M., 2006. Multiscale Modeling of Gas-Fluidized Beds, Computational Fluid Dynamics, pp. 65-149.

van Zyl, J.E., Alsaydalani, M.O.A., Clayton, C.R.I., Bird, T., Dennis, A., 2013. Soil fluidisation outside leaks in water distribution pipes - preliminary observations. P I Civil Eng-Wat M 166, 546-555.

VanGulck, J.F., Rowe, R.K., 2008. Parameter estimation for modelling clogging of granular medium permeated with leachate. Canadian Geotechnical Journal 45, 812-823.

Vardoulakis, I., Stavropoulou, M., Papanastasiou, P., 1996. Hydro-mechanical aspects of the sand production problem. Transport Porous Med 22, 225-244.

Wachs, A., 2019. Particle-scale computational approaches to model dry and saturated granular flows of non-Brownian, non-cohesive, and non-spherical rigid bodies. Acta Mechanica 230, 1919-1980.

Wachs, A., Hormozi, S., Hrenya, C., Pannala, S., 2018. New Frontiers in Multiphase CFD for the 21st Century Energy Mix, p. 8.

Wang, C., Wang, Y., Peng, C., Meng, X., 2016. Smoothed Particle Hydrodynamics Simulation of Water-Soil Mixture Flows. Journal of Hydraulic Engineering 142.

Wang, J.B., Niu, D.T., Zhang, Y.L., 2015. Mechanical properties, permeability and durability of accelerated shotcrete. Constr Build Mater 95, 312-328.

Wang, Z., Zhang, J., Shirazi, S.A., Dou, Y., 2019. Experimental and numerical study of erosion in a non-Newtonian hydraulic fracturing fluid. Wear 422-423, 1-8.

Weil, G.J., 1995. Remote infrared thermal sensing of sewer voids. P Soc Photo-Opt Ins 2454, 229-237.

Weller, H.G., Tabor, G., Jasak, H., Fureby, C., 1998. A tensorial approach to computational continuum mechanics using object-oriented techniques. Comput Phys 12, 620-631.

Wen, C.Y., Yu, Y.H., 1966 Mechanics of fluidization Chemical Engineering Progress Symposium Series 62, 100-111.

Wu, K., Yang, D., Wright, N., 2016. A coupled SPH-DEM model for fluid-structure interaction problems with free-surface flow and structural failure. Computers & Structures 177, 141-161.

Xu, B.H., Yu, A.B., 1997. Numerical simulation of the gas-solid flow in a fluidized bed by combining discrete particle method with computational fluid dynamics. Chemical Engineering Science 52, 2785-2809.

Xu, W.-J., Dong, X.-Y., Ding, W.-T., 2019. Analysis of fluid-particle interaction in granular materials using coupled SPH-DEM method. Powder Technology 353, 459-472.

Yang, J., Yin, Z.-Y., Laouafa, F., Hicher, P.-Y., 2020. Hydromechanical modeling of granular soils considering internal erosion. Canadian Geotechnical Journal 57, 157-172.

Yoo, C., 2016. Hydraulic deterioration of geosynthetic filter drainage system in tunnels - its impact on structural performance of tunnel linings. Geosynth Int 23, 463-480.

Zahari, N.M., Zawawi, M.H., Sidek, L.M., Mohamad, D., Itam, Z., Ramli, M.Z., Syamsir, A., Abas, A., Rashid, M., 2018. Introduction of discrete phase model (DPM) in fluid flow: A review.

Zeghal, M., El Shamy, U., 2004. A continuum-discrete hydromechanical analysis of granular deposit liquefaction. International Journal for Numerical and Analytical Methods in Geomechanics 28, 1361-1383.

Zeng, J., Li, H., Zhang, D., 2019. Numerical simulation of proppant transport in propagating fractures with the multi-phase particle-in-cell method. Fuel 245, 316-335.

Zhang, W., Maeda, K., Saito, H., Li, Z., Huang, Y., 2016. Numerical analysis on seepage failures of dike due to water level-up and rainfall using a water–soil-coupled smoothed particle hydrodynamics model. Acta Geotechnica 11, 1401-1418.

Zhang, Y., Lim, E.W.C., Wang, C.H., 2007. Pneumatic transport of granular materials in an inclined conveying pipe: Comparison of computational fluid dynamics-discrete element method (CFD-DEM), electrical capacitance tomography (ECT), and particle image Velocimetry (PIV) results. Ind Eng Chem Res 46, 6066-6083.

Zhao, T., 2017. Coupled DEM-CFD Analyses of Landslide-Induced Debris Flows, 1 ed. Science Press Beijing.

Zhao, T., Dai, F., Xu, N.W., 2017. Coupled DEM-CFD investigation on the formation of landslide dams in narrow rivers. Landslides 14, 189-201.

Zhong, W., Yu, A., Zhou, G., Xie, J., Zhang, H., 2016. CFD simulation of dense particulate reaction system: Approaches, recent advances and applications. Chemical Engineering Science 140, 16-43.

Zhou, F., Hu, S., Liu, Y., Liu, C., Xia, T., 2014. CFD–DEM simulation of the pneumatic conveying of fine particles through a horizontal slit. Particuology 16, 196-205.

Zhou, H., Wang, G., Jia, C., Li, C., 2019. A Novel, Coupled CFD-DEM Model for the Flow Characteristics of Particles Inside a Pipe. Water 11.

Zhou, J.-w., Du, C.-l., Liu, S.-y., Liu, Y., 2016. Comparison of three types of swirling generators in coarse particle pneumatic conveying using CFD-DEM simulation. Powder Technology 301, 1309-1320.

Zhou, Z.Y., Kuang, S.B., Chu, K.W., Yu, A.B., 2010. Discrete particle simulation of particle–fluid flow: model formulations and their applicability. Journal of Fluid Mechanics 661, 482-510.

Zhu, H.P., Zhou, Z.Y., Yang, R.Y., Yu, A.B., 2007. Discrete particle simulation of particulate systems: Theoretical developments. Chemical Engineering Science 62, 3378-3396.

Zhu, H.P., Zhou, Z.Y., Yang, R.Y., Yu, A.B., 2008. Discrete particle simulation of particulate systems: A review of major applications and findings. Chemical Engineering Science 63, 5728-5770.

Zou, Y., Chen, C., Zhang, L., 2020. Simulating Progression of Internal Erosion in Gap-Graded Sandy Gravels Using Coupled CFD-DEM. International Journal of Geomechanics 20.